



FINAL PROGRAM

2nd INTERNATIONAL CONFERENCE ON
NANOJOINING AND MICROJOINING

DECEMBER 7th - 10th, 2014

HOTEL SEEBLICK | EMMETTEN | SWITZERLAND

SPONSORS



PARTNERS



On behalf of the conference committees, we welcome you to the Second International Conference on Nanojoining and Microjoining (NMJ'2014) in the beautiful Swiss Alps arena. As highlighted during the first NMJ meeting in Beijing in 2012, micro- and nano-joining technologies are becoming key technologies for the cost-effective manufacturing of miniaturized devices and the successful integration of nanomaterials in functional multi-material assemblies. The development of cost-effective processes and materials in the fields of nano- and micro-joining much relies on improved fundamental understanding of, in particular, the size-dependence of materials behaviour and functional properties from the micrometre size down to the scale of atoms. Scientific and technological exchange among renowned experts from academia and industry worldwide is an essential step to advance the highly interdisciplinary research field of nano- and micro-joining for the benefit of industry and society.

The NMJ conference series provides the platform to exchange recent progress in the field of nano- and micro-joining. In course of our two-days technical program, the **fundamentals of nano-/micro-joining technologies, the integration of nano-/micro-scale materials and devices, the involved processing issues and the methods of nano-/micro-joint characterization will be presented by renowned experts in the field.** We cordially invite all of you to foster progress in the field by contributing your expertise to what promises to be a very exciting meeting. Please enjoy the time spent with the NMJ community in the wonderful landscape offered and get acquainted with Swiss culture and habits.

Finally, we would like to thank all the speakers, presenters, participants and sponsors for their participation and support.

Wishing you a rewarding NMJ'2014 conference

November 12, 2014

Conference Chairs



Lars P.H. Jeurgens



Jolanta Janczak-Rusch



Norman Zhou



Akio Hirose

CONFERENCE COMMITTEES

CONFERENCE CHAIRS

Lars P.H. Jeurgens	<i>Empa, Switzerland</i>
Jolanta Janczak-Rusch	<i>Empa, Switzerland</i>
Y. Norman Zhou	<i>University of Waterloo, Canada</i>
Akio Hirose	<i>Osaka University, Japan</i>

CONFERENCE SECRETARY

Claudia Frey	<i>Empa, Switzerland</i>
--------------	--------------------------

INTERNATIONAL ORGANIZING COMMITTEE

Florence Baras	<i>CNRS - Université de Bourgogne, France</i>
Mathieu Brochu	<i>McGill University, Canada</i>
Andriy Gusak	<i>University of Cherkasy, Ukraine</i>
Anming Hu	<i>University of Tennessee, USA</i>
Jae-Pil Jung	<i>University of Seoul, South Korea</i>
Michael Mayer	<i>University of Waterloo, Canada</i>
Luisa Coutinho	<i>Instituto Superior Tecnico, Portugal</i>
Wolfgang Tillmann	<i>University of Dortmund, Germany</i>
Tomokazu Sano	<i>Osaka University, Japan</i>
Wei Zhou	<i>Nanyang Technological University, Singapore</i>
Guisheng Zou	<i>Tsinghua University, China</i>

SCIENTIFIC ADVISORY BOARD

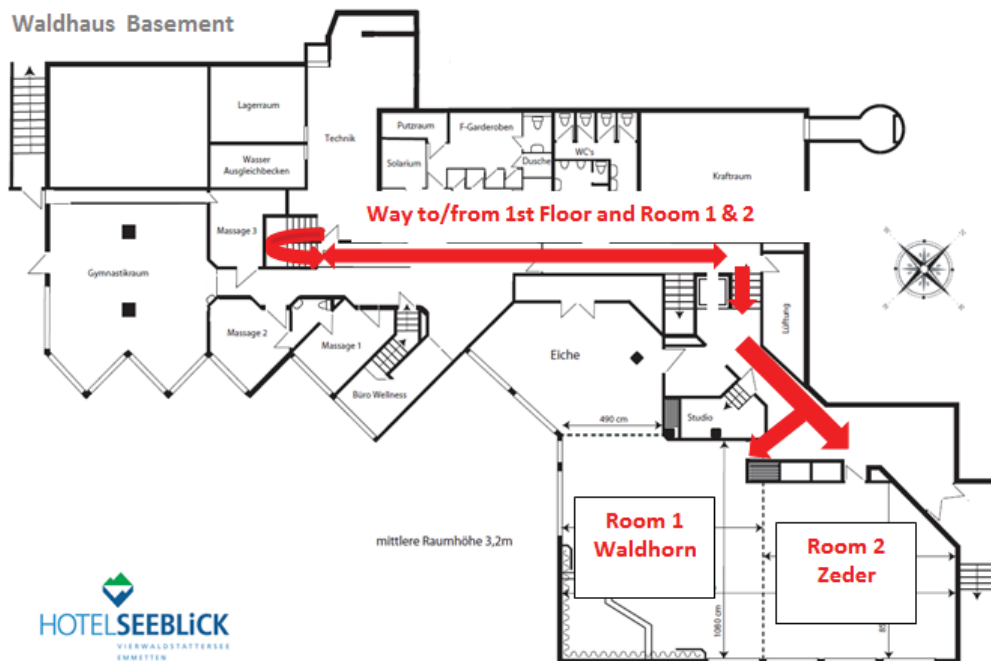
Hiroya Abe	<i>Osaka University, Japan</i>
Mark Breyen	<i>Medtronic, USA</i>
Jian Cai	<i>Tsinghua University, China</i>
Yevgenia Chvertko	<i>Kyiv Polytechnic Institute, Ukraine</i>
Alex Dommann	<i>Empa, Switzerland</i>
Dmitry Gromov	<i>Moscow Institute of Electronic Tech., Russia</i>
Pierangelo Gröning	<i>Empa, Switzerland</i>
Günther Grossmann	<i>Empa, Switzerland</i>
Peng He	<i>Harbin Institute of Techn., China</i>
George Kaptay	<i>Bay-Logi, Hungary</i>
Rosa Miranda	<i>Universidade Nova de Lisboa, Portugal</i>
Hiroshi Nishikawa	<i>Osaka University, Japan</i>
Tomo Ogura	<i>Osaka University, Japan</i>
Natalie Sobczak	<i>Foundry Institute, Poland</i>
Teresa Vieira	<i>University of Coimbra, Portugal</i>
Bernhard Wielage	<i>University of Chemnitz, Germany</i>
Mustafa Yavuz	<i>University of Waterloo, Canada</i>

SITUATION PLAN HOTEL SEEBLICK

BUILDING 1 SEEBLICK (ARRIVAL, REGISTRATION, MEALS, PLENARY & POSTER SESSION)



BUILDING 2 WALDHAUS (ROOM 1 & 2, INDOOR POOL, STEAM BATH)



MEETING AT A GLANCE

TIME	SUNDAY 7.12.14	MONDAY 8.12.14	TUESDAY 9.12.14	WEDNESDAY 10.12.14	THURSDAY 11.12.14
08:00– 08:20	ARRIVAL/ CHECK IN	OPENING			
08:20– 10:00		ORAL SESSION I	ORAL SESSION V	EXCURSION MOUNT RIGI	EMPA VISIT
10:00– 10:30		COFFEE BREAK	COFFEE BREAK		
10:30– 12:10		ORAL SESSION II	ORAL SESSION VI		
12:10– 13:30		LUNCH	LUNCH		
13:30– 15:30	REGISTRATION	ORAL SESSION III	PARALLEL ORAL SESSIONS VII AND VIII	ARRIVAL LUCERNE	
15:30– 16:00		COFFEE BREAK	COFFEE BREAK		
16:00– 18:00		ORAL SESSION IV	PARALLEL ORAL SESSIONS IX AND X	VISIT CHRISTMAS MARKET	
18:00– 19:00	WELCOME RECEPTION	BREAK	POSTER SESSION	TRANSFER TO HOTEL OR AIRPORT ZURICH	TRANSFER TO AIRPORT ZURICH
19:00– 20:00		DINNER &	BREAK		
20:00	CLOSING	SOCIAL EVENT (TORCH-LIT WALK)	SWISS GALA DINNER		
20:00– 23:00					

SOCIAL EVENTS

Welcome Reception (Sunday, 7th Dec.)

The conference will start with a welcome reception on Sunday, 7th of December, starting at 6:00 pm. Refreshments and drinks will be served in the Seeblicksaal with magnificent view on the "Vierwaldstättersee", the famous lake of the city of Luzern. The welcome reception is included in the registration fee.

Torch-lit walk with punch and chestnuts (Monday evening, 8th Dec.)

After dinner, you are invited to join for a promenade in the near-surroundings with torches, where you will be served with hot wine punch and sweet chestnuts – a typical Swiss tradition in winter time. This social event is included in the registration fee.



Swiss Gala Dinner (Tuesday evening, 9th Dec.)

On Tuesday, we will have our Swiss Gala Dinner with musical entertainment of accordion and contrabass – the traditional Swiss sound. The gala dinner is included in the registration fee.



Excursion to Mount Rigi and Luzern (Wednesday, 10th Dec.)

On Wednesday morning, we will organize a conference excursion to Mount Rigi, followed by a visit to the Christmas Market of Luzern. After the excursion, you will have the option to go directly from Luzern to Zürich Airport (or some other favourite Swiss destination).

We will leave the Hotel in the morning and drive to Vitznau, at the foot of mount Rigi. Rigi is also called the Queen of the Mountains, because she thrones majestically in the surrounding landscape. From Vitznau, we will take the first mountain railway of Europe to the top of the Rigi to enjoy our lunch with magnificent view at the Hotel Rigi Kulm. After a 2 hours break, we will take the mountain railway back to Vitznau and continue by bus to Luzern (arrival at approx. 15:30 pm). Here you can take an individual walk through the city and visit the traditional Christmas Market. About 70 homelike market stands offer all kind of fancy things and souvenirs to buy. The cultural programme offers performances with Christmas music from wind instrument players and choirs, with mainly local, young performers. A particular gem of the Christmas market is the unique nativity scene. The life-size, lifelike figures have been reproduced very realistically to reflect that era. At 17:15 pm, we will meet again to drive back to the Hotel by bus. Alternatively, you can start your home journey from Luzern or continue your journey to some another favourite Swiss destination.

Visit to Empa with subsequent transfer to Airport Zürich (Thursday, 11th Dec.)

On Thursday after breakfast, the local organizers from Empa will offer a free transfer from Emmetten to their materials research institute, the Swiss Federal Laboratories for Materials Science and Technology, in Dübendorf, which is very close to the Airport and city of Zürich. After the laboratory tours and a joined lunch, you can have a free transfer to the Airport. Please advise in the registration form, if you would like to take part in the laboratory tours at Empa. This scientific and technological experience is included in the registration fee.

TECHNICAL PROGRAM

	MONDAY, DECEMBER 8TH, 2014	PART NO.
08:00-08:20	OPENING – WELCOME - INTRODUCTION L.P.H. Jeurgens¹, J. Janczak-Rusch¹, Y.N. Zhou², A. Hirose³ ¹ <i>Empa, Swiss Federal Laboratories for Materials Science and Technology, Switzerland</i> ² <i>University of Waterloo, Centre for Advanced Materials Joining, Canada</i> ³ <i>Osaka University, Division of Materials and Manufacturing Science, Japan</i>	CHAIRS
Session	ORAL SESSION I (PLENARY)	
Room	SEEBLICK	
Chair	Y.N. Zhou, L.P.H. Jeurgens	
08:20	ASSEMBLY AND PACKAGING TECHNOLOGIES FOR POWER DEVICES AND MODULES Y. Kashiba <i>Manufacturing Engineering Center, Mitsubishi Electric Corporation, Japan</i>	KEYNOTE K1
09:00	HIGH TEMPERATURE VIABLE INTERCONNECTION REALIZED BY SINTERING Sn-M IMC NANOALLOYS AT LOW TEMPERATURE C. Wang, Y. Zhong, Z. Zheng <i>State Key Lab. of Advanced Welding & Joining, Harbin Institute of Technology, China</i>	KEYNOTE K2
09:40	SYNTHESIS AND CHARACTERIZATION OF NANOTHERMITE FOR MICRO-JOINING APPLICATIONS J.Z. Wen <i>Dept. of Mechanical & Mechatronics Engineering, University of Waterloo, Canada</i>	INVITED I4
10:00-10:30	COFFEE BREAK	
Session	ORAL SESSION II (PLENARY)	
Room	SEEBLICK	
Chair	A. Hirose, J. Janczak-Rusch	
10:30	SIZE EFFECTS ON THE THERMODYNAMIC PROPERTIES OF NANOALLOYS C. Ricolleau¹, G. Prévot², J. Nelayah¹, G. Wang¹, D. Alloyeau¹ ¹ <i>Laboratoire Matériaux et Phénomènes Quantiques, Université Paris 7 – CNRS, France</i> ² <i>Institut des Nanosciences de Paris, Université Paris 6 – CNRS, France</i>	INVITED I2
10:50	MICROSTRUCTURAL EVOLUTION OF NANO-STRUCTURED Ag-Cu/AlN BRAZING FILLERS UPON HEATING M. Lewandowska¹, M. Andrzejczuk¹, G. Pigozzi², L.P.H. Jeurgens², J. Janczak-Rusch² ¹ <i>Warsaw University of Technology, Faculty of Materials Science and Engineering, Poland</i> ² <i>Empa, Swiss Federal Laboratories for Materials Science and Technology, Switzerland.</i>	INVITED I3
11:10	SILVER SINTER JOINING AND NEW THIN FILM BONDING FOR WBG DIE-ATTACH K. Suganuma, S. Nagao, T. Sugahara, C. Oh, H. Zhang, S. Koga, S. Park <i>Institute of Scientific and Industrial Research, Osaka University, Japan</i>	INVITED I5
11:30	COPPER NANOCOMPOSITE PASTE FOR HIGH RELIABLE INTERCONNECTION AND ITS JOINING CHARACTERISTICS K.-S. Kim, S.-B. Jung <i>School of Advanced Materials Science and Eng., Sungkyunkwan University, Republic of Korea</i>	RO
11:50	NANO BRAZING TECHNOLOGY IN INDUSTRIAL ENVIRONMENT M. Türpe <i>MAHLE Behr GmbH & Co. KG, Stuttgart, Germany</i>	R1
12:10-13:30	LUNCH	

MONDAY, DECEMBER 8TH, 2014		PART NO.
Session	ORAL SESSION III (PLENARY)	
Room	SEEBLICK	
Chair	G. Zou, W. Tillmann	
13:30	BRIDGING THE GAP BETWEEN ATOMISTICS AND THERMODYNAMICS OF INTERFACES TO CONTROL WETTING AND PHASE FORMATION FOR METAL-CERAMIC JOINS <u>W.D. Kaplan</u> <i>Israel Institut of Technolgy, Israel</i>	KEYNOTE K3
14:10	STATE-OF-THE-ART LOCAL ELECTROCHEMICAL CHARACTERISATION OF MICRO- AND NANO-JOINTS <u>T. Suter</u> , P. Schmutz, J. Janczak-Rusch <i>Empa, Swiss Federal Laboratories for Materials Science and Technology, Switzerland</i>	R2
14:30	JOINING TECHNOLOGY THROUGH SINTERING OF SILVER NANOPARTICLES DERIVED FROM SILVER OXIDE PASTE <u>T. Ogura</u> , <u>A. Hirose</u> <i>Division of Materials and Manufacturing Science, Graduate School of Engineering, Osaka University, Japan</i>	R3
14:50	JOINING OF COPPER BY AG NANOPASTE: MICROSTRUCTURE AND STRENGTH BEHAVIOUR <u>B. Wielage</u> , S. Weis, H. Podlesak, <u>S. Hausner</u> <i>Institute of Materials Science and Engineering, Germany</i>	R4
15:10	SYNTHESIS AND LIGHT INDUCED NANOJOINING OF SILVER NANOWIRES <u>Y. Tian</u> , S. Ding, C. Wang <i>State Key Laboratory of Advanced Welding and Joining, Harbin institute of technology, China</i>	R5
15:30-16:00	COFFEE BREAK	
Session	ORAL SESSION IV (PLENARY)	
Room	SEEBLICK	
Chair	A. Hu, B. Wielage	
16:00	RELIABILITY OF LEAD-FREE SOLDER JOINTS IN MICROELECTRONICS <u>E. Hodúlová</u> , B. Šimeková, I. Kovaříková <i>Slovak University of Technology in Bratislava, Faculty of Materials Science and Technology in Trnava Institute of Production Technologies, Slovak Republic</i>	INVITED I6
16:20	WIREBONDER-MADE MICRO ELECTRO MECHANICAL SYSTEMS <u>J.G. Korvink</u> ¹ , <u>U. Wallrabe</u> ² ¹ University of Freiburg, Dept. of Microsystems Eng., Laboratory for Simulation, Germany ² University of Freiburg, Dept. of Microsystems Eng., Laboratory for Microactuator, Germany	INVITED I7
16:40	EFFECT OF RAPID SOLIDIFICATION ON MICROSTRUCTURE AND PROPERTIES OF Sn-Ag-Cu LEAD-FREE SOLDER <u>S. Lu</u> , F.J. Wang, Z.X. Zheng <i>Provincial Key Laboratory of Advanced Welding Technology, Jiangsu University of Science and Technology, China</i>	R6
17:00	LEAD FREE BGAS SOLDERED WITH SnPb SOLDER <u>G. Grossmann</u> ¹ , G. Nicoletti <i>EMPA, Swiss Federal Laboratories for Materials Science and Technology, Switzerland</i>	R7
17:20	EFFECT OF ISOTHERMAL AGING ON IMPACT STRENGTH OF Sn-Ag-Cu SOLDER BUMPS <u>J.X. Wang</u> ^{1,2} , H. Nishikawa ² ¹ Jiangsu Provincial Key Laboratory of Advanced Welding Technology, Jiangsu University of Science and Technology, China ² Joining and Welding Research Institute, Osaka University, Japan	R8
17:40	EFFECT OF THERMAL TREATMENT ON Cu EXTRUSION OF TSV AND SOLDER BUMPING FOR THREE-DIMENSIONAL PACKAGING S.H. Kee, M.H. Roh, S.J. Lee, <u>J.P. Jung</u> , W.J. Kim <i>Dept. of Materials Science and Engineering, University of Seoul, Korea</i>	R9
18:00-19:00	BREAK	
19:00	DINNER & SOCIAL EVENT (TORCH-LIT WALK)	

TUESDAY, DECEMBER 9th, 2014		PART NO.
Session	ORAL SESSION V (PLENARY)	
Room	SEEBLICK	
Chair	M. Mayer, P. Gröning	
08:20	FEMTOSECOND LASER NANOSTRUCTURING, PRINTING OF NANOPARTICLES, AND MICRO-JOINING <u>B. Chichkov</u> <i>Laser Zentrum Hannover e.V., Germany</i>	KEYNOTE K4
09:00	FORMATION AND CHARACTERIZATION OF SUBCLUSTER SEGREGATED NANOALLOY WITH FEMTOSECOND LASER IRRADIATION Z. Jiao ^{1,2} , W. Duley ³ , N. Zhou ^{2,4} , P. He ¹ ¹ <i>State Key Laboratory of Advanced Welding Production Technology, Harbin Institute of Technology, Harbin 150001, China</i> ² <i>Centre for Advanced Materials Joining, University of Waterloo, Canada</i> ³ <i>Dept. of Physics & Astronomy, University of Waterloo, Canada</i> ⁴ <i>Dept. of Mechanical and Mechatronics Engineering, University of Waterloo, Canada</i>	INVITED I 8
09:20	ULTRA-LOW POWER INTEGRATED PH NANOSENSORS <u>A.M. Ionescu</u> , S. Rigante, E. Buitrago <i>Nanolab, Ecole Polytechnique Fédérale de Lausanne, Switzerland</i>	INVITED I 9
09:40	GROWTH AND ASSEMBLY OF GRAPHENE THIN FILMS ON INSULATING SUBSTRATES <u>T. Ogino</u> <i>Division of Electrical and Computer Engineering, Yokohama National University, Japan</i>	INVITED I 10
10:00-10:30	COFFEE BREAK	
Session	ORAL SESSION VI (PLENARY)	
Room	SEEBLICK	
Chair	F. Baras, H. Nishikawa	
10:30	JOINING REFRACTORY AND DISSIMILAR MATERIALS USING REACTIVE NANOFOILS <u>A.S. Rogachev</u> ^{1,2} , A.S. Mukasyan ^{2,3} , S.G. Vadchenko ¹ , A.A. Nepapushev ² ¹ <i>Inst. of Structural Macrokineics & Material Science Russian Academy of Science (ISMAN), Russia</i> ² <i>Center of Functional Nano-Ceramics, National University of Science and Techn., "MISIS", Russia</i> ³ <i>Dept. of Chemical and Biomolecular Engineering, University of Notre Dame, USA</i>	INVITED I 11
10:50	ADVANCED NANOSTRUCTURE FORMATION VIA INTERFACE AND GRAIN BOUNDARY TAILORING S. Baylan ¹ , G. Richter ¹ , M. Beregovsky ² , D. Amram ² , E. Rabkin ² ¹ <i>Max Planck Institute for Intelligent Systems, Germany</i> ² <i>Dept. of Materials Science and Engineering, Technion, Israel</i>	INVITED I 12
11:10	NANOJOINING: FROM NANOSINTERING TO 3D NANOMANUFACTURING <u>A. Hu</u> ¹ , R. Li ^{1,2} , Q. Ma ¹ , D. Bridges ¹ ¹ <i>Dept. of Mechanical, Aerospace and Biomedical Eng., University of Tennessee Knoxville, USA</i> ² <i>Dept. of Electrical Engineering, Southeast University, China</i>	INVITED I 13
11:30	PATTERNING OF INDIUM TIN OXIDE MICROWIRES USING LASER-INDUCED THERMAL PRINTING METHOD <u>T. Sano</u> ¹ , S. Iwasaki ¹ , S. Katsura ² , K. Yoshida ³ , A. Nakayama ⁴ , A. Hirose ¹ ¹ <i>Div. of Materials and Manufacturing Science, Graduate School of Eng., Osaka University, Japan</i> ² <i>Nippon Denki Kagaku Co., Japan</i> ³ <i>General Co., Ltd., Japan</i> ⁴ <i>Ion Technology Center Co., Ltd., Japan</i>	INVITED I 14
11:50	EX- AND IN-SITU X-RAY BASED ANALYTICAL STUDIES ON SOLDER MATERIALS FOR MICROSYSTEMS PACKAGING APPLICATIONS <u>A. Neels</u> ¹ , T. Bandi ² , R. Kaufmann ¹ , J. Janczak-Rusch ¹ , L.P.H. Jeurgens ¹ , A. Dommann ¹ ¹ <i>Empa, Swiss Federal Laboratories for Materials Science and Technology, Switzerland</i> ² <i>SSC, Ecole Polytechnique Fédérale de Lausanne (EPFL), Switzerland</i>	R10
12:10-13:30	LUNCH	

TUESDAY, DECEMBER 9th, 2014		PART NO.
Session	ORAL SESSION VII (PARALLEL)	
Room	WALDHORN (ROOM 1)	
Chair	L. Quintino, J-P. Jung	
13:30	SOLID-LIQUID DIFFUSION BONDING OF COPPER USING Sn/Ag MULTILAYERED FILMS S. Fukumoto ¹ , K. Miyake ² , M. Matsushima ¹ , K. Fujimoto ¹ ¹ Graduate School of Engineering, Osaka University, JAPAN ² Graduate Student of Osaka University, JAPAN	R12
13:50	NANO-SIZE Ag/AIN MULTILAYERS FOR LOW TEMPERATURE JOINING APPLICATIONS M. Chiodi, F. Moszner, C. Cancellieri, G. Pigozzi, J. Janczak-Rusch, L.P.H. Jeurgens Empa, Swiss Federal Laboratories for Materials Science and Technology, Switzerland	R14
14:10	AQUEOUS Cu NANOPARTICLE INK STABILIZED BY PVP-SDS A.Y. Li ^{1,2} , B.H. Wang ² , C. Yao Huo ² ¹ State Key Laboratory of Advanced Welding & Joining, School of Materials Science & Engineering Harbin Institute of Technology, China ² School of Materials Science and Engineering, Harbin Institute of Technology at Weihai, China	R16
14:30	MELTING, MIXING AND NUCLEATION AT INTERFACES IN Ni-AI NANOFOILS : A MOLECULAR DYNAMICS APPROACH V. Turlo, O. Politano, F. Baras Laboratoire ICB, UMR 6303 CNRS-Université de Bourgogne, FRANCE	R18
14:50	START TEMPERATURE MANIPULATION AND EFFICIENCY IMPROVING OF SELF-PROPAGATION CHEMICAL REACTIONS IN MULTILAYERED THERMITE MATERIALS BASED ON ALUMINUM-COPPER NITRIDE COMPOSITE D.G. Gromov ¹ , E.A. Lebedev ¹ , S.P. Timoshenkov ¹ , Y.I. Shilyaeva ¹ , V.A. Galperin ² , D.I. Smirnov ³ , E.P. Kirilenko ⁴ ¹ National Research University of Electronic Technology, Russia ² Science Manufacturing complex "Technological Center", Russia ³ Lebedev Physical Institute of Russian Academy of Science, Russia ⁴ Science-Technological center "Nano- and Microsystems technics", Russia	R20
15:10	INVESTIGATION OF COPPER-BASED NANOSTRUCTURED MULTILAYER SYSTEMS FOR BRAZING APPLICATIONS W. Tillmann, B. Lehmert, L. Wojarski, M. Kuck TU Dortmund, Institute of Materials Engineering, Germany	R22
15:30-16:00	Coffee Break	
Session	ORAL SESSION VIII (PARALLEL)	
Room	WALDHORN (ROOM 1)	
Chairperson	P. He, M. Yavuz	
16:00	FEMTOSECOND LASER INDUCED NANOJOINING L. Liu ^{1,2} , L. Lin ¹ , D. Shen ¹ , H. Bai ¹ , G. Zou ¹ , Y.N. Zhou ³ ¹ Dept. of Mechanical Engineering, Tsinghua University, China ² The State Key Laboratory of Tribology, Tsinghua University, China ³ Dept. of Mechanical & Mechatronics Engineering, University of Waterloo, Canada	R24
16:20	TRANSIENT THERMAL IMPEDANCE OF IGBT MODULES JOINED BY LEAD-FREE SOLDER AND SINTERED NANOSILVER M.Y. Wang ¹ , Y.H. Mei ¹ , X. Li ¹ , G.Q. Lu ^{1,2} ¹ Tianjin Key Laboratory of Advanced Joining Technology, School of Material Science and Engineering, Tianjin University, China ² Dept. of Material Science and Engineering, Virginia Tech, USA	R26
16:40	LASER ASSISTED LOW TEMPERATURE HERMETIC SEALING OF OPTOELECTRONICS DEVICES R. Jose James ¹ , E. Rutz ¹ , T. Stadelmann ¹ , S. Berchtold ¹ , M. Lützel Schwab ¹ , Ch. Bosshard ¹ , M. Epitax ² , A. Hold ² , C. Vélez ² ¹ CSEM SA, Switzerland ² Exalos AG, Switzerland	R28
17:00	EFFECTS OF HEAT TREATMENT ON RESISTANCE MICROWELDING JOINTS OF CROSSED NITINOL WIRES Y. Huang ^{1,2} , A. Pequegnat ² , N. Zhou ² ¹ National Defense Key Disciplines Laboratory of Light Alloy Processing Science and Techn. Nanchang Hangkong University, China ² Centre for Advanced Materials Joining, University of Waterloo, Canada	R30
17:20	Transfer to Poster Session SEEBLICKSAAL	
17:30	POSTER SESSION SEEBLICK	

TUESDAY, DECEMBER 9th, 2014		PART NO.
Session	ORAL SESSION IX (PARALLEL)	
Room	ZEDER (ROOM 2)	
Chairperson	T. Ogura, G. Grossmann	
13:30	IMPROVEMENT OF IMPACT RELIABILITY OF SOLDER BUMPS USING LASER PROCESS H. Nishikawa¹, N. Iwata² ¹ Joining and Welding Research Institute, Osaka University, Japan ² Graduate School of Engineering, Osaka University, Japan	R13
13:50	DISPLACEMENT ANALYSIS OF BONDING WIRES UNDER DC CURRENT T. Dagdelen¹, M. Khater², S. Park², R. Saritas¹, E. Abdel-Rahman², M. Yavuz¹ ¹ Mechanical and Mechatronics Engineering Department, University of Waterloo, Canada ² Department of System Design Engineering, University of Waterloo, Canada	R15
14:10	INTERMETALLIC COMPOUND JOINTS PRODUCED BY ULTRASONIC SOLDERING PROCESS IN Cu/Sn/Cu SYSTEM M. Li^{1,2}, Z. Li¹, C. Wang² ¹ Shenzhen Key Laboratory of Advanced Materials, Harbin Institute of Technology Shenzhen Graduate School, HIT Campus, The University Town of Shenzhen, China ² State Key Laboratory of Advanced Welding and Joining, Harbin Inst. of Techn., China	R17
14:30	MECHANICAL RESPONSE ON Cu-Sn INTERMETALLICS F. Wang, X. Li, and K. Qi <i>Provincial Key Lab. of Adv. Welding Techn., Jiangsu University of Science & Techn., China</i>	R19
14:50	SHEAR STRENGTH DEGRADATION OF Pb-FREE SOLDER JOINT WITH MOUNTED LOCATION IN AUTOMOBILE W.S. Hong, A Young Kim <i>Components & Materials Physics Research Center, Korea Electronics Technology Institute</i>	R21
15:10	3D STEREOLITHOGRAPHIC PRINTING OF TERAHERTZ WAVE PHOTONIC CRYSTALS THROUGH MICRO JOINING OF OXIDE AND METALLIC GLASSES S. Kirihara <i>Joining and Welding Research Institute, Osaka University, Japan</i>	R23
15:30-16:00	Coffee Break	
Session	ORAL SESSION X (PARALLEL)	
Room	ZEDER (ROOM 2)	
Chairperson	D.G. Gromov, T. Sano	
16:00	INSPECTION OF MICRO DEFECTS USING BACTERIAL CELLS T.G. Santos¹, R.M. Miranda¹, L. Quintino², C.C.C.R. de Carvalho³ ¹ UNIDEMI, Departamento de Engenharia Médica e Industrial, Faculdade de Ciências e Tecnologia, Universidade Nova de Lisboa, Portugal ² IDMEC, Instituto Superior Técnico, Universidade de Lisboa, Portugal ³ Institute of Biotechnology and Bioengineering, Centre for Biological and Chemical Eng., Dept. of Bioengineering, Instituto Superior Técnico, Universidade de Lisboa, Portugal	R25
16:20	STABILITY AND MELTING OF FCC TRUNCATED OCTAHEDRAL AG NANOPARTICLES BY MOLECULAR DYNAMICS SIMULATION H. Alarifi¹, M. Atiş², C. Özdoğan³, A. Hu⁴, M. Yavuz⁵, Y. Zhou⁵ ¹ King Abdulaziz City for Science and Technology, Saudi Arabia ² Kayseri Vocational School, Dept. of Electricity and Energy, Erciyes University, Turkey ³ Dept. Materials Science and Engineering, Cankaya University, Turkey ⁴ Dept. Mechanical, Aerospace & Biomedical Eng., University of Tennessee Knoxville, USA ⁵ Dept. Mech. & Mechatronics Eng., Centre for Adv. Mater. Joining, Univ. of Waterloo, Canada	R27
16:40	NUMERICAL ANALYSIS OF MICROBUBBLE BEHAVIOR AND MICROPOROSITY FORMATION IN LASER BEAM WELDS OF ALUMINIUM ALLOY H. Mori¹, Q. Zhou¹, K. Koyama¹, F. Miyasaka², Y. Murakami³, Y. Kawahito³, M. Mizutani³, S. Katayama³ ¹ Osaka University, Graduate School of Eng., Dept. of Mngt. of Industry & Techn., Japan ² Osaka University, Department of Adaptive Machine Systems, Japan ³ Osaka University, Joining and Welding Research Institute, Japan	R29
17:00	EFFECT OF ITO INTERLAYER ON THE Au/Hg₃In₂Te₆ SCHOTTKY CONTACT CHARACTERISTICS L. Yapeng, C. Liu, L. Fu <i>State Key Laboratory of Solidification Processing, School of Materials Science & Eng. Northwestern Polytechnical University, China</i>	R31
17:20	Transfer to Poster Session SEEBLICKSAAL	
17:30	POSTER SESSION SEEBLICK	

TUESDAY, DECEMBER 9th, 2014		PART NO.
Session	POSTER SESSION	
18:00	<p>LOW-TEMPERATURE COMBUSTION JOINING OF CARBON/CARBON COMPOSITES A.A. Nepapushev¹, Ya-Cheng Lin², A.S. Rogachev^{1,3}, P.J. McGinn², A.S. Mukasyan^{1,2}, ¹<i>National University of Science and Technology, Russia</i> ²<i>Dept. Chem. & Biomolec. Eng., University of Notre Dame, USA</i> ³<i>Inst. of Structural Macrokinetics & Materials Science Russian Acad. of Sciences, Russia</i></p>	P1
	<p>THE MECHANISM OF MELTING POINT DEPRESSION AISi/AIN IN NANOMULTILAYERED SYSTEMS J. Lipecka¹, J. Janczak-Rusch^{1,2}, M. Andrzejczuk¹, M. Lewandowska¹, G. Richter³, L.P.H. Jeurgens² ¹<i>Warsaw University of Technology, Poland</i> ²<i>Empa, Swiss Federal Laboratories for Materials Science and Technology, Switzerland</i> ³<i>Max Planck Institute for Intelligent Systems, Germany</i></p>	P2
	<p>EFFECTS OF WARPAGE ON HIP DURING BGA PACKAGING Z. Zhao¹, Ch. Chen², Y. Wang³, Ch.Y. Park⁴, L. Liu¹, J. Cai², Q. Wang², H. Bai¹, G. Zou¹ ¹<i>Dept. of Mechanical Engineering, Tsinghua University, China</i> ²<i>Institute of Microelectronics, Tsinghua University, China</i> ³<i>Training Center for Basic Industry, Tsinghua University, China</i> ⁴<i>Samsung Electronics Co. Ltd, Korea</i></p>	P3
	<p>INVESTIGATION OF MEMORY EFFECT IN THE Ge₂Sb₂Te₅ THIN FILMS BY DC AND PULSE MEASUREMENTS P. Lazarenko¹, A. Sherchenkov¹, S. Kozyukhin², S. Timoshenko¹, D. Gromov¹, M. Michaylova¹ ¹<i>National Research University of Electronic Technology (MIET), Russia</i> ²<i>Kurnakov Institute of General and Inorganic Chemistry, RAS, Russia</i></p>	P4
	<p>RECENT R&D RESULTS OF TSINGHUA-FLEXTRONICS SMT LAB Y. Wang, T. Wang <i>Training Center for Basic Industry, Tsinghua University, Beijing 100084, China</i></p>	P5
	<p>RECENT ACHIEVEMENTS IN NANO/MICRO JOINING RESEARCHES A. Hirose, T. Sano, T. Ogura <i>Intelligent Manufacturing Process Group of Osaka University, Japan</i></p>	P6
	<p>HERMETIC TLP BONDING OF MEMS FOR HARSH ENVIRONMENTS G. Spinola Durante¹, R. Jose James¹, S. Mohrdiek¹, M. Despont², P. Niedermann² ¹<i>CSEM SA Alpnach, Switzerland</i> ²<i>CSEM SA Neuchâtel, Switzerland</i></p>	P8
	<p>LASER INDUCED MICROJOINING H. Bai¹, L. Liu^{1,2}, G. Zou¹, and Y.N. Zhou³ ¹<i>Dept. of Mechanical Engineering, Tsinghua University, China</i> ²<i>The State Key Laboratory of Tribology, Tsinghua University, China</i> ³<i>Dept. of Mechanical & Mechatronics Engineering, University of Waterloo, Canada</i></p>	P9
	<p>PREPARATION AND SEALING OF POLYMER MICROCHANNELS USING EB LITHOGRAPHY TO PATTERN ABSORBER FOR LASER WELDING I. A. Jones¹, J. Griffiths² ¹<i>TWI Ltd, Granta Park, UK</i> ²<i>Cavendish Laboratory, University of Cambridge, UK</i></p>	P10
	<p>BONDABILITY OF Mg₂Si THERMOELECTRIC ELEMENT AND NI ELECTRODE USING AI T. Tohei¹, S. Fujiwara¹, M. Tominaga², T. Jinushi², Z. Ishijima³ ¹<i>Hitachi. Ltd., Yokohama Research Laboratory, Japan</i> ²<i>Hitachi Chemical Co., Ltd., Hitachi Powdered Metals, Japan</i> ³<i>Hitachi Chemical Co., Ltd., Japan</i></p>	P11
	<p>WETTING PROPERTIES OF BOROSILICATE GLASS ON MICROSTRUCTURED KOVAR SURFACES BY HIGH-ENERGY DENSITY BEAM TEXTURING H. Li¹, M. Tie¹, Z. Li¹ and W. Tillmann² ¹<i>College of materials science and engineering, Beijing University of Technology, China</i> ²<i>Dortmund University of Technology, Germany</i></p>	P12
	<p>RECENT ADVANCES IN MICRO- AND NANOJOINING TECHNOLOGIES AT EMPA AND UNIVERSITY OF WATERLOO L.P.H. Jeurgens¹, Y. N. Zhou², J. Janczak-Rusch¹ ¹<i>Empa, Swiss Federal Laboratories for Materials Science and Technology, Switzerland</i> ²<i>University of Waterloo, Centre for Advanced Materials Joining, Canada</i></p>	P13
19:00	Break	
20:00	SWISS GALA DINNER	

Assembly and Packaging Technologies for Power Devices and Modules

Y.Kashiba

Manufacturing Engineering Center, Mitsubishi Electric Corporation, 8-1-1, Tsukaguchi-Honmachi,
Amagasaki, Hyogo, JAPAN

Email: Kashiba.Yoshihiro@ce.MitsubishiElectric.co.jp



Keywords: Power Device, Power Module, Packaging, Assembly, Reliability, SiC

1. Introduction

The concern about energy saving and CO₂ discharge reduction has been promoting the development of inverters. Electric vehicles (EVs) or air conditioners using power modules, which are thermal designed to dissipate the heat from insulated gate bipolar transistors (IGBTs). Moreover, the power modules are demanded high current, insulation capability and small size. The power modules for the EVs or the hybrid EVs, which are remarkably increasing, are demanded structural and production design for high reliability and low cost.

In this paper, a trend of new structure and reliability of power modules are discussed.

2. The structure of power modules and its trend

The power modules are constructed by circuits using some IGBTs and diodes. Fig.1 shows the package of modules, which are divided into a conventional gel sealing structure and a mold resin sealing one.

In order to improve the thermal resistance property, it is important to construct the package using materials having high thermal conductivity. The thermal conductivity of the solder is about 50 W/m·K. Ag sintered materials instead of solder can expect to achieve high heat dissipation and heat resistance property.

The recent industrial modules, especially for the EVs or the hybrid EVs, realize low thermal resistance with significant changing of its structure, as shown in Fig. 2. One of the structures is the double-sided cooling structure. The output per volume increase 60% by cooling the power device from its double-side. Moreover, direct water cooling module is developed by removing thermal grease used between the module and the heat sink. This structure can decrease 30% of thermal resistance. It is important to remove the thermal grease which has the worst thermal conductivity. In addition, double-sided direct water cooling module is proposed [1]. The power density of the module is improving by a low loss power device and a high heat dissipation package year by year as shown in Fig.3. The SiC devices, which can reduce losses significantly and use in high junction temperature, are begin to use in power modules. Consequently, it will be able to achieve further downsizing.

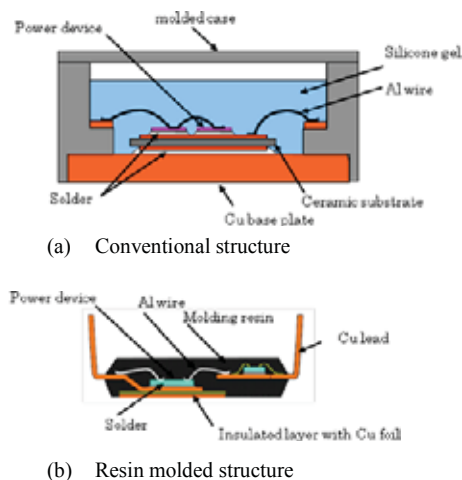


Fig.1 Package structure of power modules.

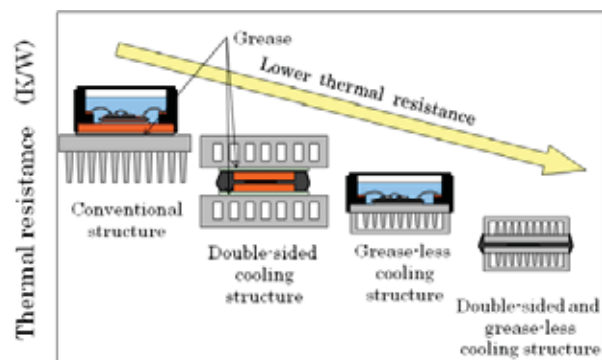


Fig.2 Trend of industrial power module package structure to reduce of thermal resistance.

3. Reliability of power modules

The power module consists of various materials in order to exert some features such as electrical circuit, insulation and heat dissipation. The thermo-mechanical reliability design is very important as the difference of the thermal expansion coefficient between the materials is large.

The thermal stress is divided into two types. One is the power cycle life. In this case, thick Al wire bonds fracture because of heating generated by short periodic current. The other is the heat cycle life. The cracks in solder layer are caused by relatively gradual temperature change due to operation of the power device or variation of the environmental temperature.

At the wire bonds, the Al electrode on the power device and the Al wire are joined directly by the ultrasonic joining. In order to improve the power cycle life, Cu lead is directly soldered on metalize layer of the power device [2]. Using this Cu lead structure and a mold resin sealing package, the power cycle life of the power device becomes 10 times longer than that of using a gel sealing package with Al wire bonding, as shown in Fig. 4. On the other hand, in order to improve the power cycle life without Cu lead, Cu wire has been considered to use [3]. Ag sinter joining is expected to improve reliability under high temperature environment [4].

In the heat cycle test, temperature is changed from 233 to 398K, its cycle time is 60 minutes. In this case, at the solder layer under the ceramic substrate, cracks propagate in solders. It is effective way to bond directly between the ceramic substrate and the heat sink, instead of using the solders.

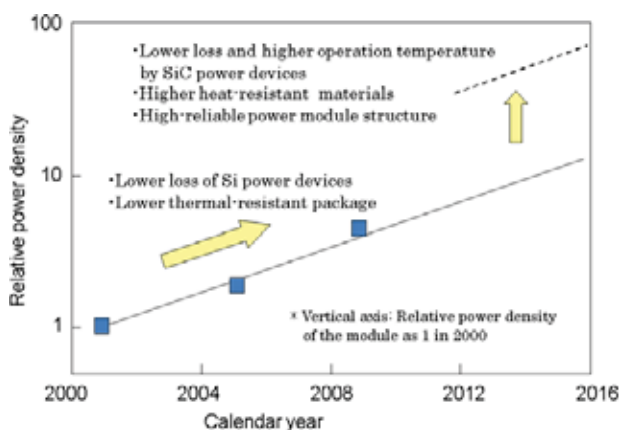


Fig. 3. Increase of power density by innovation of power devices and modules.

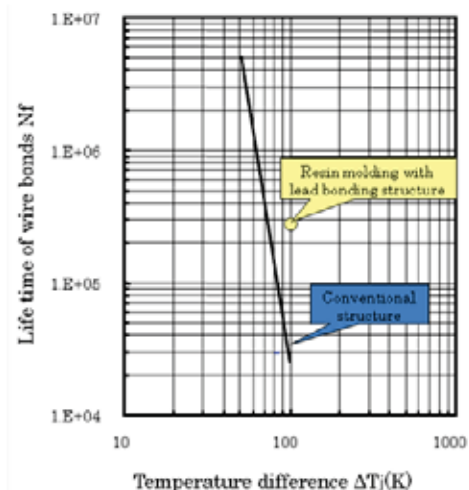


Fig.4. Power cycle results compared with conventional structure and resin molding with lead bonding structure.

4. Summary

In this paper, the trend of package structure and reliability of power modules are described.

According to downsizing the power modules, large capacity and enhancement of use application, a new structural design and reliability design will be more important. Especially, one of the expected performances of the power modules is to operate the power device under higher temperature environment. Higher reliability and wide use power module can be realized through development of a high performance power device, a structural design of package and materials which can be used under high temperature. Moreover, it is expected to expand the use of the power module, according to the SiC device which can break through the Si device is put to practical use.

References

- [1] K.Nakatsu, A.Nishihara, K.Sasaki, "A Novel Direct Water and Double-Sided Cooled Power Module and a Compact Inverter for Electrified Vehicles" EPE, 15th European Conference on (2013).
- [2] S.Sudo, A.Narazaki, H.Maeda, T.Takayama, S.Hirakawa, and Y.kashiba "Wire-bonding-less Interconnection Technique for High Current Power Modules", IMAPS(2004), 101-104.
- [3] Alexander Ciliox, Jens Gorlich, Karsten Guth, Frank Hille, Sandra Krasel, Piotr Luniewski, Dirk Siepe, Piotr Szczupak, Frank Umbach, "New module generation for higher lifetime", PCIM (2010), 238-243
- [4] G-Q. Lu, "Nanosilver Paste: Its Sintering Behavior and Applications for Chip Interconnections" IEEE International Symposium on Advanced Packaging Materials (2013)

High temperature viable interconnection realized by sintering Sn-M IMC nanoalloys at low temperature

Chunqing Wang, Ying Zhong, Zhen Zheng

*State Key Lab. of Advanced Welding & Joining, Harbin Institute of Technology, 150001 Harbin,
P. R. China*

Email: wangcq@hit.edu.cn, Zhongying@hit.edu.cn



Keywords: low temperature soldering, tin-based IMC, nanoalloys, high temperature interconnection, sintering

Abstract

The conventional interconnect materials like lead-free solders which cannot survive higher than 200°C are hindering the progress of extension of wide band gap semiconductors (like SiC or GaN), improvement of functional density, minimization of electronic devices, etc., which need long term reliable interconnection at temperature higher than 300°C. Sintering nano silver paste has been a popular approach during recent years. However, its high cost and long sintering time caused by high melting point drags it back from practical application. This paper comes up with a total novel concept of utilizing the most common IMCs (like Cu₆Sn₅, Cu₃Sn, Ni₃Sn₄, etc.) in solder bumps as interconnect materials. Taking advantage of nano-size effect (melting point reduces with particle size), the sintering of IMCs nanoalloys can be tailored to be compatible with conventional soldering process, not only in the aspect of processing temperature but also time needed. After sintering, the transformation from nano into bulk renews IMCs their bulk melting points, allowing the interconnection to survive higher than 300°C. Coprecipitation reduction is used to synthesize monocrystalline IMC nanoparticles with diameters around 10nm. The melting point of the product can be 100°C lower than IMC bulk, which is 5 times better than the reported best data about nano solders. Increasing the amount of Sn precursor produces mixed nanoparticles of pure Sn and IMC. Thanks to the melted Sn nanoparticles and its fast reaction with Cu substrate, the interconnection can be realized at 250°C in a short time, generating a whole IMC bump meanwhile.

Bridging the Gap Between Atomistics and Thermodynamics of Interfaces to Control Wetting and Phase Formation for Metal-Ceramic Joins

W.D. Kaplan

Department of Materials Science & Engineering, Technion – Israel Institute of Technology, Haifa, Israel

kaplan@tx.technion.ac.il



Keywords: Adsorption, Complexions, Interfaces, Segregation, Reconstruction

For many years it has been recognized that grain boundaries (GBs) can adopt a diffuse structural nature, forming so called “intergranular films” which have a thickness in the nanometer length-scale and a chemical content significantly different from the bulk phases in a particular system [1]. More recently, diffuse interface theory has been used to describe this phenomenon, where both the structure and chemistry of an internal or free surface can change in order to minimize the energy of the system [2]. This 2-D behavior of surfaces is very similar to the behavior of bulk phase transitions, although of course a surface is not a phase in that it cannot exist without the presence of an adjacent bulk phase. In order to clearly differentiate between this phenomenon and the bulk phases of the system, the equilibrium 2-D surface states are now often called ‘complexions’ [3]. To date, almost all studies on complexion transitions have been conducted on GBs in single phase polycrystalline systems, which by definition are not at equilibrium, and in some cases it is not even clear if the identified complexions are at steady-state [4-5]. Similar questions have been raised regarding interfaces in thin film studies, where the deposition process may be very far from equilibrium.

We have conducted a series of model experiments focusing on structural *and* chemical changes at internal surfaces (interfaces), correlated with measurements of interface energy [6-11]. This cumulated with specific model experiments demonstrating that complexions are indeed an equilibrium phenomenon [12-13], and can be directly associated with both Gibbsian excess (adsorption) and 2-D structural changes at an interface [14-15].

It is also well known that so called ‘active elements’ can be used to enhance joining of ceramics, or ceramics to metals, where an example is Ti added to braze alloys. Active elements are reported to improve wetting during the joining process, and in some cases improve the thermodynamic work of adhesion of the resulting solid-solid join. Recently it has been demonstrated that bulk reactions involving the ‘active element’ at the interface are *not* required to improve wetting, but rather that first order complexion transitions can be utilized to improve wetting during joining processes and the subsequent adhesion of the final join, without formation of undesirable interface reaction products which often accompany the use of active elements (see figure 1) [16].

This presentation will focus on an experimental approach to address the structure, chemistry, and energy of complexions at metal-ceramic interfaces which are fully equilibrated, and how complexion transitions can be used to improve joining and joins. Complexions at solid-solid metal-ceramic interfaces will be compared to complexions at solid-liquid interfaces, where a region of ordered liquid exists adjacent to the interface at equilibrium. Finally, the details of a solid-solid interface where the reconstructed interface structure accommodates lattice mismatch for a nominally incoherent interface will be described in terms of adsorption transitions.

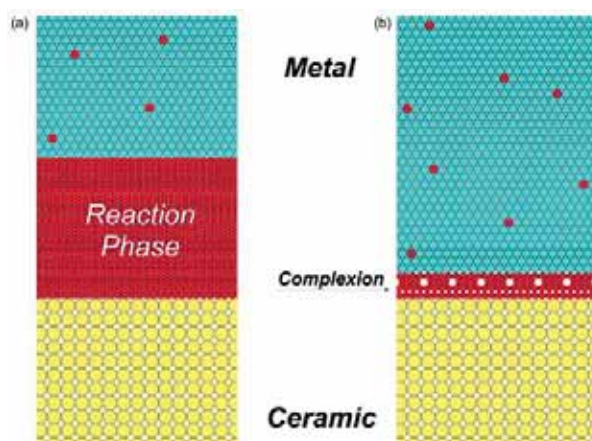


Fig. 1. Schematic drawing of an interface between a metal and a ceramic, containing either (a) a bulk reaction phase; or (b) a complexion comprised of a multilayered adsorbate of “red” atoms with a structure limited to 2-D and different from either of the bulk phases.

References

- [1] D. R. Clarke, “On the Equilibrium Thickness of Intergranular Glass Phases in Ceramic Materials,” *Journal of the American Ceramic Society*, 70, 15-22 (1987).
- [2] M. Tang, W. C. Carter, R. M. Cannon, “Grain boundary order-disorder transitions,” *Journal of Materials Science*, 41, 7691-7695 (2006).
- [3] S. J. Dillon, M. Tang, W. C. Carter, M. P. Harmer, “Complexion: A new concept for kinetic engineering in materials science,” *Acta Materialia*, 55, 6208-6218 (2007).
- [4] R. H. French, H. Mullejjans, D. J. Jones, G. Duscher, R. M. Cannon, M. Ruhle, “Dispersion forces and Hamaker constants for intergranular films in silicon nitride from spatially resolved-valence electron energy loss spectrum imaging,” *Acta Materialia*, 46, 2271-2287 (1998).
- [5] S. J. Dillon, M. P. Harmer, “Relating grain-boundary complexion to grain-boundary kinetics I: Calcia-doped alumina,” *Journal of the American Ceramic Society*, 91, 2304-2313 (2008).
- [6] S. H. Oh, Y. Kauffmann, C. Scheu, W. D. Kaplan, M. Ruhle, “Ordered Liquid Aluminum at the Interface with Sapphire,” *Science*, 310, 661-663 (2005).
- [7] S. H. Oh, M. F. Chisholm, Y. Kauffmann, W. D. Kaplan, W. Luo, M. Rühle, C. Scheu, “Oscillatory Mass Transport in Vapor-Liquid-Solid Growth of Sapphire Nanowires,” *Science*, 330, (489-493)(2010).
- [8] G. Levi, W. D. Kaplan, “Aluminium-alumina interface morphology and thermodynamics from dewetting experiments,” *Acta Materialia*, 51, 2793-2802 (2003).
- [9] A. Hashibon, J. Adler, M. W. Finnis, W. D. Kaplan, “Atomistic study of structural correlations at a liquid-solid interface,” *Computational Materials Science*, 24, 443-452 (2002).
- [10] C. Scheu, G. Dehm, W. D. Kaplan, “Equilibrium amorphous silicon-calcium-oxygen films at interfaces in copper-alumina composites prepared by melt infiltration,” *Journal of the American Ceramic Society*, 84, 623-630 (2001).
- [11] A. Avishai, C. Scheu, W. D. Kaplan, “Intergranular films at metal-ceramic interfaces Part I - interface structure and chemistry,” *Acta Materialia*, 53, 1559-1569 (2005).
- [12] M. Baram, W. D. Kaplan, “Intergranular films at Au-sapphire interfaces,” *Journal of Materials Science*, 41, 7775-7784 (2006).
- [13] M. Baram, D. Chatain, W. D. Kaplan, “Nanometer-Thick Equilibrium Films: The Interface Between Thermodynamics and Atomistics,” *Science*, 332, 206-209 (2011).
- [14] H. Meltzman, D. Mordehai, W. D. Kaplan, “Solid-Solid Interface Reconstruction at Equilibrated Ni–Al₂O₃ Interfaces,” *Acta Materialia*, 60, 4359-4369 (2012).
- [15] M. Baram, S. H. Garofalini, W. D. Kaplan, “Order in nanometer thick intergranular films at Au-sapphire interfaces,” *Acta Materialia*, 59, 5710-5715 (2011).
- [16] E. Nussbaum, H. Meltzman, W. D. Kaplan, “Equilibrium segregation of Ti to Au-sapphire interfaces,” *Journal of Materials Science*, 47, 1647-1654 (2012).

Femtosecond laser nanostructuring, printing of nanoparticles, and micro-joining

Boris Chichkov

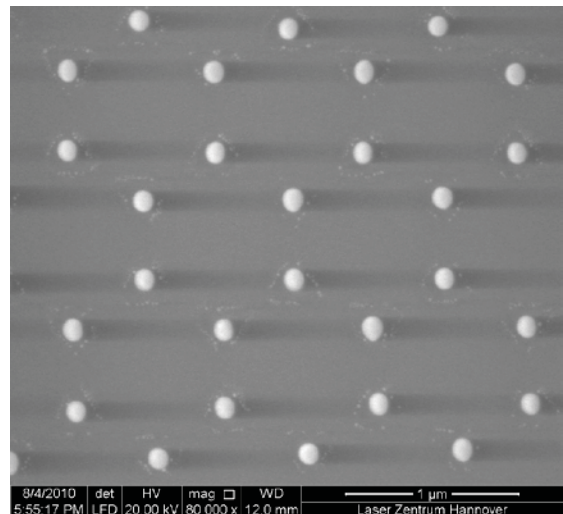
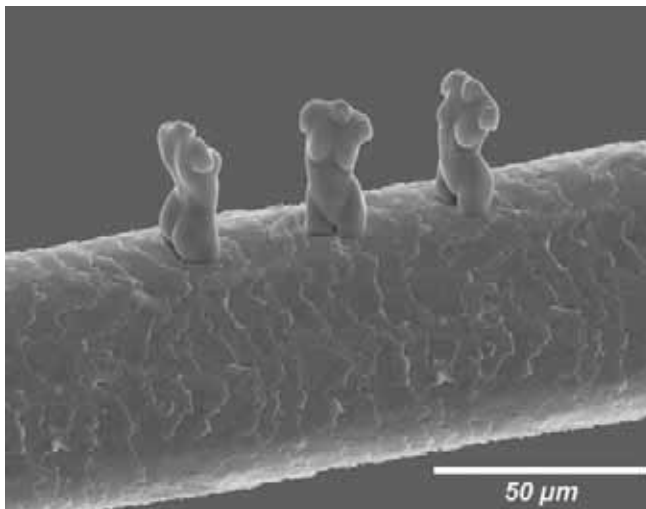
*Laser Zentrum Hannover e.V., Hollerithallee 8, 30419 Hannover, Germany
Email: b.chichkov@lzh.de.*



Keywords: Laser nanotechnology, Nanoparticles.

I will report on the development of laser-based nanomanufacturing technologies for applications in photonics and medicine. Fabrication of 3D nanostructured objects by two-photon polymerization (2PP) of photosensitive materials, generation of microstructures and nanoparticles by laser ablation, and direct laser printing of nanoparticle arrays will be discussed. Applications of these techniques for the realization of photonic and plasmonic components, sensors, and micro-joining will be demonstrated.

Two examples of laser fabricated 3D structures on a human hair and an array of 100 nm spherical gold nanoparticles are shown below.



Size effects on the thermodynamic properties of nanoalloys

C. Ricolleau¹, G. Prévot², J. Nelayah¹, G. Wang¹ and D. Alloyeau¹

¹Laboratoire Matériaux et Phénomènes Quantiques, Université Paris 7 – CNRS, Paris, France

²Institut des Nanosciences de Paris, Université Paris 6 – CNRS, Paris, France

Email: Christian.ricolleau@univ-paris-diderot.fr



Phase transition, size effect on order/disorder transformation, Ostwald ripening, Electron microscopy

Chemically ordered bimetallic nanoparticles (NPs) also called nanoalloys are promising candidates for applications in catalysis and magnetic-storage areas. However, the use of sub-10nm NPs requires further study of possible size effects on their physical properties. In the first part of this work, the effects of size and morphology on the order–disorder phase transition temperature of CoPt nanoparticles ($[T_C]^{NP}$) have been investigated experimentally, using transmission electron microscopy (Figures 1a and 1b), and theoretically, with canonical Monte Carlo simulations. For 2.4 – 3 nm particles, T_C^{NP} is found to be 325 – 175°C lower than the bulk material transition temperature (Figure 1c), consistent with our Monte Carlo simulations [1]. Furthermore, we establish that T_C^{NP} is also sensitive to the shape of the nanoparticles, because only one dimension of the particle (that is, in-plane size or thickness) smaller than 3nm (as shown by electron tomography experiment in Figure 1b) is sufficient to induce a considerable depression of $[T_C]^{NP}$. This work emphasizes the necessity of taking into account the three-dimensional morphology of nano-objects to understand and control their structural properties.

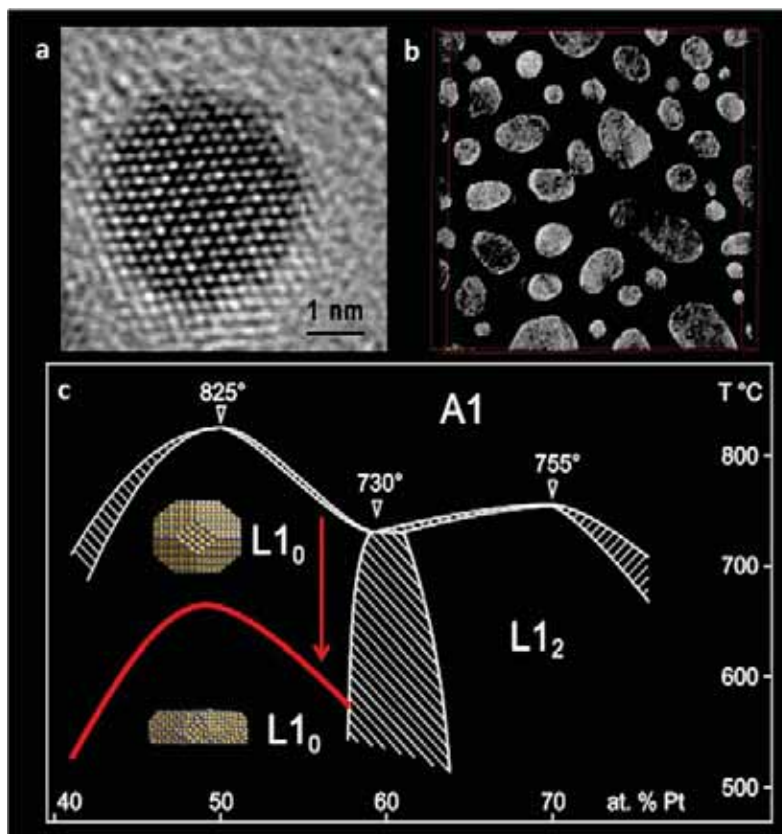


Fig. 1. (a) HRTEM image of $L1_0$ ordered CoPt nanoparticle oriented along the $[110]$ zone axis. The chemical ordered is well evidenced by the contrast difference between two successive planes along the $[001]$ direction indicating the stacking of pure Co and Pt planes. (b) 3D reconstruction of CoPt nanoparticles by electron tomography. (c) Influence of the effect of the nanoparticles shape on the decreasing of the order / disorder transition temperature in the CoPt system.

In the second part of my talk, I will focus on the size effect on the composition of bimetallic nanoalloys. This is a central question when dealing with nanoalloys because, the design of nanosystems with new and tunable properties requires understanding the phenomena that influence cluster size and composition. Ostwald ripening is a major mechanism in the heat-induced size change of nanoparticles on a substrate or in solution.

This thermo-activated process was firstly described by the Lifshitz-Slyozov-Wagner theory [2]. When they receive energy in form of heat, larger particles are more energetically favored than smaller particles. Consequently, smaller clusters shrink and the released atoms redeposit on the surface of larger particles. However, this phenomenon becomes more complex when considering the coarsening of multi-element nanoparticles. Here, we have exploited the performances of both analytical microscopy and aberration-corrected high resolution imaging to understand the atomic mechanisms involved in the coarsening of CoPt NPs.

Although NPs coarsening has been intensively studied, very little attention has been paid to the impact of this phenomenon on the composition of nanoalloys. Nanoscale analyses of the chemical composition of CoPt NPs show that the relative composition of CoPt NPs is strongly modified during annealing and displays a size-dependent behavior. To explain this effect, we have developed a thermodynamic model that takes into account the surface energy of the NPs. The consistency of our theoretical and experimental results demonstrates that the size-dependent composition of nanoalloys measured after annealing, originates from the fact that the evaporation rate of atoms from particles is about a few orders of magnitude higher for Co than for Pt. Consequently, the system tends towards the thermodynamic equilibrium for Co atoms due to their higher mobility meaning that the bigger NPs present a large excess of Co [3].

To provide experimental evidence that the exchange of atoms between the NPs is faster for Co than for Pt, we performed a quantitative analysis of single moving atoms by using aberration-corrected high resolution TEM [4]. This step forward in characterizing single atom diffusion revealed that during the coarsening of CoPt nanoparticles, the amount of atoms exchanged between the NPs is larger for Co than for Pt. Thus, this result confirms that the energy barrier for atomic evaporation from a NP to the substrate is higher for Pt than for Co, leading to faster Ostwald ripening for Co.

These results emphasize that the compositional changes due to the multiple kinetics of Ostwald ripening are expected for all nanoalloys (binary or more) as soon as they contain species with different mobilities, as it was already observed for AuPd NPs [5,6] and IrPd NPs [7]. Therefore, it is very complex to control together size and composition in nanoalloys, which is nevertheless crucial for understanding and exploiting their physical and chemical properties.

Finally, we will report on the alloying and chemical ordering in epitaxially-grown Au-Pd NPs using aberration-corrected TEM. Upon high-temperature annealing, high degree of chemical ordering was observed in nanometer-sized NPs. Electron microscopy measurements showed that both $L1_0$ and $L1_2$ phases are stabilized in the Au-rich region of the Au-Pd phase diagram. These ordered phases exist at temperatures as high as 600 °C.

Moreover, compositional analysis of single annealed particles revealed that the observed chemical ordering occurs in parallel to inhomogeneous Ostwald ripening process. The complex composition change as a result of annealing is a major obstacle in the precise control of NPs structure upon annealing. Our results, besides clarifying some controversial aspects about long-range order in the Au-Pd system, sheds light on the structural stability of Au-Pd nanoalloys at elevated temperatures.

References

- [1] D. Alloyeau, C. Ricolleau, C. Mottet, T. Oikawa, C. Langlois, Y. Le Bouar, N. Braïdy, A. Loiseau *Nature Materials*, **8**, 940-946 (2009)
- [2] I. M. Lifshitz and V. V. Slyozov, *J. Phys. Chem. Solids*, **19**, 35 (1961).
- [3] D. Alloyeau, G. Prévot, Y. Le Bouar, C. Langlois, A. Loiseau and C. Ricolleau, *Phys. Rev. Lett.*, **105**, 255901 (2010).
- [4] D Alloyeau, T. Oikawa, J. Nelayah, G. Wang and C. Ricolleau, *Appl. Phys. Lett.*, **101**, 121920 (2012).
- [5] M. Di Vece, S. Bals, J. Verbeeck and G. Van Tendeloo, *Phys. Rev. B*, **80**, 125420 (2009).
- [6] A.A. Herzing, M. Watanabe, J.K. Edwards, M. Conte, Z.R. Tang, G. J. Hutchings and C. J. Kiely, *Faraday Discuss.*, **138**, 337 (2008).
- [7] L. Piccolo, S. Nassreddine, M. Aouine, C. Ulhaq and C. Geantet, *J. Catal.*, **292**, 173 (2012).

Microstructural Evolution of Nano-structured Ag-Cu/AlN Brazing Fillers upon Heating

M. Lewandowska¹, M. Andrzejczuk¹, G. Pigozzi², L.P.H. Jeurgens², J. Janczak-Rusch²

¹Warsaw University of Technology, Faculty of Materials Science and Engineering, Poland

²Empa, Swiss Federal Laboratories for Materials Science and Technology

Email: malew@inmat.pw.edu.pl



Keywords: nanojoining, thin films, melting behaviour, nanoeffects, TEM

1. Introduction

Nanomaterials get more and more implemented into industrial applications, because of their superior mechanical and physical properties as compared to the corresponding bulk materials. Unfortunately, due to intrinsically high driving forces for interfacial reactions and/or microstructural transformations (e.g. grain growth), nanomaterials are inherently thermally unstable. Integration of nanomaterials in complex material assemblies and nanotechnologies thus requires relatively fast joining processes at reduced temperatures to preserve their tailored functional properties. Moreover, such advanced joining technologies should be cost effective and environmental friendly.

Recently, a new low-temperature brazing concept was proposed [1-3], which exploits the size-dependent melting behaviour of a metal or alloys at the nanoscale [4]. Nanomultilayered (NML) brazing fillers, constituted of alternating nanolayers (thickness < 10 nm) of a Ag-Cu alloy and a chemically inert AlN barrier layer have already been successfully applied as a nanostructured brazing filler for the joining steel well below the melting temperature of bulk eutectic Ag-Cu alloy, which hints at a significant melting point depression (MPD). The microstructural factors that govern the underlying mechanism of the MPD in such NMLs are currently under investigation. It is evidenced that the melting behaviour of the nanosized brazing fillers depends on many microstructural factors, such as the nanolayer thickness, the number of layer repetitions, the grain size, the texture, the interface structure, the alloy composition and the type of barrier. Evidently, controlling the MPD requires comprehensive understanding of the delicate and complex interplay between all these microstructural variables [3]. Previously we have investigated the effects of the size and shape of freestanding Ag-Cu nanoparticles on the phase diagram of the nano Ag-Cu system [5], as well as the Ag/AlN and Cu/AlN interface structures in nanostructured Ag-Cu/AlN brazing fillers [6]. In the present study, the microstructural transformations in Ag-Cu/AlN NMLs during heating and subsequent melting were revealed using high resolution scanning transmission electron microscopy (HRSTEM).

2. Experiments

Ag-Cu/AlN NMLs, comprising of 10 alternations of a 10 nm-thick Ag-40at.%Cu sublayer and a 10 nm-thick AlN sublayer, were deposited on sapphire substrates using reactive DC sputtering in a high vacuum chamber (base pressure < 10⁻⁶ Pa) at room temperature. The NMLs were annealed at various temperatures in the range from 400 to 900°C. The surfaces of the annealed NMLs were observed in dual beam Focus Ion Beam mode. Next cross-sectional lamellae were cut using a Focused Ion Beam. The HRSTEM observations were performed using Hitachi HD2700 HESTEM.

3. Results and Discussion

In the as-deposited state, the NMLs have a uniform thickness and a homogenous chemical composition. No phase separation between Cu and Ag is observed: i.e. a metastable amorphous Ag-Cu solid solution is formed. This means that the deposition brings about a non-equilibrium structure of highly supersaturated solid solution. Upon annealing, such a solution becomes unstable and phase separation into Ag-rich and Cu-rich regions is observed.

First droplets on the top surface of NMLs can be seen after annealing at 450°C for 30 minutes, much below the eutectic melting temperature of this alloy. The surface droplets preferentially appear at defects in the top AlN

layer, such as cracks, pores and grain boundaries. The droplets are enriched in Cu, which indicates off-eutectic melting behavior. Beside Cu-rich surface droplets, surface hillocks arise due to a local deformation of the AlN top layer. Cross-sectional TEM indicates that the Cu has accumulated underneath the hillocks, as illustrated in Fig.1. The phase separation into larger Cu-rich and Ag-rich regions is clearly visible.

At higher annealing temperatures, the NMLs structure collapses and significant outflow of brazing material is observed (Fig. 2), which principally allows joining at temperatures much below conventional brazing temperatures of corresponding bulk filler materials.

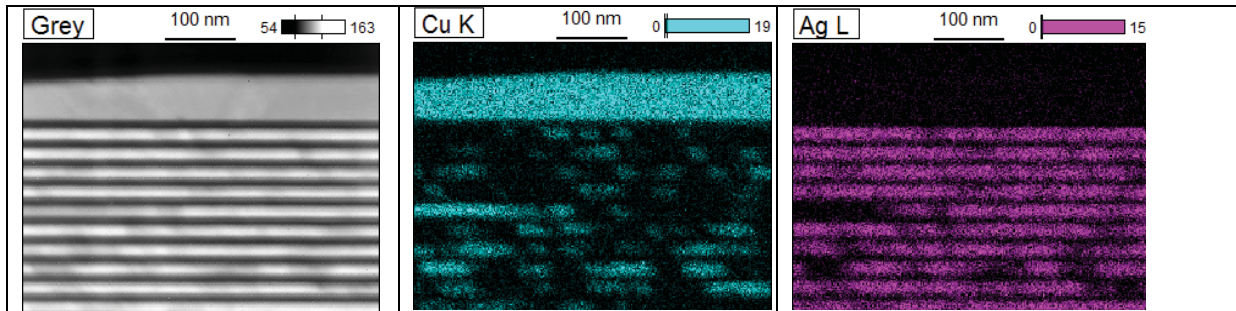


Fig. 1. Microstructure and chemical composition of Ag-Cu/AlN NMLs annealed at 600°C. Accumulation of Cu-rich braze under a top AlN layer and chemical decomposition of NMLs are visible.

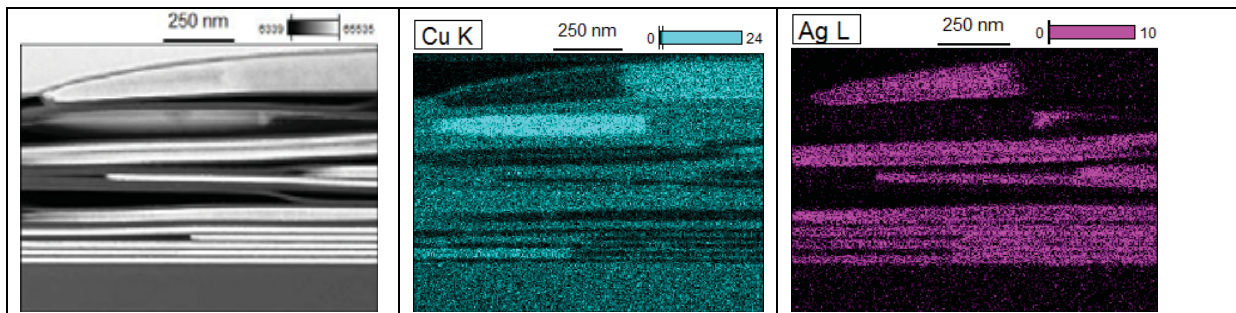


Fig. 2. Microstructure and chemical composition of the Ag-Cu/AlN NMLs annealed at 700°C. The collapse of the NML structure is observed.

4. Conclusions

This study evidences an off-eutectic melting behaviour of a nanostructured Ag-Cu alloy with a bulk eutectic composition, which is confined between AlN barriers. The off-eutectic melting is accompanied by a strong melting point depression of Cu. The observed MPD is much more pronounced than the corresponding melting point depression of the free-standing nanolayers.

References

- [1] J. Janczak-Rusch, G. Pigozzi, B. Lehmert, M. Parlinska, V. Bissig, W. Tillmann, L. Wojarski, F. Hoffmann, *Deposition and utilization of nano-multilayered brazing filler systems designed for melting point depression*, Proc. of the 5th IBSC 2012, Eds. R. Gourley and C. Walker, Las Vegas, Nevada, USA, pp. 162-168.
- [2] M. Türpe, J. Janczak-Rusch, B. Grünenwald, V. Bissig, *Approach for Al brazing with nano filler metals*, DVS-Berichte, Band 289 (2012) 125-129.
- [3] J. Janczak-Rusch, G. Kaptay and L.P.H. Jeurgens, *Interfacial design for joining technologies – An historical perspective*, JMEP 23(2014) 1608–1613.
- [4] P. Pawlow, “Über die Abhängigkeit des Schmelzpunktes von der Oberflächenergie eines festen Körpers”, *Z. Phys. Chem.*, 55, 545–548 (1908)
- [5] G. Garzel, J. Janczak-Rusch, L. Zabdyr, *Reassessment of Ag-Cu phase diagram for nanosystem including particle size and shape effect*, CALPHAD 36 (2012) 52–56.
- [6] G. Pigozzi, A. Antusek, J. Janczak-Rusch, M. Parlinska-Wojtan, D. Passerone, C.A. Pignedoli, V. Bissig, J. Patscheider, L.P.H. Jeurgens, *Phase constitution and interface structure of nano-sized Ag-Cu/AlN multilayers: Experiment and ab initio modelling*, Applied Physics Letters 101 (2012) 181602.
- [7] G. Kaptay, J. Janczak-Rusch, G. Pigozzi, and L.P.H. Jeurgens, *Theoretical Analysis of Melting Point Depression of Pure Metals in Different Initial Configurations*, JMEP 23(2014)1600-1607.

Synthesis and Characterization of Nanothermite for Micro-Joining Applications

J. Z. Wen¹

¹*Department of Mechanical & Mechatronics Engineering, University of Waterloo
200 University Avenue West, Waterloo, Ontario, N2L 3G1, Canada*

Email: john.wen@uwaterloo.ca



Keywords: Thermite, Nanothermite, Composite, Micro-joining, Heat transfer, Reactions

1. Introduction

Thermite is a pyrotechnic mixture of metal powder (fuel) and metal oxide. After ignited in air, thermite produces an exothermic oxidation-reduction reaction. If arranged appropriately this process exposes a small area of metal to high temperatures and generates an intensive heating spot which can be used to cut metals and weld components. The joining mechanism of thermite usually involves melting metal by heat and injecting molten metal as the products of the thermite reaction itself [1]. Thermite based technologies have been developed for fast and in-place repair of heavy components and quick cut or weld of rail tracks and underwater mechanisms. Copper based thermite has been used by the electrical utilities and telecommunications industries for joining together conductive copper wires and connections. The major disadvantages of these technologies, generally speaking, are product defects such as slags and voids which are often present at the joined junctions and the process controllability which requires properly handling of the ignition source, chemical reaction rates and heat transfer processes.

The metastable intermolecular composites (MIC, or nanothermite) are made of nanosized aluminum powders (n-Al, as the fuel) and a nanostructured oxide component such as CuO, Fe₂O₃, NiO, Bi₂O₃, and MoO₃, etc. Some SEM images are shown in Figure 1. After ignition, n-Al reacts rapidly with the oxide and forms new material phases, accompanied with intensive energy release and, subsequently, generation of a pressure or thermal wave in a constrained environment. Since these reactions occur at the heterogeneous solid state, their characteristics highly depend on how two reactants are mixed in the composite. Compared to conventional thermite which are mixed at the larger length scale and usually cannot react completely, nano-sized MIC have the minimized mass transport path through their intimate contact and hence provide higher power and larger total energy, thanks to the faster and more complete reactions [4]. MIC have found their promising applications in propellants, explosives, and pyrotechnics, due to fast heat and gas generation, while new research activities have been recently arranged to explore their uses in developing micro-joining and micro-welding technologies. A few review articles have recently become available, which summarize the research progress in MIC development and characterization [2] and in enabling their micro-energetics applications [5]. These articles suggest, successful development of a novel MIC requires, i) identification of its constituent elements according to their formation enthalpies; ii) synthesis and characterization of nanostructures of these components; iii) fabrication of MIC powders or certain patterns by mixing or assembling these nanoparticles; iv) characterization of thermal-chemical properties including energy and gas generation; v) integration of MIC into micro-joining and other technologies for providing energy and power in practical situations.

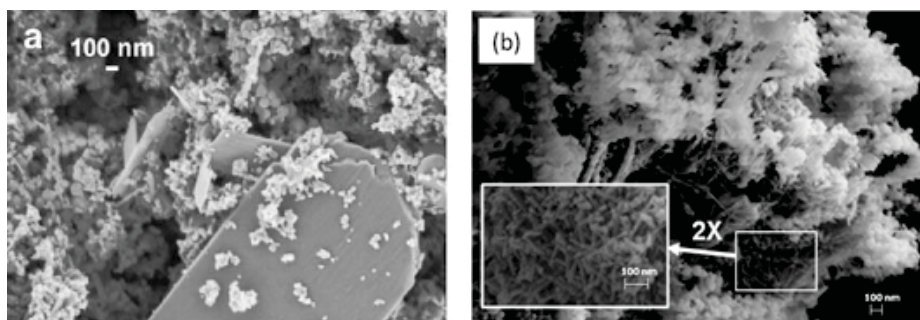


Fig. 1. Spherical nanoparticles reported in literature [2] and the NiO nanowires produced in Dr. Wen's group [3].

The fabrication methods of n-Al are relatively known and classified into vapor phase condensation and liquid phase chemistry approaches [2]. The produced n-Al are often covered with a 4-5 nm thick layer of Al₂O₃ which acts as a passivation shell and ensures safe handling and storage. While most MIC have been formulated with oxide nanoparticles, which are fabricated in a similar way to n-Al, recently CuO and NiO nanowires have shown their improved contacting with n-Al and subsequently faster reaction rates [6,7]. Ultrasonic mixing in a solvent bath is often used to make the MIC power, while recently a supercritical dispersion technique using CO₂ was reported [2]. Sol-gel processing is an alternative approach, during which n-Al are arranged to reside in the pores of a matrix made of the oxidizer. The sol-gel chemistry provides a process advantage over ultrasonic mixing with reduced cost and improved safety, with the identified limitations of inhibited self-sustaining reactions and lower heat generation rates [8]. Vapor deposition has been developed to deposit or sputter a thin film of MIC on the substrate under vacuum condition [9]. Two components can be deposited simultaneously or separately, which results in a variable thickness of the intermixed region that controls reaction rates. Another interesting technique is the molecular self-assembly, which belongs to the bottom-up approach and aims at assembling core-shell, layer-by-layer, and membrane-like fuel/oxide structures. Those methods, however, are still under development for potential scaling up in engineering applications.

Despite intensive research activities in studying MIC over the past 10 years, a throughout understanding of thermochemistry and reaction characteristics of MIC is still missing. With the advanced microscopy (Scanning electron (SEM) and transmission electron (TEM)) and analytical chemistry techniques (BET, selective area X-ray diffraction (SAD) and powder x-ray diffraction (XRD)) to examine the material, morphological, compositional and contacting properties of fuel and oxide nanoparticles, TGA and DSC are often used to quantify the onset temperature and energy release from the thermite reactions of MIC. Recently researchers urged to investigate ignition mechanism and combustion kinetics of MICs, which are poorly understood, mainly attributed to the uncertainties in quantifying the intimate degree of the composite and difficulties of imaging nanostructure transformations and phase changes under chemically reacting and rapid energy evolving conditions. To achieve those, advanced diagnostic technologies are needed in characterizing the combustion rate and flame propagation speed of MICs, which vary often with the shape and type of testing MIC specimen.

In this talk, Dr. Wen will provide a general review on challenges and opportunities of developing MIC based technologies for micro-joining and welding applications. Some examples and demonstrations will be taken from the recent results of his research group. Both experimental and numerical studies will be highlighted.

References

- [1] http://en.wikipedia.org/wiki/Thermite#Civilian_uses. Accessed on May 20, 2014.
- [2] E.L. Dreizin, "Metal-based reactive nanomaterials," *Progress in Energy and Combustion Science*, 35, 141-167 (2009).
- [3] J.Z. Wen, S. Ringuette, G. Bohlouli-Zanjani, A. Hu, H.N. Ngoc, J. Persic, C.F. Petre, Y.N. Zhou, "Characterization of thermochemical properties of Al nanoparticle and NiO nanowire composites," *Nanoscale Research Letters*, 8, 2013, 8:184 (2013).
- [4] A. Miziolek, "Nanoenergetics: an emerging technology area of national importance," *The AMPTIAC Newsletter (Special Issue: Nanotechnology)*, 6, 43-48 (2002).
- [5] C. Rossi, K. Zhang, D. Esteve, P. Alphonse, P. Tailhades, C. Vahlas. "Nanoenergetic materials for MEMS: A review," *Journal of Microelectromechanical Systems*, 16, 919-931 (2007).
- [6] G. Bohlouli-Zanjani, J.Z. Wen, A. Hu, J. Persic, S. Ringuette, Y.N. Zhou, "Thermo-chemical characterization of a Al nanoparticle and NiO nanowire composite modified by Cu powder," *Thermochimica Acta*, 572, 51-58 (2013).
- [7] R. Shende, S. Subramanian, S. Hasan, S. Apperson, R. Thiruvengadathan, K. Gangopadhyay, S. Gangopadhyay, P. Redner, D. Kapoor, S. Nicolich, W. Balas, "Nanoenergetic composites of CuO nanorods, nanowires, and Al-nanoparticles," *Propellants Explos Pyrotech*, 33, 122-130 (2008).
- [8] D. Prentice, M.L. Pantoya, A.E. Gash, "Combustion wave speeds of sol-gel-synthesized tungsten trioxide and nano-aluminum: The effect of impurities on flame propagation," *Energy & Fuels*, 20, 2370-2376 (2006).
- [9] N. Quang, K.Y. Park, K.Y. Jung, S.B. Cho, "Vapor-phase synthesis of a solid precursor for alpha-alumina through a catalytic decomposition of aluminum triisopropoxide," *Materials Research Bulletin*, 46, 2199-2203 (2011).

Silver Sinter Joining and New Thin Film bonding for WBG die-attach

K. Suganuma, S. Nagao, T. Sugahara, C. Oh, H. Zhang, S. Koga, and S. Park

*Institute of Scientific and Industrial Research, Osaka University
8-1 Mihogaoka, Ibaraki Osaka 567-0047, Japan*

Email: suganuma@sanken.osaka-u.ac.jp



Keywords: Silver, Sinter joining, Stress migration bonding, Silver film, Die-attach, SiC, GaN

1. Introduction

High temperature lead-free solder has been under development though several candidates have been already proposed such as Bi alloys and pure Zn/Zn-Sn alloys as well as the conventional Au alloys [1-3]. Transient liquid phase bonding is also examined for off-eutectic Au or Ag alloys. Nowadays, wide band gap power semiconductors (WBGs) such as SiC or GaN with their excellent performances have been expected to be used in harsh environments. Among various proposals for die-attach materials and processes, Ag sinter joining is a promising approach for power semiconductors as well as for power LED, providing excellent heat-resistant of stable joint structures beyond 200 °C. This paper summarizes the present status of the Ag sinter joining and of the new approach with Ag film bonding, both of which have developed by the authors' group.

2. Ag sinter joining in air

Sinter joining with Ag nanoparticles under pressure is an attractive choice of die-attach [4, 5]. Nevertheless, the high pressure beyond 5 MPa required for the joining may become a critical issue for thin and brittle semiconductor dies. In contrast, sinter joining with micron-sized Ag hybrid particle pastes provide a stable bonding structure at 200 °C without applied high pressure [1, 6]. Figure 1 shows an example of a LED die-attach with the hybrid paste [6].

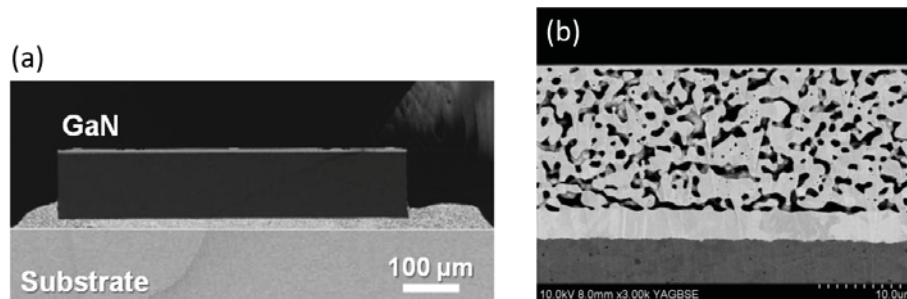


Fig.1 (a) GaN LED die-attach structure with Ag hybrid paste, and (b) sintered microstructure observed in cross-section of (a) [6].

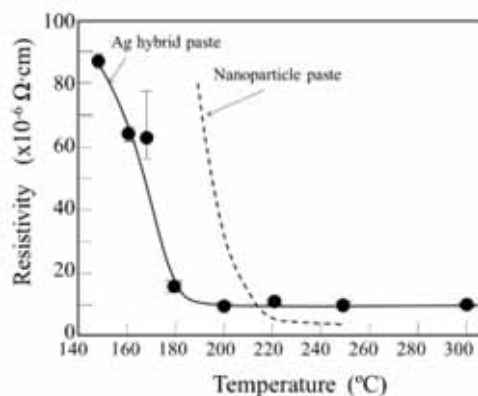


Fig. 2 Resistivity change of printed lines of Ag hybrid paste compared with nanoparticle paste as a function of sintering temperature [2].

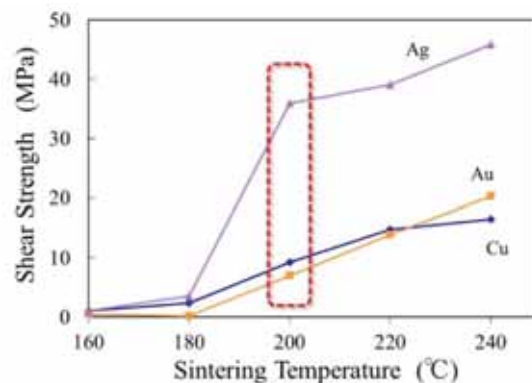


Fig. 3 Bonding shear strength as a function of temperature with Ag microflake paste on three substrates [9].

The presence of oxygen plays a key role in cleaning the surface of Ag at around 200 °C in air resulting in a successful low-temperature low-pressure Ag sintering joining [7]. Ag can clean its surface around 200 °C in air atmosphere. Fig.2 shows the resistivity change, which is a good scale of sintering, of printed Ag hybrid paste tracks as a function of sintering temperature [2]. The Ag hybrid paste lowers its resistivity even below 200 °C in contrast to the Ag nanoparticle paste being higher by 40 °C. Fig. 3 shows the effect of substrate metallization on the joint strength [8]. At 200 °C, Ag coating provides the highest strength due to Ag sintering ability in air. Thus, Ag sintering joining can be benefitted from the presence of oxygen, which is a great advantage as compared with other sintering materials.

3. Ag film bonding by stress migration

Recently, the Ag thin film stress migration bonding method has been developed, providing a perfect bonding without any voids performed in ambient pressure at 250 °C in air as shown in Fig.4 [9, 10]. This joining has two key aspects. One is the reduction reaction of Ag oxides or of other Ag compounds on the surface of Ag at around 200 °C as mentioned above. The other is thermo-mechanical stress caused by thermal expansion mismatch between Ag plating layer and substrates, resulting in massive stress migration of Ag atoms from the bottom of the plating to the surface.

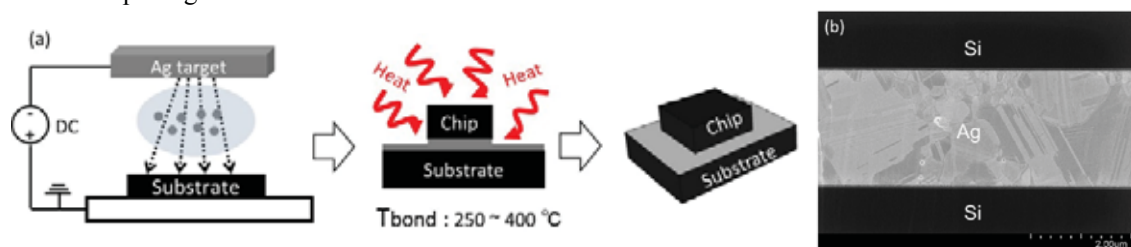


Fig. 4 (a) Schematics of stress migration bonding and (b) Si/Si bonded interface [10].

4. Conclusions

This paper briefly describes the current status of Ag sinter joining and Ag film stress migration bonding. Ag has great advantages in both the surface reaction in air benefitting joining quality and the excellent electric/thermal properties. Ag sinter joining has already exhibited a great potential in the market as high temperature interconnection technology, while our Ag film stress-migration bonding is expected to provide an alternative route. Similar bonding methods using Cu or other metal materials instead of Ag would be explored as cost-effective interconnections in future.

References

- [1] K. Sukanuma, S.-J. Kim, K.-S. Kim, “High-temperature lead-free solders: Properties and possibilities”, *JOM*, vol.61, 64-71 (2009).
- [2] K. Sukanuma, S. Sakamoto, N. Kagami, D. Wakuda, K. -S. Kim, M. Nogi, “Low-temperature low-pressure die attach with hybrid silver particle paste”, *Microelectron. Reliab.*, vol.52, 375-380 (2012).
- [3] E. Ide, S. Angata, A. Hirose, K.F. Kobayashi, “Metal–metal bonding process using Ag metallo-organic nanoparticles”, *Acta Mater.*, vol.53, 2385–2393 (2005).
- [4] K. S. Siow, “Mechanical properties of nano-silver joints as die attach materials”, *J. Alloys Compd.* vol.514, 6-19 (2012).
- [5] T. Wang, X. Chen, G.-Q. Lu, G.-Y. Lei, “Low-temperature sintering with nano-silver paste in die-attached interconnection”, *J. Electron. Mater.*, vol. 36, 1333-1340 (2007).
- [6] M. Kuramoto, S. Ogawa, M. Niwa, K.-S. Kim, K. Sukanuma, “Die-bonding for a nitride light-emitting diode by low-temperature sintering of micrometer size silver particles”, *IEEE Trans. CPMT*, vol.33, 801-808 (2010).
- [7] M. Kuramoto, S. Ogawa, M. Niwa, K.-S. Kim, K. Sukanuma, “New silver paste for die-attaching ceramic light-emitting diode packages”, *IEEE Trans. CPMT*, vol.1, 653-659 (2011).
- [8] S. Sakamoto, S. Nagao, K. Sukanuma, “Microstructural stability of Ag sinter joining in thermal cycling”, *J Mater. Sci. Mater. Electron.*, vol.24, 2593-2601 (2013).
- [9] T. Kunimune, M. Kuramoto, S. Ogawa, M. Niwa, M. Nogi, K. Sukanuma, “Low-temperature pressure-less silver direct bonding”, *IEEE Trans. CPMT*, vol. 3, 363-369 (2013).
- [10] C. Oh, S. Nagao, T. Kunimune, K. Sukanuma, “Pressureless wafer bonding by turning hillocks into abnormal grain growth in Ag films”, *Appl. Phys. Letters*, vol.104, 161603 (2014).

Reliability of Lead-free Solder Joints in Microelectronics

E. Hodúlová¹, B. Šimeková¹, I. Kovaříková¹

¹*Slovak University of Technology in Bratislava, Faculty of Materials Science and Technology in Trnava
Institute of Production Technologies, Slovak Republic
J. Bottu 23, 917 24 Trnava, Slovak Republic
Email: erika.hodulova@stuba.sk*



Keywords: Pb-free alloys, solder joints, joints interface, activation energy, structural integrity, failure of IMC layer.

Abstract

The development of Cu–Sn intermetallic compound (IMC) at the solder/Cu joints interface had been studied using five Pb-free solders as Sn–3.0Ag–0.5Cu, Sn–3.5Ag–0.7Cu, Sn–1.0Ag–0.5Cu–1.0Bi, Sn–1.5Ag–0.7Cu–9.5In and Sn–0.67Cu–2.0In alloys (composition given in weight %). The effects of Bi and In additions on the intermetallic phase formation in the lead-free solder joints with copper substrate were studied. The soldering of the copper plate was conducted at 250 °C for 5 s. The solder joint reliability production with Sn–3.0Ag–0.5Cu and Sn–0.67Cu–2.0In alloys was assessed to evaluate the thermal cycling test in the range from -40 °C to 150 °C. Altogether 1500 cycles were carried out. Solder joints were exposed to the thermal cycling due to practice requirement. The solder joints with Sn–3.5Ag–0.7Cu, Sn–1.0Ag–0.5Cu–1.0Bi and Sn–1.5Ag–0.7Cu–9.5 In alloys were subsequently aged at temperatures of 130 – 170 °C for 2-16 days in a convection oven. The joints interface, activation energy, structural integrity were studied on the produced solder joints with optical microscopy, energy dispersive x-ray spectroscopy (EDX) microanalysis. Designed solder alloys reached the most suitable result for microelectronic. With the increase of the strain rate, the failure mode migrates from the ductile fracture in the bulk solder to the brittle fracture in the IMC layer.

Wirebonder-made Micro Electro Mechanical Systems

Jan G. Korvink¹ and Ulrike Wallrabe²

¹ University of Freiburg, Department of Microsystems Engineering, Georges-Koehler-Allee 103, 79110 Freiburg, Germany, Laboratory for Simulation

², University of Freiburg, Department of Microsystems Engineering, Georges-Koehler-Allee 102, 79110 Freiburg, Germany, Laboratory for Microactuators

korvink@imtek.uni-freiburg.de



Keywords: MEMS, Wirebonding, Micro-solenoids, Looping simulation

1. Introduction

Wirebonding experiments started in 1956 at Bell Telephone Laboratories, where scientists very rapidly realised that silicon needs to be wired up with other devices [1]. Remarkably, these early experiments already worked with wire diameters all the way down to 5 μm . One could stop here, and say that the rest is history. What we found rather remarkable was the fact that, apart from a few scattered reports in scientific journals, wirebonding was always industrially used for its primary purpose, namely, to wire up chips. Yet wirebonding machines are capable of so much more, and have such a unique position in semiconductor process technology, not only because as back-end equipment they possess very high process reliability, but also that they uniquely introduce wire as a feedstock into the microtechnology business that is dominated by a wafer orientation.

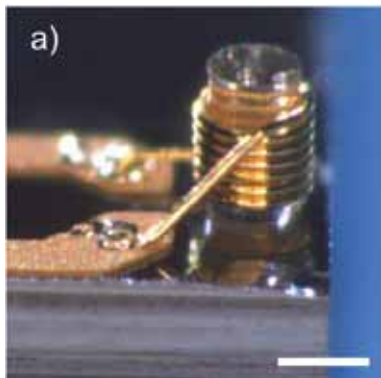


Fig. 1: Micro coil for NMR wound on a 150 μm diameter post. The coil has 7 windings, and is 210 μm high. [6]

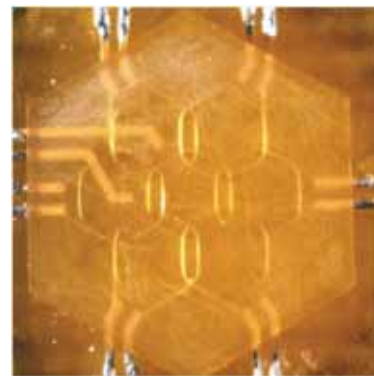


Fig. 2: Phased-array of 7 overlapping micro coils, each with a diameter of 2 mm. Each coil is wound around 6 pillars spanning up a hexagon.

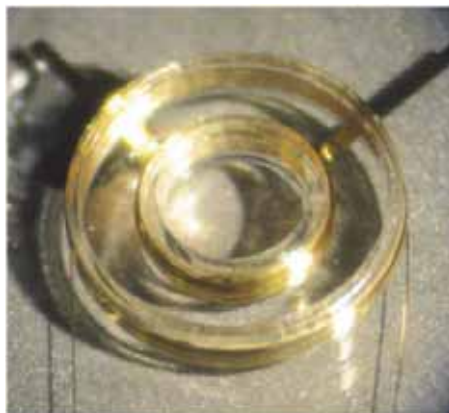


Fig. 3: Two concentric coils wound on SU8 ring structures. Both coils are operated in the low MHz regime and driven with a 180° phase shift. The inner coil levitates an aluminium platelet, whereas the outer coils ensures radial stabilization.

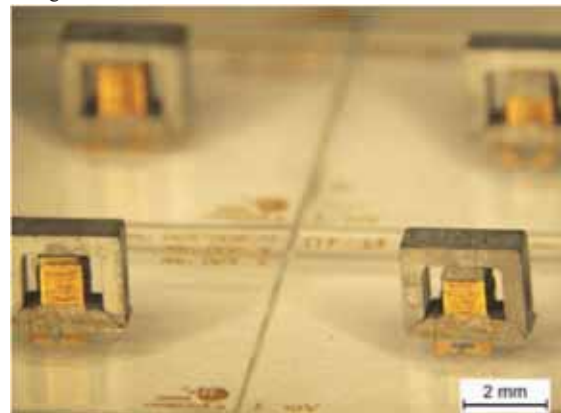


Fig. 4: Closed-flux-loop on-chip power transformers. The cores are made of laminated multi-layer metglas foils, which are cut to shape using EDM and subsequently assembled onto a glass substrate. The primary and a secondary coils are wound directly on top of each other.

We, and others of course [1], have recognised this opportunity and have, based on the support of a wirebonding company who allowed us to influence process parameters via the controlling software, pushed bond wire based

microsystems into a few interesting application domains where microstructuring via wire feedstock would bring a decided advantage. These applications include inductive sensors, energy conversion devices, and magnetic field generators.

2. Experiments

Because wirebonders are capable of moving along freely programmable 3D trajectories, our initial purpose of “misusing” a wirebender was to fabricate micro solenoids. Typically, we fabricate a post of arbitrary shape and out of a variety of materials on different substrates, to then wind a solenoidal structure in one or several layers on the post. The coil process starts and ends on metallic pads via ball and wedge bonds. Coils as small as 150 μm in diameter for micro nuclear magnetic resonance spectroscopy (NMR) [2], overlapping phased-arrays coils for micro magnetic resonance imaging (MRI) [3], concentric coils for micro magnetic levitation [4], and coils on rectangular magnetic posts for on-chip transformers [5], are only some examples of the “zoo” which has emerged so far. To avoid electrical shorts, we prefer to use 25 μm diameter insulated Au or Cu X-Wire™ from MicroBonds Inc, Canada. The move from Au to Cu has also benefited our applications, for example on-chip buck converters [5], by helping to reduce power consumption, resistive losses, and cost. Current process challenges that face novel applications are associated with long wire spans, or winding multilayer coils in a precise manner. For this purpose we are currently developing a process simulation tool that completely captures the looping behaviour of the wirebender, including plastic deformation of the wire due to arbitrary capillary kinematics.

3. Conclusions

In this presentation we will review the exciting new focus in which new electrical or mechanical features are integrated into micro electro mechanical systems, primarily with the aid of an automatic wirebender, and we will show interesting recent results from our own work. We will wrap up the presentation with a provocative suggestion for the wirebonding industry: *We will discuss what it will take to develop this new approach into a viable business, which will hopefully greatly broaden your client base without significant risk on your side, and help to decrease the dependence of your turnover on fluctuations in the IC industry.*

3. Acknowledgements

We thank our financial sponsors, such as the European Union (MicroMR, NMCEL) and the German science foundation (WiredMST, Micro Energy Harvesting, Embedded Microsystems), our collaborators, and our staff. We also would like to sincerely acknowledge Michael Mayer who supported us with advice, training, and contacts to industry.

References

- [1] A.C. Fischer, J.G. Korvink, N. Roxhed, G. Stemme, U. Wallrabe, F. Niklaus, Unconventional applications of wire bonding create new opportunities for microsystems integration, *J. Micromech. Microeng.* 23 (2013), 083001, 18pp, [DOI: 10.1088/0960-1317/23/8/083001](https://doi.org/10.1088/0960-1317/23/8/083001).
- [2] V. Badilita, B. Fassbender, K. Kratt, C. Bonhomme, D. Sakellariou, J.G. Korvink, U. Wallrabe, NMR single chip microprobe for sub-nanoliter magic angle coil spinning (MACS) spectroscopy via inductive coupling, *PLoS ONE* 7, no.8 (2012), e42848, [DOI:10.1371/journal.pone.0042848](https://doi.org/10.1371/journal.pone.0042848).
- [3] O.G. Gruschke, N. Baxan, L. Clad, K. Kratt, D. v. Elverfeldt, A. Peter, J. Hennig, V. Badilita, U. Wallrabe, J.G. Korvink, Lab on a chip MR multi-platform analysis system, *Lab Chip*, no. 12 (2012), pp. 495-502, [DOI: 10.1039/C2LC20585H](https://doi.org/10.1039/C2LC20585H)
- [4] V. Badilita, S. Rzesnik, K. Kratt, U. Wallrabe, Characterization of the 2nd generation magnetic microbearing with integrated stabilization for frictionless devices, *TRANSDUCERS 2011*, Peking, PR China, June 2011, pp. 1456-1459
- [5] A. Moazenzadeh, N. Spengler, R. Lausecker, A. Rezvani, M. Mayer, J.G. Korvink, U. Wallrabe, Wire bonded 3D coils render air core microtransformers competitive, *J. Micromech. Microeng.* 23 (2013), 114020, 11pp, [DOI: 10.1088/0960-1317/23/11/114020](https://doi.org/10.1088/0960-1317/23/11/114020)
- [6] R. Kamberger, Private communication.

Formation and Characterization of Subcluster Segregated Nanoalloy with Femtosecond Laser Irradiation

Z.Jiao^{1,2}, W. Duley³, N. Zhou^{2,4}, and P. He¹

¹State Key Laboratory of Advanced Welding Production Technology, Harbin Institute of Technology, Harbin 150001, China

²Centre for Advanced Materials Joining, University of Waterloo, Ontario N2L 3G1, Canada

³Department of Physics & Astronomy, University of Waterloo, Ontario N2L 3G1, Canada

⁴Department of Mechanical and Mechatronics Engineering, University of Waterloo, Ontario N2L 3G1, Canada

Email: hithepeng@hit.edu.cn



Keywords: Femtosecond laser, Nanoalloy, Nanoparticles, Joining

1. Introduction

Metallic nanoparticles have widespread applications in materials science, chemistry and biology areas due to their unique characteristics [1-3]. This is followed by a tremendous attention to nanoalloys, since mixing several metals together at nanoscale provides another opportunity for tuning their physical and chemical properties. Typically, there are four types of nanoalloy structure, which are core-shell segregated nanoalloys, subcluster segregated nanoalloys, mixed nanoalloys and multishell nanoalloys [4]. Both experimental and theoretical research have been carried out to different types of nanoalloys [5-9]. Exceptionally, although subcluster segregated nanoalloys are in principle possible [10, 11], practical evidence is barely seen by far. The subcluster segregated nanoalloys consist of two dissimilar nanocluster, which may share a mixed interface or numbers of bonds [4].

Joining of dissimilar metallic nanoparticles is one possible method to form subcluster segregated nanoalloys. Most of previous work only focused on the simulation of joining dissimilar free clusters [10, 11]. However, few investigations were carried out in terms of joining supported NPs, which is of great importance in the field of surface nanostructuring [12]. An important factor of joining at the nano-scale is the proper control of melting depth in NPs [13], preventing the NPs merging to form a large particle [14]. Fs laser irradiation provides new promise in nanofabrication field due to its non-thermal effects [13, 15].

In this work, we present the first experimental evidence of subcluster segregated nanoalloy by fs laser irradiation. The nanostructure characterization of Al-Fe, Ag-Ni and Ag-Fe joints are discussed. The results provide a new approach to generate subcluster segregated nanoalloys, and present valuable information for joining miscible as well as immiscible elements at nano-scale.

2. Experiments

The experiments involved preparation and joining of NPs in vacuum with an fs laser system (1 KHz, 800nm, Coherent, Inc.). The maximum pulse energy was 3.5 mJ at a pulse duration of 35 fs. NPs were first deposited on an ultrathin carbon film (400mesh, <3nm carbon film, copper TEM grid, Ted Pella) in vacuum by separated laser ablation of different material targets. The resulting NPs were then exposed to fs laser irradiation for 5 seconds at fluences between 0.5-1.3 mJ/cm² to investigate the joining process. Ablation and irradiation of the deposited sample were carried out in vacuum at a base pressure of 10⁻⁶ Torr. High resolution transmission electron microscopy (HRTEM, JEOL 2010F) together with electron diffraction X-ray (EDX) was used to investigate the nanostructure and elemental distribution of the samples.

3. Results and Discussion

High resolution TEM images of joined miscible Al-Fe and immiscible Ag-Ni are shown in Fig. 1 and Fig. 2. Amorphous phase was found at Al-Fe interface, while direct bonding with a specific angle was found at Ag-Ni interface. The results confirms the formation of subcluster segregated nanoalloy with mixed interface (Fig. 1) and subcluster segregated nanoalloy with shared bonds (Fig. 2)

For miscible Al-Fe interface, the amorphous phase has lower energy so that it can exist after joining. For immiscible Ag-Ni interface, phase segregation occurred due to large positive mixing energy and a specific angle was formed to compensate the lattice mismatch.

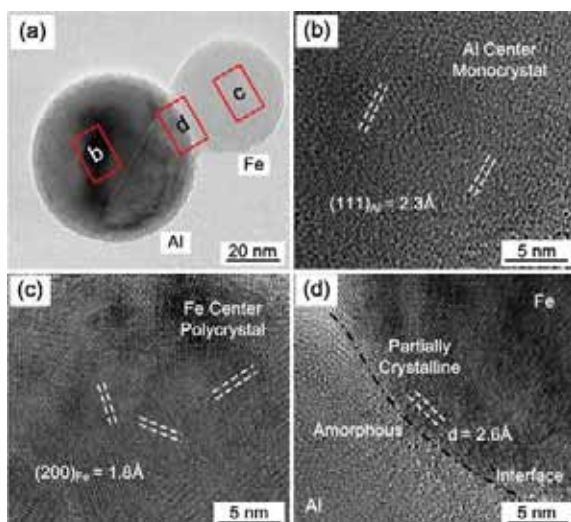


Fig.1. High resolution TEM images of Al-Fe NPs joined by exposure to fs laser radiation. (a) Morphology of joined Al-Fe NPs. The letters show the corresponding high resolution image and the red squares indicate the corresponding area. (b) (c) (d) High resolution TEM image of the corresponding area.

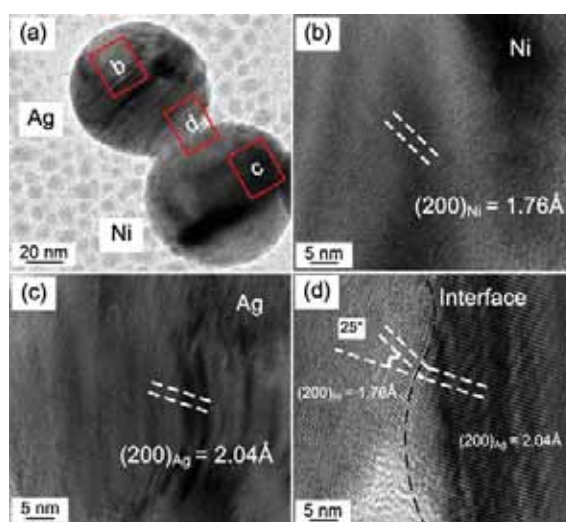


Fig.2. High resolution TEM images of Ag-Ni NPs joined by exposure to fs laser radiation (a) Morphology of joined Al-Ni NPs. The letters show the corresponding high resolution image and the red squares indicate the corresponding area. (b) (c) (d) High resolution TEM image of the corresponding area.

4. Conclusions

This work presents the first experimental approach to generate subcluster segregated nanoalloys, which is by joining metallic NPs with fs laser irradiation. Joining miscible Al-Fe NPs formed subcluster segregated nanoalloy with a mixed interface. While joining immiscible Ag-Ni and Ag-Fe nanoparticles formed subcluster segregated nanoalloy only with shared bonds at the interface. The results show that amorphous phase was formed at Al-Fe interface and no mixing layer was found at the Ag-Ni and Ag-Fe interface. It suggests that surface segregation occurred at Ag-Ni and Ag-Fe interface after fs laser irradiation due to their high mixing energy. TEM results display a specific angle between two matching planes at immiscible elements interface, which is driven by reduction of surface energy. Calculation of lattice mismatch shows the angles are favorable to form the interface with lower surface energy.

References

- [1] A.N. Shipway, E. Katz, and I. Willner, Nanoparticle arrays on surfaces for electronic, optical, and sensor applications. *Chemphyschem*, 2000. 1(1): p. 18-52.
- [2] S.H. Sun, et al., Monodisperse FePt nanoparticles and ferromagnetic FePt nanocrystal superlattices. *Science*, 2000. 287(5460)
- [3] S. Arrii, et al., Oxidation of CO on gold supported catalysts prepared by laser vaporization: Direct evidence of support contribution. *Journal of the American Chemical Society*, 2004. 126(4): p. 1199-1205.
- [4] R. Ferrando, J. Jellinek, and R.L. Johnston, Nanoalloys: From theory to applications of alloy clusters and nanoparticles. *Chemical Reviews*, 2008. 108(3): p. 845-910.
- [5] D. Ferrer, et al., Three-layer core/shell structure in Au-Pd bimetallic nanoparticles. *Nano Letters*, 2007. 7(6): p. 1701-1705.
- [6] A. Rapallo, et al., Global optimization of bimetallic cluster structures. I. Size-mismatched Ag-Cu, Ag-Ni, and Au-Cu systems. *Journal of Chemical Physics*, 2005. 122(19).
- [7] T. Shibata, et al., Size-dependent spontaneous alloying of Au-Ag nanoparticles. *Journal of the American Chemical Society*, 2002. 124(40): p. 11989-11996.
- [8] A. Aguado, and J.M. Lopez, Structural and thermal behavior of compact core-shell nanoparticles: Core instabilities and dynamic contributions to surface thermal stability. *Physical Review B*, 2005. 72(20).
- [9] F. Baletto, C. Mottet, and R. Ferrando, Growth simulations of silver shells on copper and palladium nanoclusters. *Physical Review B*, 2002. 66(15).
- [10] H. Y. Kim, et al., Preferential segregation of Pd atoms in the Ag-Pd bimetallic cluster: Density functional theory and molecular dynamics simulation. *Physical Review B*, 2007. 75(21).
- [11] M. M. Mariscal, S.A. Dassie, and E.P.M. Leiva, Collision as a way of forming bimetallic nanoclusters of various structures and chemical compositions. *Journal of Chemical Physics*, 2005. 123(18).
- [12] P. Jensen, Growth of nanostructures by cluster deposition: Experiments and simple models. *Reviews of Modern Physics*, 1999. 71(5): p. 1695-1735.
- [13] A. Hu, Y. Zhou and W.W. Duley, Femtosecond Laser-Induced Nanowelding: Fundamentals and Applications. *The Open Surface Science Journal*, 2011. 3.
- [14] J. K. Chen, and J. Q. Qui, Patterned 3D assembly of Au nanoparticle on silicon substrate by colloid lithography. *Journal of Nanoparticle Research*, 2012. 14(6).
- [15] A. Hu and Y. Zhou. From Microjoining to Nanojoining. *The Open Surface Science Journal*, 2011. 3.

Ultra-low power integrated pH nanosensors

Adrian M. Ionescu, Sara Rigante, Elisabeth Buitrago

Nanolab, Ecole Polytechnique Fédérale de Lausanne, Switzerland

adrian.ionescu@epfl.ch



Keywords: Field Effect Transistor (FET) sensors, FinFET, label-free sensor, nanoelectronics, pH sensor, biochemical sensing, high-k dielectric, low power, sensing integrated circuits, long-term stability.

1. Introduction

Field Effect Transistors (FET) are promising ultrasensitive sensors for direct and label-free detection of ionic and biological species. With respect to their mechanical and optical counterparts they can guarantee a direct response, durability and direct integration with the readout. Their potential as pH sensors has been widely demonstrated [1], but large-scale production and circuit integration have not been achieved yet. Carelessness of the device architecture optimization and low power and CMOS constraints represents an obstacle to the spreading of such technologies in healthcare systems. Monitoring of pH is not an overdue task. In many applications the sensor integration within a low power, ultra-accurate and wireless electronic system may play a crucial role. Continuous intra-arterial blood pH monitoring is, for example, highly desirable in clinical practice [2], either during anesthesia in major surgery (at least 10 hours) or for post-operative monitoring (several days). Also, the gastric acid output (GAO) has to be monitored continuously to address chronic acid-related diseases, but the absence of a non-invasive and stable tool has slowed down its clinical use [3].

Herein, we explore state-of-the-art nanoelectronics devices as nanosensors, looking forward to a definitive integration of such sensing units into smart and wireless systems.

2. Experiments

Two fully-depleted n-channel FET architectures are presented: 2D arrays of FinFETs (Fig. 1.b, 1.c and 1.d) and 3D stacked vertical SiNW/Fins (Fig. 1.e, 1.f and 1.g). A FinFET features two lateral conductive channels, as shown in Fig. 1.a. The gate, whether metallic or liquid, generates an electrostatic potential surrounding the almost totality of the device and providing an excellent channel control. This results in a steeper subthreshold slope, i.e. higher readout sensitivity, upon scaling. Thanks to a precise assessment of the technological development, it also provides high stability and repeatability. FinFET advantages are well known in electronics [4] and 22 nm FinFETs are today implemented in the last Intel's microprocessor on Si-bulk.

The fabrication of both architectures with critical features down to 15-30 nm has been demonstrated on Si-bulk substrate [5,6], allowing to reduce the production cost. The electronic performance of the devices can be tested independently from the microfluidic set-up through metallic gates.

3. Results and Discussion

Excellent outputs are achieved: Subthreshold Slope (SS) values are overall < 100 mV/dec with maximum SS ≈ 72 mV/dec for the 2D FinFETs and SS ≈ 100 mV/dec for the 3D stacked SiNWs at the same condition of backgate potential $V_{bg} = 0$ V. By applying $V_{bg} = 3$ V also the 3D stacked SiNWs can reach SS ≈ 75 mV/dec, as presented in Fig. 2. The difference is due to a more accessible control of the FinFET thickness for all wires for the 2D FinFETs. The ratio I_{on}/I_{off} is for both $> 10^6$. The 3D stacked SiNWs have the advantage of performing higher transconductance values up to $g_m > 10$ μ S.

From the technological point of view, 2D FinFETs can be fabricated with similar output on Si-bulk and silicon-on-insulator (SOI) substrates. The 3D stacked SiNWs should preferably be fabricated on SOI, since the bulk insulation is not possible through the same spacers technology used for the 2D arrays and may result into a severe performance degradation.

In order to achieve maximum pH sensitivity, a careful assessment of HfO₂ as sensing gate oxide has been performed. The use of a high-k oxide is in perfect accordance with Moore's scaling law. A final gate stack of SiO₂/HfO₂ allows not only to achieve the maximum pH response but it also addresses the problem of hysteresis (≈ 5 mV), which, despite its relevance, is rarely treated in SiNW sensing related works. A TEM image of the gate stack and the corresponding CV measurement is presented in Fig. 3. Alternatively, a SiO₂ gate oxide can be optimized by APTES functionalization.

The experimental results leave no doubts on the efficiency of the presented devices. The measurement setup is shown in Fig.4. Both can reach the maximum pH response with threshold voltage variation $\Delta V_{th} \approx 59$ mV/pH (Fig. 5.a) and current variation up to 0.8 dec/pH (Fig. 5.b and 5.c). According to the desired current level and specific power constraints, 2D or 3D arrays can be implemented. The overall power dissipation is extremely low. For the 2D FinFET array it varies from tens to hundreds of nW, i.e. $8nW < P_{Fin} < 150nW$ for $V_{ds} = 100$ mV, according to the operation regime. For biological applications, where extremely low current are preferred, the overall power can reach even lower values, down to $P_{Fin} \approx 0.4$ nW. Being the number of SiNW for the 3D

arrays 10 times higher, the power consumption varies accordingly. To guarantee the compatibility of the sensor with CMOS ICs, the backgate is preferably grounded.

Long-term stability has been verified for the 2D FinFETs continuously for 5 days at a fixed pH = 6. The FinFETs behaved in an extremely stable way with drift $\delta V_{th}/\delta t = 0.14$ mV/h for multiple wire FinFETs (5 SiNWs), and $\delta V_{th}/\delta t = 0.10$ mV/h for the single wire FinFETs, which corresponds to 0.07% variation of the nominal V_{th} value, as shown in Fig. 6.a. Such results overcome many previous results [7,8] and even the ones provided by commercial devices [9]. In addition, by monitoring two identical entities located at different wafer positions the two data set superpose. The subtraction of the two population of data returns a residual average $\Delta V_{th} = 0.6$ mV. The long term reliability of the 3D stacked SiNW has been tested by measuring the sensor response with respect to pH 10 days after the initial measurements, as shown in Fig. 6.b. In this case, the drain current shift was overall found to be $\approx 5\%$.

The 2D FinFETs are highly apt to circuit integration. They have been tested in a common source amplifying configuration achieving a pH readout sensitivity beyond the Nernst limit [10] and a linear $V_{out}(V_{in})$ correlation, as shown in Fig. 7.a. The amplification has been achieved by connecting a metal gate FinFET as load to a FinFET sensor and without applying additional potentials to back or side gates. In [11], a pH-dependent frequency circuit based on FinFETs has also been demonstrated. For all designs, the circuit and pH sensor units present the exact same architecture. On the other hand, 2D array of FinFETs suffer from a poor topography which may lead to a low sensitivity for biological applications. For pH sensing, in fact, the H^+ concentration is sufficiently important to make any highly dense surface fully responsive. Small biological entities, such as molecule and virus, need a higher functionalized surface to make the interaction event more probable. Moreover, the 3D SiNW/Fins are located into cavities which act as traps for biological species which need a higher interaction time to bond with the functionalization chains onto the sensor surface. The detection of ultra-low concentrations (down to ≈ 17 aM) of the protein streptavidin has been demonstrated with a biotinylated SiO_2 sensing gate for the 3D stacked SiNWs (Fig. 7.b). To the best of our knowledge this is one of the lowest protein concentrations ever measured by SiNW-based FET sensors.

4. Conclusions

Multiple arrays of SiNWs are an essential requirement for the monitoring of vital signals and differential measurements are irrevocable in order to understand the meaning of a single measurement (“Is it a heart attack or just a muscle cramp?”).

We believe 2D FinFETs arrays are the optimal technological choice for ultra-low power chemical applications, especially where a full monolithic CMOS integration is required. Instead, for ultra-sensitive biological applications, the use of 3D SiNW/Fins embedded into microfluidic cavities is more recommended.

Acknowledgements: This work has been funded by the Swiss Nanotera and the FP7 programme of the European Commission.

References

- [1] F. Patolsky et al., “Nanowire nanosensors”, *Mater. Today*, vol. 8, pp. 20-28, 2005
- [2] M. T. Ganter et al., “How often should we perform arterial blood gas analysis during thoracoscopic surgery?” *Journal of Clinical Anesthesia*, vol. 19, no. 8, pp. 569–575, 2007
- [3] S. R. Majumdar et al., “Chronic acid-related disorders are common and underinvestigated,” *The American journal of gastroenterology*, vol. 98, no. 11, pp. 2409–2414, 2003
- [4] J. P. Colinge, *FinFETs and Other Multi-Gate Transistors*. Springer, 2008
- [5] S. Rigante et al., “Technological Development of High-k Dielectric FinFETs for Liquid Environment”, *Solid-State Electronics*, Vol. 98, pp. 81-87, 2014
- [6] E. Buitrago et al., “The top-down fabrication of a 3D-integrated, fully CMOS-compatible FET biosensor based on vertically stacked SiNWs and FinFETs”, *Sensors and Actuators B: Chemical*, vol. 193, pp. 400-412, 2014
- [7] T.-E. Bae et al., “High Performance of Silicon Nanowire-Based Biosensors using a High-k Stacked Sensing Thin Film”, *ACS applied materials & interfaces*, vol. 5, no.11, pp. 5214-5218, 2013.
- [8] J.-H. Ahn et al., “A pH sensor with a double-gate silicon nanowire field-effect transistor,” *Applied Physics Letters*, vol. 102, no. 8, p. 083701, 2013.
- [9] Microsens. Ion sensitive field effect transistor-isfet. [Online]. Available: <http://www.microsens.ch/products/chemical.htm>
- [10] S. Rigante et al., “Low Power FinFET pH-Sensor with High-Sensitivity Voltage Readout”, in *Proceedings of the European Solid-State Device Research Conference (ESSDERC)*, IEEE, Bucharest, Romania, 2013
- [11] S. Rigante et al., “FinFET integrated low-power circuits for enhanced sensing applications”, *Sensors and Actuators B: Chemical*, vol.162, pp. 789-795, 2013.

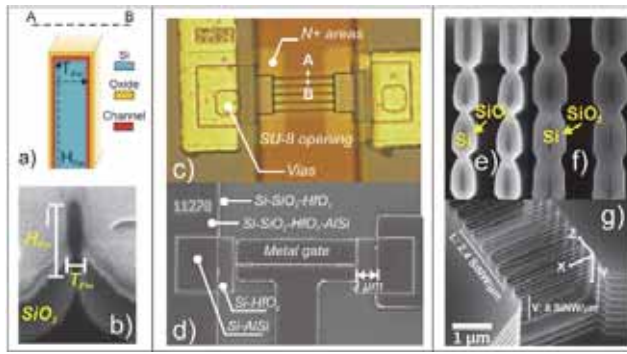


Figure 1: a) sketch of a FinFET cross-section; b) SEM FinFET cross-section obtained by FIB after the SiO_2 bulk insulation; c) optical top image of a 2D FinFET array for sensing applications with an SU-8 opening next to the FET channels; d) SEM top image of a single FinFET with metal gate; e) SEM cross sections of 3D stacked SiNWs formed with a combination of anisotropic and isotropic etches; f) sharp scallops, FinFET like structures; g) top-side view of the cavity containing the 3D stacked SiNWs after release from the oxide.

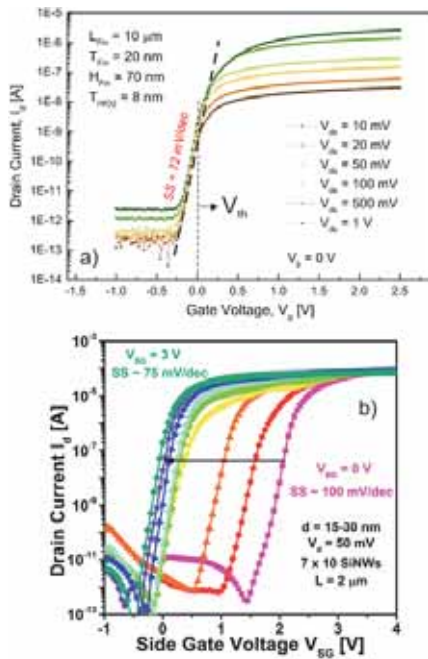


Figure 2: Electrical characterization of FinFETs and SiNWs: a) $I_d(V_g)$ for a metal gate 2D FinFET (on Si-bulk substrate) and $I_d(V_{sg})$ obtained with lateral side gates for the 3D SiNWs (on SOI substrate).

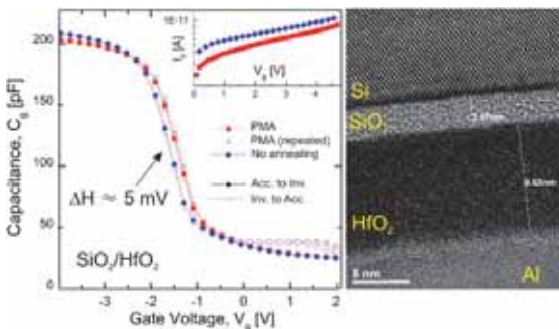


Figure 3: CV measurement obtained by a MOSCAP structure with the gate stack $\text{SiO}_2/\text{HfO}_2$ (TEM image on the right). The CV curve is obtained by a V_g sweep from accumulation to inversion and vice versa; the inset shows the leakage current up to 4V.

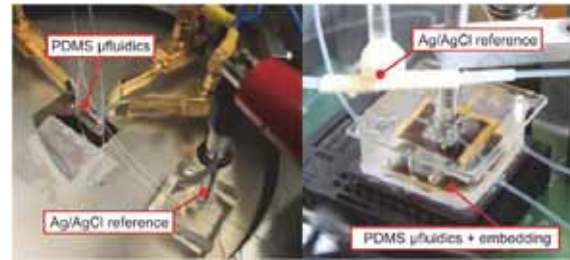


Figure 3: (left) measurement setup of the 3D stacked arrays of SiNWs within a Cascade probe station with PTFE tubes externally connected to an active pumping system used to hydrodynamically transfer fluid to/from the device; (right) the 2D FinFET arrays have been mounted onto a chip carrier connected to a PCB; in both measurement setups the microfluidic channels have been realized by PDMS and the Ag/AgCl reference electrode has been externally connected.

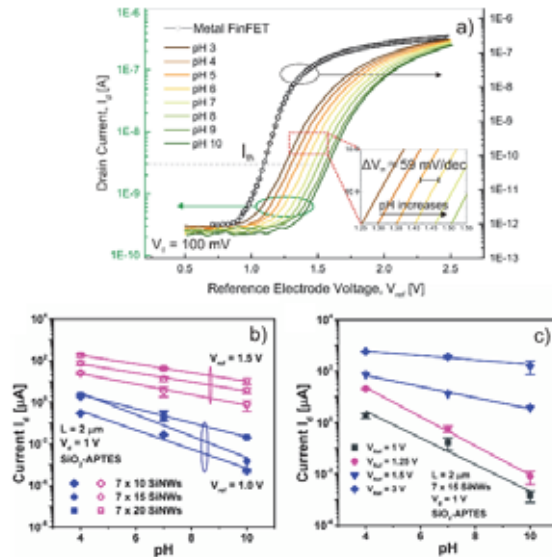


Figure 5: Electrical characterization of liquid gate SiNWs: (a) $I_d(V_{ref})$ transfer characteristic for a 2D array of FinFETs with $T_{Fin} = 30$ nm for $3 \leq \text{pH} \leq 10$ with the inset showing the curve shift ΔV_{th} ; the gate oxide is HfO_2 ; (b) $I_d(\text{pH})$ for the 3D stacked SiNWs for an increasing number of SiNWs 7×10 , 15 , 20 as the device is operated in subthreshold and weak inversion with $V_{ref} = 1$, 1.5 V, respectively and (c) as the device is operated below threshold $V_{ref} = 1$, 1.25 V and in weak inversion $V_{ref} = 1.5$ V and strong inversion $V_{ref} = 3$ V for 7×15 SiNWs array.

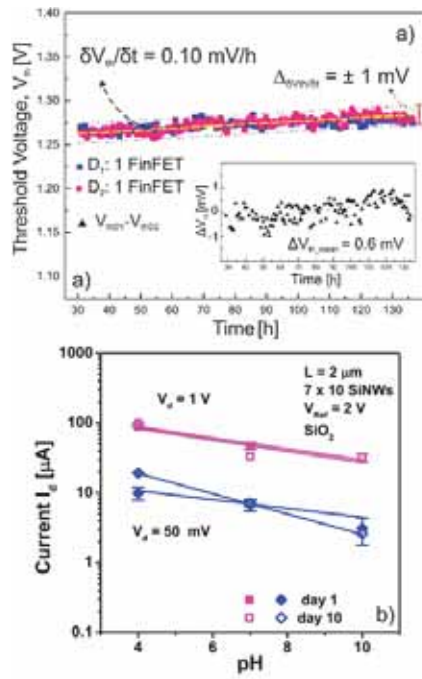


Figure 6: a) 2D high-k FinFET long-term stability measurement at constant pH = 6 with V_{th} monitored over 5 days for equal single-wire FinFET sensors at different die locations with the inset showing the two data set difference; b) $I_d(t)$ for the 3D stacked SiNWs as the pH value is changed from pH = 4 to 10 as the device is operated at $V_{ref} = 2$ V at high ($V_d = 1$ V) and low ($V_d = 50$ mV) drain potentials and 10 days after the initial measurement for an unmodified SiO_2 gate oxide.

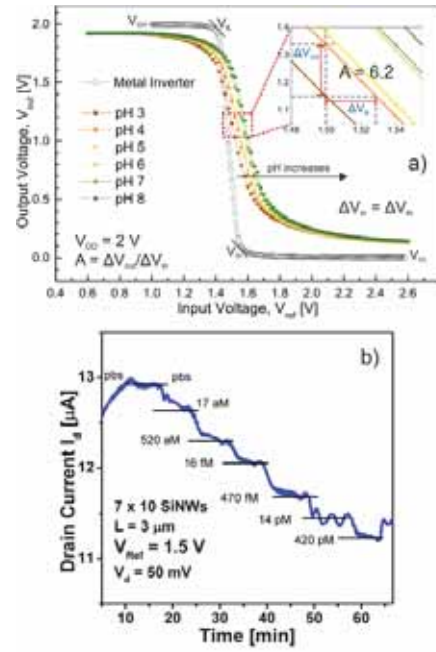


Figure 7: Other applications of the pH nanosensors: a) sensing common source amplifier based on 2D FinFETs, with V_{out} (V_{ref}) of a metal gate (black curve) and sensing (colored curves), V_{out} (V_{ref}) was measured for $3 \leq pH \leq 8$, the inset shows the curve shift ΔV_{th} along with the corresponding amplification ΔV_{out} ; b) $I_d(t)$ of the 3D stacked SiNWs implemented as biological sensors for the detection of streptavidin in PBS solutions as the device is operated in the weak inversion regime $V_{ref} = 1.5$ V and $V_d = 50$ mV.

Growth and Assembly of Graphene Thin Films on Insulating Substrates

T. Ogino¹

¹*Division of Electrical and Computer Engineering
Yokohama National University
79-5, Tokiwadai, Hodogayaku, Yokohama, 240-8501, Japan*

Email: togino@ynu.ac.jp



Keywords: Graphene, Thin Film, Chemical Vapor Deposition, Graphene Oxide, Sapphire, atomic force microscopy, surface modification

1. Introduction

Graphene is a two-dimensional material of sp^2 -bonded carbon atoms and attracts much attention owing to its unique properties, such as extremely high electron mobility, large mechanical strength and high thermal conductivity. The most important technology toward its industrial applications is fabrication of thin films. In this lecture, we show direct growth of graphene films on insulating substrates and fabrication of well-ordered, single-layered graphene oxide (GO) film. In the first topic, we describe metal-catalyst-free direct-growth of graphene films on sapphire (Al_2O_3) surfaces by chemical vapor deposition (CVD), focusing on the growth mechanism using morphologically phase-separated substrates [1]. In the second topic, we demonstrate that a graphene oxide (GO) film covering the whole substrate surface can be fabricated without piling-up even from irregularly-shaped GO flakes by their self-shaping mechanism on a solid surface [2].

2. Direct Growth of Graphene Films on Sapphire Surfaces

In the direct growth of graphene films, we used single crystalline sapphire (0001) and (11-20) substrates and an atmospheric pressure CVD apparatus equipped with a CH_4 - H_2 -Ar gas system. To investigate growth mechanism, we prepared phase-separated sapphire (0001) surfaces, whose atomic force microscopy (AFM) images are shown in Fig. 1. This is very powerful to unambiguously demonstrate effects of substrate surface on the direct growth of graphene films.

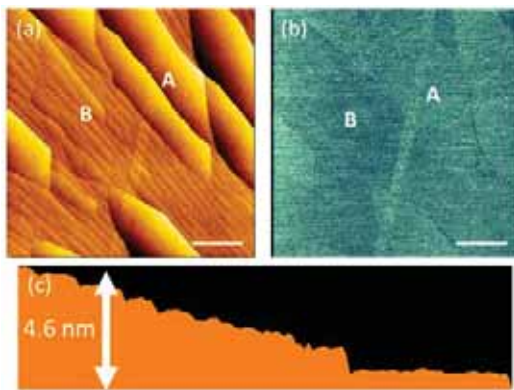


Fig. 1. AFM images of a phase-separated sapphire (0001) surface before graphene growth; (a) morphology, (b) frictional force image. (c) Cross-sectional profile around the center of panel a. Scale bars are $1\ \mu\text{m}$. The surface consists of stepped areas and flat terraces.

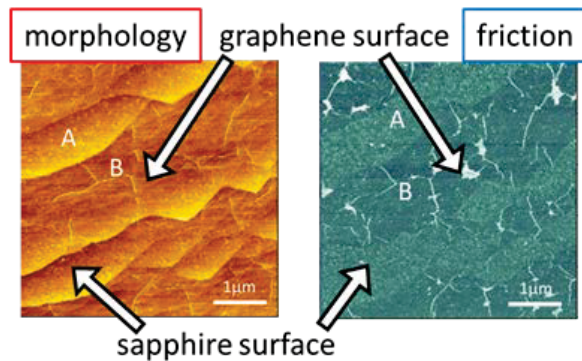


Fig. 2. (a) AFM images of morphology and (b) frictional force on the phase-separated sapphire (0001) surface after the graphene growth for 120 min.

Fig. 2 shows (a) morphology and (b) a frictional force image after the graphene growth on a sapphire (0001) surface for 120 min. The morphology and frictional force image differ between the domains, stepped areas and flat terraces. Wrinkles, which mean growth of large area graphene films, were observed in the stepped areas, whereas no wrinkle formed on the flat terraces. The frictional force image, which is subject to the meniscus force [3], demonstrates that the graphene films unambiguously grew only in the stepped regions. We found that the growth proceeds through pit formation by gas-etching of the sapphire surface, nucleation of graphene films inside the pits, expansion of graphene domains and finally coalescence of those domains.

3. Self-Assembly of a Monolayer Graphene Oxide Film

Graphene oxide flakes are water-soluble and expected to be the key materials to form large-area graphene films by a simple process. We recently demonstrated that a monolayer GO film covering the almost entire substrate surface can be assembled by modifying the substrate surface with an aminopropyltriethoxysilane (APTES) self-assembled monolayer (SAM), as shown in Fig. 3. This process is based on tight attachment of the negatively charged GO flakes to the positively charged APTES-modified surface. On a patterned substrate surface that consists of both positively and negatively charged areas, patterned monolayer GO films are self-assembled from irregularly-shaped GO flakes, as shown in Fig. 4. Figure 5 shows the self-shaping mechanism that can well explain the self-cover of the monolayer GO film that occurs on an entirely APTES-modified surface. By using this mechanism, we can obtain an almost continuous monolayer GO film without piled GO flakes.

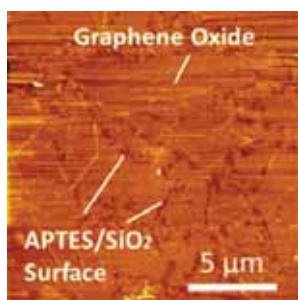


Fig. 3. AFM image of a GO film on an APTES/SiO₂/Si surface.

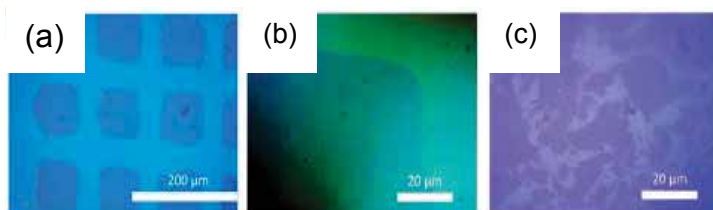


Fig. 4. Selective deposition of GO flakes to form an array of square GO films on a SiO₂/Si substrate with a chemical pattern of APTES-SAM. (a) An optical microscope image of the GO film pattern after sonication and subsequent reduction by thermal annealing, (b) its magnified image and (c) shape and size of the reduced GO flakes deposited on a SiO₂/Si surface without an APTES overlayer pattern.

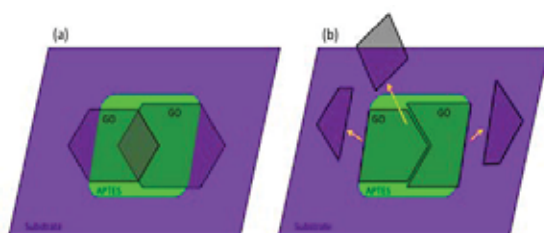


Fig. 5. Mechanism of the self-cover assembly to form a single layer GO film and the self-shaping to form a square-patterned GO film islands with well-defined edges. (a) GO flakes just after deposition and (b) after the sonication.

4. Conclusions

Growth of high-quality films on insulating substrates and assembly of large-area films by a simple process are crucial challenges toward wide range of potential applications of graphene. Moreover, interface control between graphene films and substrate surfaces is important because graphene film properties are strongly affected by the substrate [4], even in aqueous environment [5].

Acknowledgements

This work was partly supported by Grant-in-Aid for Scientific Research from the Ministry of Education, Culture, Sports, Science and Technology. The sapphire wafers were supplied from Namiki Precision Jewel Co. Ltd.

References

- [1] K. Saito and T. Ogino, "Direct growth of graphene films on sapphire (0001) and (11-20) surfaces by self-catalytic chemical vapor deposition", *J. Phys. Chem. C*, 118, 5523-5529 (2014).
- [2] T. Takami, T. Ito and Toshio Ogino, "Self-assembly of a monolayer graphene oxide film based on surface-modification of substrates and its vapor-phase reduction", *J. Phys. Chem. C*, 118, 9009-9017 (2014).
- [3] T. Tsukamoto and T. Ogino, "Morphology of graphene on step-controlled sapphire surfaces," *Appl. Phys. Exp.*, 2, 075502-1-3 (2009).
- [4] H. Komurasaki, T. Tsukamoto, K. Yamazaki and T. Ogino, "Layered structures of interfacial water and their effects on Raman spectra in grapheme-on-sapphire systems", *J. Phys. Chem. C*, 116, 10084-10089 (2012).
- [5] K. Yamazaki, S. Kunii and T. Ogino, "Characterization of interfaces between graphene films and support substrates by observation of lipid membrane formation", *J. Phys. Chem. C*, 117, 18913-18918 (2013).

Joining refractory and dissimilar materials using reactive nanofoils

A.S.Rogachev^{1,2}, A.S.Mukasyan^{2,3}, S.G.Vadchenko¹, and A.A.Nepapushev²

¹*Institute of Structural Macrokinetics and Material Science Russian Academy of Sciences (ISMAN), acad. Osipyan str. 8, Chernogolovka, 142432, Russia;*

²*Center of Functional Nano-Ceramics, National University of Science and Technology, "MISIS", Moscow 119049, Russia*

³*Department of Chemical and Biomolecular Engineering, University of Notre Dame, Notre Dame, IN 46556, USA*

Email: rogachev@ism.ac.ru



Keywords: eactive multilayer nanofoil, joining materials, solid flame.

1. Introduction

Reactive multilayer nanofoils (RMNF) possess many unique properties, such as very high rate of the reaction wave spreading, up to 10^2 m/s, and extremely short time of reaction and product phase formation, $10^{-7} - 10^{-6}$ s. These features makes RMNFs attractive objects for various applications, e.g., joining of dissimilar materials and items. The foils obtained by magnetron deposition technique consist of relatively flat layers with thickness from several nanometers to microns, while number of the layers "stacked" in one foil may achieve several thousand [1, 2]; the overall thickness of the foil usually do not exceed 200 micron. The most studied compositions of the deposited RMNFs are bimetals Me/Al, where Me = Ni, Ti, Co, Pd, Pt, Cu, Nb, Ta. An alternative method for production of the reactive films is a combination of high-energy ball milling of the powder mixtures with cold rolling [2, 3]. The ball milled and cold rolled foils possess relatively high non-uniformity, intermittence and tortuosity, as compared to the magnetron deposited films. However, reactive properties of the foil depend mostly on the thickness of the reactants layers, while their shape has negligible effect on the reactivity. The mechanical methods allow production not only bimetal foils, but also foils Me/Nm, where Nm is a non-metal reactants, such as Si, B, C. Often metal-nonmetal compositions have higher exothermicity than the bimetal ones. In the present work, reactive mechanisms of the RMNF produced by different methods are considered in relation with its possible application for joining refractory and dissimilar materials.

2. Experiments

Propagation of the reactive waves in the Ni/Al RMNFs placed between heat-absorbing materials (items) is studied using high-speed video camera Miro M310 and high-frequency photo-diode sensors. This configuration simulates the real conditions of heat exchange during joining of materials. Combinations of the deposited and cold-rolled films are considered in order to decrease the reaction onset temperature. The influence of additional Joule heating by passing electric current through the contact area is also studied using the Spark Plasma Sintering setup Labox-650.

3. Results and Discussion

The temperature-time profile of the reaction wave in the Ni/Al RMNF measured by high-frequency photo-sensor is shown at Figure 1,a. Two stages of the exothermic reaction can be recognized: the first stage with *extremely rapid* ($\sim 3 \cdot 10^6$ K/s) temperature rise and short duration (less than 0.5 ms), and the relatively slow second stage with duration of ~ 10 ms or more. When the RMNF was placed on the copper heat sink, the second stage of reaction was completely suppressed, but the first reaction front propagated as a thin glowing line with the same velocity, as in the free-standing RMNF. The mechanism of such reactions is currently under experimental and theoretical investigation [4, 5]. Therefore, depending on the film thickness, thermal conductivity of the joining materials and heat transfer through the boundaries, the total or partial heat release (related to the first stage only) takes place in the joining zone. Moderate peak temperature in the range 1000 – 1500 °C and very short duration of the thermal pulse make this method most appropriate for joining of the heat-sensitive materials and items, such as electronic components etc. Joining of refractory materials requires thicker films with higher heat evolution. Mechanically activated and cold rolled films can fit these requirements. Figure 1, b represent the carbon-carbon composites joined using mechanically prepared reactive layers. The Ni+Al

mixture was ball-milled in argon atmosphere in the planetary ball mill in order to increase its reactivity. The obtained lamellar composite powder was cold-rolled to obtain the foil with thickness of 100 – 300 μm . This foil was placed between the C-C composite cylindrical samples. Thin layers of Ti were placed between the Ni/Al foil and CC-composite. Heat generated by chemical reaction $\text{Ni}+\text{Al}=\text{NiAl}$, together with additional Joule heat from electric current passed through the samples, caused melting of Ti, which spreaded over the carbon surface and formed TiC layers. The tensile strength of the joint weld is larger than that of the bulk C-C material, as can be seen from Figure 1, b. Investigation of the bonding regions revealed formation of the cemented carbide composed of TiC grains with NiAl binder [6]. More exothermic foils based on Ti-Si compositions also allow joining of C-C composites, titanium alloys or pairs of dissimilar materials, e.g., carbon – titanium. It was found that combination of the magnetron deposited Ni/Al films with mechanically produced Ti/Si bands can provide complex joining reactive systems with low temperature of initiation and high heat generation for various applications.

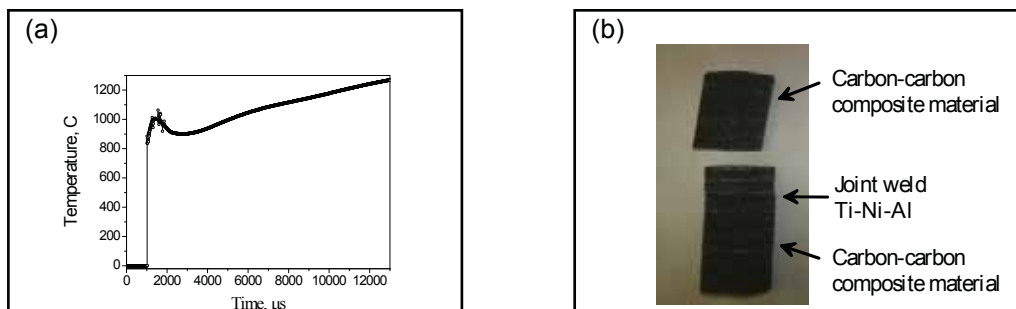


Fig. 1. (a) Temperature-time profile of the reaction front in the Ni/Al RMNF. (b) Carbon-carbon composites joined using the Ti-Ni-Al-Ti intermediate layers produced by high energy ball mills and cold rolling technique.

4. Conclusions

The reactive nanofoils provide wide range of options for solving various practical tasks associated with joining of materials. Different approaches, based on layer-by-layer deposition or mechanical structuring, can be used for production of the RMNFs. In all cases, understanding of the reaction and structure formation mechanisms during the joining process has a great importance for proper choice of the foil composition and structure.

References

- [1] T.P. Weihs Self-propagating reactions in multilayer materials. In: Glocker D.A., Shah S.I., eds. Handbook of thin films process technology. Bristol: Institute of Physics Publishing; 1998 Part F.
- [2] A.S. Rogachev Exothermic reaction waves in multilayer nanofilms. *Russ. Chem. Rev.*, 77(1), 21-37 (2008).
- [3] S.G. Vadchenko., and A.S. Rogachev Method for production of multilayer energetic nanostructured films for the permanent connection of metals. Russian Patent №2479382 (20.04.2013).
- [4] A.S. Rogachev, S.G. Vadchenko, and A.S. Mukasyan, Self-sustained waves of exothermic dissolution in reactive multilayer nano-foils, *Appl. Phys. Lett.*, 101(6) Article No.063119, (2012).
- [5] O. Politano, F. Baras, A.S. Mukasyan, S.G. Vadchenko, and A.S. Rogachev, Microstructure development during NiAl intermetallic synthesis in reactive Ni–Al nanolayers: Numerical investigations vs. TEM observations, *Surface and Coating Technology*, 215, 485-492 (2013).
- [6] Ya-Cheng Lin, A.A. Nepapushev, P.J. McGinn, A.S. Rogachev, and A.S. Mukasyan Combustion joining of carbon/carbon composites by a reactive mixture of titanium and mechanically activated nickel/aluminum powders. *Ceramics International*, 39, 7499–7505 (2013).

Advanced nanostructure formation via interface and grain boundary tailoring

S. Baylan¹, G. Richter¹, M. Beregovsky², D. Amram², and E. Rabkin²

¹Max Planck Institute for Intelligent Systems, Heisenbergstr. 3, 70569 Stuttgart, Germany

²Department of Materials Science and Engineering, Technion -Israel Institute of Technology, 32000 Haifa, Israel

Email: richter@is.mpg.de



Keywords: Nanostructure, interface, grain boundary, diffusion, physical vapour deposition

1. Introduction

Physical properties change with decreasing dimensions of devices and structures. Therefore, the bulk often does no longer govern these structures, but the influence of defects as interfaces, grain boundaries or dislocations dominate. Decreasing structures even more nano-devices have the tendency to behave similar to perfect single-crystals since there are no longer enough atoms available to accommodate defects. The classical example for this is the “small is stronger” trend for mechanical properties found for nano-sized objects. Though challenges remain, opportunities arise from decreasing dimensions. Bespoke properties can be achieved by tailoring microstructures in devices. Especially bottom-up or condensation methods have the prospect to realize the given task. We present a method, employing physical vapor deposition, to fabricate one-dimensional metal nanostructures with defined microstructures. Atomistic diffusion processes are utilized to synthesize advanced nano-structures, e.g. hollow metal nano-tubes which are the main topic of the presentation.

2. Experiments

Hollow metal (e.g. Au) nano-tubes are synthesized in a three-step process. First silver is grown by means of physical vapor deposition (PVD), under ultra-high vacuum conditions, on substrates (Si single crystals, W and Mo foils) covered by 30 nm C at 650°C. Secondly, after cooling to room temperature 30 nm Au is deposited on the surfaces. As third step the composite is annealed at 170°C for several hours.

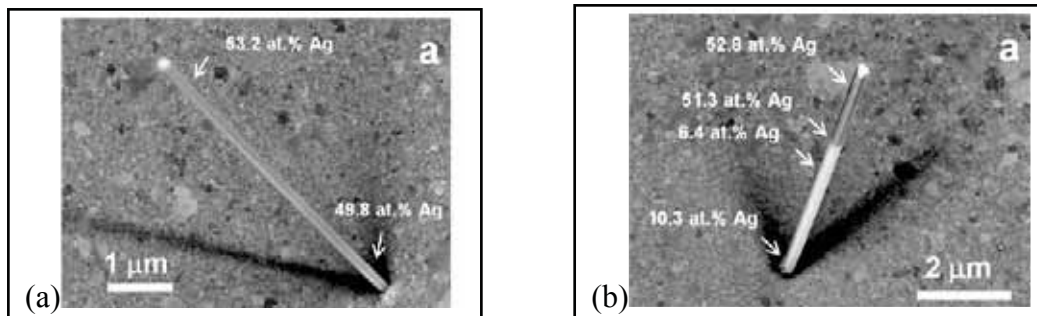


Fig. 1. SEM micrograph of a core-shell nano-whisker. (a) after Ag and Au deposition; (b) after annealing at 170°C.

3. Results and Discussion

The first deposition step results in single crystalline Ag nano-whiskers on the substrates. Deposition at room temperature yields single crystalline core-shell nano-fibers (based on the nano-whiskers, see Fig 1a) and a polycrystalline Au film on the rest of the substrate. Silver is concentrated in the cores of the nano-structures as confirmed by energy dispersive X-ray spectroscopy (EDXS). No Ag can be detected in the Au film. After annealing hollowing can be observed in the nano-structures; the content of Ag decreases (Fig. 1b). At the same time Ag can be detected by EDXS in the polycrystalline Au film on the C-covered substrate. A detailed analysis by scanning electron microscopy and EDXS was performed to gain quantitative data on the hollowing process. Additionally we propose a kinetic model of hollowing based on the competition between the energy decrease driving the hollowing process (formation of Au-Ag solid solution in the grain boundaries), and the energy increase associated with the creation of new surfaces. The model predicts an inverse dependence of the hollowing rate on the inner radius of the nanowhiskers, in good agreement with the experimental data.

4. Conclusions

From the results of the present study, the following conclusions can be drawn:

1. Core-shell Ag-Au nano-whiskers were produced employing the PVD deposition technique.
2. The nano-whiskers were partly or fully hollowed during annealing at a temperature of 170 °C.
3. For the 23 studied nano-whiskers the rate of hollowing scaled inversely with their internal radius.
4. The proposed model predicted an upper limit for the length of hollowed section, and an inverse dependence of the hollowing rate on the nano-whisker inner radius, in good agreement with the experimental data.

Additionally we want to emphasise, that the synthesis of metal nano-tubes is only feasible by tailoring the microstructure, especially the grain boundary structure on and at the vicinity of the nano-whisker root.

Nanojoining: from nanosintering to 3D nanomanufacturing

A. Hu¹, R. Li^{1,2}, Q. Ma¹ and D. Bridges¹

¹*Department of Mechanical, Aerospace and Biomedical Engineering, University of Tennessee Knoxville
1512 Middle Drive, Knoxville, TN 37916-2210, USA*

²*Department of Electrical Engineering, Southeast University, Nanjing 210096, PR China
Email: ahu3@utk.edu*



Keywords: nanojoining, nonthermal sintering, photonic sintering, nanosintering nanomanufacturing

1. Introduction

Nanomanufacturing composes of both the synthesis of nanomaterials and the production of nanodevices through either a “bottom-up” procedure initiating from nanomaterials or a “top-down” processing with highly precise. Nanojoining is thus a critical “bottom-up” manufacturing which bridges technical gaps between nanomaterial synthesis and functional nanodevices. The developing of nanojoining can significantly facilitate the nanomanufacturing of devices for energy, environment, microelectronic and biomedical applications [1,2].

One of nanojoining methods is nanosintering [3]. The sintering is a mass transfer through a solid state or liquid phase atomic diffusion. The nanosintering can be dramatically speed up by the size effect, the shape effect and /or the surface melting [1].

In this work, we presented the shape effect by investigating the nanosintering of silver nanoplates. We displayed that the shape-induced nanosintering of nanoplates was remarkably higher than both nanoparticle and nanowire pastes. The experiments showed the bonding strength of nanoplates was 2 times stronger than nanowires. We compared the photonic sintering using static light and the flashing light. The latter provided a better bonding performance. These results are further compared to nonthermal nanosintering by femtosecond laser irradiation. We discussed that it is possible to develop 3D nanomanufacturing by combining nanoplate inkprinting and photonic sintering.

2. Experiments

Silver nanoplate inks were synthesized through a modified hydrothermal processing with polyvinylpyrrolidone (PVP) as the surface capped agent. The concentration was controlled by the centrifugal process. Statistic analysis showed the average size was 150 nm and the thickness is about 10 nm (Fig. 1a). The bonding was carried out with spring dripping. The 2D to 3D patterns were developed with a 2D programmed writer and an air-brush spraying.

The photonic sintering was carried out with a 250 W tungsten lamp, 1,500 W flashing Xeon lamp or 2W 500 fs fibre laser, respectively. The temperature was monitored by a thermal couple and controlled with a ventilation fan. The bonding strength was measured by a tensile strength machine with 10 micrometer resolution in displacement. Microstructure and crystalline orientation were characterized with scanning electron microscopy (SEM), transmission electron microscopy (TEM) and X-ray diffractometer. Optical properties were measured with a UV-NIR spectroscopy. The conducting and sensing properties were determined with transporting measurement.

3. Results and Discussion

Fig. 1 (a) shows a typical photo of bonded Cu wires with silver nanoplate paste and the SEM image of the paste. The bonding performance is compared with various nanopastes and nanosintering. Shown in Fig. 1(b) for the thermal nanosintering, the bonding strength of nanoplate pastes is double as the bonding of nanowire pastes [4]. The photonic sintering with a static wide band white light displays 25% enhancement. At 80°C, the bonding strength of silver nanoplate pastes is about 20 MPa. With a flash light the bonding strength is further improved

to 24 MPa. Even at the room temperature, the bonding strength is 20 MPa, good enough for practical application for room temperature packaging of thermal sensitive devices.

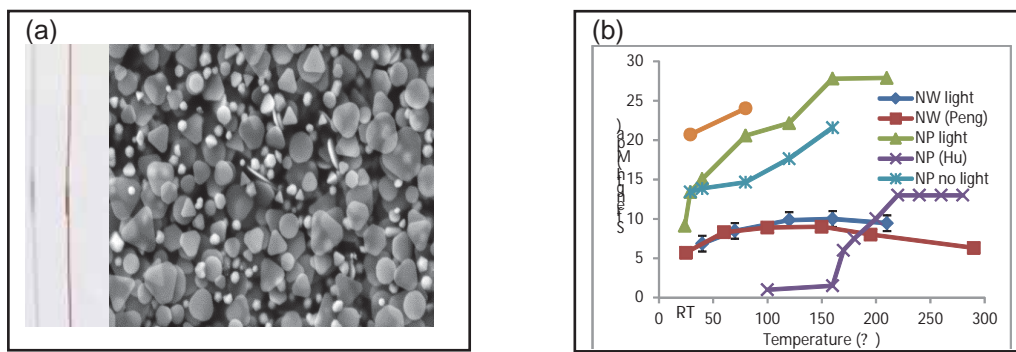


Fig. 1. (a) Images of bonded Cu wires and silver nanoplate pastes. (b) Bonded strength with various nanopastes and nanosintering

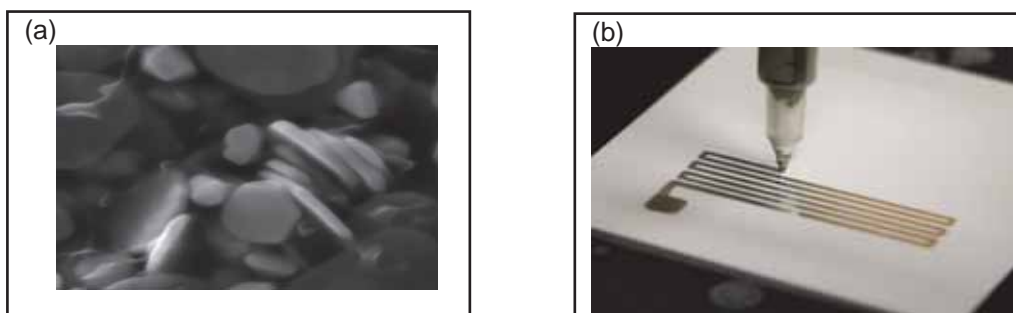


Fig. 2. (a) Sintered silver nanoplates. (b) 2D printed sensor circuits with silver nanoplate inks

Fig. 2 (a) shows SEM images of sintered silver nanoplate plates. Both the side to side and plate to plane sinters are founded. It is obvious that the current paste displays a higher density than nanowire pastes [4]. This may partially explain why nanoplate pastes have a better bonding performance. Fig. 2(b) shows a circuit written with the nanoplate ink. We investigate the rheological properties of nanoplate inks and developed the appropriate formula with controlled viscosity and density for printable electronics applications [5].

4. Conclusions

We successfully developed an innovative silver nanoplate pastes for excellent bonding applications close to room temperature and nanoinks for printable electronics. We compared different photonic nanosintering with static wide band light, flashing light and pulsed laser. We demonstrate that appropriate parameters and nanosintering controlling allow us develop high sensitive sensors for application.

References

- [1] A. Hu, G. L. Deng, S. Courvoisier, O. Reshef, C. C. Evenas, E. Marzur, Y. Zhou, "Femtosecond laser induced surface melting and nanojoining for plasmonic circuits," Proc. of SPIE Vol. 8809, 880907-1-880907-6 (2013).
- [2] A. Hu, J. Y. Guo, H. Alarifi, G. Patane, Y. Zhou, G. Compagnini, C. X. Xu, "Low temperature sintering of Ag nanoparticles for flexible electronics packaging", Appl. Phys. Lett. 97, 1531171-1531173 (2010).
- [3] A. Hu, P. Peng, H. Alarifi, X. Y. Zhang, J. Y. Guo, Y. Zhou, W. W. Duley, "Femtosecond laser welded nanostructures and plasmonic devices", J. Laser Appl. VI. 24, 042001-1-7, (2012)
- [4] P. Peng, A. Hu, H. Huang, A. P. Gerlich, B. Zhao, Y. Zhou, "Room-temperature pressless bonding with silver nanowire paste: towards organic electronic and heat-sensitive functional devices packing", J. Mater. Chem. Vol: 22, 12997-13001 (2012).
- [5] R. Li, A. Hu, "Developing silver nanoplate pastes and inks for printable electronics", to be published.

Patterning of Indium Tin Oxide Microwires using Laser-induced Thermal Printing Method

T. Sano¹, S. Iwasaki¹, S. Katsura², K. Yoshida³, A. Nakayama⁴, and A. Hirose¹

¹*Division of Materials and Manufacturing Science, Graduate School of Engineering, Osaka University,
2-1 Yamada-oka, Suita, Osaka 565-0871, Japan*

²*Nippon Denki Kagaku Co., Ltd., 18 Nishinogoto-cho, Yamashina-ku, Kyoto 607-8356, Japan*

³*General Co., Ltd., 18 Satsukigaoka, Minakuchi-cho, Koka, Shiga 528-0062, Japan*

⁴*Ion Technology Center Co., Ltd., 2-8-1 Tsudayamate, Hirakata-shi, Osaka 573-0128, Japan*

Email: sano@mapse.eng.osaka-u.ac.jp



Keywords: Indium Tin Oxide (ITO), patterning, laser-induced thermal printing

1. Introduction

Indium tin oxide (ITO) is widely used in many electronic devices such as flat panel displays, cell-phones and touch panels. ITO possesses high conductivity due to oxygen vacancies and donation of a free electron caused by substitution of Sn for In because they have different valences. Photolithographic and wet etching methods are wet process, which are well known to be used generally for ITO patterning. Although these methods achieve fine patterns, they also involve discharge of chemical pollutions. Laser direct writing method is a dry process without generating the chemical pollutions. Here we report the development of the laser-induced thermal printing method, which is a kind of laser direct writing method. Although patterning methods of ITO using laser pulses were reported [1-3], the laser-induced thermal printing method differs from other methods in using Diamond-like Carbon (DLC) layer as a laser absorption layer and heat source. In addition, it is expected that this method achieves printing and annealing of ITO by heat from DLC at the same time, and resistivity of the printed ITO decreases than the donor ITO. Furthermore it is available for substrate of low heat resistance because this method affects narrow heat zone. The purpose of this study is to investigate the line width and resistivity of the printed ITO as a function of the incident laser power aiming to establish the laser-induced thermal printing method as a new method of ITO patterning which can pattern microwires and achieve low resistivity.

2. Experiments

Figure 1 shows the schematic illustration of the laser-induced thermal printing method. We used a donor sheet, which consisted of three layers: a PET layer (100 μm in thickness), a DLC layer (200 nm in thickness) and an ITO layer (250 nm in thickness), and a substrate sheet, which consisted of two layers: a PET layer (100 μm in thickness) and an adhesive layer. Two kinds of adhesives were prepared, one was polyester series adhesive which was spread 1.56 g/m^2 on the PET and adheres above 88 $^{\circ}\text{C}$. The other was polyether sulfone series adhesive which was spread 0.99 g/m^2 on the PET and adheres above 225 $^{\circ}\text{C}$. The donor sheet was stacked on the substrate sheet and scanned by continuous wave laser (Spectra Physics, Millennia Vs) focused on the DLC using objective lens (NA 0.13). Wavelength of the laser beam was 532 nm, and irradiated laser power and scanning speed were varied. The DLC layer performs as a laser absorption layer and heat source, and the adhesive melts and adheres to ITO. If adhesive force between ITO and adhesive is sufficiently strong, ITO is sheared and printed when the two sheets are separated. The printed ITO microwires was observed using Scanning Electron Microscope (SEM).

3. Results and Discussion

Figure 2(a) shows the SEM image of the printed ITO microwire using the laser-induced thermal printing method under optimized conditions (polyester series adhesive, scanning speed was 1 mm/s, incident power was 0.030 W). We succeeded in printing of ITO microwires with around 10 μm line width. The line width of the printed ITO microwires is proportional to the incident laser power. The line width varies with the kind of adhesive even same incident laser power. While the line width becomes narrower with decrease of the incident laser power, there is a threshold value of the line width. Because in case of the lower laser power incidence, the adhesive does not adhere or only a little area adheres, and the ITO film is not sheared and printed. In case of higher laser power incidence, appearance of printed ITO microwires is observed ununiformly as shown in

Figure 2(b) (scanning speed was 1 mm/s, incident power was 0.190 W). We succeeded in patterning multiple ITO microwires under optimum conditions without damaging the PET substrate as shown in Fig. 3.

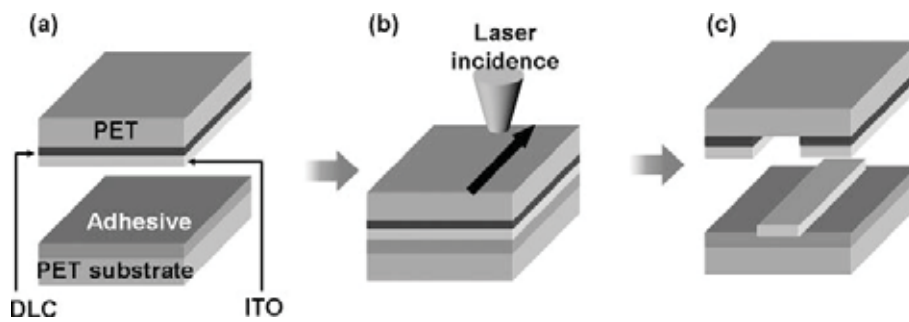


Fig. 1. Schematic illustration of the laser-induced thermal printing method. (a) Before, (b) during and (c) after the laser irradiation.

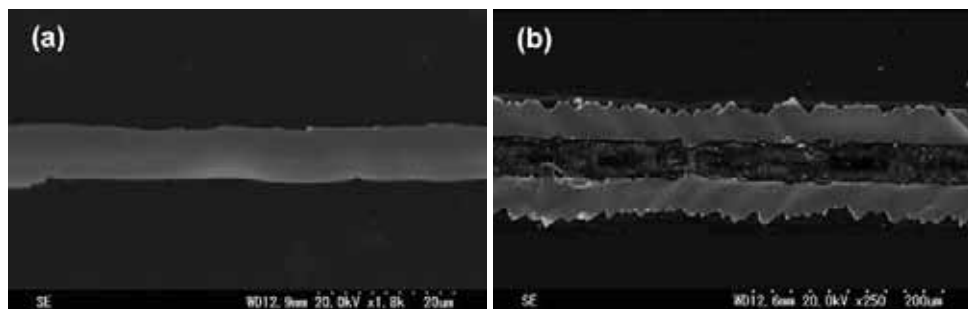


Fig. 2. Fabricated ITO line with the laser power of (a) 0.030 W and (b) 0.190 W.

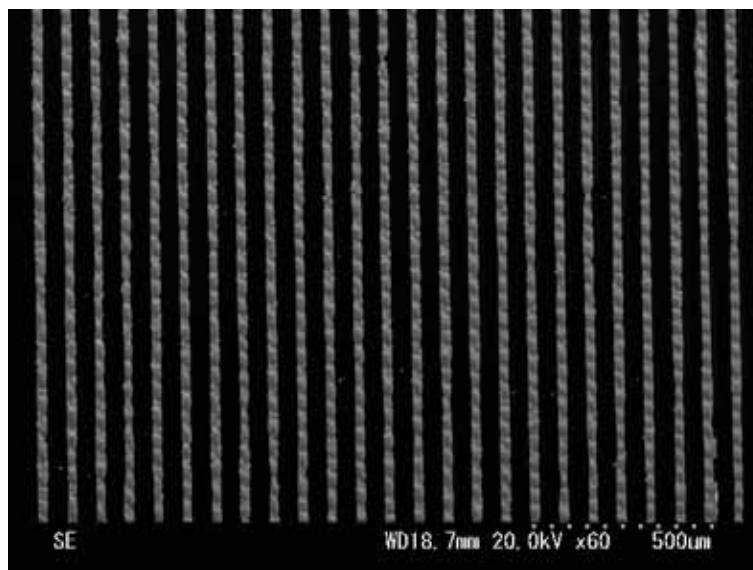


Fig. 3. Patterned ITO microwires without damaging the PET substrate.

4. Conclusions

We succeeded in printing and patterning of ITO microwires with around 10 μm line width on the PET substrate using the laser-induced thermal printing method. We found that the line width of the printed ITO microwires is proportional to the incident laser power, and that the line width varies with the kind of adhesive even same incident laser power because of difference of the adhering temperature. Experimental results and discussions on the resistivity of the patterned ITO microwires will be addressed in the talk.

References

- [1] M. Y. Xu, J. Li, L. D. Lilge, and P. R. Herman, *Appl. Phys. A* 85, 7 (2006).
- [2] M. F. Chen, Y. P. Chen, W. T. Hsiao, and Z. P. Gu, *Thin Solid Films* 515, 8515 (2007).
- [3] G. Račiukaitis, M. Brikas, M. Gedvilas, and T. Rakickas, *Appl. Surf. Sci.* 253, 6570 (2007).

Copper nanocomposite paste for high reliable interconnection and its joining characteristics

Kwang-Seok Kim, and Seung-Boo Jung

*School of Advanced Materials Science and Engineering, Sungkyunkwan University,
2066 Seobu-ro, Jangan-gu, Suwon 440-746, Republic of Korea*

Email: sbjung@skku.edu



Keywords: Nanocomposite, Copper nanoparticle, Copper nanowire, Multi-walled carbon nanotube, Joining characteristic, Sintering

1. Introduction

Nanojoining technology has received great attention due to low-temperature bonding process, high working temperature and various applications in a wide range of electronic devices. Metallic nanoparticle has been widely used as a conductive filler in general conductive nanopaste which can be applied to bonding process. While joints can be achieved by sintering of metallic nanoparticle paste at relatively low temperature due to large surface energy and high surface area to volume ratio [1-3], they show poor joining characteristics induced by defects including inner voids and loose cohesion between metallic clusters. During sintering of the metallic particles which are nanoscale in diameter, surface diffusion causes particle necking and coarsening thus the microstructure of the nanoparticle-based joints is not completely dense. In order to overcome these problems, our group has focused on the nanocomposite fillers containing 1- or 2-dimensional nanomaterials at the metallic nanoparticle-based matrix, instead of longer process times with higher pressure in bonding.

2. Experiments

Copper (Cu) nanocomposite paste was manufactured with Cu-decorated multi-walled carbon nanotubes (MWNT) and Cu nanowires (NWs) dispersed in an organic solvent. The joints were prepared via screen printing of the Cu nanocomposite paste on Cu plates and sintering at various temperatures and pressures. The microstructural evolution of the Cu nanocomposite joints was observed by field emission scanning electron microscopy. The bonding strength of Cu nanocomposite joints was assessed by a single lap shear test and compared with that of Cu nanoparticle joints. The failure mode of the joints was analyzed by fracture observation with an optical microscopy and fracture energy calculated from force-displacement curves.

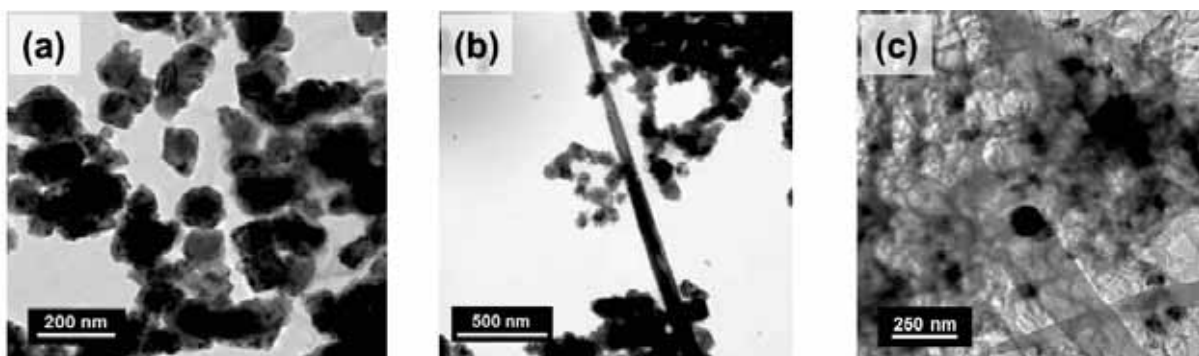


Fig. 1 Typical HRTEM micrographs of (a) Cu nanoparticle, (b) Cu nanoparticle and nanowire, and (c) Cu-MWNT composite particle.

3. Results and Discussion

Figure 2 (a) shows the bonding strength of the Cu nanocomposite joints with various sintering temperatures. As the sintering temperature increases the bonding strength increases, which means that the higher sintering temperature accelerated the formation of network among fillers and strong bonding of joint interface between Cu nanocomposite and Cu plate. Overall, when the joint containing 3 wt.% MWNT shows similar or slightly lower bonding strength compared to that comprising of Cu nanoparticles only. It may be related with sintering behavior of Cu-decorated MWNTs at a Cu nanoparticle-based matrix and removal of organic residues in the vicinity of the interface between Cu nanocomposite paste joint and the Cu plate surface. Figure 2 (b) shows the variation of bonding strength as a function of shear test time. Although the maximum bonding strength decreases at Cu-3 wt.% MWNT, MWNT networks occur reinforcement effect, leading to stiffness improvement

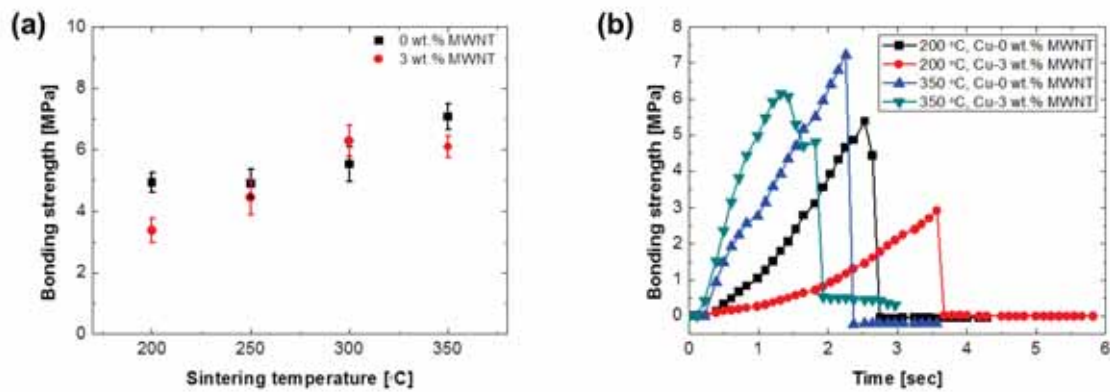


Fig. 2 Variation of bonding strength of the Cu-MWNT nanocomposite joints with (a) sintering temperature and (b) time of lap shear testing.

and greater fracture energy of the MWNT nanocomposite joints. It is noted that joining characteristics of Cu nanocomposite paste are determined by the dispersion of MWNTs in the metallic nanoparticle-based matrix, filler composition, and optimization of sintering condition.

4. Conclusions

Joining characteristics of the Cu nanocomposite paste joints were investigated by sintering temperature and filler composition rate. The Cu-decorated MWNT nanocomposite filler can provide uniform distribution of the MWNTs and formation of larger clusters, leading to the high-reliable and robust joints. Based on the observation of microstructural evolution and fracture surfaces, it is found that MWNT networks are formed between Cu-decorated MWNTs and the Cu nanoparticle-based matrix.

References

- [1] Y. Jianfeng, Z. Guisheng, H. Anming and Y.N. Zhou, "Preparation of PVP coated Cu NPs and the application for low-temperature bonding," *J. Mater. Chem.*, 21, 15981-15986 (2011).
- [2] H. Nishikawa, T. Hirano, T. Takemoto and N. Terada, "Effects of joining conditions on joint strength of Cu/Cu joint using Cu nanoparticle paste," *The open surface science journal*, 3, 60-64 (2011).
- [3] S. Krishnan, A.S.M.A. Haseeb and M.R. Johan, "Preparation and low-temperature sintering of Cu nanoparticles for high-power devices," *IEEE Trans. Compon. Packag. Manuf. Technol.*, 2, 587-592 (2012).

Nano Brazing Technology in Industrial Environment

M. Türpe¹

¹MAHLE Behr GmbH & Co. KG, Stuttgart, Germany

Email: matthias.tuerpe@mahle.com



Aluminium Brazing, Heat Exchanger, Industrial Application, Holistic Approach.

Abstract

Aluminium heat exchangers for vehicles are state of the art for more than 30 years. Actually, domestic applications change from copper to aluminium as well. For all these products, brazing is the dominating joining technology. Due to service conditions, especially corrosion requirements, the use of AlSi filler metals is mandatory. Their main disadvantage is the low temperature range between brazing temperature needed and melting temperature of parent metals to be brazed. Therefore, any technology offering a reduction of brazing temperature would be welcome.

In recent years, different developments based on metallurgy have been undertaken, but with no possibility for application in mass production, e.g. of automotive heat exchangers. The only promising approach had been the idea of nano Al(Si) filler metals. Although first steps had been successful, intensive fundamental research as important starting point before any industrial application turned out to be necessary [1].

From the scientific point of view, a second item has to be followed at the same time. With increasing complexity of products and production processes, a complete understanding of interactions in production processes as well as with design and industrial environment is needed. Based on such approaches [2,3], the opportunities and challenges of nano brazing technologies are presented and assessed in this lecture.

References

- [1] M. Türpe, J. Janczak-Rusch et al., "Approach for Al brazing with nano filler metals," DVV-Berichte, Band 289, p. 125-129, (2012).
- [2] M. Türpe, "Lecture Brazing, chapter 3 Interactions in engineering science," script, TU Dresden, (2014).
- [3] U. Füssel, "Zusammenarbeit mit der Industrie in Lehre und Forschung. Wege – Ergebnisse – Perspektiven", Proc. X. Dresdner Füge-technisches Kolloquium 2013, p. 22 (2013)

State-of-the-art local electrochemical characterisation of micro- and nano-joints

T. Suter, P. Schmutz, J. Janczak-Rusch

Empa, Materials Science & Technology, Überlandstrasse 129, CH 8600 Dübendorf, Switzerland

Email: thomas.suter@empa.ch



Keywords: microcell technique , micro- and submicro-electrochemical corrosion tests, chemical durability of micro-and nano-joints

1. Introduction

A detailed evaluation of the chemical durability of micro- and nano-joints is challenging. Immersion tests are possible and they are often performed. However, they usually provide only information about the general corrosion behavior. In order to gain information about the corrosion mechanism and about the critical factors that trigger the onset of (localized) corrosion, electrochemical corrosion tests are required. Electrochemical tests allow controlling the surface potential of the specimen and measuring the corresponding corrosion current. In this way the redox potential of different environments can be scanned. Thus the critical conditions that lead to the onset of stable (localized) corrosion can be evaluated.

Due to the small dimensions of micro- and nano-joints, large-scale electrochemical tests are not possible - local measurements are required. Furthermore, the microstructures of most joints are typically optimized for their mechanical properties. Fine-grained microstructures and a high number of micro/nanometer heterogeneities or reinforcing particles are usually the consequence. To study these preferential corrosion initiation sites micro- and submicroelectrochemical studies were performed. Figure 1 left shows the principle of the used local electrochemical technique. The use of small tapered glass capillaries as miniaturized corrosion test cell allows exposing only small surface areas to an aggressive test solution. Thus, the corrosion behavior of single heterogeneities in structure can be evaluated.

Microelectrochemical tests are usually performed to study the corrosion behavior of structural features with dimensions $> 1 \mu\text{m}$ [1]. To characterize phases or particles $< 1 \mu\text{m}$ tests on exposed areas in the submicrometer range are highly beneficial. Therefore, for the first time, a specially optimized electrochemical measuring system was used that allows to use capillaries with submicrometer tips as electrochemical cell and to control currents $< 1 \text{fA}$. Thus tests can be performed on exposed areas $< 1 \mu\text{m}^2$.

In the frame of this work local electrochemical corrosion measurements were performed for testing lead-free reinforced solders, evaluating the corrosion behavior of different zones of laser welds, and for evaluating the melting point depression of nanostructured brazing joints.

2. Technique

The used electrochemical corrosion technique bases on pulled glass capillaries, which act as a miniaturized electrochemical cell [1]. They are fixed at the revolving nosepiece of a microscope replacing an objective (Fig. 1 middle). Micro- and submicro capillaries with a silicone sealant at the tip were used (Fig. 1 right).

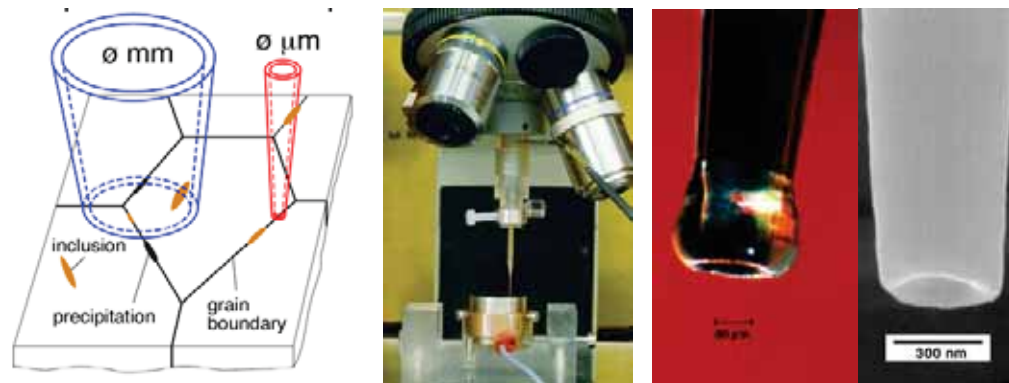


Fig. 1. : Microcell / Submicrocell technique

Left: Principle of local electrochemical corrosion investigations

Middle: Local electrochemical set-up

Right: coated microcapillary (50 μm) and coated submicrometer capillary (300 nm)

3. Results and Discussion

Testing lead-free reinforced solders:

At Empa new lead-free solders are being developed that contain small particles to enhance the joint mechanical performance. To evaluate the best type of reinforcing particles for a good corrosion behavior, polarization curves were measured in 1 M NaCl on different zones of a Sn-Ag-Cu (SAC) solder with reinforcing copper particles. During soldering most, but not all, Cu particles get transformed to Cu_6Sn_5 (Fig. 2 left). The measured curves indicate that noble Cu particles polarize the adjacent, less noble tin phase to potentials where corrosion can get initiated (Fig. 2 right). The less noble Cu_6Sn_5 particles cannot polarize the tin phase. Therefore it would be beneficial to use Cu_6Sn_5 particles as reinforcing particles

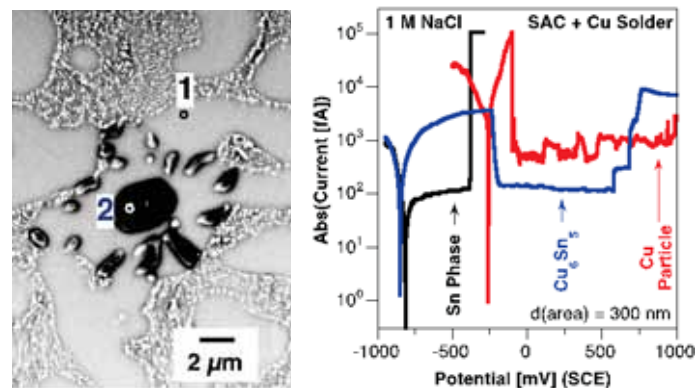


Fig. 2. : Sn-Ag-Cu solder reinforced with Cu particles
 Left: Microstructure: (1) Sn phase; (2) Cu_6Sn_5 phase
 Right: Polarization curves (characteristic corrosion curves) measured on single phases using a 300 nm capillary

Evaluating the corrosion behavior of different zones of laser welds:

A company offers a lifetime warranty for their cooking pots produced of SS 316. The handles are fixed to the pot by laser welds. In order to rank the lifetime of these joints local corrosion tests were performed on different zones of the laser welds. It was found that too much energy was applied during the welding process leading to laser weld dots with micro holes. The micro holes initiated localized corrosion already at very low potentials. The laser welding process had to be optimized.

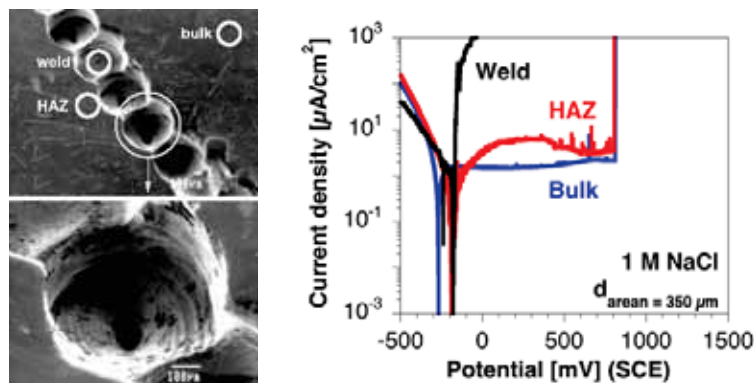


Fig. 3. : Evaluation of the corrosion behaviour of laser welding joint
 Left: SEM image of the laser weld, single laser dots form a laser weld line
 Right: Local polarization curves measured on different zones of a laser welding joint using a 350 μm capillary

4. Conclusions

The use of coated micro- and submicrometer glass capillaries acting as electrochemical cell allows evaluating the chemical durability (corrosion behavior) of micro and nano joints. The gained information helps optimizing the joining material and the joining process.

References

- [1]. T. Suter and H. Böni, "The Microcell Technique", in *Analytical Methods in Corrosion Science and Engineering*, CRC Press, (2005).

Joining technology through sintering of silver nanoparticles derived from silver oxide paste

T. Ogura¹ and A. Hirose¹

¹*Division of Materials and Manufacturing Science, Graduate School of Engineering, Osaka University, 2-1 Yamadaoka, Suita, Osaka 565-0871, Japan*

Email: tomo.ogura@mapse.eng.osaka-u.ac.jp



Keywords: Nanoparticles, Redox reaction, Sintering, Bonding, Silver oxide

1. Introduction

It is desirable that electronic devices not only work efficiently at elevated temperatures but also consume lesser power when packaged, and bonding technology that can meet these requirements needs to be developed. It is anticipated that the use of nanoparticles as bonding materials in die-attach technologies will provide feasible alternatives to the current microsoldering techniques that require the use of high-temperature solders such as Pb-10Sn or Pb-5Sn. During bonding process, rapid sintering of nanoparticles occurs after the release of the organic elements around the nanoparticles, and then the metal-to-metal bonding can be achieved through a sintered bonding layer. In this bonding process the decomposition and removal of the organic element adhering to the nanoparticles are necessary to bring out the low-temperature sintering property of the nanoparticles. This is a bottleneck of the bonding process. In practical applications, a productive cost of Ag nanoparticles is problem as well. To overcome these problems, a new bonding process through in-situ formation of Ag nanoparticles instead of the filler material of the Ag metallo-organic nanoparticles has been developed [1]. The Ag nanoparticles formed by the reduction of Ag₂O particles and immediately sintered each other. The bonding process, therefore, enabled further reduction of bonding temperature and/or bonding pressure. In this study, the bonding mechanism, mechanical and electrical properties of the joints, the effects of bonding conditions and bonding substrates on the bondability in the joining techniques through sintering of nanoparticles in copper joint are discussed.

2. Experiments

Silver oxide (Ag₂O) particles of 2 μm to 3 μm diameter were used. The particles were milled using an alumina mortar, mixed with a reducing solvent to concentration of 180 μL/g, and processed to paste or bonding. The two types of reducing solvent tested were diethylene glycol (DEG), and polyethylene glycol (PEG), which vary primarily in carbon chain length and molar weight. A copper substrate was used as the bonded material. The silver oxide paste, prepared with DEG, TEG, or PEG, was applied to the lower substrate using a 50-μm-thick mask and preheated at the optimized conditions in order to remove excess reducing solvent. Subsequently, the upper substrate was placed onto the lower substrate, and the samples were heated to 300°C at a rate of 60°C/min using an infrared heating furnace and held for 5 min at a pressure of 5 MPa. After bonding, the samples were cooled using forced air. The shear strength of the joints was measured using a strain rate of 30 mm/min. The thermal characteristics of each silver oxide paste were measured with a combination of thermogravimetric (TG) and differential thermal analysis (DTA) at a heating rate of 60°C/min in ambient atmosphere. The cross-section and fracture surface of each joint was observed by scanning electron microscopy (SEM).

3. Results and Discussion

Fig. 1(a) shows the shear strength measured for the joints prepared with each type of silver oxide paste [2]. The strength increased with the molecular weight of the reducing solvent. The redox reaction between silver oxide and reducing solvent occurred at the onset temperature of DEG, and PEG still remained after the exothermal peak until the temperature reached 300°C, which is the bonding temperature. The shear strength of the joint in the DEG/PEG mixed sample is achieved a strength of 29 MPa. This is higher than that found in gold-to-gold joints made with Pb-5Sn, which is the current industrial standard for die-bonding (=18MPa). This higher strength is explained by microstructural observation, as shown in Fig. 1(b). The dense sintered silver layer was formed and the growth of oxide film was not confirmed and direct bonding between silver and copper was achieved by the decomposition of copper oxide.

When bonding techniques involving the sintering of nanoparticles are used, attention must be paid to the ion-migration tolerance of the bonded circuits, since a sintered layer of pure Ag is formed on them [3]. In this study, the bondability of the joints formed using a reducing-solvents-containing mixed paste of silver oxide (Ag_2O) and copper oxide (CuO) as a second metal was investigated. The Ag_2O particles and CuO particles were mixed in the ratio of 9:1 (in mass%) in the combined solvents of polyethylene glycol (PEG) 400 and a viscous solvent. The strength increased with an increase in the bonding temperature, and exhibited has higher strengths than those of gold-to-gold joints formed using Pb-5Sn (29 MPa). In the water-drop test, Ag atoms of the anode were ionised and made to pass through water towards the cathode under an electric field. On reaching the cathode, these Ag precipitated, forming Ag dendrites. The Ag dendrites grew in size and eventually reached the anode. The ‘arrival time’ for the dendrites, which was defined as from the time period extending from the application of the 3 V potential to the moment the Ag dendrites reached the anode, was used as a measure of the ion-migration tolerance. Fig.2 shows the arrival time plotted against the volume fraction of CuO in the sintered layer [4]. The arrival time for the mixed paste was approximately four times as large as that of a layer of pure sintered silver. Although the quantitative evaluation such as migration rate is not clarified yet, thus, the addition of CuO improved the ion-migration tolerance of the sintered silver layer.

4. Conclusions

1. Direct bonding between silver and copper was achieved by the decomposition of copper oxide. Combination of DEG and PEG produced higher shear strength in the copper joint, as PEG suppressed the growth of copper oxide and DEG promoted the formation of a dense sintered silver layer.
2. The ion-migration tolerance of the bonded layer was improved by the addition of second metal. The ion-migration arrival time of the $\text{Ag}_2\text{O}/\text{CuO}$ mixed paste was approximately four times that of pure sintered silver.

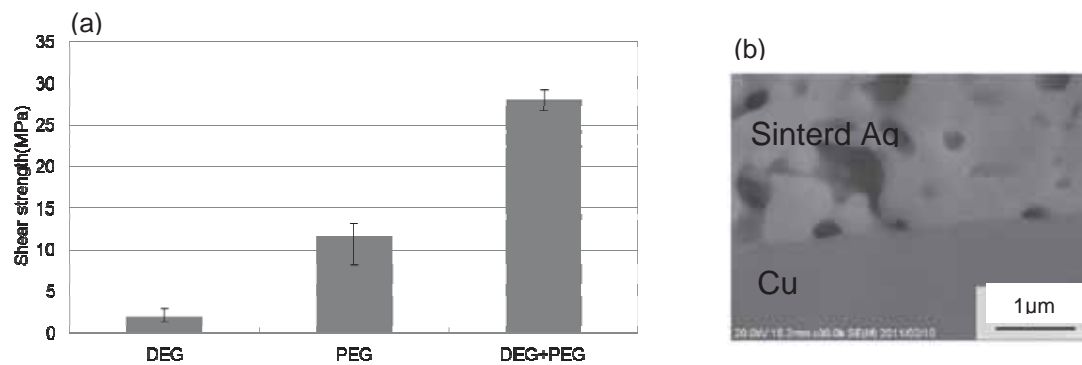
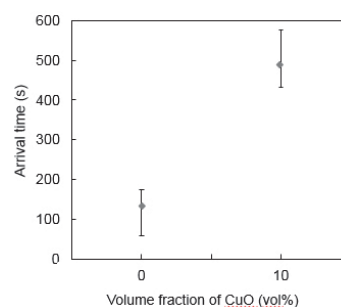


Fig.1(a) Shear strength of the Cu-to-Cu joint using various silver oxide pastes and (b) SEM image of the copper/silver interface using DEG/PEG mixed silver oxide paste [2].

Fig.2 Time taken by the silver dendrites in the sintered layer to grow from the anode and reach the cathode during the water-drop test. This parameter was termed the ‘arrival time’ of the dendrites [4].



References

- [1] A. Hirose, N. Takeda, H. Tatsumi, Y. Akada, T. Ogura, E. Ide and T. Morida, “Low Temperature Sintering Bonding Process Using Ag Nanoparticles Derived from Ag_2O for Packaging of High-temperature Electronics”, *Materials Science Forum*, 706-709, pp.2962-2967 (2012).
- [2] S. Takata, T. Ogura and A. Hirose, “Effects of solvents in polyethylene glycol series on the bonding of copper joints using Ag_2O paste”, *Journal of Electronic Materials*, 42, pp.507-515 (2013).
- [3] T. Ito, T. Ogura and A. Hirose, “Effects of Au and Pd Additions on Joint Strength, Electrical Resistivity and Ion-migration Tolerance in Low-temperature Sintering Bonding using Ag_2O Paste”, *Journal of Electronic Materials*, 41, pp.2573-2579 (2012).
- [4] T. Ogura, T. Yagishita, S. Takata, T. Fujimoto and A. Hirose, “Bondability of copper joints formed using a mixed paste of Ag_2O and CuO for low-temperature sinter bonding”, *Materials Transactions*, 56, 6, pp.860-865 (2013).

Joining of copper by Ag nanopaste: microstructure and strength behavior

B. Wielage, S. Weis, H. Podlesak, and S. Hausner

*Institute of Materials Science and Engineering
Technische Universität Chemnitz,
Erfenschlager Str. 73, 09125 Chemnitz*

Email: susann.hausner@mb.tu-chemnitz.de



Keywords: Ag nanopaste, low temperature joining, copper joining, nanoparticle, nano size effect, alternative brazing, alternative soldering

1. Introduction

Due to the large specific surface area, nanoparticles exhibit a decrease in sintering and melting temperature with decreasing particle size [1]. This effect, which is already known since the 1950s [2], was technically implemented only a few years ago and is now the subject of intense research. Especially in the area of microelectronics, many research papers deal with printing and sintering of electrically conductive structures with nanoparticle inks [3], but the utilization of this effect is also of great interest for joining technologies. After melting of the nanoparticles, the material behaves like the bulk material. Therefore, high-strength and temperature-resistant joints can be produced at low temperatures. This results in a high potential for the joining of high-performance materials, the joining of temperature-sensitive components in electronic applications, the joining of mixed joints such as aluminum and steel and the joining of materials with different thermal expansion coefficients, such as ceramic and metal.

2. Experiments

A commercially available Ag nanopaste of the company Harima Chemicals, Inc. (Japan) was used for the experiments. The spreadable paste (application similar to conventional solder paste) has a very high particle content of 81.8 wt%, which is advantageous for joints with low porosity.

The shape, distribution and size of the nanoparticles were determined using TEM. The thermal behavior of the nanopaste was characterized by simultaneous thermal analysis (STA). The determination of the tensile shear strength and the investigations of the microstructure were performed with joints of pure copper (EN: CU-ETP) as base material with a joining area of 9 mm x 7.5 mm. For the experiments, the process parameters joining pressure, joining temperature, holding time, thickness of paste application and heating rate were varied and the influence of a pre-drying process was investigated.

3. Results and Discussion

Fig. 1 shows exemplarily the joint microstructure of a joint produced with a joining pressure of 40 MPa, a temperature of 300 °C, a holding time of 10 min, a heating rate of 150 K/min and a paste application of 20 µm. Mostly a dense joining seam with a grain size of 100 nm to 200 nm can be observed (Fig. 1b). It is assumed that the nanoparticles fuse to larger particles for a short time, until the effect of the large surface energy is consumed. Through the joining pressure, the molten particles are compacted to a dense structure. Furthermore some diffuse areas are visible in the joining seam. Fig. 1c) represents the transition area between dense and diffuse areas. The size of the particles increases significantly towards the right hand side, i.e. in the direction of the diffuse area. Finally on the right side of Fig. 1c), only very small particles can be observed. Therefore it is assumed that in some areas, the nanoparticles still exist in their original form in the joining seam.

Fig. 2 shows the achievable tensile shear strengths and the porosities as a function of selected varied process parameters. In particular, the joining pressure, but also the temperature, the holding time and the thickness of the paste application have a decisive influence on the strength behavior. The influence of heating rate and pre-drying are negligible and therefore not shown. With increasing joining pressure, a significant compression of the joint seam as well as an improved adhesion to the base materials can be observed, resulting in higher strength values. The increasing strength up to a temperature of 400 °C correlates with the results for the thermal behavior. At a temperature of 400 °C, there occurs a complete fusion of the nanoparticles. The increasing strength with longer holding times is affiliated to an improved adhesion to the base materials. Regarding to the paste application, an optimum thickness of 20 µm was determined, by which the highest strengths are obtained.

For a thinner application, the surface roughness of the base materials can partially not be compensated. For a thicker application, an incomplete melting of the particles over the entire thickness of the seam is observed. Both result in lower strengths.

The results of the TEM and STA investigations will be part of the oral presentation.

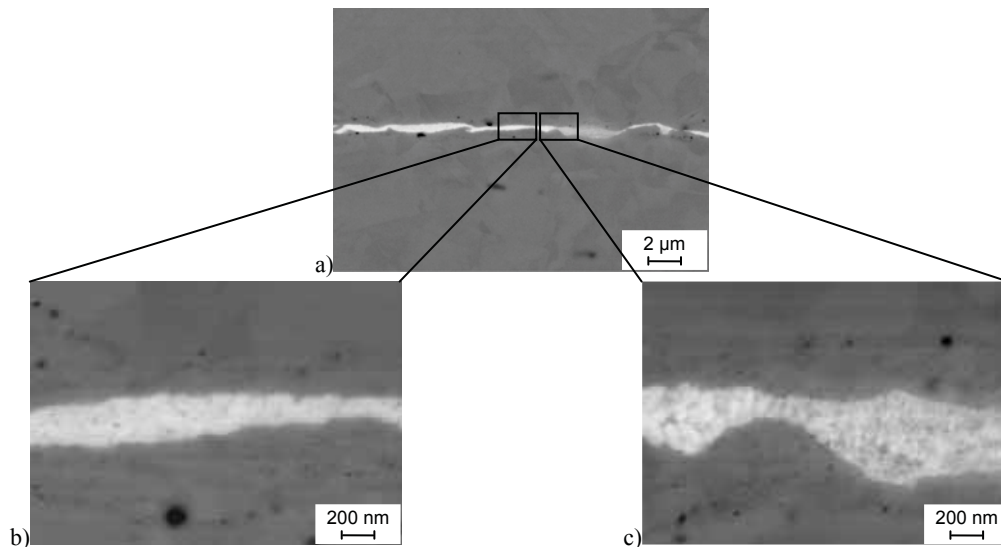


Fig. 1: Microstructure (pressure: 40 MPa, temperature: 300 °C, holding time: 10 min, heating rate: 150 K/min, paste application: 20 μm)

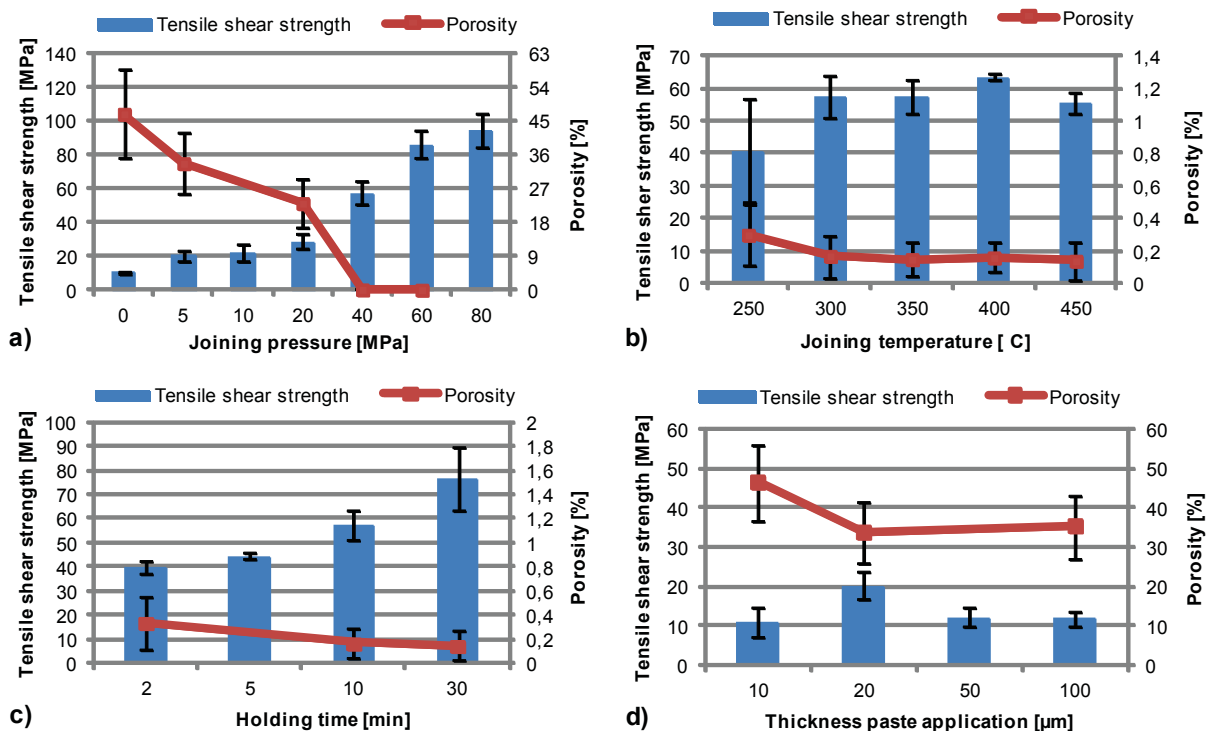


Fig. 2: Tensile shear strength as a function of a) joining pressure (temperature: 300 °C, holding time: 10 min, paste application: 20 μm); b) joining temperature (pressure: 40 MPa, holding time: 10 min, paste application: 20 μm); c) holding time (temperature: 300 °C, pressure: 40 MPa, paste application: 20 μm); d) paste application (temperature: 300 °C, pressure: 5 MPa, holding time: 10 min)

References

- [1] Q. Jiang, S. Zhang, M. Zhao, "Size-dependent melting point of noble metals", *Materials Chemistry and Physics* 82, 225–227 (2003).
- [2] M. Takagi, "Electron-Diffraction Study of Liquid-Solid Transition of Thin Metal Films", *J. Phys. Soc. Jpn.* 9, 359–363 (1954).
- [3] N. Mathews, Y.M. Lam, S.G. Mhaisalkar, A.C. Grimsdale, "Printing materials for electronic devices", *International Journal of Materials Research* 101, 236–250 (2010).

Synthesis and light induced nanojoining of silver nanowires

Yanhong Tian, Su Ding, Chunqing Wang

State Key Laboratory of Advanced Welding and Joining, Harbin institute of technology, HIT

Harbin, China, 150001

Email: Tianyh@hit.edu.cn



Keywords: silver nanowires, nanojoining, surface enhanced Raman scattering

1. Introduction

With the development of electronics, miniaturization and intellectualization become important trends of electronics. It is an emergency need to do research on nanotechnology and nanoscience. There are a lot of achievements on fabrication of nanomaterials, including metal[1-3], semiconductor materials[2, 4-5] and complicated compounds[6]. Compared to the synthesis of nanomaterials, the nanojoining technology is a fairly new field lacking of basic theory and enough experimental data. There are many methods have been reported, such as joule heating by electric[7], electron or ion beam welding[8], cold welding[9], ultrasonic nanowelding[10], femtosecond laser induced joining[11], and soldering[12]. Recently, a light induced nanojoining technology has been reported[13]. The technology involves melting of nanowires only at the points of contact through a surface enhanced Raman scattering(SERS) effect that greatly reduces the damage to the substrate. This technology could apply to optoelectronics, especially convenient for transparent electrodes. Transparent electrodes are widely used for touch screen, solar cells, liquid crystal display panels, light-emitting diodes (LED) and so on. Metal nanowire, especially silver nanowire, transparent film with low cost and flexibility is a promising candidate to instead of indium tin oxide (ITO) electrodes which is mostly used now. One crucial drawback impeding the application of silver nanowires films is that the high contact resistance between nanowires exists due to the insulating surfactant or solvent used in the fabrication process. The light induced nanojoining technology has been developed to improve the electrical property between nanowires further to apply in transparent films[13]. The goal of our study is to connect silver nanowires using light induced nanojoining technology and discuss the formation mechanism.

2. Experiments

Silver nanowires have been fabricated by a polyol method, employing Polyvinylpyrrolidone (PVP) as surfactant and ethylene glycol (EG) as reduction. A small amount of ferrum nitrate($\text{Fe}(\text{NO}_3)_3$) was added to adjust the shape of products. The precipitate was collected by centrifugal separation and dispersed in alcohol for later use. The synthesized nanowires were characterized by X-Ray diffraction (XRD) and scanning electron microscope (SEM). XRD patterns were collected with a Rigaku D/max- γ B diffractometer with Cu $K\alpha$ irradiation. Morphology and structure of the nanowires were checked with a field-emission SEM (FEI Quanta 200F) and a FEI Tecnai G² F30 microscope operated at 300 kV.

The silver nanowires solution was dispersed on silicon or polyethylene terephthalate (PET) polymer, followed by heating at 60°C for 5minutes. A halogen tungsten lamp with a colour temperature at 3000K was used to illuminate silver nanowire networks. The nanowires were processed at different illumination intensity and power that affected the quality of joints.

3. Results and Discussion

To synthesize the Ag nanowires, 0.8mmol silver nitrate, 1mmol PVP and 2.2 μmol $\text{Fe}(\text{NO}_3)_3$ were dispersed in a flask heating in an oil bath at 160°C for 1 hour. Fig.1 shows the XRD pattern and SEM images of the Ag nanowires. XRD pattern in Fig. 1a states that the obtained product is phase-pure Ag (JCPDS 65-2871). The nanowires have smooth surfaces with diameters around 100nm and lengths up to 50 μm as shown in Fig. 1b and 1c. The silver nanowires were further characterized by TEM as shown in Fig. 3. For keeping a long time in alcohol the nanowires began to connect at the ends without PVP attached to the surface as indicated in Fig.2a. The SAED pattern in Fig. 3b ensured that the obtained nanowires is silver nanowires with penta-twinned structure that the two sets of spots indexed in the figure clearly show the twinned structure and the presence of a sequence of diffraction spots marked by arrows in Fig.2b indicates the five-fold structure. The growth direction of silver nanowires is along [110] according to the HRTEM image.

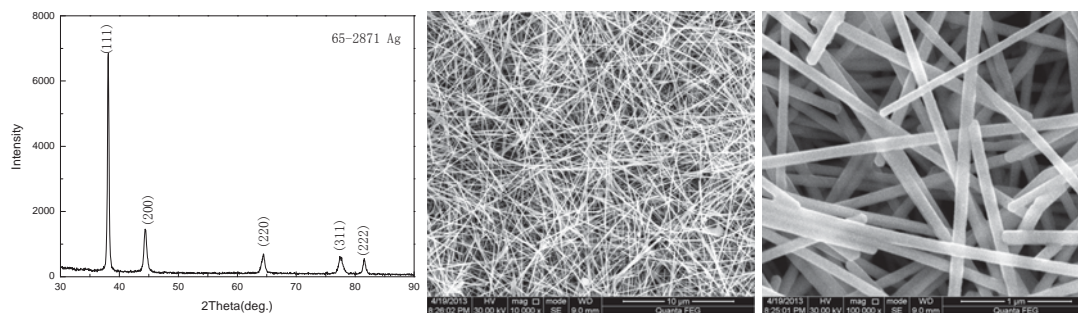


Fig. 1 XRD pattern and SEM images of silver nanowires.

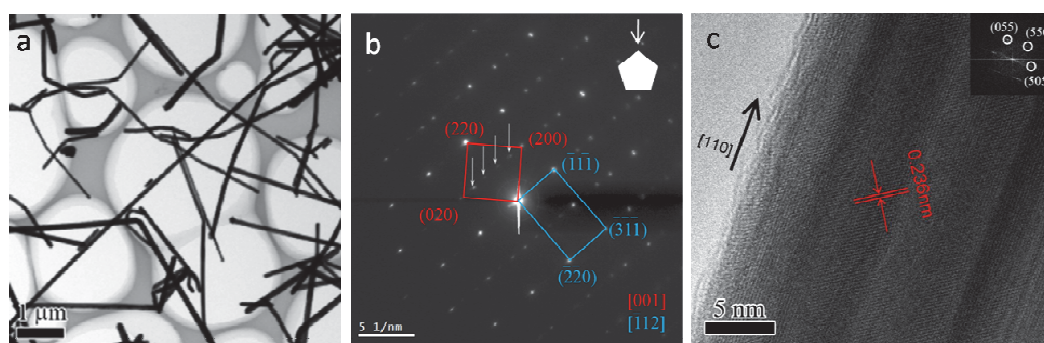


Fig.2 (a) TEM image of silver nanowires; (b) Corresponding SAED patterns; (c) HRTEM image of silver nanowire.

4. Conclusions

Silver nanowires with uniform diameter have been fabricated by a polyol method. Silver nanowires growth along $[110]$ direction and have five-fold structure. The nanojoining induced by a halogen tungsten lamp with a colour temperature at 3000K was completed.

Acknowledgement

This work has been supported by Program for New Century Excellent Talents in University (NCET-13-0175)

References

- [1] C. Murphy, T. Sau, A. Gole, C. Orendorff, J. Gao, L. Gou, S. Hunyadi, and T. Li. "Anisotropic metal nanoparticles: synthesis, assembly, and optical applications," *Journal of Physical Chemistry C*, 109, 13857-13870 (2005)
- [2] C. Rao, F. Deepak, G. Gundiah, and A. Govindaraj, "Inorganic nanowires," *Progress in Solid State Chemistry*, 31, 5-147 (2003)
- [3] M. Rycenga, C. Cobley, J. Zeng, W. Li, C. Moran, Q. Zhang, D. Qin, and Y. Xia, "Controlling the Synthesis and Assembly of Silver Nanostructures for Plasmonic Applications," *Chemical Review*, 111, 3669-3712 (2011)
- [4] Wei Lu, and Charles M Lieber, "Semiconductor nanowires" *Journal of Physics D: Applied Physics*, 39, R387-R406 (2006)
- [5] Z. Wang, "Nanostructures of zinc oxide," *Materials today*, 26-33 (2004)
- [6] Y. Mao, T. Park, F. Zhang, H. Zhou, and Stanislaus S. Wong, "Environmentally friendly methodologies of nanostructure synthesis," *Small*, 0, 1-19 (2007)
- [7] H. Tohmyoh, T. Imaizumi, H. Hayashi, and M. Saka. "Welding of Pt nanowires by Joule heating," *Scripta Materialia*, 57, 953-956 (2007)
- [8] S. Xu, Mi. Tian, J. Wang, J. Xu, J. Redwing, and M. Chan. "Nanometer-scale modification and welding of silicon and metallic nanowires with a high-intensity electron beam," *Small*, 1, 1221-1229 (2005)
- [9] Y. Lu, J. Huang, C. Wang, S. Sun, and J. Lou. "Cold welding of ultrathin gold nanowires," *Nature Technology*, 5, 218-224 (2010)
- [10] C. Chen, L. Yan, E. Kong, and Y. Zhang. "Ultrasonic nanowelding of carbon nanotubes to metal electrodes," *Nanotechnology*, 17, 2192-2197 (2006)
- [11] L. Liu, P. Peng, A. Hu, G. Zou, W. Duley, and Y. Zhou. "Highly localized heat generation by femtosecond laser induced plasmon excitation in Ag nanowires," *Applied Physics Letters*, 102, 073107 (2013)
- [12] Y. Peng, T. Cullis, and B. Inkson. "Bottom-up Nanoconstruction by the Welding of Individual Metallic Nanoobjects Using Nanoscale Solder," *Nano Letters*, 9, 91-96 (2009)
- [13] E. Garnett, W. Cai, J. Cha, F. Mahmood, S. Connor, M. Christoforo, Y. Cui, M. McGehee, and M. Brongersma. "Self-Limited Plasmonic Welding of Silver Nanowire Junctions," *Nature Materials*, 11, 241-249 (2012)

Effect of rapid solidification on microstructure and properties of Sn-Ag-Cu lead-free solder

S. Lu¹, F. J. Wang¹, and Z.X. Zheng¹

¹ Provincial Key Laboratory of Advanced Welding Technology, Jiangsu University of Science and Technology, Zhenjiang, 212003, P.R. China

Email: lusheng88168@qq.com



Keywords: rapid solidification, Sn-Ag-Cu, microstructure, wettability, melting pointing, shear strength

1. Introduction

Several Pb-free alloys have been proposed to replace traditional eutectic Sn-37Pb solder, with SnAgCu ternary alloys among the most popular [1]. The microstructures and processing-structure-properties of SnAgCu alloys are quite different, and more complicated, than that of eutectic SnPb. The addition of Ag and Cu to the Sn results in the formation of eutectic interdendritic regions on the ternary SnAgCu phase diagram at $\sim 217^\circ\text{C}$ with intermetallic compounds particles (IMCs) of Ag_3Sn and Cu_6Sn_5 within the Sn-matrix [2]. As the concentration of Ag and Cu in SnAgCu solder increases there is a significant increase in the eutectic interdendritic regions that results in a degradation of creep properties [3]. Alloying and processing conditions greatly affect the properties of SnAgCu solders. Rare earth elements such as Ce refine the microstructure and reduce the creep strain [4-6], while small amounts of Bi increase the tensile strength of SnAgCu [7]. Increasing the cooling rate during solidification results in a fine dispersion of Ag_3Sn and a higher yield strength [8], while subsequent solid-state thermal aging coarsens the Ag_3Sn and Cu_6Sn_5 IMCs and decreases the tensile strength of the SnAgCu solder [9, 10].

In this paper, we use rapid solidification with vacuum suction casting to produce Sn-3.0Ag-0.5Cu Pb-free solder, and the properties including melting point, microstructure, wettability and mechanical properties of as-suctioned solders are researched.

2. Experiments

The Pb-free solder composition used in this study is Sn-3.0Ag-0.5Cu alloy. The as-casted samples of bulk alloy were prepared from 99.9% purity elements by vacuum melting at 500°C for several hours. The as-casted solder was placed into vacuum suction casting furnace (WK-II), melted and then suction casted with water (flowing rate: 180 ml/s) as the cooling media to get the rapid solidified solder alloy. It was named as as-suctioned solder in this paper.

The melting points of two types of solders samples, i.e. as-casted and as-suctioned, were measured using DTA analysis with heating rate of $5^\circ\text{C}/\text{min}$ and N_2 as protected atmosphere. The wettability of solders was tested using solder ball wetting balance method (SAT-5100, Rhesca Co.). The two solders were epoxy-mounted and polished to a $0.05\ \mu\text{m}$ final finish with colloidal silica suspension for the cross-section observation. The microstructure was probed by scanning electron microscopy (SEM).

To evaluate the strength of solder alloys, the resistors were soldered to Cu pads on PCB boards using the as-casted and as-suctioned solder. The shear force was tested on these solder joints using shear testing (STR-1000, Rhesca).

3. Results and Discussion

The microstructure of as-suctioned solder is shown in Fig.1 from outer side (Fig.1a) to inner side (Fig.1d). It can be found that the solidification rate obviously changed the microstructure of the solder alloy. With the vacuum suction method, we got a non uniform but refined structure. From the outer to the inner, the microstructure of as-suctioned solder is completely different. The outer region is the slim branch pointed to the center which was firstly precipitated $\beta\text{-Sn}$ phase. The crystal particles between the branches are tiny. The inner is the bulky grid shape structure with the existence of Ag_3Sn and Cu_6Sn_5 . The inner microstructure was more coarsen than outer structure.

Fig.2 shows the DTA curves and melting points on these two solder alloys. The liquidus temperature on as-suctioned solder is 219.86°C , lower than that on as-casted solder, 221.49°C .

With solder ball balance testing, the maximum wetting force and time are 0.48 mN and 0.99 s for as-casted alloy, and 0.60 mN and 0.82 s for as-suctioned solder, respectively. The wettability was little improved with rapid solidification.

With shear testing, the average shear force is 6219.5 gf for as-casted alloy, and 6323.5gf for as-suctioned alloy, respectively. The shear strength was also improved with rapid solidification.

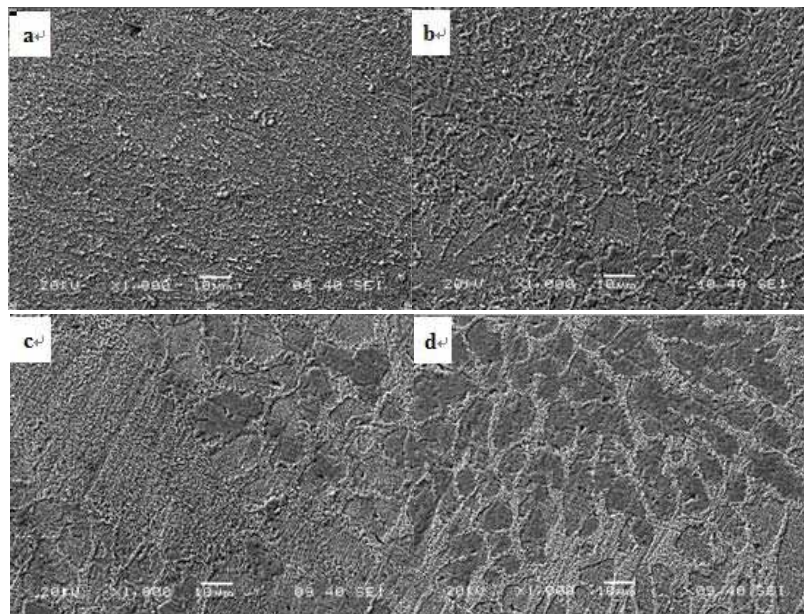


Fig. 1. Microstructure of as-suctioned solder from outer to inner

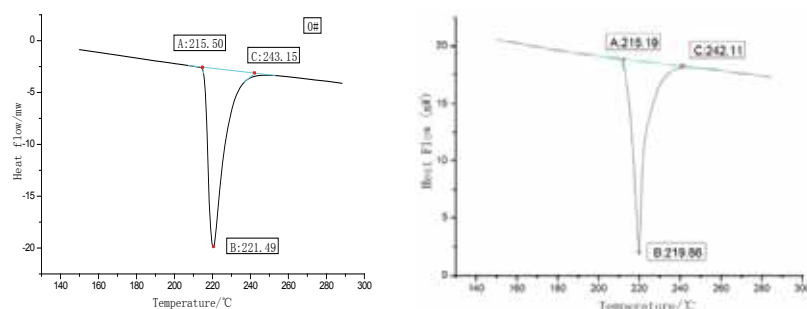


Fig.2. DTA curves of as-casted (a) and as-suctioned (b) solder alloys

4. Conclusions

With rapid solidification, Sn-3.0Ag-0.5Cu solder alloy had a refined structure, lower melting temperature, improved wettability and shear strength compared with traditional as-casted solder alloy.

References

- [1] NCMS: Report No. 0401RE96, National Center for Manufacturing Sciences, Ann Arbor, MI, August, 1997
- [2] T. Laine-Ylijoki, H. Steen, and A. Forsten: IEEE Trans. Compon. Packag. Manuf. Technol., Park C, 1997, vol. 20, pp. 194–198
- [3] T. Chen and I. Dutta: J. Electron. Mater., 2008, vol. 37, pp. 347–354
- [4] Z.G. Chen, Y.W. Shi, Z.D. Xia and Y.F. Yan: J. Electron. Mater., 2002, vol. 31, pp. 1122–1128
- [5] Z.G. Chen, Y.W. Shi, Z.D. Xia and Y.F. Yan: J. Electron. Mater., 2003, vol. 32, pp. 235–243
- [6] C.M.L. Wu, D.Q. Yu, C.M.T. Law and L. Wang: Mater. Sci. Eng. R, 2004, vol. 44, pp. 1–44
- [7] J. Zhao, L. Qi, X.M. Wang and L. Wang: J. Alloy. Compd., 2004, vol. 375, pp. 196–204
- [8] F. Ochoa, J.J. Williams and N. Chawla: J. Electron. Mater., 2003, vol. 32, pp. 1414–1420
- [9] Q. Xiao, H.J. Bailey and W.D. Armstrong: J. Electron. Packaging, 2004, vol. 126, pp. 208–212
- [10] Q. Xiao, L. Nguyen and W.D. Armstrong: J. Electron. Mater., 2005, vol. 34, pp. 617–624

Lead Free BGAs Soldered With SnPb Solder

Günter Grossmann¹, Giovanni Nicoletti

¹EMPA, Ueberlandstrasse 129, CH- 8600 Dübendorf

Guenther.grossmann@empa.ch



Soldering in electronics, lead free soldering, solder process, degradation of solder joints

1. Introduction

The semiconductors in integrated electronic components are constantly shrinking in size and increasing their complexity. The latter requires an increasing number of external connections to the printed circuit board (PCB) the components are mounted on. This leads to the situation that the size of the components is increasing to accommodate the increasing number of connections while the working device itself is shrinking. To overcome this dilemma the external connections have been moved from the edge of the components to the bottom and arranged in arrays. The connectors are made of spheres with diameters ranging from 1.25mm to 0.5mm. The spheres themselves are made of tin based alloys that usually correspond to the alloy used in the soldering process of the components to the PCB. With the introduction of the European RoHS legislation from 2003 lead has been banned from electronic solders with some exceptions mainly in the field of aerospace and military applications. Due to obsolescence reasons more and more components are made with lead free solder spheres while in aerospace and military applications tin lead solder with lower liquidus must be used in many applications because the equipment made is qualified with this technology. This rises the question of the compatibility of the components and the process. In this presentation the influence of the process parameters on the structure of the soldered BGAs is presented and the results of comparative thermal cycling tests to evaluate the degradation of the soldered connections are shown.

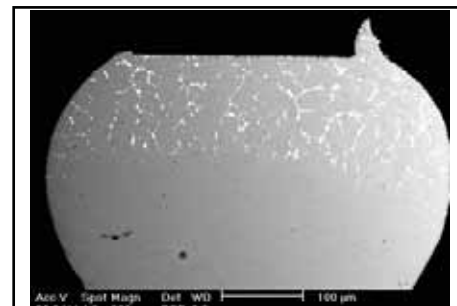
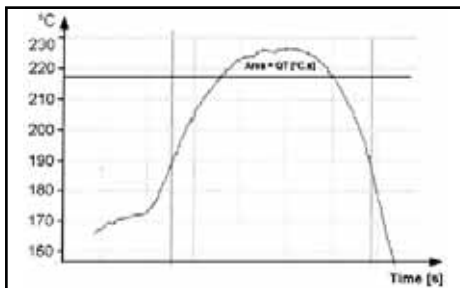


Fig. 1. Definition of QT used to characterise the solder process Fig. 2. Solder ball made of SnAg3.5Cu0.7 soldered with SnPb36Ag2

2. Experiments

The specimens have been prepared with metallographic microsections and examined with an optical microscope as well as with SEM. To investigate the influence of the process parameters PCBs have been produced in an industrial production line with a 9 zone convection furnace. The temperature- time behaviour of the components has been measured with type K thermal elements fixed below dummy components. To evaluate the degradation samples with lead free balls soldered with SnPb and samples with SnPb balls soldered with SnPb have been subject to thermal cycles between -20°C and +120°C with a temperature gradient of 2°C/min and dwell times of 30 min at the temperature extremes. Samples have been drawn after 2000, 3500 and 6000 cycles.

3. Results and Discussion

To evaluate the effect of the process parameters on soldering, the integrated time (t)/temperature (θ) approach (QT) [1] was used where the area under the temperature-time curve above liquidus serves as the process measurement parameter, which corresponds to the thermal energy added during the soldering process (Fig 1). QT can be influenced either by the peak temperature or by the time above liquidus. With low QT the lead free

balls dissolves only partially in the liquid SnPb solder until the resulting alloy reaches the soldering temperature or until the solder process ends. A sharp line separates the dissolved portion of the ball from the one that remains solid (Fig. 2). With increasing QT more volume of the solder ball dissolves in the SnPb solder which leads to smaller lead phases in the resulting alloy [2]. The results rose the question if the boundary between the solder alloy and the alloy of the ball will be the location of cracks growing due to thermomechanical stress in thermal cycles. The investigation showed that the degradation of the solder does not take place at this interphase. The cracks observed grew along the interphase of the lead free ball to the component associated with a severe degradation of the epoxy of the PCB. However, the same has been observed in solder joints made entirely of SnPb solder. There was a tendency that in the lead free solder balls the degradation of the epoxy started at an earlier stage than in the solder joints made of SnPb but the cracks along the interface to the component occurred earlier in the solder joints made of SnPb.

4. Conclusions

The investigation showed that soldering lead free solder balls with SnPb solder is no risk if a $QT > 290^{\circ}\text{C}\cdot\text{s}$ is used. The lead free solder balls dissolve partially in the solder forming a firm metallurgical bond. The dividing plane between the dissolved ball and the lead containing solder is not a weak link. The degradation due to thermal cycling occurs at the interphase of the ball and the solderable surface of the component associated with degradation of the polymer of the PCB. This is true for solder joints made entirely out of SnPb and for solder joints made of lead free solder balls soldered with SnPb solder. Thus no reduction in the lifetime of the solder joints made with lead free balls compared to the established pure SnPb process is expected.

References

- [1] Harrison, M.R. and Vincent, J.H. (1999), "Improved design life and environmentally aware manufacturing of electronics assemblies by lead-free manufacturing", IDEALS Report, Marconi Materials Technology, Caswell, Towcester, UK
- [2] G.Grossmann, J. Tharian, and P. Jud, "Microstructural investigation of lead-free BGAs soldered with tin-lead solder," Soldering&Surface Mount Technology, vol.17, pp. 10- 21 .

Effect of isothermal aging on impact strength of Sn-Ag-Cu solder bumps

J. X. Wang^{1,2}, and H. Nishikawa²

¹ Jiangsu Provincial Key Laboratory of Advanced Welding Technology, Jiangsu University of Science and Technology, Zhenjiang, 212003, China

² Joining and Welding Research Institute, Osaka University, Osaka 567-0047, Japan

Email: jianxin.wang.just@gmail.com



Keywords: Impact test, Joint strength, Fracture morphology, Isothermal aging

1. Introduction

The issue of mechanical reliability becomes increasingly urgent for the miniaturization of the solder joints. The shear failures are very often in the BGA joints, which are caused by thermal mismatch [1]. Traditional ball shear test is a widely used method to assess the bonding quality of solder joints, but it is typically limited to quasi-static conditions, as the shear speed usually ranges from 0.6mm/min (0.01mm/s) to 60mm/min (1mm/s).

The impact reliability of lead-free solder joints has been one of the critical concerns due to the failure of joints in portable electronic products under drop impact loading [2, 3]. Compared with the board level test method, the impact shear test for the single solder bump is more convenient and economical, and is actively pursued by the industries.

In this study, in order to investigate the shear strength and fracture behavior of Sn-3.0Ag-0.5Cu solder bumps under high-speed impact and static shear condition during isothermal aging, the solder bumps after various aging treatments were tested with the speed of 1m/s and 0.02mm/s, respectively. The composition of the fracture surface was identified by means of electron probe microanalyzer (EPMA) so that the visualization in elements distribution of fracture surface was obtained to study the fracture behavior of solder bumps during isothermal aging.

2. Experiments

Sn-3.0Ag-0.5Cu solder balls with the diameter of 0.76mm were soldered on Cu pads in nitrogen atmosphere. After the reflow soldering, solder bumps were aged in an isothermal oil bath at 423K for 168h, 504h, and 1008h, respectively.

The microstructure of solder/ IMC interface during isothermal aging was analyzed, and the shear strength of solder bumps was tested by means of high speed impact test as well as low speed shear test. In the impact test, when the angle (θ) of test hammer (25.44 gram) was $\pi/3$ radian, the test speed was about 1m/s, as illustrated in Figure 1, and the impact behavior was examined by evaluating the maximum load values and energies in the load-displacement curves.

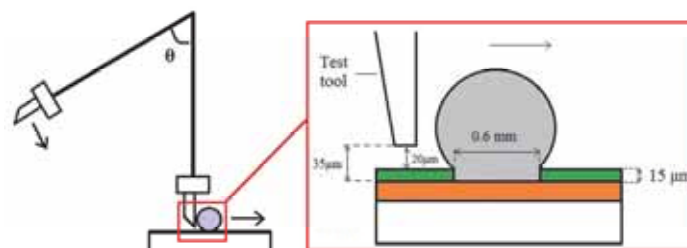


Figure 1 Schematic of high speed impact test.

Besides the impact test, the conventional shear test was also conducted, and the shear speed was 0.02mm/s. The distance from the test tool to the surface of the solder resist on the Cu pads was 20 μ m in both shear and impact tests. Twenty joints were measured under each condition, and the average value was used for evaluation.

3. Results and Discussion

The relationship between the test load and displacement of solder bumps for high speed impact test and static shear test is shown in Figure 2. Furthermore, the maximum load value under the novel high speed impact test is much higher than that under the tradition static shear test owing to the test strain rate, thus the shapes of load-displacement curve under high-speed impact test and static shear test shown in Figure 2a and 2b are quite different.

In Figure 2a, the slope of the ascending part of the impact force profile decreased with increasing aging time, as the hardness of the solder decreased with increasing aging time. The peak of load-displacement curve moved left and below, owing to the interfacial strength decrease with increasing IMC layer thickness in accordance with the increase in the aging time.

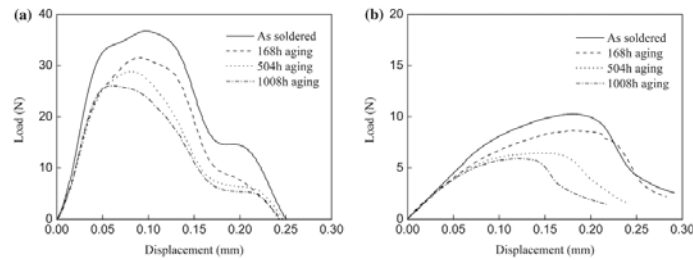


Figure 2 Load-displacement curves of as-soldered and aged joints. (a) in high speed impact test, (b) in static shear test.

Figure 3 shows the maximum load of solder bumps in high speed impact test and in static shear test. With the increase of aging time, the maximum force decreases gradually under both high speed and static test conditions. That is to say, the crack is easy to initiate and propagate after long time isothermal aging.

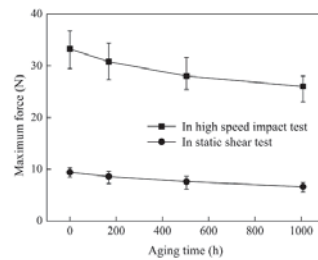


Figure 3 Maximum load of as-soldered and aged joints.

4. Conclusions

- (1) The fracture is found inside the bulk solder in low speed shear test regardless of the aging effect, and the ductile failure mode is identified from the fracture morphologies, thus the static shear test is more a measure of solder strength than the adhesion bonding to pad interface.
- (2) Under 1m/s impact condition, the crack initiation position is changed from solder/ Cu6Sn5 interface to Cu3Sn/ Cu interface after long time isothermal aging. The fracture occurs inside the bulk solder accompanying with IMC in both of the as-soldered and aged solder bumps, and ductile as well as brittle failure modes are identified.
- (3) The thickened multiple IMC layers during isothermal aging account for the degraded impact resistance, and the change of the solder matrix is another factor for reduced impact resistance owing to Sn residue on the fracture surface.

References

- [1] Y.H. Tian, C.J. Hang, C.Q. Wang. Effects of bump size on deformation and fracture behavior of Sn3.0Ag0.5Cu/Cu solder joints during shear testing. *Mater Sci Eng A*, 529 (2011), pp. 468-478.
- [2] Y. S. Lai, J. M. Song, H. C. Chang, Y. T. Chiu. Ball impact responses of Ni- or Ge-doped Sn-Ag-Cu solder joints. *J Electron Mater*, 37 (2) (2008), pp. 201-209.
- [3] T. Daito, H. Nishikawa, T. Takemoto, T. Matsunami. Explanation of impact load curve in ball impact test in relation to thermal aging. *Microelectron Reliab*, 53 (12) (2013), pp. 2005-2011.

Effect of thermal treatment on Cu extrusion of TSV and solder bumping for three-dimensional packaging

S. H. Kee¹, M. H. Roh¹, S. J. Lee¹, J. P. Jung^{1,*} and W. J. Kim¹

^{1,*}Dept. of Materials Sci. and Eng., University of Seoul, Seoul 130-743, Korea

Email: jujung@uos.ac.kr



Keywords: three-dimensional packaging, through silicon via, electroplating, thermal shock test, extrusion

1. Introduction

In recent years, the demand for electronic products with multi functions has greatly increased, creating a need for high density and light weight electronic components. To fulfill these needs, three dimensional (3D) packaging technologies using through silicon via (TSV) has attracted much research and development effort. Through-silicon-via (TSV) is an essential technology that enables vertical stacking of several semiconductor chips for 3-dimensional packaging [1-2]. However, thermo-mechanical reliabilities of TSV such as Cu extrusion, crack or delamination between Cu-plug and Si via wall, and void within Cu –plug become important issues [3-4]. In this study, Cu was filled in TSV by electroplating, and the effect of thermal shock and annealing on Cu extrusion of TSV was investigated.

2. Experiments

A Si wafer of <100> p-type having a thickness of 525 μm and diameter of 4 inch was used as a substrate. Via holes were drilled in the Si wafer by etching with deep reactive ion etching (DRIE) process. SiO_2 of dielectric layer, Ti and Au of adhesion and seed layer, respectively, were deposited in via walls as functional layers. The Si wafer was cut into chips sized of $5 \times 5 \text{mm}^2$ and used as a cathode for Cu electroplating. A Pt plate with size of $10 \times 10 \text{mm}^2$ was selected as an anode. Cu filled TSV sample having a diameter of 30 μm and depth of 70 μm was fabricated by electroplating using minimized additives and the effect of thermal shock on Cu extrusion of TSV were studied. Thermal shock test was conducted from -65°C to 150°C for 250, 500, and 1000 cycles. Annealing was also applied to the Cu-filled TSV at 450°C for 30 min. The experimental results showed that Cu-filled TSV with defect free was obtained by electroplating using periodic pulse-reverse current form (Fig. 1).

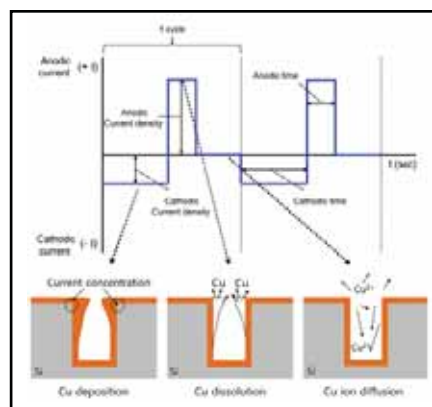


Fig. 1. Schematic and mechanism of periodic pulse reverse.

3. Results and Discussion

Cu filled TSV sample having a diameter of 30 μm and depth of 70 μm was fabricated by electroplating using minimized additive. Thermal shock test was conducted from -65°C to 150°C for 250, 500, and 1000 cycles. Annealing was also applied to the Cu-filled TSV at 450°C for 30 min. Cu extrusion was occurred after thermal shock test, and the average height of extruded Cu increased from -0.3 to $0.78 \mu\text{m}$ with increasing thermal shock

cycles from 0 to 1000. The interfacial crack between Cu and Si was observed after 1000 cycles (Fig. 2). The average grain size of Cu during thermal shock test from 0 to 1000 cycles increased from 0.65 to 0.83 μm . Cu extrusion by annealing became 1.36 μm . The Cu extrusion can be suppressed by deposition of Cu alloy and composite.

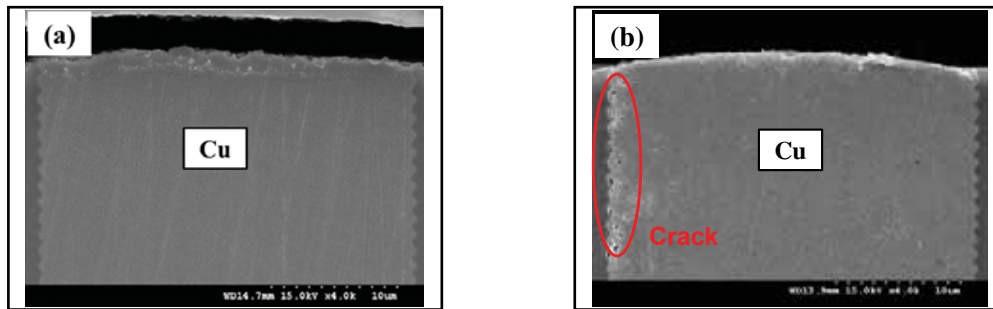


Fig. 2. Cross-section of Cu filled TSV with thermal cycles; (a) after 500 cycles and (b) after 1000 cycles.

4. Conclusions

Cu extrusion was occurred after thermal shock test, and height of pumped Cu increased with increasing cycles. Also, Cu extrusion by annealing became 1.36 μm . Thus, Cu extrusion was occurred not only high temperature process such as BEOL but also reliability test like thermal shock test.

Acknowledgement

This work was supported by Business for Cooperative R&D between Industry, Academy and Research Institute funded Korea Small and Medium business Administration (Grants No. C0213709).

References

- [1] A. S. Budiman, H. A. S. Shin, B. J. Kim, et al., "Measurement of stresses in Cu and Si around through-silicon via by synchrotron X-ray microdiffraction for 3-dimensional integrated circuits," *Microelectron. Reliab.*, Vol. 52, pp. 530-533 (2012).
- [2] X. Liu, Q. Chen, V. Sundaram, R. R. Tummala, and S. K. Sitaraman, "Failure analysis of through-silicon vias in free-standing wafer under thermal-shock test," *Microelectron. Reliab.*, Vol. 53, pp.70-78 (2013).
- [3] T. C. Tsai, W. C. Tsao, W. Lin, C. L. Hsu, C. L. Lin, C. M. Hsu, J. F. Lin, C. C. Huang, and J. Y. Wu, "CMP process development for the via-middle 3D TSV applications at 28 nm technology node" *Microelectron. Eng.*, Vol. 92, pp.29-33 (2012).
- [4] I. E. Wolf, K. Croes, O. V. Pedreira, R. Labie, A. Redolfi, M. V. D. Peer, K. Nanstreels, C. Okoro, B. Vandeveld, E. Beyne, "Cu pumping in TSVs: Effect of pre-CMP thermal budget" *Microelectron. Reliab.*, Vol. 51, pp. 1856-1859 (2011).

Ex- and in-situ X-ray based analytical Studies on Solder Materials for Microsystems Packaging Applications

**A. Neels¹, T. Bandi², R. Kaufmann¹, J. Janczak-Rusch¹, L.P.H. Jeurgens¹,
A. Dommann¹**

¹ Empa, Überlandstrasse 129, CH-8600 Dübendorf, Switzerland

² SSC, Ecole Polytechnique Fédérale de Lausanne (EPFL), CH-1015 Lausanne, Switzerland

E-Mail: antonia.neels@empa.ch



Keywords: microsystems, packaging, HRXRD, in-situ analysis

1. Introduction

The development of joining technologies for integration and packaging are of importance for the assembling of materials and components at ever-lower temperatures. There is an urgent need for key technologies in the fields of e.g. micro-electronics, medical implants or sensing devices. For microsystems, hermetic sealing is an important issue which is still an intensive research topic. This becomes crucial when regarding applications with high reliability requirements such as medicine or the space industry.

Advanced materials and related technologies require at the same time research and development of adequate analytical tools. Empa's Center for X-ray Analytics actively develops and supplies tools in materials research and materials processing by analyzing structures of raw materials such as metals, composites, ceramics and polymers and also more complex systems for various applications such as automotive, space, and watch industry. X-ray based methods such as X-ray diffraction (XRD, HRXRD), Small Angle Scattering (SAXS), Phase Contrast and dark field Imaging (XPCI) and Micro- and Macro-CT (μ CT, XCT) are applied (Fig. 1). New processes can be accompanied and qualified through a non-destructive analytical approach.

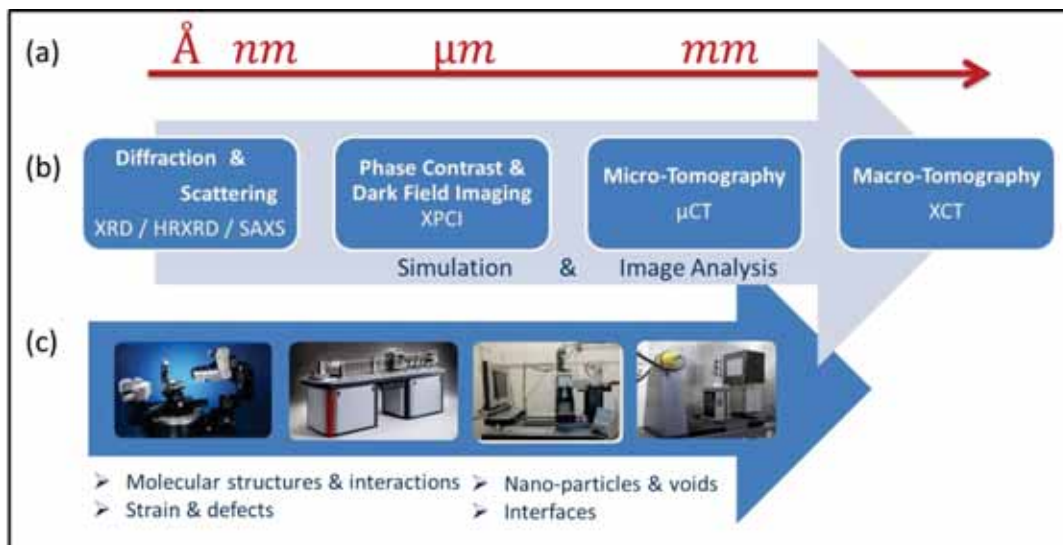


Fig. 1 Novel platform for multi-scale X-ray analytics in material science showing (a) the resolution for the analysis of structures, (b) the applied X-ray method and (c) a choice of available instruments at EMPA for the analysis of nano, micro-materials and systems.

2. Experiments, Results and Discussions

Examples of applications of advanced analytical X-ray based analytics will be demonstrated for different solder materials / systems in various applications. In addition, in-situ studies on solder materials will be shown. The synergies between different X-ray tools and other complementary methods such as microscopy help to understand mechanisms in the solder materials under investigation and as a result the joining technology.

In the fabrication of Micro Electro Mechanical Systems (MEMS), the application of advanced packaging methods involves the development of new solder materials with improved properties [1]. The joining of advanced metallic alloys is limited by high brazing or soldering temperatures. The nanoscale effect of melting

point depression offers a possibility of lowering the filler metal melting temperature without the compromises resulting from alloying [2].

In-situ high temperature XRD studies have been conducted in order to follow the melting behavior of mixed metal nano-layer systems (Fig. 2) and to enable a direct observation not only on the materials melting points but also on the formation of intermetallic phases. The influence of internal and external interfaces in the material is crucial and has also been studied.

The melting point depression effect has been studied for nanolayer brazing fillers in a multilayer system in which the layers of the brazing filler were separated by diffusion barrier layers. The example of the Ag-Cu/AlN nano-layer system is shown in Figure 2. For the 7.7 nm thick Ag-Cu brazing filler layers, a heterogeneous melting process starting at around 520°C was observed. In this case, the eutectic Ag-Cu brazing filler separated in two single phases and the local material interfaces Ag/AlN, Cu/AlN were formed [3].

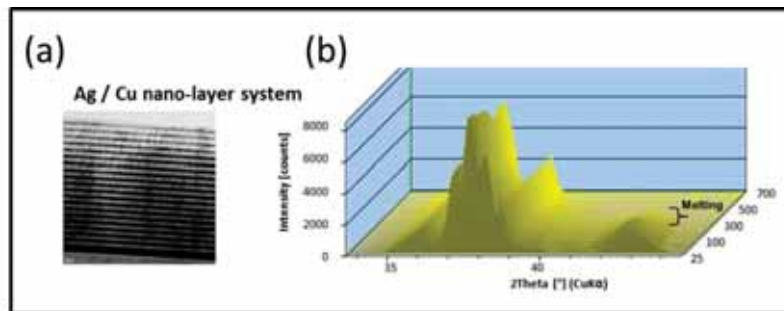


Fig. 2. (a) SEM picture of the nano-layer system Ag-Cu and (b) XRD in-situ high-temperature study.

In microsystems packaging and assembly, the processes introduce and modify stresses and defects. The reliability assessment for MEMS foreseen to operate in space environment is especially demanding but crucial for their applications. The application of HRXRD methods allows, in addition to the study of structures and structural changes in the solder material, also the detailed evaluation of packaging strains. Strain will impact on device functioning and its aging behaviour and therefore its long-term stability. The AuSn eutectic bonding is used in many applications [4] and especially for hermetic resonator MEMS with the aim of accurate pressure / leak rate sensing [5]. Information concerning the solder material during fabrication and after packaging has been obtained and strain gradients close to the interface have been determined using HRXRD (Fig.3).

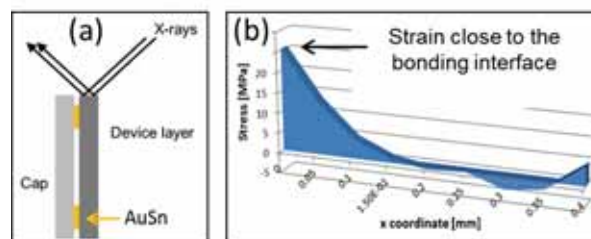


Fig. 3. (a) Schematic cross-sectional view of a MEMS package with a solder and (b) HRXRD result showing the strain gradient introduced by the soldering process in the Si close to the bonding interface.

[1] “Reliable hermetic MEMS chip-scale packaging” G. Spinola Durante, R. Jose Jamesa, C. Bossharda, C. Muller, J. Baborowski, A. Pezous, F. Cardot, M.-A. Dubois, A. Neels, A. Dommann, EMPC2011, Brighton, UK, 2011.

[2] V.Bissig, J.Janczak, "Nanoscale effect-based melting point reduction for brazing filler metals", Empa Activities, p.8, 2009/10.

[3] O. Sereida, A. Neels, A. Dommann, V. Bissig, M. Parlinska-Wojtan, J. Janczak-Rusch, “High Temperature XRD Studies on Nano-multilayer Systems as a Support for Packaging Technologies”, CSEM Scientific and Technical Report, p. 22, 2011.

[4] T. A. Tollefsen, A. Larsson, M. M. Visser Taklo, A. Neels, X. Maeder, K. Høydalsvik, D. W. Breiby, K. Aasmundtveit, “Au-Sn SLID Bonding: A Reliable HT Interconnect and Die Attach Technology”, Metallurgical and Materials Transactions B, p.406-413, 2013.

[5] T. Bandi “Reliability Aspects of Micromechanical Systems for Space Applications – Mechanical Properties of Structural Materials and Analysis of Packaging Strains, PhD Thesis, EPFL 2014.

Solid-Liquid Diffusion Bonding of Copper using Sn/Ag Multilayered Films

**Shinji FUKUMOTO¹, Kanta MIYAKE², Michiya MATSUSHIMA¹
and Kozo FUJIMOTO¹**

¹ Graduate School of Engineering, Osaka University, 2-1 Yamadaoka, Suita, 565-0871, JAPAN

² Graduate Student of Osaka University, 2-1 Yamadaoka, Suita, 565-0871, JAPAN

Email: fukumoto@mapse.eng.osaka-u.ac.jp



Keywords: Copper, Silver, Tin, Bonding, Intermetallic compounds, Isothermal solidification

1. Introduction

Power modules could be one of key devices that control relatively high electrical power in an efficient way for energy saving. As SiC and GaN semiconductors are expected instead of Si, new assembly and interconnect beyond standard Sn based solder come into request. There are several interconnections in power modules such as chip-to-wire connection, chip-to-substrate joint and substrate-to-baseplate joint. [1] In the case of chip-to-wire connection, when aluminum wire is bonded onto a Si chip, a crack is propagating through the bond wire. However, when copper wire is used instead of aluminum wire to flow higher current, the interconnection would be limited by the bond interface and/or bond layer. Fujimoto *et al.* reported that solid-liquid diffusion bonding was applied to Si chip-to-copper wire interface to produce Cu₃Sn intermetallic compound (IMC) bond layer that exhibited better reliability than Sn-5Sb solder joint. [2] The solid-liquid diffusion bonding is composed of several stages as shown in Fig. 1. The process is carried out above the melting temperature of insert metal, and the IMCs bond layer is formed at the bonding temperature due to solid-liquid interdiffusion. The advantage of the process is to form a bond layer with higher melting point than the insert metal. However, most IMCs are brittle and exhibit high Young's modulus, resulting in large stress concentration on the Si chip at the edge of bond. In the present study, copper was bonded to copper by using silver-tin multilayered films to simulate the interconnection of copper wire to Si chip with Cu metallization layer.

2. Experiments

The materials used were oxygen-free Cu rods whose faying surfaces were polished with emery paper of #4000. They were then pickled in a 5% HCl solution, and rinsed in ethanol. Tin/silver multilayer thin films with various designs as shown in Fig. 2 and Table 1 were produced on the copper faying surface by vapor deposition coating. The bonding was carried out at 573 K for bond times from 0 to 3.6 ks. The microstructures of bond layers were observed by scanning electron microscopy (SEM) and transmission electron microscopy (TEM) with energy dispersive X-ray spectroscopy (EDX). The dynamic hardness (DH) and Young's modulus of the IMC bond layers were evaluated by the dynamic micro-hardness tester (Shimadzu Co. Ltd., DUH-211) under the load of 10 g with a trigonal pyramid indenter. Finite element analysis was carried out to estimate thermal stress distribution around the bond layer between Cu wire and Si chip with Cu metallization layer.

3. Results and Discussion

Cross sections of bond layers using the Design-1 faying surface that is the 2Sn/1Ag/2Sn multilayered film, are shown in Fig. 3. The bond layer was composed of three IMC layers. TEM observations revealed that Ag₄Sn was formed at the center and Cu₃Sn was formed between Ag₄Sn and Cu base metals. Ag₃Sn as a minor phase was also observed in Ag₄Sn layer. Ag₄Sn intermetallic compound has wide range of composition in Ag-Sn binary phase diagram. In the present study, the composition of Ag₄Sn layer showed non-stoichiometry as well as stoichiometry depending on the measurement points and bond time. The Cu₃Sn layer grew up and the Ag₄Sn layer decreased with increasing bond time. Many voids were formed at the interface of Cu₃Sn/Ag₄Sn and Cu₃Sn/Cu, that might be caused by Kirkendall effect. The dynamic hardness and Young's modulus of Cu₃Sn layer were DH500 and 129 GPa, respectively. Ag₄Sn layer showed hardness of DH175 and Young's modulus of 76 GPa, respectively. Then the bonding was carried out using the other faying surface designs including less Sn than Design-1 to decrease the thickness of bond layer and to suppress the growth of brittle Cu₃Sn layer. Fig. 4 shows the cross sections of bond layers using Design-2, -3 and -5 faying interfaces. The thickness of bond layer was decreased as the thickness of Ag layer decreased. Only the limited Cu₃Sn layer was formed at the interface between Ag₄Sn and Cu when the amount of Sn in multilayered film decreased. As a result, the bond layer was mostly occupied by Ag₄Sn phase. When the Young's modulus of bond layer decreases from 129 GPa to 76 GPa, that means Cu₃Sn is replaced by Ag₄Sn as a bond layer, approximately 20% decrease in the thermal stress on Si chip was estimated by finite element analysis.

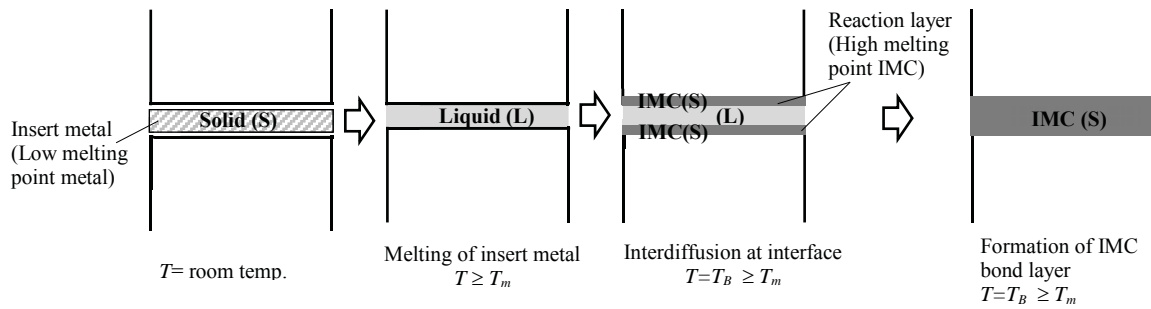


Fig.1 Schematic showing the flow of the solid-liquid diffusion bonding process. (T_m : melting point of insert metal, T_B : bonding temperature)

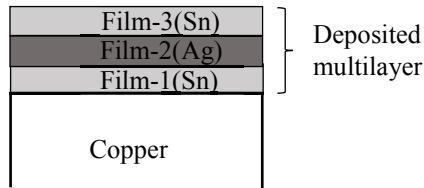


Fig.2 Schematic illustration of faying surfaces with multilayered thin films. The Ag/Sn multilayered films were formed by vapor deposition coating. Thickness of each film is shown in Table 1.

Table 1 Design of faying surfaces with multilayered film.

No.	Design	Thick of each film (μm)		
		Film-1	Film-2	Film-3
		Sn	Ag	Sn
1	2Sn/1Ag/2Sn	2	1	2
2	1Sn/0.5Ag/0.5Sn	1	0.5	0.5
3	1Sn/1Ag/0.5Sn	1	1	0.5
4	2Sn/1Ag/0.5Sn	2	1	0.5
5	1Sn/2Ag/0.5Sn	1	2	0.5
6	2Sn/2Ag/0.5Sn	2	2	0.5
7	3Sn/2Ag/0.5Sn	3	2	0.5

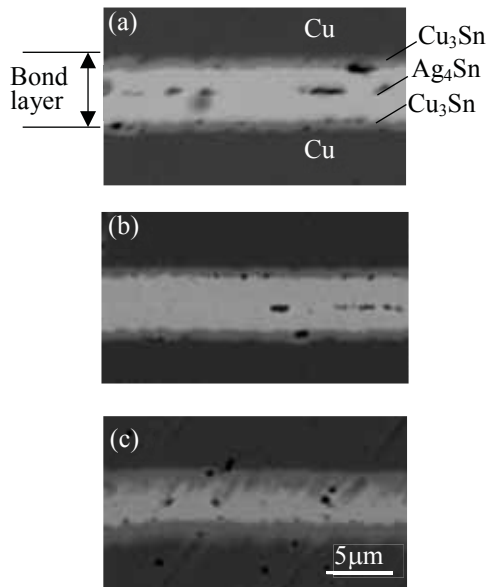


Fig.3 Cross sections of bond layer using Design-1 faying surface with various bond time of (a) 0s, (b) 300s, and (c) 600s at 573 K.

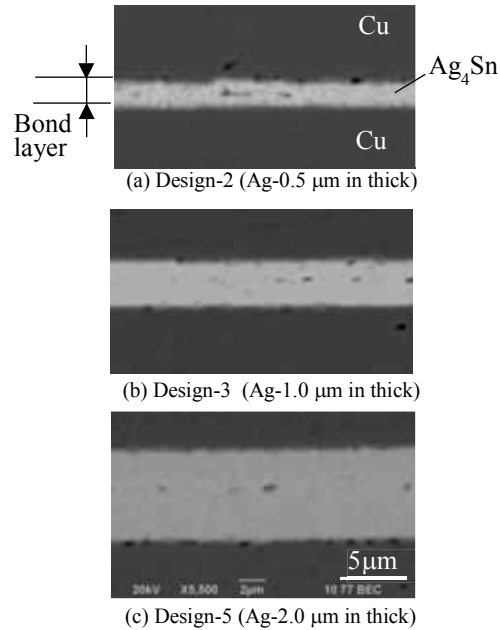


Fig.4 Effect of thickness of Ag film on IMC layers. Cross sections of bond layer using Design-2, (a), Design-3, (b) and Design-5, (c), faying surfaces for 600 s of bond

Conclusions

Copper was diffusion bonded by using Ag/Sn multilayered insert films. Ag_4Sn intermetallic compound was major phase in the bond layer, which showed lower hardness and Young's modulus than those of Cu_3Sn . The thermal stress on the Si chip at the edge of bond could be reduced by replacing Cu_3Sn by Ag_4Sn in bond layer.

Acknowledgements

This work was partially supported by the Ministry of Education, Science, Sports and Culture, Grant-in-Aid for Scientific Research (C), 24560883.

References

- [1] K. Guth, D. Siepe, J. Gorlich, H. Torwesten, R. Roth, F. Hille and F. Umbach, "New assembly and interconnects beyond sintering methods", Proc. PCIM 2010, 4-6 May, 2010, Nuremberg, Germany, 232-237 (2010).
- [2] T. Fujimoto, S. Fukumoto, T. Miyazaki, Y. Kashiba, K. Shiotani and K. Fujimoto, "Bonding of copper to silicon chips using vapor-deposited tin film", Journal of Physics: Conference Series 379, 012026 (2912).

Improvement of impact reliability of solder bumps using laser process

H. Nishikawa¹ and N. Iwata²

¹Joining and Welding Research Institute, Osaka University, 11-1 Mihogaoka, Ibaraki, Osaka, Japan

²Graduate School of Engineering, Osaka University, 2-1 Yamadaoka, Suita, Osaka, Japan

Email: nisikawa@jwri.osaka-u.ac.jp



Keywords: Keyword1, Lead-free solder, laser process, impact reliability, intermetallic compound

1. Introduction

Currently Sn-Ag and Sn-Ag-Cu solders are considered the most promising for both conventional wave and reflow soldering processes. One of distinguishing characteristics of Sn-Ag and Sn-Ag-Cu solders is the high reaction rate of metals with these solders in molten form, i.e., the high dissolution rate of metals in these solders in molten form, as compared to the reaction rate of metals with the Sn-Pb eutectic solder. Thus, during heating, a thick layer of an intermetallic compound (IMC) is readily formed at the interface between such lead-free solders and the Cu substrate. The thickness of the IMC layer at the interface in the case of Sn-Ag-Cu solders is drastically higher than that for the Sn-Pb eutectic solder. In particular, the thickness of the IMC layer affects the drop reliability and long-term reliability of the soldered joints.

Reflow soldering has been widely used in electronic packaging and assembly process. With the miniaturization of electronic devices and the use of heat-sensitive electronic components, the use of the conventional reflow soldering process often gives rise to difficulties. Recently, a laser soldering process has been introduced in industry because of its unique properties such as localized and noncontact heating, rapid rise and fall in temperature, and ease of automation compared to the reflow soldering process. In addition, the laser process allows for the mounting of individual components and customized printed circuit board (PCB) assemblies. Then, the laser process with a contactless temperature measurement is becoming more and more significant to minimize thermal damage for heat-sensitive components. So there has been some practical research and discussion of the laser soldering process for the industrial application[1-4]. There has been limited discussion for the basic phenomena and performance of the joints soldered by this process.

In this study, the impact strengths of solder bumps using the laser process after soldering and after aging were investigated to clarify the impact reliability of the solder bumps..

2. Experiments

Sn-3.0 mass%Ag-0.5 mass% Cu solder balls with a diameter of 1.0 mm were used in this study. Cu pads that had thickness of 35 μm and a diameter of 0.8 mm and were fabricated on an FR-4 printed wiring board were used as the substrate. A commercially available rosin mildly activated (RMA) flux was used. In this study, the solder balls were heated in the atmosphere with a power of 40 W for 1 s or a power of 10 W for 5 s plus 40 W for 1 s. As a reference, a soldered joint was also formed using reflow soldering at 523K for 60 s in a nitrogen atmosphere. After the soldering, some of the soldered joints were then subjected to isothermal aging at 423 K for either 168 h or 504 h. Then, to evaluate the soldered joints, impact tests were performed using a microimpact tester (MI-S, YONEKURA Mfg. Co., Ltd.) with the impact height being 100 μm and the impact speed being 1 m/s. Figure 1 shows a schematic illustration of the procedure for the impact tests and a typical force-displacement curve resulting from such a test. The maximum loads that the soldered joints could be subjected to were obtained from the load-displacement curves resulting from the impact tests. To obtain average values, impact tests were performed on 10 solder balls for each soldering condition.

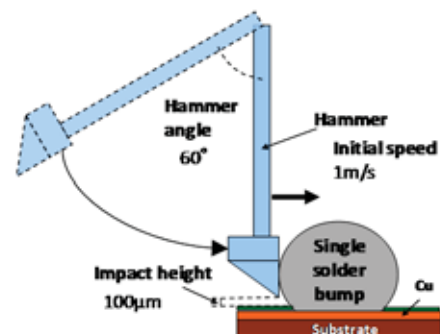


Fig. 1 Schematic illustration of miniature impact test.

3. Results and Discussion

Figure 2 shows SEM micrographs of the interfaces between the Sn-Ag-Cu solder and Cu pads after soldering and after aging using both the laser soldering and the reflow soldering processes. The morphology of the IMC

layer at the interface in the case of laser soldering is quite different from that in the case of reflow soldering. In the case of the reflow soldering, the IMC layer at the interface has a typical scallop-like morphology. In contrast, a relatively thin IMC layer is formed at the interface in the case of the laser soldering and the thickness of this IMC layer was less 1 μ m. After isothermal aging for 168 h, a distinct second layer was noticed at the interface between the Cu pad and the first layer, and the total thickness of the IMC layer increased regardless of the soldering method. In particular, the growth of the IMC layer was faster in the case of laser soldering than in the case of reflow soldering. As the aging time was increased to 504 h, the thickness of the first and second layers increased.

Figure 3 shows the effect of aging time on the maximum load of the load-displacement curve obtained from the microimpact tester. The solder balls were heated in the atmosphere with a power of 40 W for 1 s. In the as-soldered condition, the maximum load of solder bumps using the laser process was superior to that of solder bumps using the reflow process because of the extremely thin IMC layer at the interface. After aging for 168 h, the maximum load of solder bumps using the laser process gradually decreased. After aging for 504 h, the maximum load of the solder bumps using the laser process at 40 W for 1 s degraded and was clearly lower than that of the joints soldered by the reflow process.

On the other hand, Figure 4 shows the effect of aging time on the maximum load of the load-displacement curve for the solder bumps heated with a power of 10 W for 5 s plus 40 W for 1 s. Although the maximum load degraded gradually, the maximum load of the solder bumps was superior to that soldered by the reflow process after aging for 504 h.

4. Conclusions

In this study, the impact reliability of the solder joint using laser soldering was examined. As a result, it has been made clear that the laser soldering under certain conditions is certainly effective for reducing the formation of IMC at the interface and ensuring the impact reliability of the joint.

References

- [1] H. Banse, E. Beckert, R. Eberhardt, W. Stockl, J. Vogel, "Laser beam soldering – a new assembly technology for microoptical systems," *Microsystem Technologies*, 11, 186-193 (2005).
- [2] S. Britten, A. Olowinsky, A. Gillner, "Stress-minimized laser soldering of h-pattern multicrystalline silicon solar cells," *Physics Procedia*, 41, 153-163 (2013).
- [3] J.H. Lee, Y.H. Lee, Y.S. Kim, "Fluxless laser reflow bumping of Sn-Pb eutectic solder," *Scripta Mater.* 42, 789-793 (2000).

Acknowledgments

This work is supported by a grant –in-aid for scientific Research (C) from Japan Society for the Promotion of Science (JSPS).

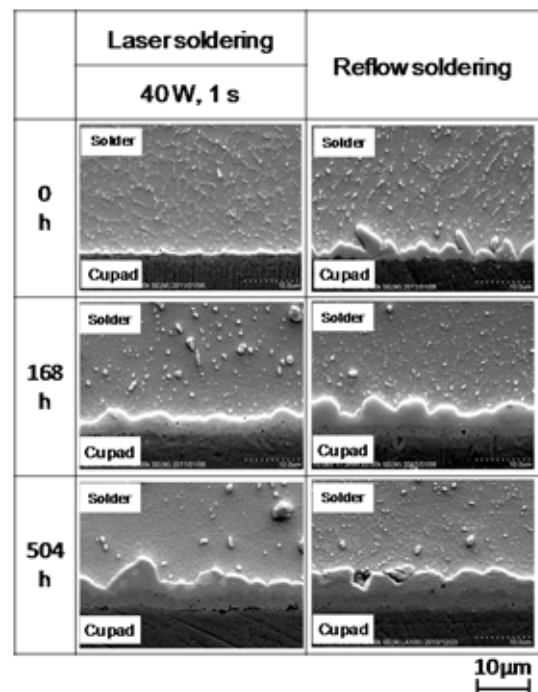


Fig. 2 SEM images of the interface between the solder and Cu pad after soldering and after aging.

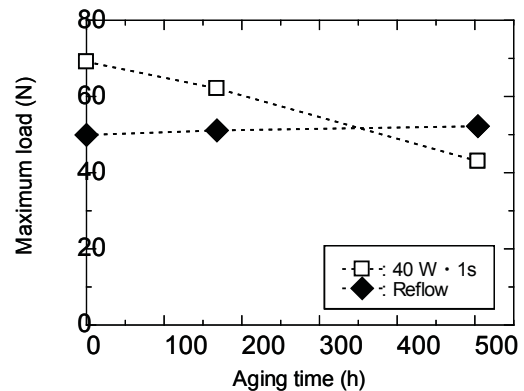


Fig. 3 Effect of aging time on maximum load obtained from microimpact test for the solder bumps heated at 40 W for 1 s.

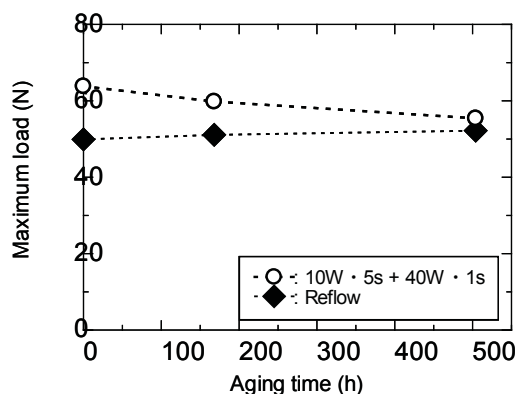


Fig. 4 Effect of aging time on maximum load obtained from microimpact test for the solder bumps heated at 10 W for 5 s + 40 W for 1 s.

Nano-size Ag/AlN multilayers for low temperature joining applications

M. Chiodi, F. Moszner, C. Cancellieri, G. Pigozzi, J. Janczak-Rusch, L.P.H. Jeurgens

Empa Swiss Federal Laboratories for Materials Science and Technology, Überlandstrasse 129, CH-8600 Dübendorf, Switzerland

Email: mirco.chiodi@empa.ch



Keywords: brazing, joining, nano-multilayers

1. Introduction

In the last decade, the industrial need for complex, multi-component material assemblies and devices has grown exponentially. Such assemblies comprise heterogeneous materials, which are very susceptible to reactions and microstructural transitions during processing. Thus, novel approaches towards joining of dissimilar materials at ever reduced temperatures are emerging. Among the others, a promising new route towards low-temperature joining involves the use of nanostructured films consisting of alternating layers of metallic brazing fillers and chemically inert barriers [1]. The delicate interplay between the spatial confinement, internal stress gradients, the film's microstructure and the interface structures can lead to a strong Melting Point Depression (MPD) of the metallic brazing filler [2]. A fine control over the system's properties can enable the possibility to join efficiently at temperatures far below the melting point of the corresponding bulk metal filler.

This work presents a comprehensive investigation of the microstructural evolutions in Ag/AlN multilayers as a function of temperature and deposition parameters. Morphology and crystalline structure of the constituents were studied using Synchrotron Transmission-X-Ray Diffraction (XRD) and Scanning Electron Microscopy (SEM). The system shows extremely interesting properties, with Ag exhibiting a strong melting point depression of around 500°C. This results in the outflow of the metallic filler up to the surface, where it can be exploited for joining.

2. Experiments

Ag/AlN Nano-Multilayers (NMLs) were deposited on Al₂O₃(1-102) substrates using reactive DC magnetron sputtering in high vacuum conditions ($P < 10^{-7}$ mbar). The individual layer thicknesses were varied between 5 and 10 nm. The as-deposited samples were then cut and analyzed ex-situ using XRD and SEM/EDX. Fast-response XRD measurements were carried out at MS-Powder Diffraction beamline at PSI Synchrotron facility (Villingen, CH). Diffraction profiles were acquired during fast heating (variable rate up to 50°C/min) up to 420°C and subsequent isothermal phase (30 minutes). After synchrotron XRD measurements, the same samples were further characterized using SEM.

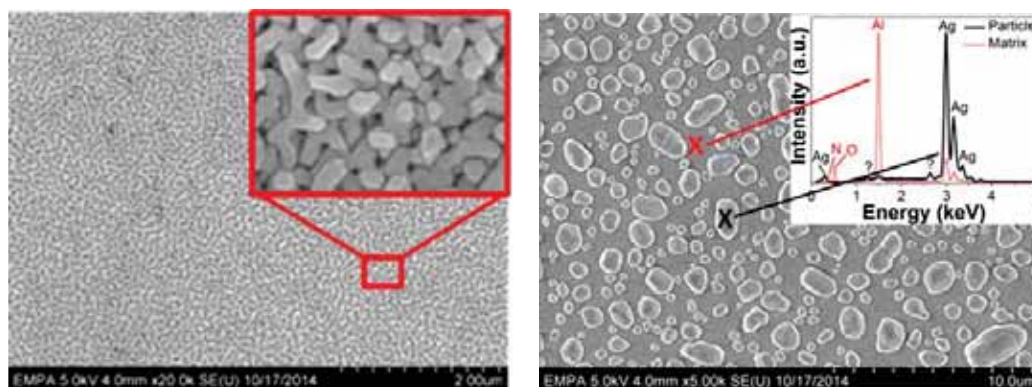


Fig. 1. (a) As-deposited Ag/AlN NML surface. The inset shows in more details the porous structure of the terminating AlN layer. (b) Same sample after fast heating up to 420°C: large Ag droplets appear on the surface (as confirmed by EDX; see inset).

3. Results and Discussion

The as deposited Ag/AlN NMLs possess a porous surface, as evident from SEM analysis (Fig.1a), which originates from the island-like (i.e. Stranski–Krastanov) growth mode of Ag on AlN, as confirmed by cross-sectional analysis of the as-deposited film. The XRD measurements (carried out at RT) indicate that the Ag and AlN layers have preferential orientations of the Ag(111) and AlN(001) planes parallel to the sample surface, respectively. These pronounced Ag(111) and AlN(0001) textures were also confirmed by pole figures measurements. Upon heating, the system shows a structural evolution, which is thermally activated at around 275°C, as indicated by Transmission XRD data (Fig. 2). Between 275°C and 340°C all the typical reflections associated with polycrystalline Ag become evident. This result is compatible with an outflow and subsequent recrystallization of the Ag filler on the outer sample surface.

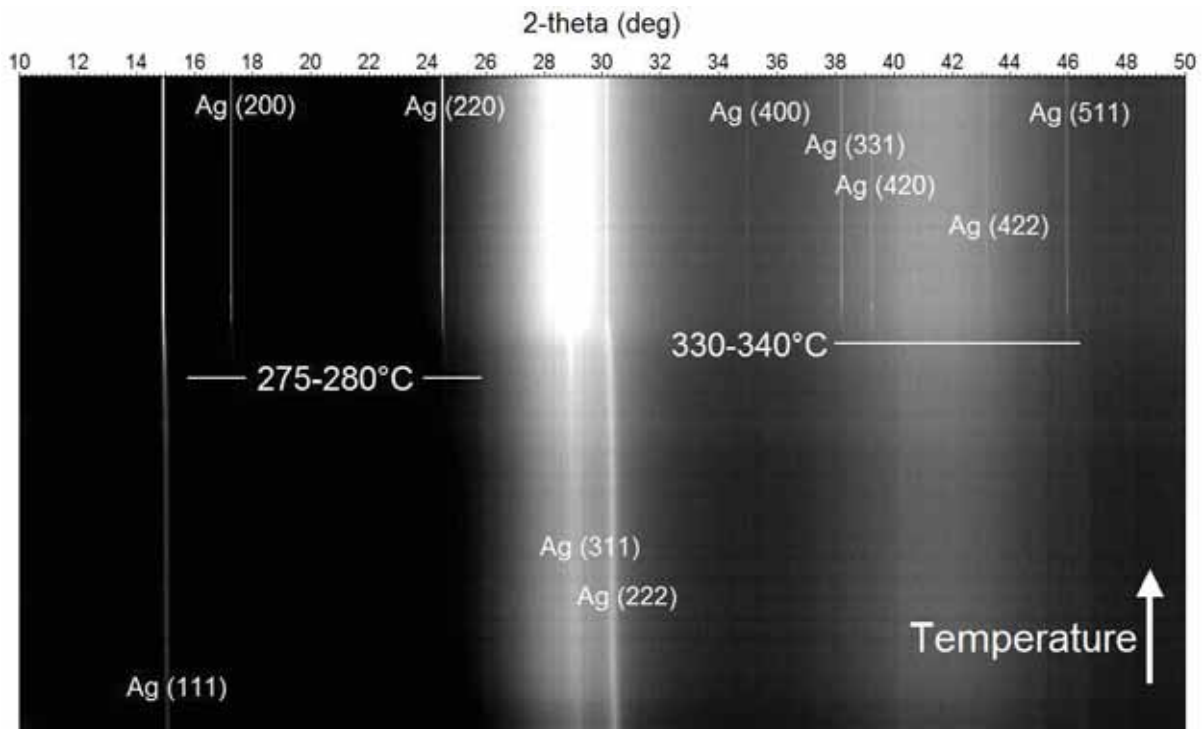


Fig 2. 2D plot of XRD spectra taken in transmission mode as a function of temperature on a Ag/AlN sample. After 275°C a clear structural evolution is observed with the appearance of several new reflections.

After the synchrotron analysis, the surface was investigated by SEM/EDX. The morphology is remarkably different as compared to the as-deposited sample. A high density of Ag droplets with diameters in the range of 250 nm to several microns appear on the sample surface, compatible with liquid outflow of molten Ag through the porous AlN structure (instead of stress-driven solid state diffusion of Ag).

4. Conclusions

Ag/AlN NMLs were deposited and characterized before and after fast annealing treatment up to 420°C. The analysis of the samples after heating is compatible with a MPD (of more than 500°C) of Ag. Molten Ag appears and remains on the surface of the film upon cooling. The NML approach is a promising route towards low temperature processing – high operating temperature joining.

References

- [1] G. Pigozzi et al., *Phase constitution and interface structure of nano-sized Ag-Cu/AlN multilayers: Experiment and ab initio modeling*, Applied Physics Letters 101 (2012) 181602.
- [2] J. Janczak-Rusch, G. Kaptay, L.P.H. Jeurgens, *Interfacial design for joining technologies – An historical perspective*, JMEP 23 (2014) 1608–1613.

Displacement Analysis of Bonding Wires Under DC Current

T. Dagdelen¹, M. Khater², S. Park², R. Saritas¹, E. Abdel-Rahman², and M. Yavuz¹

¹Mechanical and Mechatronics Engineering Department, University of Waterloo, Waterloo, ON, Canada

²Department of System Design Engineering, University of Waterloo, Waterloo, ON, Canada

tdagdele@uwaterloo.ca



Keywords: Wire Bond, Reliability, Laser Vibrometer

1. Introduction

In power modules, such as IGBTs (Integrated Gate Bipolar Transistors), wire bonding is the main interconnection technique. These wires change in diameter between 100-500 μ m and carry high current during service life. While Aluminum (Al) is the dominant wire material, Copper (Cu) and Aluminum Coated Copper (CuCorAl) wires are introduced to industries in last few years. One of the main failure mechanisms in Al wires is fatigue problem [1-3]. The wire makes repetitive motion under high current, and it leads wire to crack from heel part. Since the wires experience considerable displacements in vertical axis rather than other axes [4], we use laser vibrometer to obtain vertical displacements for different wire geometries and materials under constant currents to address reliability issues.

2. Experiments

We performe Polytec MSV-400 laser Doppler vibrometer on the wire to obtain Y-axis displacement(Figure 1-a). Different geometries of Al, and CuCorAl wires are used with 300 μ m in diameter while there is only one Cu material for certain dimension. The PSV-400 Vibrometer is a measurement tool for non-contact measurement-structural vibration analysis and, it can determine the operational deflection shape. As shown in Figure 1-b, the wires are placed under vibrometer and laser beam focuses on the top of the wires. While power supply sends constant currents ranging from 1A to 10A, vibrometer reads displacements.

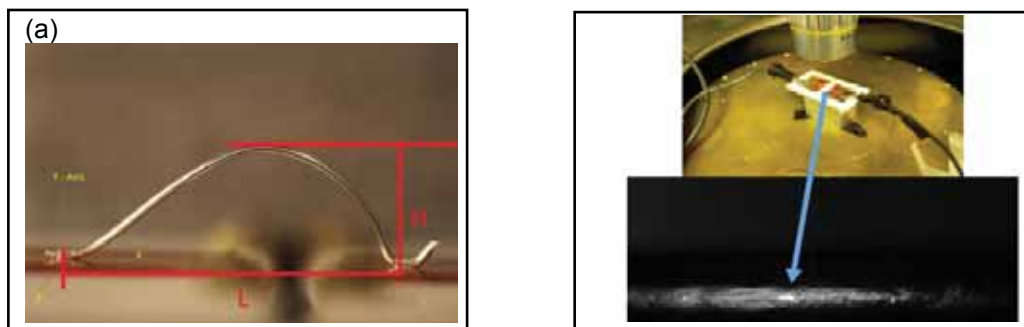


Fig. 1. (a) Wire Geometry, H: Height, L: Length. (b) Experimental Setup.

3. Results and Discussion

As shown Figure 2 and 3, this experimental setup reveals different wires vertical displacements under constant currents.

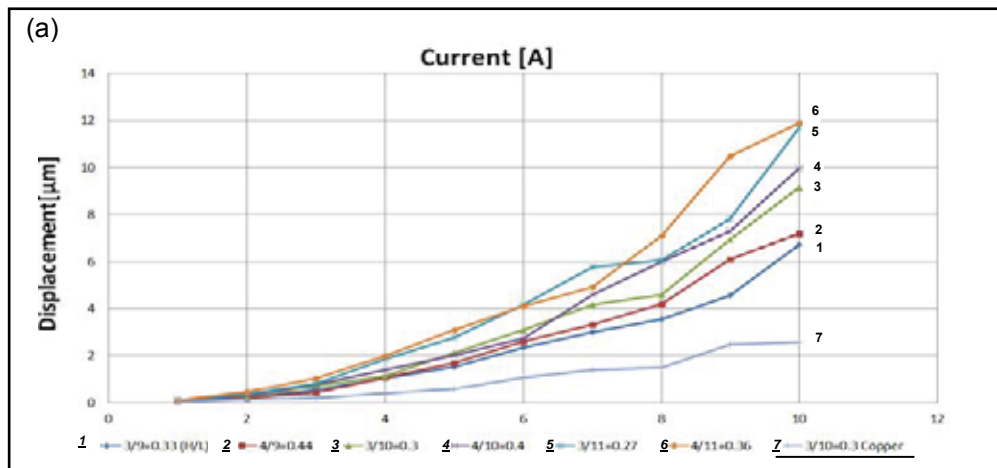


Fig. 2. Al and Cu Wire Displacement.

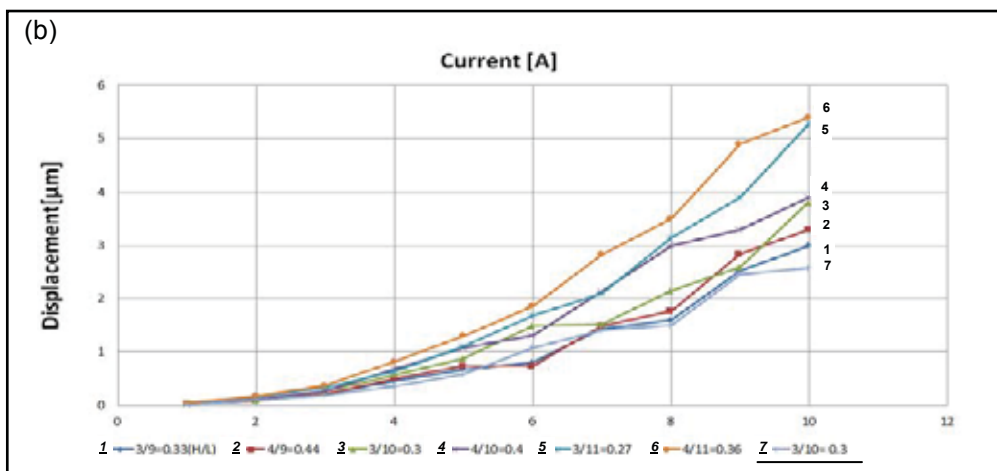


Fig. 3. CuCorAl Wire Displacement.

There are several conclusion can be made based on the results shown in Figure 2 and 3,

- Displacement increases as current increases: Joule heating is quadratically proportional to current
- Longer and higher wire loops undergo larger displacement
- As aspect ratio increases for the same loop length or height wire displacement increases.
- Al wires displace more than CuCorAl: Al thermal expansion coefficient is more than Cu.
- Comparing Al, CuCorAl is more reliable: experiences less deformation due to high current.

4. Conclusions

In this study, we use laser vibrometer to measure wire vertical displacement and address this to wire geometry and material effect on displacement. For same geometries, Cu shows excellent stability in all materials. Comparing Al, CuCorAl is more deformation resistant to currents.

References

- [1] Harman G., Wire Bonding in Microelectronics: Materials, Processes, Reliability, and Yield, 2nd ed., McGrawHill, New York, 1997.
- [2] A. Meyyappan, K. N., "Failure Prediction of Wire Bonds Due to the Flexure" - Maryland, 2004.
- [3] Merkle, L., Kaden, T., Sonner, M., Gademann, A., Turki, J., Dresbach, C., Petzold, M. "Mechanical fatigue properties of heavy aluminium wire bonds for power applications" Proceedings - 2008 2nd Electronics System Integration Technology Conference.
- [4] Medjahed, H., Vidal, P., Noarede, B "Comparison between electromagnetic and thermal stress induced by Direct Current flow in IGBT bond wires", CIPS 2012, March, 6-8, 2012, Germany

Aqueous Cu Nanoparticle Ink stabilized by PVP-SDS

A. Yujie Li^{1,2}, B. Hongliang Wang², and C. Yao Huo²

¹State Key Laboratory of Advanced Welding & Joining, School of Materials Science and Engineering, Harbin Institute of Technology, Harbin 150001, P. R. China

²School of Materials Science and Engineering, Harbin Institute of Technology at Weihai, Wenhua West Road 2, Weihai, Shandong, 264209, P. R. China

Email: liyujie@hit.edu.cn



Keywords: Cu nanoparticle ink, aqueous dispersion, PVP-SDS, stability

1. Introduction

Inkjet printing of highly conductive patterns demands for stable conductive ink usually composed of metal nanoparticles uniformly dispersed in organic or aqueous solutions. Cu nanoparticle ink has attracted increasing interest due to the low resistivity and cost of copper [1-3]. An important issue for its utilization is oxidation. Either organic or inorganic protection layers were used to prevent Cu nanoparticles from being oxidized. Cu nanoparticles coated with PVP (poly (vinylpyrrolidone)) were found to be stable even after being annealed at 100 °C for 30 min in air. This ensured the robust and low-resistivity bonding of Cu wires to Cu pads through sintering of the Cu nanoparticles [1]. Another critical issue for Cu nanoparticle ink is the stability of the colloidal solution over long storage time. The large density of Cu and the high surface energy of nanoparticles always lead to fast particulation and precipitation of the dispersion.

In the present work, chemical reductions taking place in the presence of templates formed by PVP-SDS (sodiumdodecylsulphate) complexes and in the absence of inert gas were used to produce copper nanoparticles of uniform size and high crystallinity. The obtained particles were found to be capped by polymer-surfactant complexes. They oxidized much more slowly than their non-capped counterpart. The particle size could be controlled by the template host. Nanoparticles capped with PVP-SDS could be easily dispersed in isopropanol. To disperse the particles in water, PVP concentration used and the pH value of the solution were found to be crucial for the stability of the aqueous solution.

2. Experiments

SDS was dissolved in water and stirred. 2 minutes later, PVP was added. After another 5 minutes, CuSO₄•5H₂O (10 mM) was mixed in. Further stirring was continued for 8 minutes. The NaOH aqueous solution was added dropwise to adjust the pH value of the solution in the range of 8-10. The mixture was then heated to reach a temperature of 50 °C. Hereafter, Hydrazine hydrate, whose concentration had been diluted to 50%, was added until a ratio [N₂H₄] : [CuSO₄] = 20 : 1 was reached. The final reaction mixture was a dark brownish dispersion. A VEGAII SBH scanning electron microscope (SEM, TESCAN) and a Tecnai G2 F30 field emission transmission electron microscope (FETEM, FEI) operated at 300 kV were used to record images of the nanoparticles. X-ray diffraction (XRD) spectra were acquired with a Bruker D8 Advance X-ray diffractometer (Cu K α).

3. Results and Discussion

Fig. 1a and b are typical SEM and TEM images of the particles synthesized with the concentration of SDS, C_{SDS} = 9 mM. The particles were of quite uniform dimensions. As C_{SDS} varied from 9 mM to 50 mM, the average particle diameter could be linearly adjusted in the range of 90-300nm. A layer of non-crystalline organic material, which should correspond to the PVP-SDS complexes, was found to cap around the particles as shown in Fig. 1b.

Newly prepared samples gave rise to sharp XRD peaks corresponding to those of Cu (Fig. 2a) only. Though no inert gas was applied throughout the synthesis processes, no oxides have been detected. After the nanoparticle powder had been stored for two weeks in air, no obvious peaks from the oxides were recorded (Fig. 2b). Fig. 2c shows a XRD spectrum of the powder synthesized without PVP and SDS in a comparative experiment. Extraordinary fine grains were produced with relatively low crystalline quality. After two weeks of exposure to air, the estimated mass fraction of Cu₂O valued to be about 55%.

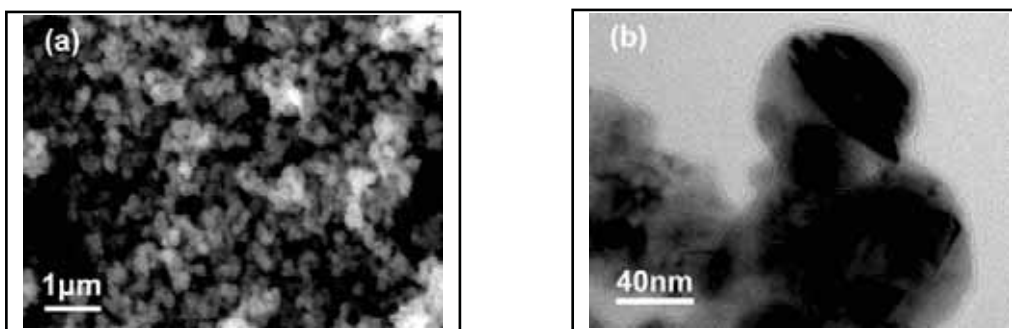


Fig. 1. Structural characterization of the particles. (a) A SEM image and (b) a TEM image of nanoparticles synthesized with $C_{\text{SDS}} = 9 \text{ mM}$

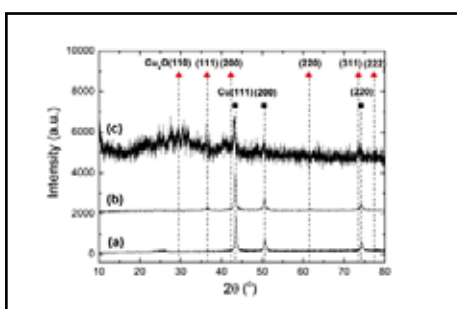


Fig. 2. XRD patterns of particle powders synthesized (a) with PVP-SDS, as-grown; (b) with PVP-SDS, stored in air for two weeks; and (c) without PVP-SDS, also stored in air for two weeks (intensity magnified 10 times).

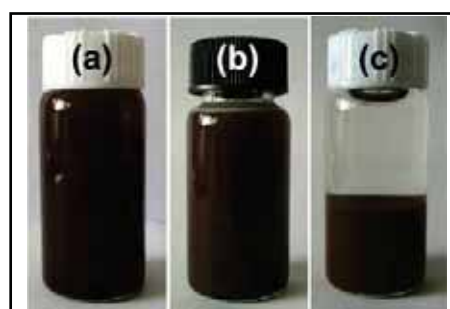


Fig. 3. Photographs of (a) the final reaction mixture with $\text{pH} = 10.0$; (b) and (c) 1 g Cu nanoparticles re-dispersed in 20 ml isopropanol and water, respectively.

In the presence of PVP, the final reaction mixture was found to be a uniform stable aqueous dispersion under the condition that the pH value of the solution is larger than 10 (Fig. 3a). Cu nanoparticles were separated from the reaction mixture by centrifuging. They could be washed and then re-dispersed in water or isopropanol. A PVP concentration of at least 4 g/L is necessary for the re-dispersed solution to be stable. 1g Cu nanoparticles could be uniformly re-dispersed in isopropanol with the volume of 20 ml (Fig. 3b) to 200 ml. To re-disperse the same amount of Cu nanoparticles in water, if extra water is used, the re-dispersed aqueous solution always undergoes a layering phenomenon (Fig. 3c). The lower layer is only about 10 ml and can be stable over months.

4. Conclusions

Cu nanoparticles of high crystalline quality were synthesized by reduction reactions taking place in the presence of PVP and SDS. PVP-SDS complexes were found to be wrapped around the nanoparticles and worked as a kind of template (1) to control the size of the particles; (2) to uniformly disperse the particles in water or isopropanol as colloidal dispersions stable for months; (3) to prevent Cu particles both dispersed in and separated from the solvents from fast oxidation.

References

- [1] J. Yan, G. Zou, A. Hu, Y. Zhou, "Preparation of PVP coated Cu NPs and the application for low-temperature bonding", *J. Mater. Chem.*, 21, 15981-1586(2011).
- [2] S. Jeong, H. Song, and W. Lee et al, "Stable aqueous based Cu nanoparticle ink for printing well-defined highly conductive features on a plastic substrate", *Langmuir*, 27, 3144-3149(2011).
- [3] X. Tang, Z. Yang, and W. Wang, "A simple way of preparing high-concentration and high-purity nano copper colloid for conductive ink in inkjet printing technology", *Colloids Surf. A*, 360, 99-104(2010).

Intermetallic Compound Joints Produced by Ultrasonic Soldering Process in Cu/Sn/Cu System

Mingyu Li^{1,2}, Zhuolin Li¹, and Chunqing Wang²

¹ Shenzhen Key Laboratory of Advanced Materials, Harbin Institute of Technology Shenzhen Graduate School, HIT Campus, The University Town of Shenzhen, Xili, Nanshan District, Shenzhen, P. R. China

² State Key Laboratory of Advanced Welding and Joining, Harbin Institute of Technology, 92 West Dazhi Street, Nangang District, Harbin, P. R. China

Email: myli@hit.edu.cn



Keywords: Intermetallic Compound Joints, Ultrasonic Soldering, Cavitation

1. Introduction

In the microelectronics industry, packaging technologies have advanced dramatically in the past decade, the complexity of the joints has been increased while the size of system has been decreased. In the latest three-dimensional (3D) packaging technology, multiple chips are stacked vertically and connected electrically through via holes, which can provide many advantages such as high package density, parallel processing, short wire length and so on. 3D packaging technology requires that the repeated stacking of additional layers without remelting the joints at lower levels of the stack. This can be achieved by forming intermetallic compound joints with high-remelting-temperature through transient liquid phase (TLP) soldering process at lower bonding temperature[1]. In simple terms, a TLP soldering process is extending the processing time until the liquid phase of a low-melting-temperature interlayer, e. g. Sn or In, sandwiched between two base metals disappears and the joints consists of intermetallic compounds (IMCs) and/or solid solution of the interlayer metal in the base metal[2]. However, a common drawback for TLP process is its very long processing time, up to tens of minutes, which will lead extra thermal stress and seriously affect the reliability of packaging system. In our study, we successfully used the ultrasonic soldering process instead of TLP soldering process to form intermetallic compound joints in Cu/Sn/Cu system at room temperature with a remarkably reduced processing time in the order of seconds.

2. Experiments

The sandwich Cu/Sn/Cu system and ultrasonic bonding are schematically illustrated in Fig. 1 (a) and (b). The interlayer is one piece of pure Sn foil with thickness of 25 μm , and the base metals are two pieces of pure Cu substrate with thickness of 0.3 mm. Both the Sn interlayer and Cu substrates were cut into $3 \times 3 \text{ mm}^2$ in area and manually flattened using a level press. Ultrasonic soldering process was performed at room temperature and the ultrasonic parameters including ultrasonic frequency, pressure, power, had been fixed at 20kHz, 0.6MPa, and 750 W in advance. The processing time varied from 2s to 8s. To detect the overall temperature profile of the interconnection system during soldering process, a thermal couple was put underneath the bottom Cu substrate, and connected to oscilloscope and data acquisition system. Metallographic cross-sections of the joint samples were prepared for the microstructural characterization under scanning electron microscope (SEM). The IMCs consisted in the joints were identified using a X-ray diffraction (XRD) analysis.

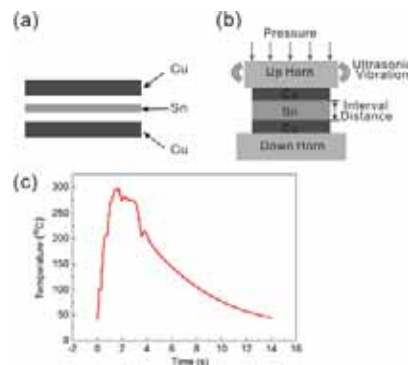


Fig. 1. (a)-(b) Schematic illustration of the Cu/Sn/Cu interconnection system and the ultrasonic bonding. (c) Overall temperature profile of the interconnection system during the ultrasonic soldering process of 3s and succedent cooling procedure.

3. Results and Discussion

Figure 1c indicates the overall temperature profile of the interconnection system in an ultrasonic soldering process of 3s. The temperature firstly rose to 297 °C and then sustained around 277 °C until processing over. As the melting point of Sn is 232 °C, the formation of liquid Sn interlayer in the ultrasonic soldering process is doubtless. The initial abrupt temperature increase is due to the frictional heat generation at the rubbing interfaces between the solid solder and base metal. As to the thermal effect after liquid interlayer formation, it is because the propagation of ultrasonic waves in the liquid interlayer will induce acoustic cavitation phenomenon, where bubble collapse results in enormous concentration of energy from the conversion of the surface energy, kinetic energy of liquid motion into heat and chemical energy, hence sustaining the bonding temperature[3].

The cross-sectional SEM images of the joints formed at processing times ranged from 2s to 8s are shown in Fig. 2. After 2s, the Sn interlayer completely consumed and the joint fully consisted of IMCs. XRD analysis revealed that the IMCs were Cu_6Sn_5 (η). With the processing time increasing to 4s, the joint presented coexisting of Cu_6Sn_5 (η) and Cu_3Sn (ϵ) phases. As to the 8s joint sample, the IMC layer was totally Cu_3Sn (ϵ) phase. This ultrarapid formation of IMC phases can be wholly attributed to the sonochemical effects induced by cavitation erosion at the liquid/solid interface. Propagation of ultrasonic waves in the liquid interlayer induces acoustic cavitation, when bubble collapses at or near the base metal surface, it generates many complex effects including liquid-solder micro-jets, shock waves and localized high temperatures. All these effects work together producing microscale damages (pits) on the base metal surface, which phenomenon is known as cavitation erosion[4]. In our study, this cavitation erosion dramatically accelerated the interdiffusion of Cu from the base metal into the molten Sn during the ultrasonic soldering process, and rapidly made the liquid alloy interlayer maintained in a dynamically unequilibrium state with supersaturation of Cu. Upon subsequent cooling, IMC nuclei rapidly precipitated and grew as a result of reaction crystallization, driven by the supersaturation of Cu in the liquid solder interlayer, eventually forming the joints fully consisted of IMCs.

The amount of Cu released into the liquid Sn interlayer during the soldering process is in direct proportional to the processing time. An increase in the processing time resulted in more mass transportation of Cu metal and increased the concentration ratio of Cu in the Cu/Sn reaction system. Therefore, with the processing time increased from 2s to 8s, we observed that the IMC phase of the joint transformed from a homogeneous Cu_6Sn_5 (η) phase to coexisting Cu_6Sn_5 (η) and Cu_3Sn (ϵ) phases, and homogeneous Cu_3Sn (ϵ) phase.

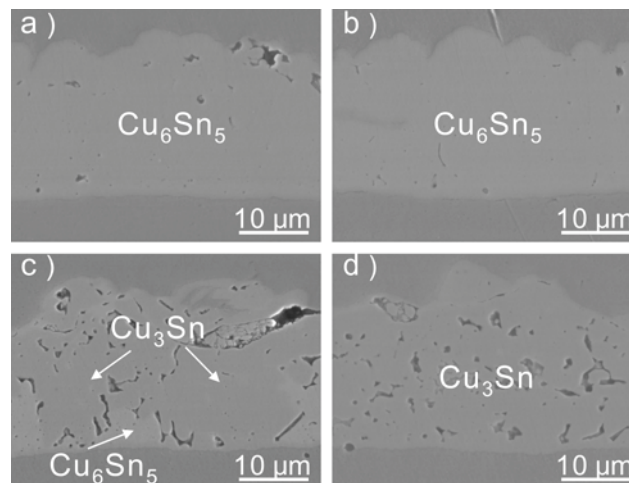


Fig. 2. Cross-sectional SEM images of the ultrarapidly formed joints using ultrasonic soldering process with the processing time varying from 2s to 8s. (a) 2s. (b) 3s. (c) 4s. (d) 8s.

4. Conclusions

In summary, we formed IMC joints in Cu/Sn/Cu system using ultrasonic soldering process at room temperature. Compared with TLP soldering process, the processing time of present method were dramatically reduced, which is due to the accelerated interdiffusion of Cu from the base metal to the liquid solder interlayer, induced by the acoustic cavitation erosion at the liquid/solid interface.

References

- [1] W. Zhang, W. Ruythooren, "Study of the Au/In Reaction for Transient Liquid-Phase Bonding and 3D Chip Stacking," *J. Electron. Mater.*, vol. 37, 1095-1101 (2008).
- [2] J. F. Li, P. A. Agyakwa, C. M. Johnson, "Interfacial Reaction in Cu/Sn/Cu System during The Transient Liquid Phase Soldering Process," *Acta Mater.*, vol. 59, 1198-1211 (2011).
- [3] D. G. Shchukin, S. Ekaterina, V. Belova, H. Möhwald, "Ultrasonic Cavitation at Solid Surfaces," *Adv. Mater.*, vol. 23, 1922-1934 (2011).
- [4] A. Karimi, J. L. Martin, "Cavitation Erosion of Materials," *Int. Met. Rev.*, vol. 31, 1-26 (1986).

Melting, mixing and nucleation at interfaces in Ni-Al nanofoils : a molecular dynamics approach

V. Turlo, O. Politano, and F. Baras

Laboratoire ICB
UMR 6303 CNRS-Université de Bourgogne
Dijon, FRANCE

Email: fbaras@u-bourgogne.fr



Keywords: Nanoscale effects, multilayer thin films, molecular dynamics modeling, reaction mechanism

1. Introduction

Nanometric metallic multilayers (N2M) are known for their ability to deliver a large amount of energy in a very localized way. Such energetic systems are good candidates for micro- and nano-joining without damaging the properties of the pieces to solder. Typically, the nanofoil is placed in between the materials to solder under a strong compression. The local heating of the nanofoil leads to the formation of an extremely rapid self-propagating reaction wave. After initiation, the reaction wave propagates along the foil with high velocity (several dozens of meters per second), which increases the temperature up to 1500-2000 K in a time span of milliseconds. The use of these materials for technological purposes requires a good understanding of the mechanisms involved in the exothermic processes associated with the propagation of the reaction front.

2. Modeling

We have studied the reactivity of Ni-Al nanometric multilayers using a molecular dynamics approach based on the EAM method potential which is well appropriated for metallic systems. This approach allows to capture the basic mechanisms driving the reaction such as diffusion, creation of defects, local ordering/disordering, phase transformations, ... Specific characteristics like the relatively low ignition temperature or the formation of intermetallic grains can be addressed [1,2]. It proves to be a good modeling to explain the main features of experiments carried with nanofoils [3]. This modeling also offers a complementary point of view to a thermodynamic description of fundamental aspects like the depression of the melting temperature [4]. In this work, we will focus on the behavior at a solid-liquid interface to understand the process of mixing, interdiffusion of species, nucleation and growth of new phases in the case of Ni-Al multilayer at high temperatures ($T = 1000\text{K} - 1400\text{K}$).

3. Results

The mixing process is the key phenomenon which drives the reaction. Using MD simulations, the behaviour of the system at a solid (Ni)-liquid (Al) interface is followed. As shown in Fig. 1, three main stages in the dissolution are delineated: 1) Whereas some Ni atoms are dissolved in the liquid layer, they are replaced by Al atoms; 2) The process of dissolution is amplified but all the atoms are keeping the original fcc local structure until most of the layer is covered by Al atoms; 3) Progressively, the crystalline structure is lost and the plane becomes part of the melted layer.

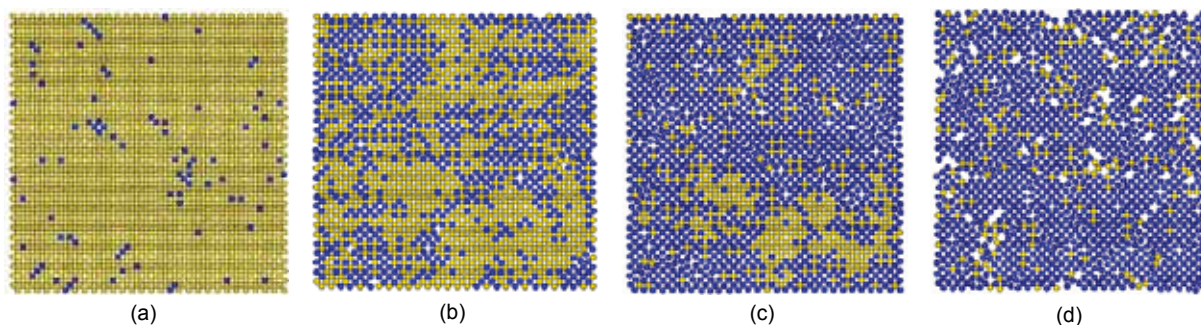


Fig. 1 : Snapshots of the Ni atomic plane close to the interface between Ni and Al during the mixing process at $t = 40$ ps (a), 240 ps (b), 400 ps (c) and 800 ps (d). Al and Ni are shown as blue (black) and yellow (light grey) spheres, respectively. The temperature is fixed to 1050K.

The interdiffusion between Ni and Al allows the reaction to proceed. Formation of B2-NiAl seeds occurs at the interface. Some critical nuclei grow and invade the inner liquid layer leading to the formation of large grains

(see Fig. 2). We have combined several indicators (local crystalline structure, order parameter, cohesive energy per atom, ...) to follow the intrinsic dynamics associated with the reaction. The waiting time for nucleation is found to depend on the temperature of the system: larger temperatures promote the phase transformation.

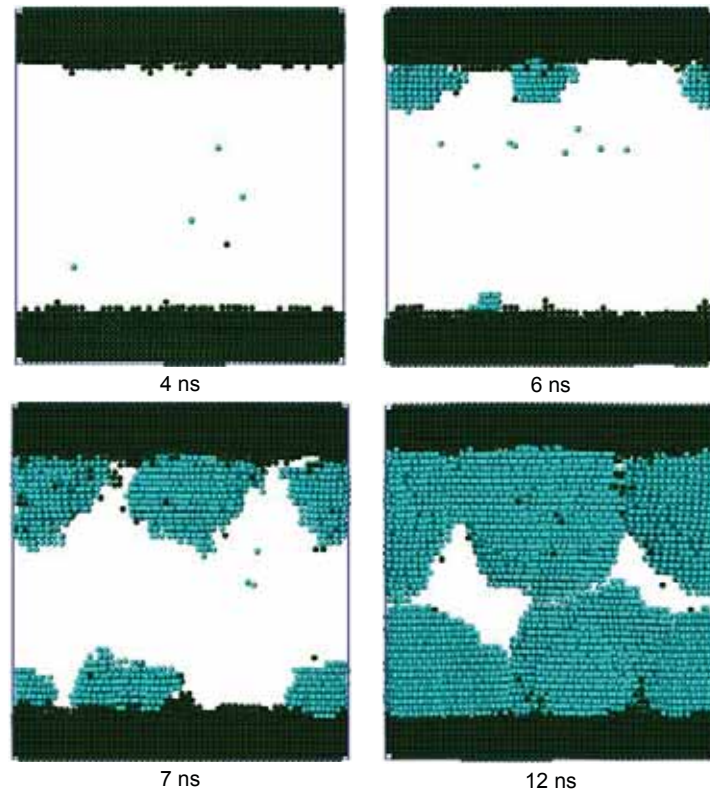


Fig. 2 : Snapshots of the nucleation process at $T = 1150\text{K}$. Dark green (black) spheres correspond to FCC atoms and light blue (grey) to BCC ones. Atoms in other local atomic structure are not shown.

4. Conclusions

This MD modeling allows to detect some key features of the processes involved in the reaction between metallic nanolayers:

- The dissolution of solid Ni layers in the Al liquid phase occurs plane by plane.
- At the time scales accessible in the simulation (typically 20 ns for about 100000 atoms), the nucleation of the intermetallic NiAl phase requires the existence of a solid-liquid interface. The process is heterogeneous by nature.
- The temperature is a key parameter since it will influence the solubility of Ni in Al liquid, and, by the way the effective nucleation and growth of B2-NiAl phase. Above a transition value, the very possibility of nucleation process is destroyed.
- The temperature influences the morphology of the grains. Larger grains with one specific orientation are observed for higher temperatures.
- The size of the sample affects the observed microstructure.

References

- [1] F. Baras and O. Politano, "Molecular dynamics simulations of nanometric metallic multilayers: Reactivity of the Ni-Al systems", *Phys. Rev B*, 84, 024113 (2011).
- [2] O. Politano, F. Baras, A.S. Mukasyan, S.G. Vadchenko and A.S. Rogachev, "Microstructure development during NiAl intermetallic synthesis in reactive Ni-Al nanolayers: Numerical investigations vs. TEM observations", *Surf. Coat. Technol.*, 215, 485-492 (2013).
- [3] L.P.H. Jeurgens, Z. Wang and E.J. Mittemeijer, "Thermodynamics of reactions and phase transformations at interfaces and surfaces", *Int. J. Mat. Res.*, 100, 1281-1306 (2009).
- [4] A.S. Rogachev, S.G. Vadchenko, F. Baras, O. Politano, S. Rouvimov, N.V. Sachkova and A.S. Mukasyan, "Structure evolution and reaction mechanism in the Ni/Al reactive multilayer nanofoils", *Acta Mater.*, 66, 86-96 (2014).

Mechanical response on Cu-Sn intermetallics

F. Wang¹, X. Li¹, and K. Qi¹

¹ Provincial Key Laboratory of Advanced Welding Technology, Jiangsu University of Science and Technology, Zhenjiang, 212003, P.R. China

Email: ffwang@just.edu.cn



Keywords: serrated flow, Cu_6Sn_5 , Cu_3Sn , nanoindentation

1. Introduction

Increasing environmental concerns over the use of tin-lead (Sn-Pb) solders in electronic packaging have prompted a significant effort to developing Pb-free solders [1, 2]. Today, most of the Pb-free solders are Sn-based with a small amount of silver (Ag) and copper (Cu). Among them, Sn-3.5Ag and Sn-3.0Ag-0.5Cu (wt.%) solders are the most common.

During the soldering process, the formation of intermetallic compounds (IMCs) between Sn-based solders and the substrates is inevitable [3, 4]. The initial formation of these IMCs at the interface between the solder and the substrate during soldering ensures a good metallurgical bond. Generally, Cu and nickel (Ni) have been the widely used solderable substrate. Interaction and interdiffusion behaviors between Sn-Ag or Sn-Ag-Cu Pb-free solder and Cu or Ni have been intensively studied. In the case of Sn-3.5Ag or Sn-Ag-Cu solder on Cu, Cu_6Sn_5 and Cu_3Sn IMC layers are formed at the interfaces. The Cu_6Sn_5 is the dominant growth phase, while Cu_3Sn is more likely to form after Cu_6Sn_5 by the diffusion and reaction of Cu with Cu_6Sn_5 [5-7]. In the case of Sn-3.5Ag/Ni, the Ni_3Sn_4 IMC layer is the only reaction layer at the interface whether soldering or thermal aging [8, 9]. For Sn-Ag-Cu/Ni solder joint, molten Sn-Ag-Cu solder reacts with the Ni metallization in a completely different manner than Sn-3.5Ag/Ni or Sn-Ag-Cu/Cu system [10]. Also, Cu concentration in the Sn-Ag-Cu solder has a vital role in the interfacial reaction with the Ni metallization by Ho et al. [11]. They reported that, above 0.5 wt.% Cu, Cu_6Sn_5 -based ternary IMC layer, usually with the formula of $(\text{Cu},\text{Ni})_6\text{Sn}_5$ formed at the interface instead of Ni_3Sn_4 in the Sn-Ag/Cu system. The growth of these intermetallics can strongly degrade fatigue and fracture toughness of the solder joints due to the brittle nature of intermetallics. Thus, knowledge of the mechanical properties of intermetallics is important for the understanding of the reliability of the solder interconnections. Also, for those IMCs with ternary in nature, e.g. $(\text{Cu},\text{Ni})_6\text{Sn}_5$ and $(\text{Ni},\text{Cu})_3\text{Sn}_4$, the influence of various alloying element in the based binary intermetallic on the mechanical properties should be evaluated.

The mechanical properties of some binary intermetallics have been investigated by several researchers. It was found that, in the previous studies on bulk intermetallics, there exists significant disagreement with regard to values of Young's modulus for Cu_6Sn_5 and Cu_3Sn . While, recently developed nanoindentation on the evaluation of actual IMCs formed at the interface of solder joints provides relatively consistent results. This discrepancy would be attributed to the differences of grain size, defects and crystallographic orientation between the bulk intermetallics and actual IMCs in solder joint.

In this study, nanoindentation has been used to measure the mechanical properties of Cu_6Sn_5 and Cu_3Sn intermetallics, formed at the interface of Sn-Ag-Cu/Cu system.

2. Experiments

Sn-3.0Ag-0.5Cu Pb-free solder is used in this study. Pure Cu with a thickness of 0.3 mm and a width of 5 mm was used as the substrate respectively. Solder paste was placed on the substrate, and the couples were reflowed in a reflow oven. The temperature profile had a peak temperature of 250 °C, 60 s above the melting temperature of solder alloy. The couples were then encapsulated in a sealed quartz glass tube that was backfilled with argon and reflowed for a week at 250 °C to promote the growth of IMCs at the interface of solder joint to a larger thickness suitable for nanoindentation.

After reflowing, the couples were epoxy-mounted in cross-section and polished with standard metallography techniques to a 0.05 μm final finish, with colloidal silica suspension.

Nanoindentation testing was carried out on diffusion couple samples using a Triboscope transducer (Hysitron, Inc., Minneapolis, MN) mounted to a Multimode atomic force microscope (AFM) with a Nanoscope III controller (DI, Santa Barbara, CA). The indentation tip was a three-sided pyramid (Berkovich) with a tip radius

of approximately 150 nm. The indentation test typically consisted of three steps: loading at 10, 50, 100 and 500 mN/min to a 50 mN load, a hold of 5 s at maximum load, and lastly, unloading in 1s.

3. Results and Discussion

Fig.1 shows the interfacial structure of Sn-3.0Ag-0.5Cu/Cu joint. It can be found that there were two intermetallics between the solder and Cu pad, Cu_6Sn_5 and Cu_3Sn , respectively. The thickness of intermetallics was enough for the nanoindentation test.

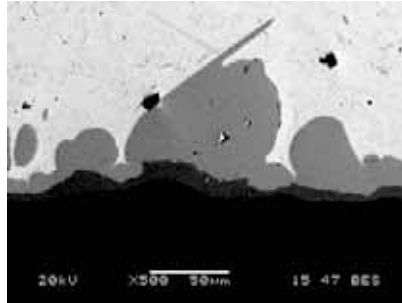


Fig.1. Interfacial structure of Sn-Ag-Cu/Cu solder joints

Fig.2 shows the effect of loading rate on nanoindentation load-displacement curves for Cu_6Sn_5 and Cu_3Sn intermetallics. As the same Cu-Sn intermetallic phases, there existed two kinds of deformation mechanisms, non-continuous plastic deformation for Cu_6Sn_5 while continuous plastic deformation for Cu_3Sn . The non-continuous plastic deformation for Cu_6Sn_5 was expressed as the serrated flow of loading curves during nanoindentation. The formation of serrated flow also depended on the loading rate or strain rate, the higher the loading rate, the weaker the serrated flow of loading curves. Some shear bands operated around the indent due to the serrated flow for Cu_6Sn_5 . From the physical analysis of nanoindentation curves, the elastic moduli of Cu_6Sn_5 and Cu_3Sn were 114.2 ± 4.5 and 138.7 ± 4.3 GPa, while the yield stresses were 2009 ± 63 and 1787 ± 108 MPa, respectively.

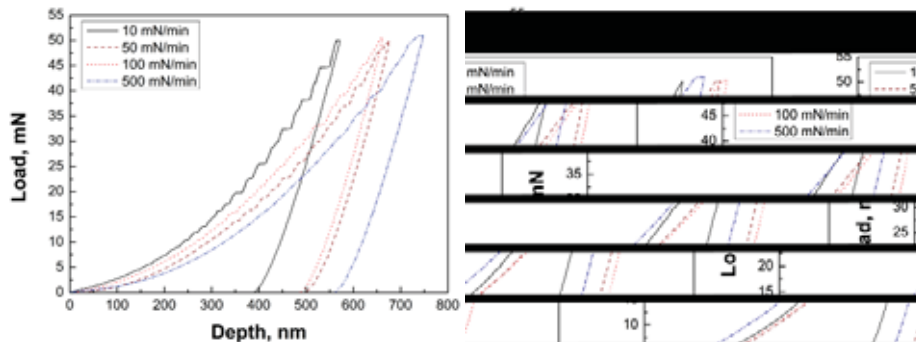


Fig.2. Effect of loading rate on P-h curves for Cu_6Sn_5 (a) and Cu_3Sn (b)

4. Conclusions

As the same Cu-Sn intermetallic phases, non-continuous plastic deformation for Cu_6Sn_5 while continuous plastic deformation for Cu_3Sn were found in this paper. The non-continuous plastic deformation for Cu_6Sn_5 was expressed as the serrated flow of loading curves during nanoindentation.

References

- [1] Abteew, M. and G. Selvaduray, Materials Science and Engineering: R: Reports, 2000. **27**(5-6): p. 95.
- [2] Zeng, K. and K.N. Tu, Materials Science and Engineering: R: Reports, 2002. **38**(2): p. 51.
- [3] Prakash, K.H. and T. Sritharan, Acta Materialia, 2001. **49**(13): p. 2481-2489.
- [4] Gorlich, J., G. Schmitz, and K.N. Tu, Applied Physics Letters, 2005. **86**(5).
- [5] Lee, T.Y., et al., Journal of Materials Research, 2002. **17**(2): p. 291.
- [6] Deng, X., et al., Journal of Electronic Materials, 2003. **32**(12): p. 1403.
- [7] Sharif, A. and Y.C. Chan, Journal of Electronic Materials, 2005. **34**(1): p. 46.
- [8] Hsu, H.-F. and S.-W. Chen, Acta Materialia, 2004. **52**(9): p. 2541.
- [9] He, M., et al., Thin Solid Films, 2004. **462-463**(SPEC ISS): p. 376.
- [10] Zribi, A., et al., Journal of Electronic Materials, 2001. **30**(9): p. 1157.
- [11] Ho, C.E., et al., Journal of Electronic Materials, 2002. **31**(6): p. 584.

Start temperature manipulation and efficiency improving of self-propagation chemical reactions in multilayered thermite materials based on aluminum-copper nitride composite

D. G. Gromov¹, **E. A. Lebedev¹**, S. P. Timoshenkov¹, Yu. I. Shilyaeva¹, V. A. Galperin², D. I. Smirnov³, and E. P. Kirilenko⁴



¹National Research University of Electronic Technology, 124498 Russia, Moscow, Zelenograd, 4806 Pas., bld. 5

²Science Manufacturing complex "Technological Center", 124498 Russia, Moscow, Zelenograd, 4806 Pas., bld. 5

³Lebedev Physical Institute of Russian Academy of Science, 119991 Russia, Moscow, Leninskij Prospekt 53

⁴Science-Technological center "Nano- and Microsystems technics", 124498 Russia, Moscow, Zelenograd, 4806 Pas., bld. 5

Email: dr.beefheart@gmail.com

Keywords: heterogeneous reactions, nanothermite composite, multilayer thermite materials, energetic materials, nano- and micro-joining

1. Introduction

In last decade a number of fundamental and applied research works in the field of thermite materials have been carrying out [1-3]. Such increasing interest is associated with active development of new areas of science and technology, among them joining for integration of nano-/micro- scale materials and devices for microelectronics, implantable medical devices and small-sized energy conversion systems. Research and development of new thermite systems, method of start temperature control, and increasing efficiency of chemical reactions in such thermite systems are still being the main technology task for scientists and researchers.

In this work thermodynamic calculations and analysis of combustion effects in aluminum-copper nitride system are presented. Experimental DCS study of multilayer thermite composite were held and possibility of start temperature manipulation and chemical reaction efficiency increasing were shown.

2. Experiments

Thermite multilayer Al/Cu_xN_y foils of different total and bilayer thickness (from micro to nanosize) were fabricated by magnetron sputtering of Al and Cu targets onto silicon substrates. The copper target is sputtered in nitrogen-argon atmosphere. For the different samples the Cu_xN_y layers were deposited at the varied nitrogen pressure from 1 to 7 mTorr in gas mixture argon-nitrogen.

Thermal effects measurements were performed by differential scanning calorimetry in temperature range from 50 to 1000 Celsius degree. Heating velocity changes from 5 to 50 degrees per minute.

Structural and elemental analysis performed by X-ray diffraction (XRD) and X-ray energy-dispersive spectroscopy (XEDS) measurements.

3. Results and Discussion

It was shown that the main DSC-peak temperature increased (pic. 1) and reaction propagation velocity decreased with bilayer thickness.

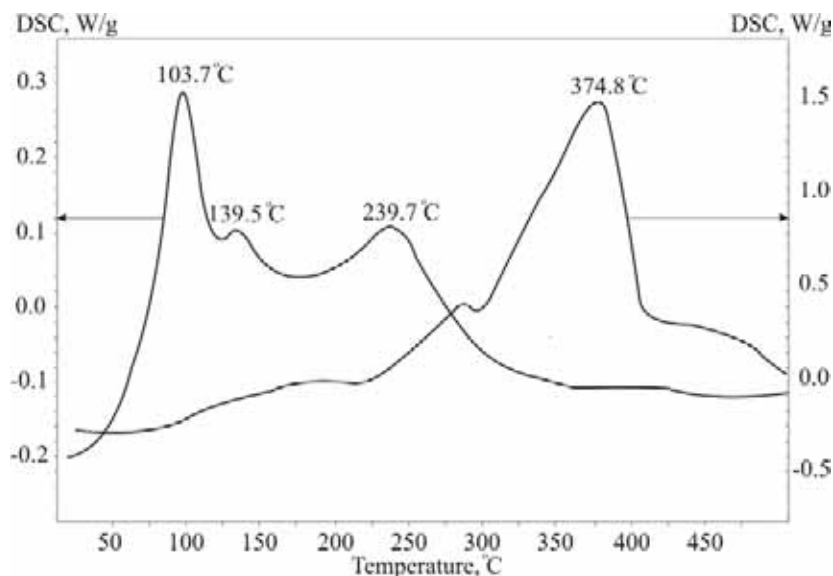


Fig. 1. DSC results for Al-CuN multilayer thermite with different bilayer thickness: 25 nm – left and 300 nm – right (exo upward).

The peak form and position and amount of released heat are also depends on nitrogen pressure during the magnetron sputtering. Approach for combustion reaction efficiency is proposed. Obtained XRD and XEDS results allowed to correct deposited composite stoichiometry.

Despite the nitrogen pressure changing during copper target sputtering process, there was only Cu_3N deposited shown by XRD. From the other hand, there is a number of intermediate compounds (CuN , Cu_3N , Cu_3N_2 , CuN_3 , CuN_6) according to Cu-N phase diagram. Such unusual effect can be connected with the fact that forming on the copper target surface Cu_3N compound equally well sputtered by both of argon and nitrogen. However, detected combustion effects have comparable and even superior values than known multilayered thermite materials.

References

- [1] M. R. Weismiller, J. Y. Malchi, J. G. Lee, R. A. Yetter, T. J. Foley, "Effects of fuel and oxidizer particle dimensions on the propagation of aluminum containing thermites", *Proceedings of The Combustion Institute*, vol.33, 1989-1996 (2011).
- [2] M. Petrantoni, C. Rossi, V. Conedera, D. Bourrier, P. Alphonsw, C. Tenailleau, "Synthesis process of nanowired Al/CuO thermite", *Journal of Physics and Chemistry of Solids*, vol. 71, 80-83 (2010).
- [3] M. Petrantoni, C. Rossi, L. Salvagnac, V. Conedera, A. Esteve, C. Tenailleau, P. Alphonse, Y. J. Chabal, "Multilayered Al/CuO thermite formation by reactive magnetron sputtering: Nano versus micro", *Journal of Applied Physics*, vol. 108 (2010).

Shear Strength Degradation of Pb-free Solder Joint with Mounted Location in Automobile

W. S. Hong¹, and A Young Kim¹

¹Components & Materials Physics Research Center, Korea Electronics Technology Institute, #25 Saenari-ro, Bundang-gu, Seongnam-si, Gyeonggi-do 463-816, Korea

Email: wshong@keti.re.kr



Keywords: Pb-free, Soldering, Automotive, Degradation, Failure Mechanism

1. Introduction

Restriction of the use of Hazardous Substances (RoHS) restriction is widely applying to electronics assembly from July 2006 [1]. Even though automotive adopted many electronic control unit (ECU) modules, End-of-Vehicle (ELV) will be started to restrict to the vehicle from January 2016. In focused on the use environment and service life for automobiles, the use of Pb-free solder in automotive electronics is quite different when compared to use in normal electronics such as mobile electronics. Because of very long service life spanning 10 years and over 100 thousand miles and high reliability expectations in cars. Also, ECU modules have a different operating temperature with mounting location in the automotive. In case of mounted in passenger room, normal operation temperature need from -30 to 85 deg. C, but, in module for engine room, its temperature is -30 to 125 deg. C. Because of difference of use environment temperature, Pb-free solder joints show a different degradation property of solder joint strength. Due to this difference, it is need to understand the degradation characteristic of Pb-free solder joint in car electronics. So, we have measured the solder joint strength with diverse chip components size under thermal cycling condition. Based on these results, we confirmed the tendency of failure mechanism and degradation property of solder joint under automotive environment.

2. Experiments

Test vehicles were prepared as shown in Fig. 1 (a). Sn-40Pb (eutectic) and Sn-3.0Ag-0.5Cu (SAC305) solders were used. The eutectic solder used for comparing shear strength with SAC305. 145 deg.C Middle Tg (glass transition temperature) PCB and organic solderability preservative (OSP) surface finish were utilized for test coupon. Thermal cycling (TC) tests were conducted from -40 ~ 85 deg. C for cabin room condition and from -40 ~ 125 deg. C for engine room condition until 1500 cycles and each one cycle time was 67 minutes. To investigate chip size effect, we used various chip resistor and capacitor which were 0402, 0603, 1206, 1608, 2012, 3216 size. To compare the degradation tendency of shear strength, we measured shear strength at 500, 750, 1000, 1200, and 1500 cycles using by bonding test machine (Dage 4000, England). We have also observed solder joint interface and crack generation mechanism using a field emission scanning microscope (FESEM).

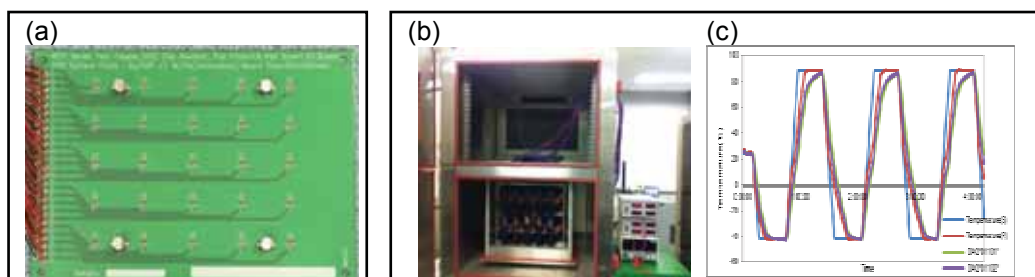


Fig. 1. Photographs of (a) test vehicle, (b) equipment set-up, and (c) temperature profile.

3. Results and Discussion

Void content of solder joint in test vehicles was under 15% with compared to up to 25% of industry guideline. All kinds of solder joint shear strength were decreased with thermal cycling number. In the same test condition, with increasing the chip components size, higher initial shear strength was shown in eutectic and SAC305 solder joints. Even though SAC305 solder joint indicated higher shear strength than eutectic solder alloys, with thermal cycling number, degradation rate of SAC305 is dramatically decreased than eutectic solder joint. Intermetallic

compound layer (IMC) thickness was increased with thermal cycling number, and total IMC formation of engine room condition was a slightly thicker than cabin condition. After 1500 thermal cycling, IMC was growth 3.84~4.06 micron meter. Comparing with IMC growth rate which was calculated the deviation with as-reflowed and final TC cycles, engine room and cabin condition were 67% and 54%, respectively. Furthermore, cracks were developed at the solder joints and progressed with solder and IMC interfaces. With increasing the thermal cycling number, crack propagation length was increased. In case of same TC number, crack length of engine room condition was longer than Cabin condition. This result is caused by a large CTE mismatch due to a large temperature deviation ($\Delta T=165$ deg. C) of engine room condition rather than cabin ($\Delta T=125$ deg. C). It is well known that solder joints crack is generally addressed to thermo-mechanical fatigue stress [2,3]. Initial crack was occurred at the solder matrix and progressed along the IMC and solder interfaces. This was good evidence that those crack generation mechanism was the same phenomenon. From these results, we estimated that SAC305 solder can be used in cabin automotive electronics instead of Pb-contained solder alloy. But, if harsh environment, we known that new solder candidate is need for engine room electronics.

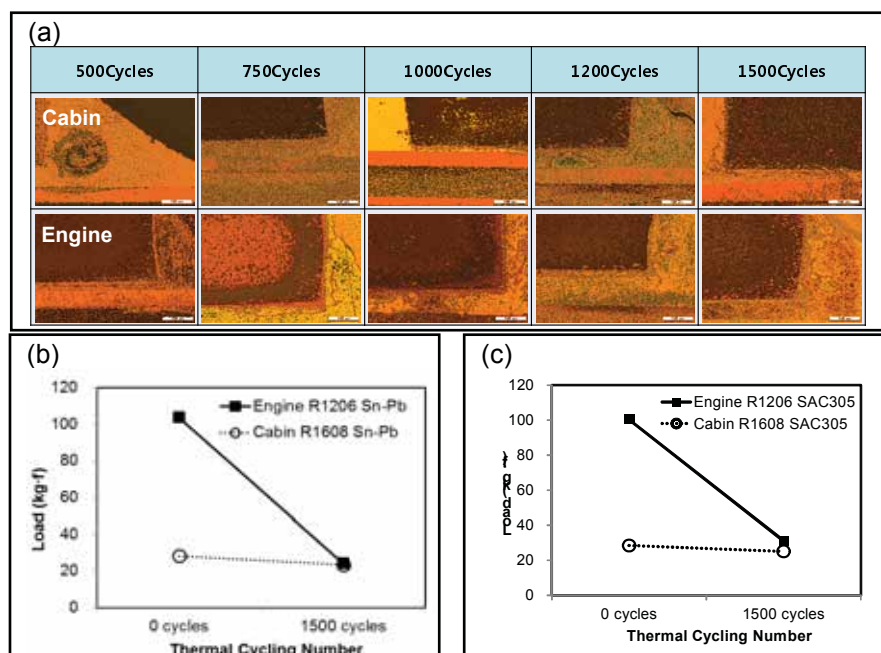


Fig. 1. (a) Cross-sectional micrographs of lead-free solder joints with thermal cycling number. Shear strength degradation curves of (b) eutectic solder and (c) SAC305 solder of 1206 and 1608 chip resistor with engine room and cabin electronics conditions

4. Conclusions

To apply Pb-free solder in car electronics, we have examined the degradation rate of solder joints with various chip components size under use environment conditions of cabin and engine room electronics. With increasing the chip size, degradation rate of shear strength is a larger. Also, in case of same size of component, degradation rate in engine room condition is faster than cabin condition, which was normally 4-5 times faster than cabin environment. Based on these results, we can guess that SAC305 solder is possible to replace the eutectic solder in cabin electronics. Even though having a similar shear strength of SAC305 and eutectic after TC 1500 cycles, crack length of SAC305 is quite longer than eutectic solder joint. Therefore, we known that new solder alloy for harsh environment automotive is needed.

References

- [1] Directive 2002/95/EC of the European Parliament and of the Council, Restriction of the Use of Certain Hazardous Substances in Electrical and Electronic Equipment, EU (2003)
- [2] W. S. Hong, and K. B. Kim : Tafel Characteristics by Electrochemical Reaction of SnAgCu Pb-Free Solder, Korea Journal of Materials Research, Vol.15, No.8 , 536-542 (2005)
- [3] C.W. Han, N.C. Park, W.S. Hong, Study on Failure Mechanism of Chip Resistor Mounting Solder at Thermal Cycling for Prognostics and Health Monitoring, Vol.35, No.7, pp.799-804 (2011)

Investigation of copper-based nanostructured multilayer systems for brazing applications

W. Tillmann¹, B. Lehmert², L. Wojarski³ and M. Kuck⁴

¹TU Dortmund, Institute of Materials Engineering, Leonhard-Euler Str. 2, 44227 Dortmund

Email: wolfgang.tillmann@tu-dortmund.de



Keywords: Joining, brazing, nanoscale, nanomultilayers, nanostructured, melting point depression

1. Introduction

The scientific field of nanotechnology is gaining increasing importance in all industrial sectors as this technology enables previously unimaginable new approaches. Materials sciences use advantages resulting from the changing ratio between the volume and the surface on a nanoscale to adapt the properties and characteristics of materials. One of the most dominating parameters for the quality of joints in the joining technology is the temperature used during the joining process. The temperature has to be high enough to melt the brazing filler metal, yet it is also a restricting factor due to its thermal influence on the base material. One possibility to keep the thermal influence on the substrate at a minimum, and thus to prevent the decline of the mechanical properties, is to decrease the temperature during the brazing process. While conventional brazing techniques use alloying elements, the physical effect of the nanoscale offers new promising approaches: The short distances and thus the fast diffusion of materials as well as the melting point depression within the nanoscale. Both approaches, or a combination of these two approaches can be used to achieve solid joints with lowered process temperatures.

The effect of the melting point depression was predicted by Pawlow's theoretically investigations in 1909. He proved a correlation between the radius of a particle and its melting temperature in the dimensions below 100nm [1]. First experiments by Takagi in 1954 with lead films of a thickness of 5nm, yielded a temperature 41°C lower than that of the bulk material [2]. In 1986, Allen et al. observed the melting point depression of size-reduced particles with the help of a transmission electron microscope [3]. Nowadays, the production of nanostructured multilayer configurations by sputtering processes for the utilization in the joining technology to obtain lower temperatures in joining processes is increasingly focused on [4]. While further investigations on an Ag-Cu/C system with C layers acting as diffusion barriers for nanostructured Ag-Cu brazing fillers showed a formation of a metallurgical bond at a temperature below the bulk melting point [5] the investigations of this project examines copper-based nanostructured multilayers. The preparation, as well as the utilization of nanomultilayer systems with alternating layers of copper as filler metal and diffusion barrier layers of different materials were conducted.

2. Experiments

In this study, three different nanomultilayer systems were investigated: Cu-W, Cu-AlN, and Cu-Ag. For all systems 200 repetitions of 10nm thin alternating layers of filler metal and diffusion barriers were deposited on different samples (see Fig. 1(a)) by means of magnetron sputtering with a common, industrially used PVD device (CC 800 / ml sinox, CemeCon, Germany): TiAl4V6 (TAV) samples for the purpose brazes and for further analyses on Si-wafers as well as NaCl-samples. In order to produce the aspirated layer design, it was necessary to measure the thickness of single layers with the help of ellipsometry (M 2000V by J.A. Woollam Co., Inc), thus determining the deposition rate. Beside further investigations of the structure by means of X-ray reflection (XRR) the achieved melting point depression was determined as well by means of differential scanning calorimetry (DSC) and differential thermal analysis (DTA) with a STA PT 1600 by Linseis. Therefore, coated NaCl-samples were dissolved to generate freestanding foils that can be analyzed. For the brazing investigations, two samples coated with the identical nanomultilayer system, were placed in a mounting device with the coated sides facing each other. The pressure on the samples was varied between 25 and 50MPa by a screw on top of the jig used. By means of a high temperature vacuum furnace type TORVAC, the samples were first heated up with 20K/min to a temperature of 200°C below the final joining temperature. After keeping the temperature at this level for 15 minutes to ensure a homogeneous distribution of the heat, the samples were heated with 10K/min to the desired joining temperature, which was retained for 5 minutes.

The cross-sections of the produced brazements were subsequently analyzed by means of light microscopy as well as electron microscopy (JSM 7001F by Joel). Additionally, energy-dispersive x-ray (EDX) spectroscopy was used to characterize the joining area. Besides the quality of the produced joints, it was a further aim to clarify the influence of the numbers of layers that corresponds with the thickness of the layer system, the temperature, and the pressure during the brazing process.

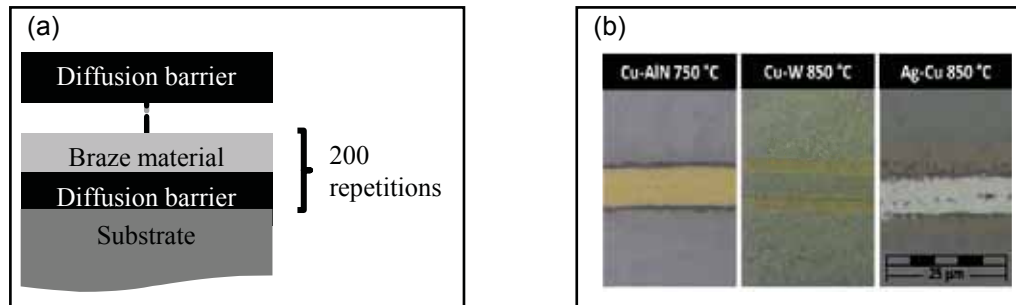


Fig. 1. Schematic overview of the nanomultilayer film (a). Brazed samples at 100 MPa (b).

3. Results and Discussion

The DTA measurements confirmed an endothermic reaction below the normal melting temperature, which indicates a melting point depression resulting from the nanostructure of the filler metal for all systems.

The analyses of the cross-sections showed different results. While the layer system of the Cu-AlN system and Cu-Ag system were molten into a single brazing seam and a clear Cu diffusion zone was visible, the Cu-W system showed three individual brazing seams (see Fig. 1(b)). The EDX-measurements for all three systems confirmed that the Cu of the nanomultilayer coating system was squeezed out, leading to remnants in the brazing gap consisting of diffusion barriers. This result underlines the suggestion that the melting point depression leads to a liquid Cu-phase during the brazing process. Further investigations are necessary to verify these assumptions.

The comparison of the cross-sections of two samples, brazed with different pressures, showed that a higher pressure avoids potential gaps in the joining area and leads to a bigger diffusion zone of the filler metal in the substrate, indicating that more Cu leaves the previous nanomultilayer system and is available for the brazing process.

4. Conclusions

This work demonstrates that a nanostructured multilayer system, consisting of alternating nanolayers of Cu as a brazing filler and AlN, Ag and W as diffusion barrier layers, can be used as brazing fillers for TAV samples. The investigations proved a significant melting point depression for all systems. Further preliminary results show the influence of the temperature as well as pressure on the joints. Currently conducted investigations will determine and evaluate the mechanical properties of the produced joints.

References

- [1] P. Pawlow, "Über die Abhängigkeit des Schmelzpunktes von der Oberflächenenergie eines festen Körpers," *Zeitschrift für physikalische Chemie, Stöchiometrie und Verwandtschaftslehre* 1, 545 (1909)
- [2] M. Takagi, "Electron-Diffraction Study of Liquid-Solid Transition of Thin Metal Films," *J Phys. Soc. Japan*, 9, 359-363 (1954)
- [3] Allen et. al., "Small particle melting of pure metals," *Thin Solid Films* 2, 297-308 (1986)
- [4] V. Bissig, J. Janczak, "Nanoscale effect-based melting point reduction for brazing filler metals," *Empa Activities 09/10*, 8, *Advanced Materials and Surfaces* (2010)
- [5] J. Janczak-Rusch, G. Pigozzi, B. Lehmert, M. Parlinska, V. Bissig, W. Tillmann, L. Wojarski, F. Hoffmann, "Deposition and utilization of nanomultilayered brazing filler systems designed for melting point depression," *IBSC 2012 - Proceedings of the 5th International Brazing and Soldering Conference*, 162 (2012)

3D Stereolithographic Printing of Terahertz Wave Photonic Crystals through Micro Joining of Oxide and Metallic Glasses

S. Kiriwara

Joining and Welding Research Institute, Osaka University

11-1 Mihogaoka Ibaraki, Osaka 567-0047, Japan

Email: kirihara@jwri.osaka-u.ac.jp



Keywords: Metallic Glass, Oxide Glass, Photonic Crystal, Terahertz Wave, Laser Scanning Stereolithography

1. Introduction

Periodic structures composed of magnetic or dielectric materials are called photonic crystals. These artificial arrangements can exhibit forbidden regions called photonic band gaps to totally reflect electromagnetic waves comparable to these lattice constants through Bragg diffraction [1]. Electromagnetic waves in terahertz frequency ranges have lately attracted considerable attentions as novel analytical light sources. Because the electromagnetic waves at terahertz frequencies can be synchronized with collective vibration modes of various harmful substances, these spectroscopic technologies are expected to be applied to novel imaging sensors for real time detection of toxic materials in aqueous phase environments [2]. However, the terahertz waves are difficult to transmit into the water solvents with large amplitudes due to electromagnetic absorptions. In our investigation group, micrometer order alumina or zirconia lattices with diamond structures were fabricated successfully by using a micro stereolithography system to resonate the terahertz waves [3]. In this study, the micrometer order magnetic and dielectric photonic crystals with the diamond structure composed of the metallic glass dispersed oxide glass were fabricated by using 3D stereolithographic printing to be applied to the novel terahertz wave sensor devices. These sensors are composed of the magnetic and dielectric crystals with through holes and micro tubes. This artificial crystal having a cylindrical defect can harmonize with the specific wavelength comparable to the diameter, and a localized mode of a transmission peak appears in the band gap. For the various water solvents flowing into the micro tube, and the terahertz wave spectra will be measured. If the resonated terahertz wave can harmonize with the collective vibration mode of the introduced water solvents, the localized mode peak in the band gap will disappear through the electromagnetic absorptions. The photonic crystal sensors will be applied to various scientific and engineering fields by utilizing the terahertz wave spectroscopic database.

2. Experiments

The magnetophotonic crystal was fabricated by using the laser scanning stereolithography. Metallic glass ($\text{Fe}_{72}\text{B}_{14.4}\text{Si}_{9.6}\text{Nb}_4$) and oxide glass ($\text{B}_2\text{O}_3\cdot\text{Bi}_2\text{O}_3$) particles of 2.6 μm and 1.0 μm diameter were dispersed into photo sensitive acrylic resins at 16:24, 17:23 and 18:22 in volume ratios by a planetary mixing and defoaming machine. The rotation and revolution speed were set at 300 and 700 rpm, respectively. Obtained paste materials were supplied on a substrate and spread uniformly by a mechanical knife edge. The thickness of each layer was controlled to 10 μm . Cross sectional layers drawn by ultraviolet laser scanning of 10 to 100 μm in variable diameter were laminated to create composite precursors. The wavelength was set at 355 nm, and the spot power was optimized at 500 mJ/mm^2 to realize the higher resolution. The three dimensional structures were built by layer stacking. The rod diameter and length were 144 and 217 μm , and the lattice constant of the diamond structure was 500 μm , respectively. The whole structure was 5 \times 5 \times 0.5 mm in size consisting of 10 \times 10 \times 1 unit cells. Under the glass transition temperature at 552 $^\circ\text{C}$ of the selected metallic glass, the formed precursor was dewaxed at 420 $^\circ\text{C}$ for 8.0 hs with the heating rate of 1.0 $^\circ\text{C}/\text{min}$, and sintered at 460 $^\circ\text{C}$ for 0.5 hs with the heating rate of 2.0 $^\circ\text{C}/\text{min}$ in an Ar atmosphere. The diamond lattice model was corrected and re-designed according to the liner shrinkage ratios. Microstructures of the lattices were observed by an optical microscope and a scanning electron microscopy (SEM), and the microstructural stabilities of the amorphous phase alloy were analyzed by a X-ray diffraction (XRD). The terahertz wave transmittance was analyzed by a terahertz time domain spectroscopy. Moreover, the profiles of transmission spectra for the photonic crystal and the distributions of electric field intensities in the structural defect were calculated and visualized by using transmission line modeling method (TLM) of a finite difference time domain (FDTD) simulation theoretically.

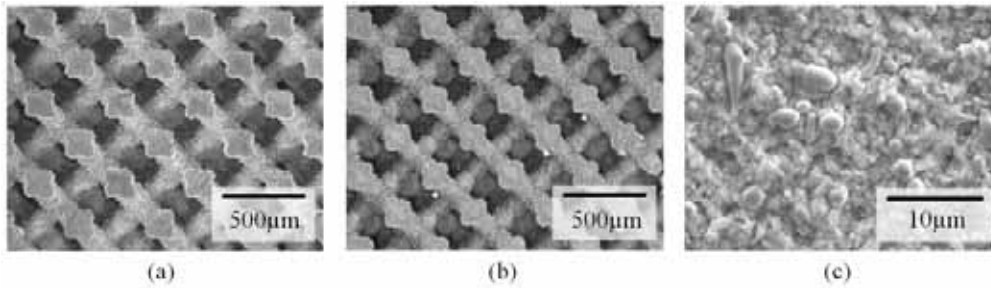


Fig. 1 Photonic crystals with diamond lattices composed of metallic glass and oxide glass particles dispersed in acrylic resin fabricated by micro stereolithography (a) and the sintered metallic glass and oxide glass composite lattices (b). A microstructure of the oxide glass lattice with metallic glass particles dispersion is observed by scanning electron microscope (c).

3. Results and Discussion

The influences of the laser power for the layer thickness and size tolerances of the solid objects were compared and investigated. The compositions of metallic glass and oxide glass were varied systematically. The thickness of one layer was required over 14.5 μm to stack layers every 10 μm successfully. The optimized slurry compositions of the acrylic resin, metallic glass and oxide glass were 60, 17 and 23 % in volume ratios, respectively. And the laser power was optimized at 700 mJ/cm^2 to create the fine cross sectional micro patterns. Figure 1-(a) shows the magnetophotonic crystals with the diamond lattices fabricated by the micro stereolithography. Tolerance between the designed model and formed sample was converged within $\pm 3\mu\text{m}$. The sintered diamond lattice structure with 500 μm in lattice constant is shown in Fig. 1-(b). A micrometer order three dimensional structure was formed successfully. The linear shrinkage ratios of horizontal and vertical axis were 10.2 % and 12.5 %, respectively. In the microstructure of the sintered metallic glass and oxide glass composite lattice, the metallic glass particles dispersed into the oxide glass matrix. The metallic glass was verified not to be crystallized through the dewaxing and sintering heat treatment by the XRD. In the transmission spectrum, the band gap can be formed at the frequency range from 0.19 to 1.02 THz.

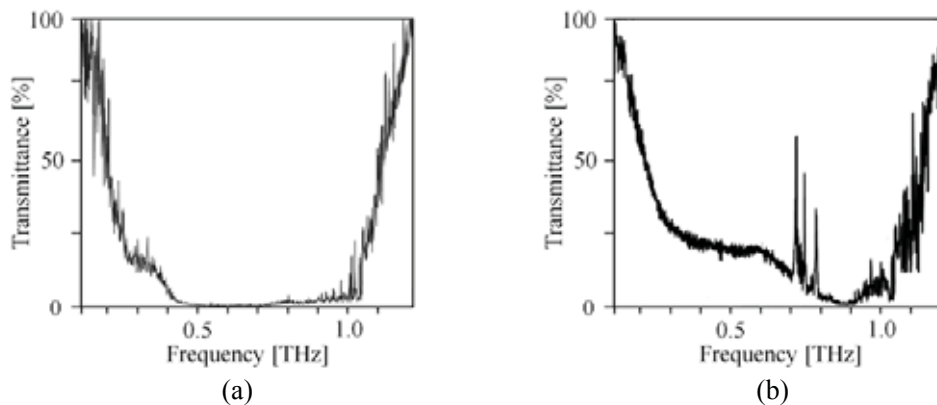


Fig. 2 Transmission spectra of terahertz waves through the photonic crystals composed of the oxide and metallic glass lattices with the diamond structure. An electromagnetic band gap is formed in the spectrum by Bragg diffraction in the photonic crystal (a). Localized modes were formed in the band gap (b). The selected wavelengths can resonate with in the defect cavity and transmit the photonic crystal.

4. Conclusions

Through careful optimizations of process parameters regarding stereolithography, micrometer order diamond lattices composed of acrylic resin including metallic glass and oxide glass particles at 17 % and 23 % in volume ratios could be fabricated. The metallic glass and oxide glass composite crystals were obtained by dewaxing and sintering processes. The metallic glass was not crystallized through the heat treatment. The sintered photonic crystals formed an electromagnetic band gap in a terahertz frequency range from 0.19 to 1.02 THz. The artificial crystals with micro through holes are expected to resonate the terahertz waves in wavelengths comparable to the hole diameters, and to be applied to real time sensing of harmful substances in aqueous phase environments.

References

- [1] K. Ohtaka, Energy Band of Photons and Low-Energy Photon Diffraction, *Phys. Rev. B*, 19 (1979) 5057-67.
- [2] D. Clery, Brainstorming Their Way to an Imaging Revolution, *Science*, 297 (2002) 761-3.
- [3] S. Kiriwara, 3D Material Tectonics for Electromagnetic Wave Control, *Ferroelectrics*, 387 (2008) 102-11.

Femtosecond Laser Induced Nanojoining

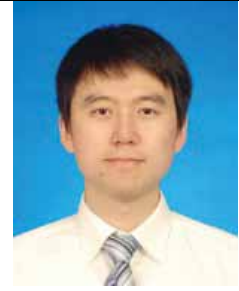
Lei Liu^{1,2}, Luchan Lin¹, Daozhi Shen¹, Hailin Bai¹, Guisheng Zou¹, and Y. Norman Zhou³

¹Department of Mechanical Engineering, Tsinghua University, Beijing, , China

²The State Key Laboratory of Tribology, Tsinghua University, Beijing, China

³Department of Mechanical & Mechatronics Engineering, University of Waterloo, Waterloo, Canada,

Email: liulei@tsinghua.edu.cn



Keywords: Femtosecond laser, nanojoining, Nanowire, Nanoparticle

1. Introduction

Further down the road of miniaturization to nanoscale, there is an emerging need to join nanoobjects to form nanoscale devices and systems.[1, 2] Nanoparticles are regarded as important parts of nanoscale devices, which make joining nanoparticles necessary as a basic integration process in nanoscale products.[3] The nanojoining methods include laser beam[4, 5], electron beam[6], soldering[3], sintering[7], resistance welding[8] etc. Femtosecond laser is a promising tool for nanojoining because of its precise controlling of heat input, outstanding focusing ability, non-linear absorption and ultra-high peak power. In this work, femtosecond laser induced nanojoining is reviewed and the future trend is discussed.

2. Experiments

A Ti-sapphire laser system (Coherent Inc) was operated to generate 50 fs polarized laser pulses at repetition rate of 1 kHz and 800 nm with Gaussian beam distribution. A mechanical shutter was used to select the number of pulses per illumination. The femtosecond laser was used to join both nanowires and nanoparticles. A pure Pt target was put in ethanol solution and the femtosecond laser was focused on the Pt target by a lens with 13cm focal length. Pt nanoparticles were ablated accompanied by the presence of a plasma plume on the Pt surface. Ablation of Ag was conducted after ablation of Pt in the same solution. Due the melting point of Ag was lower than Pt, the ablated Ag nanoparticles was used as filler metal to brazing Pt nanoparticles. The silver nanowires were prepared in water in a seeded polyol solution with PVP as a structure directing reagent as previously described.[9] Electron diffraction pattern confirmed the nanowires are fivefold twinned with pentagonal cross section, and the axially oriented along the <100> direction. TEM images showed that organic shells covering on the surface of as-synthesized Ag nanowires have a 2.5-5nm thickness. The Ag nanowires solution was drop-cast onto single crystal silicon and amorphous carbon coated copper grid for femtosecond laser illumination.

3. Results and Discussion

Figure 1 shows the brazed Pt nanoparticles by Ag nano filler metal. The size of Ag nano particles was less than 10nm, which had the melting point in the range of 373-573K.[10] Therefore, the melting temperature of Ag was much lower than that of Pt. The Ag nanoparticles was used as filler metal to braze Pt nano particles. The small radius fillets of Ag nanoparticles indicates the Ag nanoparticles melted during laser radiation. It is believed that the Brownian motion is important to the nano brazing process. The collision between nanoparticles induced the contacts of nanoparticles.

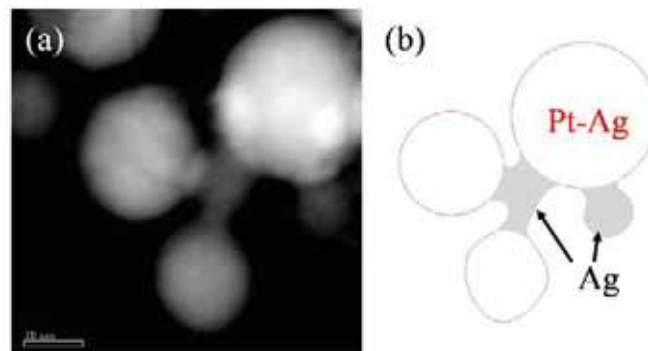


Figure 1 STEM image of nano brazed joint by femtosecond laser irradiation. The nano Ag cluster was the filler metal and Pt-Ag nanoalloy was the base metal.[3]

Figure 2 shows the morphology of joined nanowires. Figure 2(a) was SEM image of the joined nanowires. It shows that the crossed nanowires were welded together by femtosecond laser. Figure 2(b) shows the TEM image of a joint. The selected area diffraction pattern on the nanowire indicated the nanowire kept its original five twinned pentagonal structure. Our previous results indicated that femtosecond laser irradiation can induce highly localized heat in nanowire, especially at the ends of nanowire and the crossed region. Therefore, the localized heat can melt the joined area and keep the rest of the nanowire stay its original shape and structure.

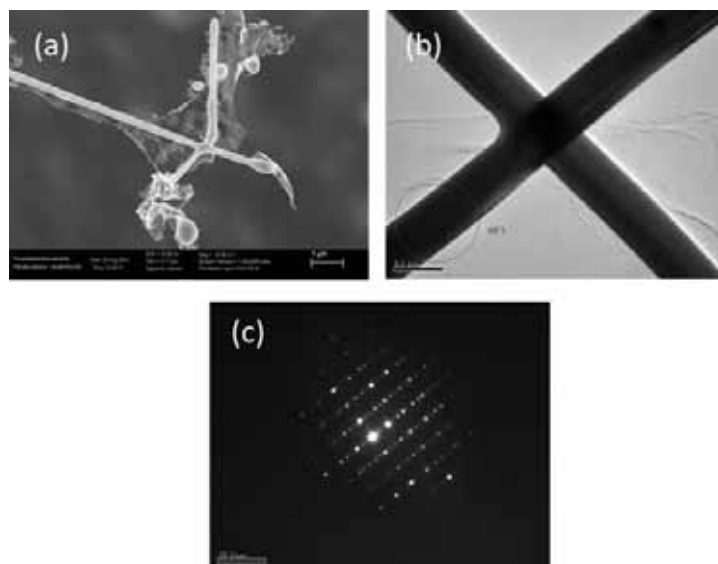


Figure 2 SEM (a) and TEM (b) pictures of welded Ag nanowires by femtosecond laser. The diffraction pattern (c) was selected area diffraction of (b)

4. Conclusions

Femtosecond laser radiation has been shown to be a useful tool for nanojoining of nanoparticles and nanowires. The femtosecond laser can precisely control the heat input which is very important to nanojoining. Femtosecond laser induced nanojoining is also highly related to the plasmonic thermal effect, due to the localized plasmon focusing the laser energy to a specific area and induce local melting.

Acknowledgement

This work was supported by National Natural Science Foundation of China (Grant No. 51375261, 51075232), by The Natural Science Foundation of Beijing (Grant No. 3132020), by the Specialized Research Fund for Doctoral Program of Higher Education (Grant No.20130002110009) and by Tsinghua University Initiative Scientific Research Program (Grant No.2010THZ 02-1, 2013Z02-1).

References

- [1] S. Guo, "The creation of nanojunctions", *Nanoscale*, 2(12), 2521-2529(2010).
- [2] Y. Zhou and A. Hu, "Microjoining and nanojoining", *The Open Surface Science Journal*, 3(32-41)(2008).
- [3] L. Liu, H. Huang, A. Hu, G. Zou, L. Quintino and Y. Zhou, "Nano Brazing of Pt-Ag Nanoparticles under Femtosecond Laser Irradiation", *Nano-Micro Letters*, 5(2), 2013).
- [4] S. J. Kim and D.-J. Jang, "Laser-induced nanowelding of gold nanoparticles", *Applied Physics Letters*, 86(3), 033112(2005).
- [5] L. Liu, P. Peng, A. Hu, G. Zou, W. Duley and Y. N. Zhou, "Highly localized heat generation by femtosecond laser induced plasmon excitation in Ag nanowires", *Applied Physics Letters*, 102(7), 073107(2013).
- [6] I. Jang, S. B. Sinnott, D. Danailov and P. Keblinski, "Molecular dynamics simulation study of carbon nanotube welding under electron beam irradiation", *Nano Letters*, 4(1), 109-114(2004).
- [7] E. Ide, S. Angata, A. Hirose and K. F. Kobayashi, "Metal-metal bonding process using Ag metallo-organic nanoparticles", *Acta Materialia*, 53(8), 2385-2393(2005).
- [8] H. Tohmyoh, T. Imaizumi, H. Hayashi and M. Saka, "Welding of Pt nanowires by Joule heating", *Scripta Materialia*, 57(10), 953-956(2007).
- [9] P. Peng, L. Liu, A. P. Gerlich, A. Hu and Y. N. Zhou, "Self - Oriented Nanojoining of Silver Nanowires via Surface Selective Activation", *Particle & Particle Systems Characterization*, 30(5), 420-426(2013).
- [10] A. Hu, J. Y. Guo, H. Alarifi, G. Patane, Y. Zhou, G. Compagnini and C. X. Xu, "Low temperature sintering of Ag nanoparticles for flexible electronics packaging", *Applied Physics Letters*, 97(153117)(2010).

Inspection of micro defects using bacterial cells

Telmo G. Santos¹, R.M. Miranda¹, L. Quintino² and Carla C.C.R. de Carvalho³

¹UNIDEMI, Departamento de Engenharia Mecânica e Industrial, Faculdade de Ciências e Tecnologia, Universidade Nova de Lisboa, 2829-516 Caparica, Portugal.

²IDMEC, Instituto Superior Técnico, Universidade de Lisboa, Av. Rovisco Pais, 1049-001 Lisboa, Portugal.

³Institute of Biotechnology and Bioengineering, Centre for Biological and Chemical Engineering, Department of Bioengineering, Instituto Superior Técnico, Universidade de Lisboa, Av. Rovisco Pais, 1049-001 Lisboa, Portugal

Email: telmo.santos@fct.unl.pt



Keywords: Inspection, Micro surface defects, bacterial cells.

1. Introduction

Microfabrication has increased very rapidly at scientific, technological and industrial levels. However, this evolution has not been followed by a parallel development of expedite characterization methods, including non-destructive techniques (NDT) and there is no capability to detect micro defects in microfabrication components with the reliability required for integrity assessment. This problem limits quality control of micromanufactured parts, as defects can seriously compromise their in-service performance. In microfabrication, defects have a dimension without parallel to defects produced by other manufacturing techniques. Typical defects in microfabrication are porosities and surface micro cracks with dimensions in the range of 5 to 10 micron, but can be below in naojoining and microjoining. [1,2].

Existing NDT techniques are not able to detect and identify such small size defects since they were developed for requirements completely out of the actual paradigm brought up by the microfabrication. The main problem when to detect defects in microfabrication is the poor sensibility of NDT for such small dimensions. According to the criteria of Probability of Detection (PoD), the limit of detection is too high for typical microfabrication defects. Although there are advanced techniques to detect submicron defects based on ultrasounds or eddy currents, these are not adaptable to micro components, since the probes cannot be coupled to the parts under inspection.

This paper presents a new concept of NDT based on the use of bacterial cells in a similar way as the one used in the dye penetrant technique. It consists of taking advantage of the bacterial cells' dimension, mobility, fluorescence and adherence to identify defects in micro manufactured components, including at the nano and micro scales. In fact bacterial cells adhere to surfaces irregularities such as roughness, cracks, voids, cleavages and low pressure points [3].

2. Experiments

Validation of the technique was performed on stainless steel AISI 304L and aluminium alloy AA1100. Artificial defects were produced using a micro hardness indenter with different loads to make Vickers indentations of different dimensions. A sample matrix with 3 lines containing 4 defects each was produced, with defects ranging between 25.5-2.6 and 19.5-1.8 micron in depth for aluminium and steel, respectively.

The bacterial cells used were strain *Rhodococcus erythropolis* DCL14 with 0.9-1.5 μm in length, stained green under fluorescent light by addition of the dye SYTO[®]9 [3]. A suspension of 1g/L of *R. erythropolis* cells was poured over the artificial defects and surrounding surface and kept for 5 minutes. After this, the excess liquid was mechanically removed in a similar procedure as in the dye penetrant technique and the surface was observed by fluorescence microscopy using an Olympus CX40 microscope.

3. Results and Discussion

The suspension of bacterial cells proved adequate to reveal very small defects in the materials under study. Figures 1 and 2 depict the defects where the bacterial cells are located allowing the identification of the smallest defect (identified by a red circle) in each material. It was verified that the bacteria are retained predominantly inside defects, and not on the surface. The technique thus allows the assessment of the integrity of micromanufactured components with open defects on the surface.

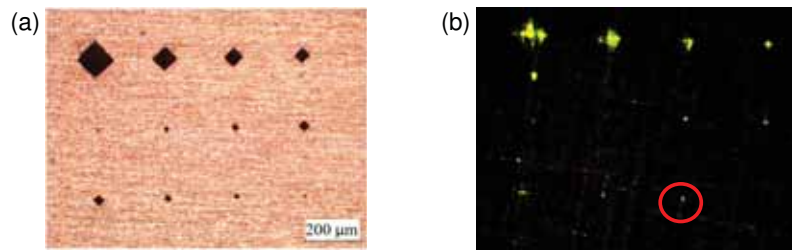


Fig. 1. Experimental results for AA1100 sample. (a) Matrix of defects. (b) Smallest defects detected (red circles) after 5 min penetration time.

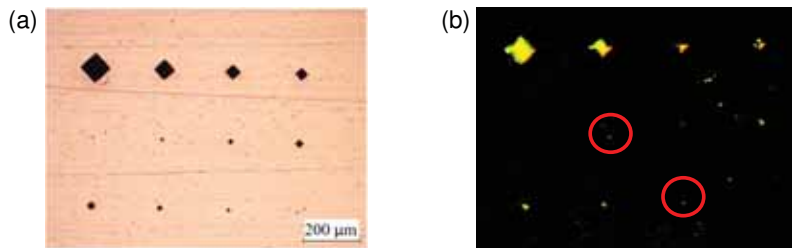


Fig. 2. Experimental results for AISI 304L sample. (a) Matrix of defects. (b) Smallest defects detected (red circles) after 5 min penetration time.

4. Conclusions

A micro defect identification and characterization technique based on bacterial cell was presented and experimentally validated. For the penetration time tested, a minimum defect size was detected for each material and these were 4.3 μm depth in aluminium, and 2.9 μm in steel. The technique was efficient in revealing very small defects in the materials under study. The technique can be therefore applied to inspect nano and micro components.

Acknowledgments

The authors would like to acknowledge Fundação para a Ciência e a Tecnologia (FCT) for funding the project "Defects Detection in Microfabrication With Bacterial Cells" – (MicroBac) (PTDC/EME-TME/118678/2010). TS and RM acknowledge Pest OE/EME/UI0667/2011. CCCRC thanks FCT for financial support ("Ciência2007" and "FCT Investigator" programs).

References

- [1] Sliker LJ, Kern MD, Schoen JA, Rentschler ME, "Surgical evaluation of a novel tethered robotic capsule endoscope using micro-patterned treads", *Surgical endoscopy and other interventional techniques*; 26, 2862-69 (2012)
- [2] Lockie k, Binns M, Fisher J, Jobbins B., "Assessment of the deformation of the bateman bipolar hip-prosthesis inner bearing due to moisture absorption and creep", *Injury-international journal of the care of the injured*, 23, 116-118 (1992).
- [3] Telmo G. Santos, R. M. Miranda, Carla C. C. R. de Carvalho, "A New NDT Technique Based on Bacterial Cells to Detect Micro Surface Defects", *NDT & E International*, 63, 43-49, (2014).

Transient thermal impedance of IGBT modules joined by lead-free solder and sintered nanosilver

M.Y. Wang¹, Y.H. Mei^{1,*}, and X. Li¹, G.Q. Lu^{1,2}

¹Tianjin Key Laboratory of Advanced Joining Technology, and School of Material Science and Engineering, Tianjin University, Tianjin, P.R. China

²Department of Material Science and Engineering, Virginia Tech, USA

*Corresponding author: yunhui@tju.edu.cn



Keywords: IGBT, Transient thermal impedance, Sintered nanosilver paste

1. Introduction

The junction temperature (T_j) within the Insulated Gate Bipolar Transistor (IGBT) module increases dramatically at high temperatures, which drives the need for thermal management since higher T_j is associated with reduced operating life. As the conventional methods of steady-state thermal resistance to evaluate the thermal performance can yield only the total value for the whole module without any information about the contributions of each component along the heat path [1], a transient thermal impedance measurement system is built using electrical method with gate-emitter voltage (V_{ge}) of IGBT as temperature-sensitive parameter (TSP) in this paper.

2. Experiments

Fig. 1 shows the structure diagram of the IGBT module and the transient thermal impedance measurement system. With the system, Z_{th} at heating time of t_h can be obtained as $Z_{th} = \frac{\Delta V_{ge}(t_h)}{K \times P}$ [1, 2], where the K -factor indicating the coefficient between V_{ge} and T_j is 10.3 mV/°C. Fig. 2 shows Z_{th} of each component within the IGBT module. The high consistency between the measured Z_{th} and values supplied by IGBT (Infineon IKP20N60T) datasheet and samples repeatability error less than 0.87% verified the high accuracy of the system.

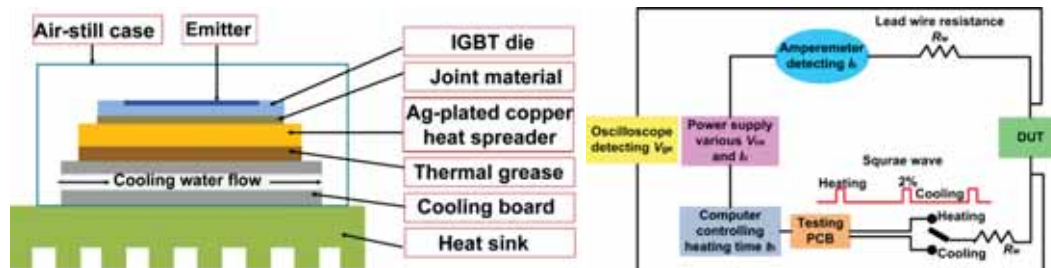


Fig. 1. The structure diagram of the IGBT module and the transient thermal impedance measurement system.

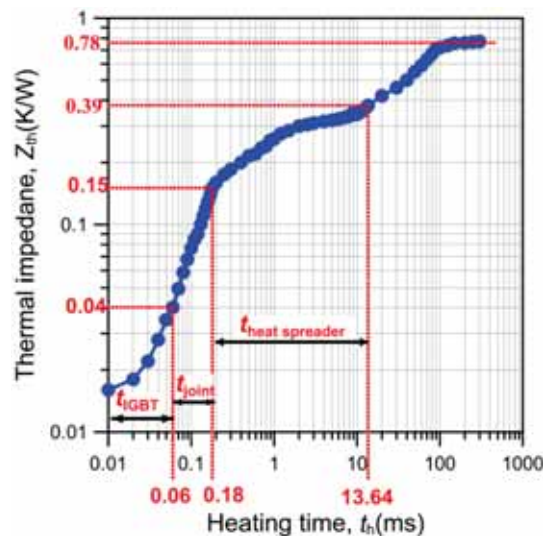


Fig. 2. Thermal impedance of each component measured based on the heating time constant (t).

3. Results and Discussion

Fig. 3 shows Z_{th} measured under different heating voltage (V_{ce}) and heating current (I_{ch}) [3]. Z_{th} increases about 0.04 K/W per volt as V_{ce} increases from 4 V to 8 V. Z_{th} increases with the larger heating power (P). When at the same P , higher I_{ch} and lower V_{ce} lead to smaller Z_{th} , and vice versa. We believe that high V_{ce} elevates the peak temperature and causes serious thermal non-uniformity, resulting in smaller active area through heat flux [3]. Fig. 4 shows Z_{th} of IGBT modules jointed by different materials. Z_{th} of modules jointed by sintered nanosilver paste is 12% lower than the counterpart of solders, resulting from its high thermal conductivity and low interfacial thermal resistance.

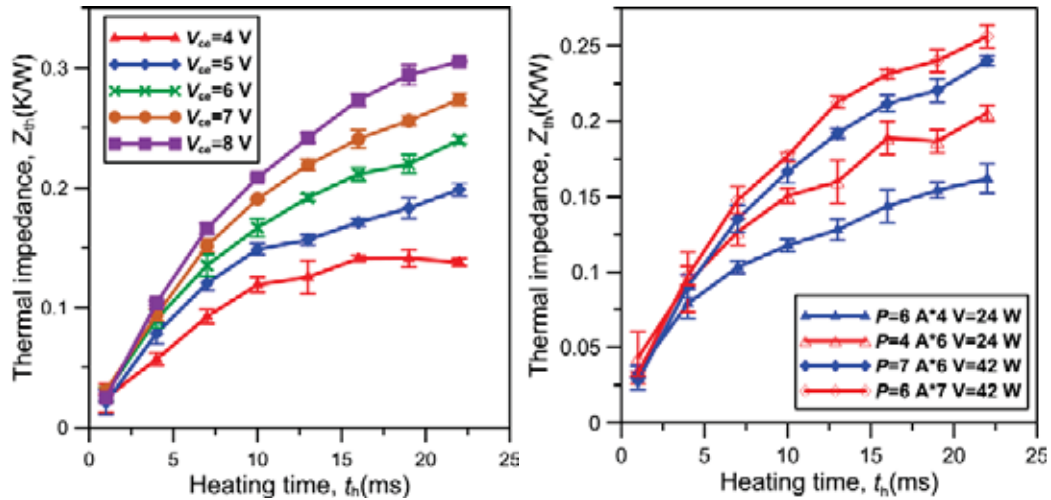


Fig. 3. Thermal impedance measured at (a) heating current $I_{ch}=6$ A and heating voltage V_{ce} from 4 V to 8 V, (b) heating power $P=24$ W and $P=42$ W with different combinations of V_{ce} and I_{ch} .

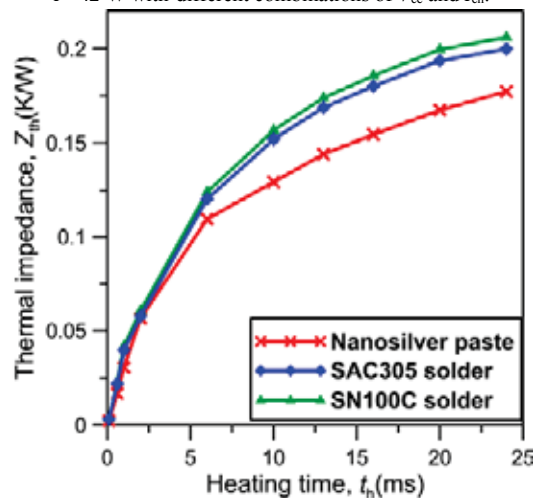


Fig. 4. Thermal impedance of IGBT modules jointed by sintered nanosilver paste and lead-free solders.

Conclusions

To evaluate the thermal performance of each component within IGBT modules, an accurate Z_{th} measurement system is built. Z_{th} increased with dissipated P and V_{ce} . Z_{th} of modules jointed by sintered nanosilver paste 12% larger than the counterpart of solders revealed that the nanosilver paste had superior thermal performance, which made it a promising lead-free joint material solution for packaging of semiconductor devices for high-power density or high-temperature applications.

References

- [1] X. Cao, T. Wang, and G.Q. Lu, *et al.*, "Characterization of lead-free solder and sintered nano-silver die-attach layers using thermal impedance," *IEEE Trans. Compon. Packag. Tech.*, 1(4), 495-501 (2011).
- [2] Y.H. Mei, T. Wang, and X. Cao *et al.*, "Transient thermal impedance measurements on low-temperature-sintered nanoscale silver joints," *J. Electron. Mater.*, 41(11), 3152-3160 (2012).
- [3] J.W. Sofia, "Fundamentals of thermal resistance measurement," *Analysis Tech*, 11, (1995).

Stability and Melting of FCC Truncated Octahedral Ag Nanoparticles by Molecular Dynamics Simulation

H. Alarifi¹, M. Atiş², C. Özdoğan³, A. Hu⁴, M. Yavuz⁵, and Y. Zhou⁵

¹King Abdulaziz City for Science and Technology, P.O. Box 6086, Riyadh 11442, Saudi Arabia.

²Kayseri Vocational School, Department of Electricity and Energy, Erciyes University, 38039 Kayseri, Turkey.

³Department of Materials Science and Engineering, Cankaya University, 06810, Ankara, Turkey.

⁴Department of Mechanical, Aerospace and Biomedical Engineering, University of Tennessee Knoxville, 1512 Middle Drive, Knoxville, TN 37996-2210, USA.

⁵Department of Mechanical and Mechatronics Engineering, Centre for Advanced Material Joining, University of Waterloo, 200 University Avenue West, Waterloo, Ontario N2L 3G1, Canada.

halarifi@kacst.edu.sa



Keywords: Ag Nanoparticles, FCC Truncated Octahedra, Melting, Solid Phases, MD Simulation.

1. Introduction

Ag nanoparticles (NPs) have been successfully used in bonding of flexible electronics [1] and as a replacement of lead based solders [2]. Fundamental understanding of the thermal properties of the Ag NPs could improve the bonding process. Metallic NPs have lower melting points (T_m) than bulk materials and could exist in different solid configurations [3]. The stable solid phase is known to be formed based on the minimization of the surface energy and the internal strain of the NP. High curvature of very small NPs increases the surface energy of the particle. In general, icosahedral configuration is characterized by high internal strain and low surface energy, makes it a favorable structure for the smallest NPs. Decahedral configuration is stable for intermediate sizes of NPs due to its higher surface energy and lower internal strain. Large NPs mostly exist in FCC truncated octahedral configuration, which is characterized by low internal strain and high surface energy. However, metallic NPs may not follow these rules due to possible kinetic effects playing a role in formation of the stable solid configuration. Solid to solid phase transitions has been observed during heating of NPs and may have been driven by thermal and kinetic effects [3]. In this work, molecular dynamics (MD) simulation based on embedded atom method (EAM) [4] has been applied to determine melting points (T_m) of FCC truncated octahedral Ag NPs in size range of 1.2 to 20 nm and to determine their solid phase stability. The melted NPs were cooled down to room temperature to find the freezing points and the frozen solid structure toward drawing a phase map of stable solid phases at each size and temperature.

2. Computational Methods

The performed simulation was based on voter-chen version [5] of embedded atom method (EAM). The atoms in each NP were initially constructed based on FCC truncated octahedral configuration shown in Fig. 1. Each NP was relaxed at 300 K, heated periodically up to 1675 K, and then cooled down with the same rate to 300 K (room temperature). The holding time at each temperature was 20 picoseconds with a step size of 2 femtoseconds. The temperature of the NP was calculated based on equation (1)

$$T = \frac{2\langle E_k \rangle}{k(3N - 6)} \quad [1]$$

where E_k is the total kinetic energy of all atoms in the NP, k is Boltzmann constant, and N is the total number of atoms.

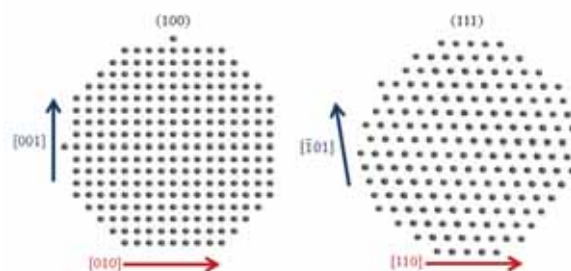


Fig. 1. Initial atomic arrangement of the 4 nm Ag particles showing (100) and (111) facets of the truncated octahedral configuration [3].

3. Results and Discussion

Fig. 2 shows the atomic arrangement and average PE values during heating and cooling of 1 nm Ag particle. Point A is the initial constructed FCC octahedral configuration. The NP passed through dynamic coexistence melting (DCM) during heating to point I, which means that the NP transits between the solid icosahedral structure at points C,E,F,H, and I and the quasi-liquid phase at points B, D, and J. The amorphous configuration is identified as quasi-liquid since the NP diameter is less than the minimum thickness of liquid Ag (1.8 nm) [6]. The quasi-liquid state shows higher average PE values than the icosahedral structure. At temperatures higher than Point I, The NP remained in the quasi-liquid-state. Thus, Point I can be considered as the T_m of the NP. During the cooling cycle, the NP froze into an icosahedral configuration at point M, which is lower than T_m showing the thermal hysteresis between melting and freezing. The NP remained into the icosahedral structure as NP cooled down to room temperature at point N.

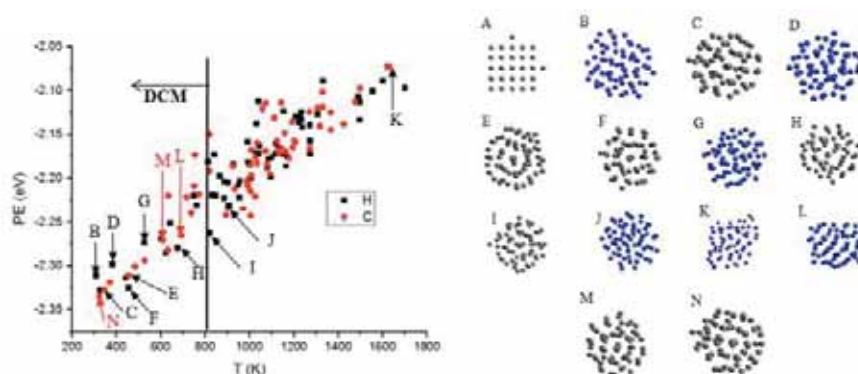


Fig. 2. (a) Potential energy (PE) values during heating and cooling cycles of 1 nm (65 Atoms) Ag particle. The vertical line shows the border between DCM and the quasi-liquid phase (b) Atomic arrangement of the particle at different temperatures shown by letters on the PE curve. Atoms are represented by dots [3].

Simulation of 1.2 nm and larger NPs has not shown DCM. The 1.2 nm particle remained stable below 385 K and then transformed to the icosahedral configuration. Larger NPs remained stable in the FCC truncated octahedral during heating below the melting point of the NP. The melting points increased as the NP size of the particle increased and reached the bulk T_m at 20 nm particle. Thermal hysteresis between melting and freezing occurred for all sizes of NPs. The 2.8 nm particle froze into decahedral configuration showing the stable configuration while smaller NP froze into the icosahedral structure. Larger NPs froze into different solid configurations that are still under investigation.

4. Conclusions

Based on freezing of liquid droplets, the most favorable structure for 2.8 nm Ag NP is decahedra. Smaller NPs froze into icosahedral structure while larger NPs showed different morphologies that are still under investigation. FCC truncated octahedral NPs of 1 nm is not stable at room temperature while the 1.2 nm is only stable below 385 K. Larger FCC truncated octahedral NPs are stable below T_m of the particle. Thermal hysteresis between melting and freezing were observed for all simulated sizes. This work aims toward constructing a phase map of Ag NPs at different sizes and temperatures.

References

- [1] A. Hu, J. Y. Guo, H. Alarifi, G. Patane, Y. Zhou, G. Compagnini, and C. X. Xu, "Low temperature sintering of Ag nanoparticles for flexible electronics packaging", *App. Phys. Lett.*, 97(15), 153117-1-3 (2010).
- [2] H. Alarifi, A. Hu, M. Yavuz, and Y. Zhou, "Silver Nanoparticle Paste for Low-Temperature Bonding of Copper", *J. Electron. Mater.*, 40(6), 1394-1402 (2011).
- [3] H. A. Alarifi, "Ag Nanoparticles and their Application in Low-Temperature Bonding of Cu", Doctoral dissertation, University of Waterloo (2013).
- [4] S. M. Foiles, M. I. Baskes, and M. S. Daw, "Embedded-Atom-Method Functions for the FCC Metals Cu, Ag, Au, Ni, Pd, Pt and their alloys", *Phys. Rev. B*, 33(12), 7983-7991 (1986).
- [5] A. F. Voter, Los Alamos Unclassified Technical Report LA-UR 93-3901(1993).
- [6] H. A. Alarifi, M. Atis, C. Ozdogan, A. Hu, M. Yavuz, and Y. Zhou "Determination of Complete Melting and Surface Premelting Points of Silver Nanoparticles by Molecular Dynamics Simulation", *J. Phys. Chem. C*, 117(23), 12289-12298 (2013).

Laser assisted low temperature hermetic sealing of optoelectronics devices

**R. JoseJames¹, E. Rutz¹, T. Stadelmann¹, S. Berchtold¹, M. Lützelshwab¹,
Ch. Bosshard¹, M. Epitoux², A. Hold² and C. Vélez²**

¹CSEM SA, Alpnach Dorf, Switzerland

²Exalos AG, Schlieren, Switzerland

Email: rony.josejames@csem.ch



Keywords: Hermetic sealing, low temperature, vacuum sealing, leak testing

1. Introduction

Miniature sensors, MEMS and electronic systems often need to be hermetically sealed for various types of applications. Specifically, hermetic sealing is very important for applications demanding long term reliability or a specific atmosphere. In these applications a very high level of hermeticity is required to avoid moisture ingress or a specific atmosphere. In many cases, the hermetic sealing needs to be done at low temperatures (<150°C). This underlines the importance of different localized sealing techniques such as resistive welding or laser based sealing. Here we present the work on hermetic vacuum sealing of two different optoelectronic systems.

The first one is a swept source produced by Exalos AG. High-speed wavelength-swept laser technology offers applications in optical coherence tomography (OCT), bio-chemical spectroscopy, and fiber-optic sensing [1]. A low vacuum level is advantageous for swept sources as it increases the deflection of the integrated MEMS mirror by helping to overcome air drag and reduce air damping (Figure 1). This enables the very fast MEMS devices (sweeping up to 200 kHz) to have a deflection angle similar to slower MEMS devices. The vacuum also reduces the operating voltage, which in turn reduces power consumption. [2]

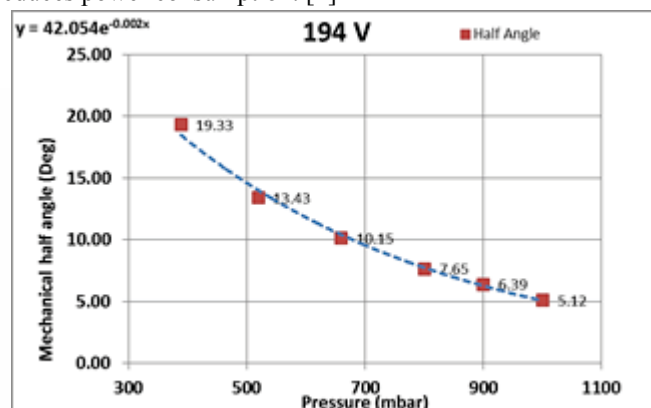
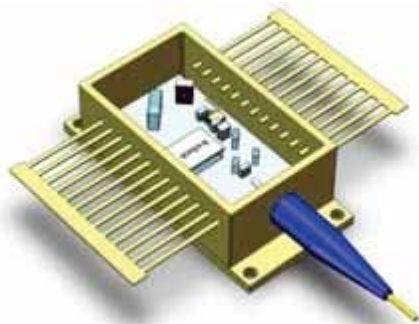


Figure 1 : Model of EXALOS external cavity swept laser (ECSL) (left); Change in deflection angle for different vacuum level measured for a MEMS mirror integrated inside

The second device is a Rubidium based atomic clock. Already a medium sized vacuum atmosphere will enable to reduce the power consumption of the atomic clock by more than 50 % (Figure 2). The vacuum helps to reduce thermal losses due to thermal convection from the temperature controlled elements such as VCSEL and the atomic cell used in the device. [3]

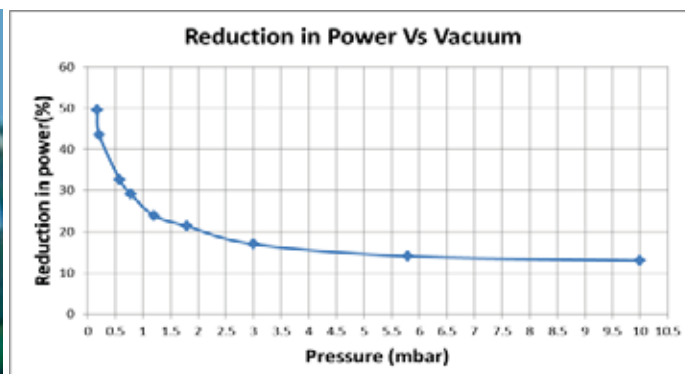


Figure 2 : Physics package of the Swiss Miniature Atomic Clock (left); Reduction in power required with vacuum (right)

2. Experiments

Both these systems were vacuum sealed with the same technology. A combination of resistance welding/soldering and laser soldering was used for sealing. The packages are sealed in two process steps. In a

first step, a lid with a 0.5 mm diameter hole is resistively welded/soldered on top of the package, and in a second process step, after a bake-out, this hole in the lid is sealed using laser soldering in vacuum (Figure 3). Resistive soldering or resistive welding is chosen based on the materials to be welding and the stress induced. The leak tightness after resistive welding is measured with a Helium leak detector using the spraying method (Figure 3).



Figure 3 : Combination of sealing using resistive welding and laser soldering (left); Helium spraying method for hermeticity check (right)

3. Results and Discussion

The results reported here are for swept sources sealed at 300 mbar vacuum. The process using a combination of resistive welding and laser soldering was found to be stable and repeatable. Helium leak tests were done on 13 resistively welded samples. All of them were leak tight with a hermeticity of less than $3E-10$ mbar-l/s. A destructive test was used to check the hermeticity. Here a hole was drilled into the bottom side of the package and the Helium spraying method was applied. This method showed that all the samples were hermetic to the same level as measured after the resistive welding. This confirmed the leak tightness of the laser soldering with a high yield. Leak testing using backfilling technique was also used to confirm the leak tightness of the laser soldered seal. An absolute pressure sensor was mounted inside the package to check the leak tightness. The pressure inside the package was measured for 3 months. The change in pressure measured was a maximum of 0.1 mbar at 300 mbar initial vacuum level. A cross section of the solder sealing can be seen in Figure 4. The solder wetted very well on the lid, the grains did not visibly grow during the process and the nickel layer was not dissolved (from an EDX measurement), confirming a good soldering process. Thermal cycling reliability tests ($-40^{\circ}C$ to $+85^{\circ}C$) against the GR-468-CORE standard were carried out on 6 samples. 3 samples were tested for 75 cycles and 3 samples were tested for 150 cycles. All of the tested samples showed a leak rate better than $3E-10$ mbar-l/s.

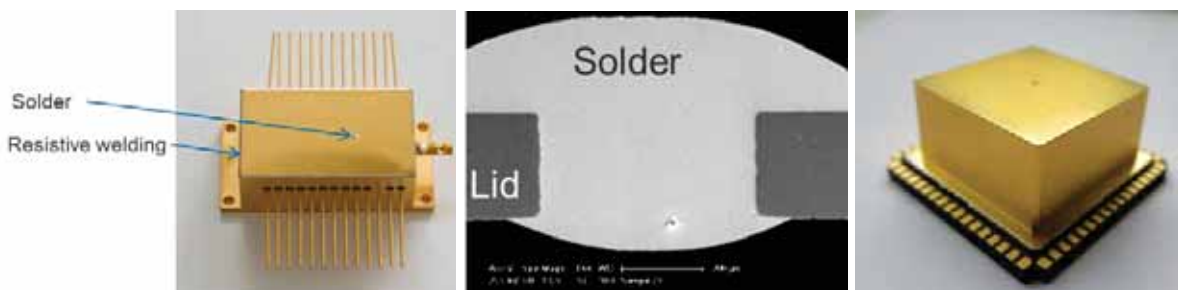


Figure 4 : A sample sealed using resistive welding and laser soldering (left); cross section of a laser soldered area (middle); resistive soldered ceramic package used for atomic clock sealing (right) with a leak rate of $<3E-10$ mbar-l/s

4. Conclusions

The combination of resistive welding and laser soldering worked well with a good yield and vacuum tight samples were achieved with hermeticity at least one order of magnitude better than needed. A significant increase in the bandwidth of the swept sources was seen for the vacuum packaged samples. Standard thermal cycling tests confirmed a reliable process. It was shown that butterfly packages and HTCC based ceramic packages can be low temperature vacuum sealed with this approach.

References

- [1] S. R. Chinn, E. A. Swanson, and J. G. Fujimoto, "Optical coherence tomography using a frequency tunable optical source," *Opt. Lett.* V.22, pp.340-342 (1997)
- [2] R. Jose James, E. Innerhofer, T. Stadelmann, et. al "Laser based vacuum hermetic sealing", *Smart System Integration*, Vienna (Austria), March 2014
- [3] R. Jose James, J. Pierer, Ch. Bosshard, et. al, "Miniature Atomic Clocks," *Smart System Integration*, Zurich (Switzerland), March 2012

Numerical Analysis of Microbubble Behavior and Microporosity Formation in Laser Beam Welds of Aluminium Alloy

**H. Mori¹, Q. Zhou¹, K. Koyama¹, F. Miyasaka², Y. Murakami³, Y. Kawahito³,
M. Mizutani³ and S. Katayama³**

¹Osaka University, Graduate School of Eng., Department of Management of Industry & Technology,
2-1 Yamadaoka, Suita, Osaka, 565-0871, Japan

²Osaka Univ., Department of Adaptive Machine Systems, 2-1 Yamadaoka, Suita, Osaka, 565-0871, Japan

³Osaka Univ., Joining and Welding Research Institute, 11-1 Mihogaoka, Ibaraki, Osaka, 567-0047, Japan

Email: mori@mit.eng.osaka-u.ac.jp



Keywords: Aluminium, Laser beam welding, Microporosity, Numerical analysis, Microfocused X-ray transmission in-situ observation

1. Introduction

Laser micro welding is one of the useful methods for micro-joining in manufacturing processes of MEMS and/or other micro-size devices required high production quality, automation potential and flexibility. But, one of the significant obstacles to overcome for practical applications of laser micro welding is prevention of weld defects such as porosity, hot cracking, and so on [1]. However, the researches about these micro-size defects in micro welded joint were not sufficiently conducted. In addition, at present, it's very difficult even to observe microbubbles and cracking behavior during laser micro welding process owing to shortage of spatial resolution of high speed cameras for micro-scale in-situ observation. That is, the mechanisms of these micro-size defects have not been clarified yet. Therefore, as the first stage, in order to clarify the mechanism of microporosity in weld metal of laser beam welding (LBW) process and suggest proper welding conditions without any defects, numerical analysis based on fluid dynamic theories and in-situ observation using X-ray transmission real-time imaging system were conducted in this study.

2. Numerical models

To simulate the motion of bubbles, which cause in porosity, in the molten metal during LBW, the numerical model based on the fundamental fluid analysis equations, such as equations of continuity, Navier-Stokes equations and thermodynamic energy equations has been used to establish the calculation model for dynamic flow of molten aluminium in weld metal of LBW. In addition, to calculate the surface of molten metal, the CIP method (Cubic Interpolation Profile scheme) [2] was adopted for advection calculation of each physical quantity. The temperature recovery method using the VOF (Volume of Fluid) method [3] was used as a handling technique to determine the free surface between molten aluminium and air interface.

3. Experiments

A1050 aluminum alloy was used as the material in this study. The size of specimen is $100^L \times 30^W \times 5^T$ [mm]. Laser beam welding (LBW) is conducted by a fiber laser with maximum power of 10kW. LBW conditions are as follows; (1) in the case of spot LBW, the power was 10kW, irradiation time was 100ms, (2) in the case of LBW, the power was 5kW, welding velocity was 4m/min, in both cases, focal point was set on the surface of specimens, and Ar was used as a shielding gas. In addition, Sn was adopted as the tracer to clarify the shape of molten pool and bubbles formed in weld metal. To understand the molten aluminium flow and microbubble behavior in weld metal during LBW process, the X-ray transmission real-time imaging system, which is developed by Prof. Katayama's research group in 2000 [4], was used for the in-situ observation for keyhole and bubbles formed and dynamic flows occurred in weld metal of LBW.

3. Results and Discussion

The behaviour of keyhole and microbubbles formation during LBW process was simulated by the developed analysis model previously described. Figure 1 shows the cross sectional view of calculated LBW welds and actual cross sectional image of spot welds obtained by the imaging system. A keyhole was formed due to lineal energy, which is corresponding to laser irradiation, put into the substrate, as demonstrated in (a). In addition,

microbubbles were recognized in the middle of weld metal after solidification, as indicated in (b). On the contrary, the actual shape of LBW's weld bead was nail-head type, even though a keyhole had been formed in the welds. Analyses results of in-situ observation for dynamic flows of molten aluminium during LBW process were demonstrated in Fig. 2. In-situ observation to chase the movement of microbubbles in weld metal revealed that two kinds of major dynamic flows occur inside the weld metal of aluminium with a keyhole in LBW. That is, one is the relatively static flow to the bottom of weld bead, the other is intense flows blowing off from a keyhole to the upper part. In this study, numerical analysis for the flow to the bottom of weld bead was conducted. From the calculation, it was clarified that, in some case, microbubble might be remained at the bottom of weld metal in the keyhole type welding of LBW.

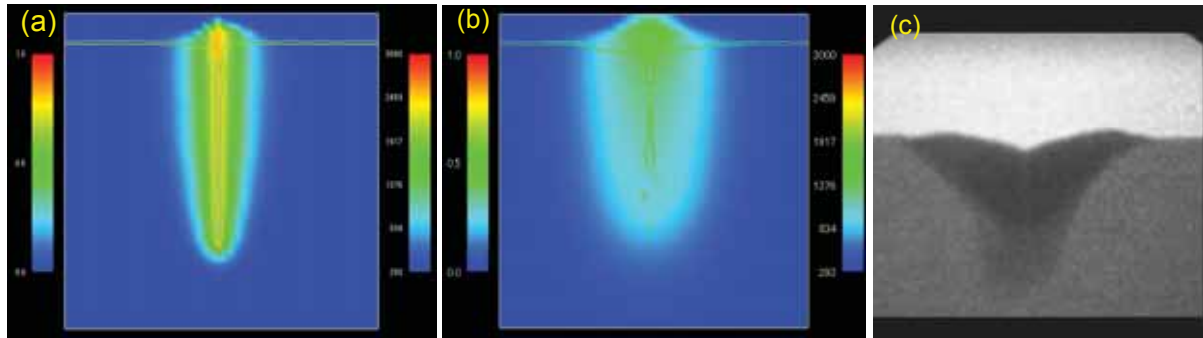


Fig. 1 Cross sectional view of keyhole and porosity formed during laser beam welding for aluminium. (a) Calculation of keyhole formation, (b) Calculation of porosity formation, (c) In-situ observation.

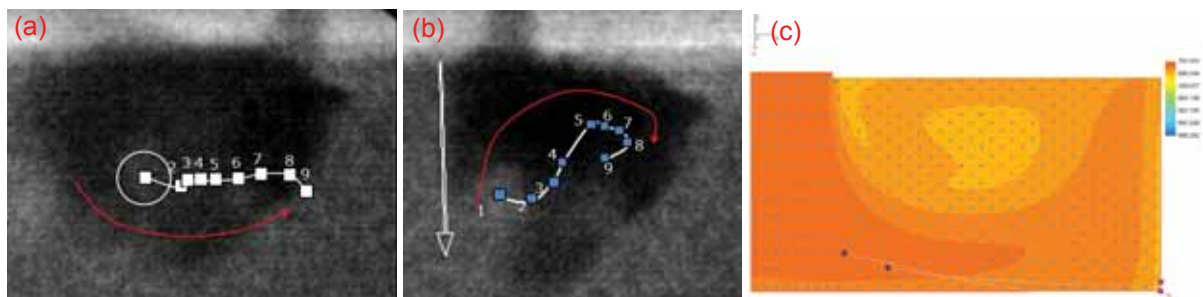


Fig. 2 Cross sectional view of molten pool during laser beam welding for aluminium. (a) In-situ observation of flow into a bottom, (b) In-situ observation of flow up to surface, (c) Calculation of bubble's behavior affected by the flow into a bottom.

4. Conclusions

To get a clear understanding of the formation mechanism of porosity in weld metal of aluminium during LBW, in-situ observation by X-ray transmission real-time imaging system and calculation of microbubble's behavior using the numerical model based on the fundamental fluid analysis equations was conducted in this study. From the observation, keyhole behavior was able to be clearly observed and two kinds of major dynamic flows were recognized in molten pool during LBW. On the basis of numerical analysis, keyhole behavior could be expressed and/or replicated. Microbubbles formed at the bottom of keyhole were maintained nearby the bottom due to the bottom side flow in molten aluminium. Therefore, these results suggest that one of the causes of porosity in LBW of aluminium is microbubbles maintained at the bottom due to molten metal flow.

References

- [1] Y.Kawahito, N.matsumoto, Y.Abe and S.Katayama, "Relationship of laser absorption to keyhole behavior in high power fiber laser welding of stainless steel and aluminum alloy", *Journal of Materials Processing Technology*, vol.211, 1563-1568 (2011).
- [2] F.Xiao, Y.Honma, and T.Kono, "A simple algebraic interface capturing scheme using hyperbolic tangent function", *International journal for numerical method in methods in fluids*, No.48, 1023-1040 (2005).
- [3] D.B.Kothe, W.J. Rider, S.J.Mosso, J.S.Brock and J.I.Hochstein "Volume tracking of interfaces having surface tension in two and three dimensions", *American Institute of Aeronautics and Astronautics (AIAA) Aerospace Sciences Meeting*, 96-120 (1996).
- [4] N.Seto, S.Katayama, A.Matsunawa, "High-speed Simultaneous Observation of Plasma and Keyhole Behavior during High Power CO₂ Laser Welding: Effect of Shielding Gas on Porosity Formation", *Journal of Laser Application*, vol.12, 245-250 (2000).

Effects of heat treatment on resistance microwelding joints of crossed nitinol wires

Yongde Huang^{1,2}, Andie Pequegnat², and Norman Zhou²

1 National Defense Key Disciplines Laboratory of Light Alloy Processing Science and Technology, Nanchang Hangkong University, Nanchang, 330063, China

2 Centre for Advanced Materials Joining, University of Waterloo, Waterloo, ON, N2L 3G1, Canada

Email: huangydhm@nchu.edu.cn



Keywords: Nitinol wire, Resistance microwelding, Heat treatment, Shape memory effect.

1. Introduction

The unconventional properties of Nitinol shape memory alloys (SMA), pseudoelasticity and shape memory effects, are what drives their use in a wide variety of applications such as medical devices, aerospace applications and micro-electrical-mechanical systems (MEMS) [1]. As the complexity of Nitinol-based devices continues to increase, other processing methods such as welding are required to help meet these expectations. The resistance microwelding (RMW) is more desired compared to other manufacturing processes due to the ease of use, low cost, and simply setup.

There are a few reported studies on resistance microwelding of crossed Nitinol wires that showed solid-state bonding in addition to good retention of base metal strength and intrinsic shape memory effect property [2]. Modifications to base metal transformation behaviours [2] have been shown to occur during the application of heat or mechanical deformation. Thus far, however, the damage of microstructures and mechanical properties of welded Nitinol to shape memory effects (SME) of weldment have not been examined in sufficient detail. Furthermore, weldments should be heat treated to recover SME or pseudoelasticity, before being put in use. Therefore, the heat treatment after welding must be thoroughly understood in order to refine the protocol for achieving functional welds. The current study has examined the effects of heat treatment on RMW joints of crossed Nitinol wires.

2. Experiments

Commercially available 0.410 mm diameter cold working Nitinol wires (Memry Corp., USA) were used in this study. The material's nominal composition comprised 55.8wt% Ni with the balanced Ti. The RMW system consisted of a MacGregor DC4000P DC power supply and a Miyachi 300 series Fast Response Weld Head coupled to a ± 0.2 μm sensitivity Heidenhain displacement sensor. Cylindrical flat-ended class 2 Cu-Cr electrodes with a diameter of 3.2 mm were used. Wires were welded at right angles to each other, using variable currents from 100 A to 400 A. Weld time was 10 ms with an upslope and down slope time of 2 ms; different welding forces of 3, 5, 8 kgf was applied during the entire welding sequence.

A tensile testing in right angle is used to determine the joint breaking force (JBF). The tensile tests and were performed using an Instron model 5548 microtensile tester manufactured by Instron, Massachusetts, USA at a crosshead speed of 4 mm/min. The pseudoelasticity was tested with setting cyclic tensile testing procedure. Three joints were tested for each set of welding conditions to obtain the average JBF. The surface appearance, fracture surfaces, and cross sections of the joints are examined using an energy dispersive X-ray spectroscopy (EDX) equipped scanning electron microscope (SEM). The joints or Nitinol wires as received was sealed in Quartz tube with replacement of air with Ar gas, and then heat-treated in universal furnace.

3. Results and Discussion

3.1 Optimization of RMW of CW Nitinol wires

The effects of welding current on JBF at different welding forces are shown in Figure 1. Under a certain welding force, JBF increased sharply with the increase of current. Further increase of current resulted in overwelding and degradation to joint strength due to the introduction of weld defects. An onset welding current of 100 A was required to initiate bonding. The maximum JBFs of 8N, 11.8N, and 12N were achieved at different welding forces of 2kgf, 5kgf, and 8kgf, respectively.

Transition of fracture modes from interfacial at low currents to HAZ at high currents was schematically shown in Figure 2. Mixed mode failure occurred when using intermediate currents. The sum of their effect determines the actual joint strength. Maximum JBFs were obtained at intermediate welding currents and higher

welding force where the fracture across the whole joint, as shown in Figure 2 (d). The sound JBF achieved in high electrode force of 8kgf was benefit from the lower heat input, which reduced heat damage to HAZ.

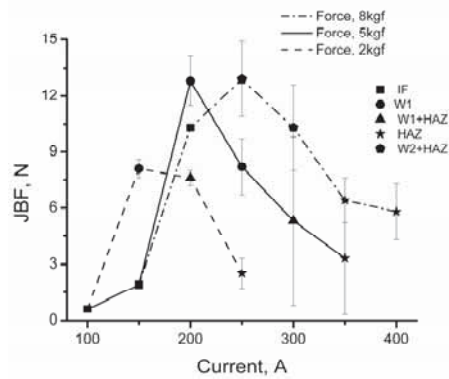


Fig. 1 JBF versus welding currents at different electrode forces

3.2 Effect of heat treatment on JBF and SME

The JBF comparison of joint as welded at the parameters of 8kgf and 250A between joints heat-treated with different aging or solid-solution parameters is shown in Figure 3. There was no sufficient change of JBF with aging at 300°C for 1h compared with as welded joint. Whereas, JBF was increased from 12N to 30N when heat treating at 800°C for 5min, but judged from the S-S curve, as shown Figure 4, the heat treatment with 800°C for 5min destroyed the SME. Unacceptably, the JBF conversely decreased, when heat treated with combination annealing at 800°C for 5min with aging @ 300°C for 1h. Micrograph of cross-sections of joints as welded and heat treated at 800°C for 5min were shown in Figure 5. The heat treatment caused the growth and unification of grains in the regions, and was helpful to release stress concentration to some extent, which contribute to the increase of JBF. But the rapid growth of grains changed the microstructure of joints which was directly related to the SME.

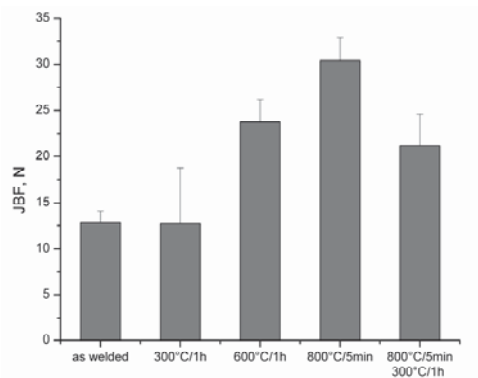


Figure 3: JBF of as welded joint and heat-treated joints at different conditions

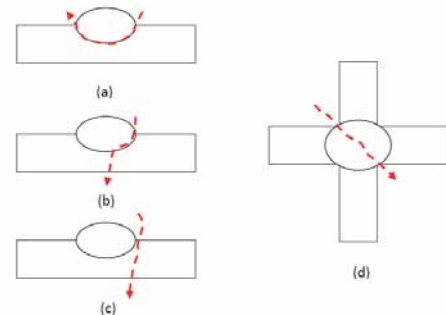


Fig. 2 Schematic of failure modes transitioning (a) Interface (IF), (b) From weld (W1), (c) From HAZ (HAZ), (d) From weld (W2)

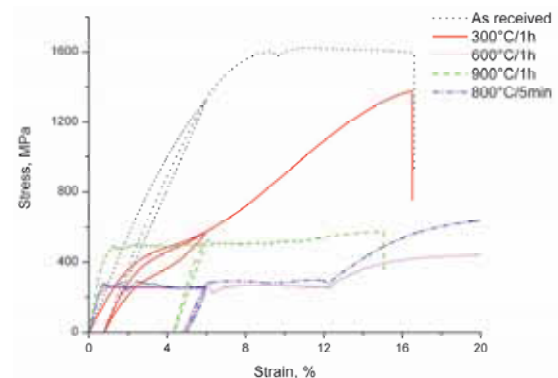


Figure 4: Curves of Strain - Stress of CW wires at different heat treatments

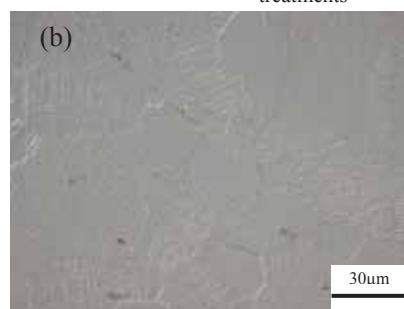
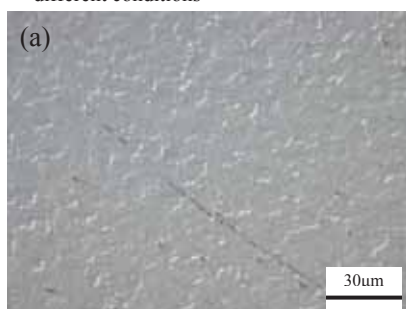


Figure 5: Cross sectional images of CW wire joint as welded (a) and heat treated joint as annealed at 800°C for 5mins(b)

4. Conclusions

The effect of heat treatment on RMW joints of crossed wires have been investigated. The major conclusions are summarized as follows: 1) Solid solution at 800°C with 5mins increased JBF from 12N to 30N; 3) Solid solution destroyed the pseudoelasticity due to the change of microstructure with grain growth.

References

- [1] G. B. Kauffman, I. Mayo, The story of Nitinol: The serendipitous discovery of the memory metal and its applications, The Chemical Educator, 1997, vol. 2(2), 1-21.
- [2] Billy Tam, Micro-Welding of Nitinol Shape Memory Alloy, Master thesis of University of Waterloo, 2010.

Effect of ITO Interlayer on the Au/Hg₃In₂Te₆ Schottky Contact Characteristics

Li Yapeng, Congyuan Liu, Li Fu*

State Key Laboratory of Solidification Processing, School of Materials Science and Engineering,
Northwestern Polytechnical University, Xi'an 710072, China

Email: fuli@nwpu.edu.cn



Abstract: ITO interlayer was deposited on the surface of Hg₃In₂Te₆ (short for MIT) wafer by Pulsed Laser Deposition method. Then element distribution and core level at the ITO/MIT interface were analyzed by X-ray photoelectron spectroscopy. In addition, the electrical characteristics of Au/ITO/MIT Schottky contact was studied by current-voltage (*I-V*). The results showed that the element diffusion at the ITO/MIT interface appeared. Meanwhile, the binding energy of O 1s, Sn 3d and In 3d increased about 0.5 eV, 0.3 eV, 0.2 eV at the interface respectively. Furthermore, the leakage current of Au/MIT schottky contact decreased from 2.28×10^{-4} A to 8.11×10^{-5} A and the Schottky barrier height increased from 0.522 eV to 0.606 eV when the ITO interlayer was applied.

Keywords: Au/Hg₃In₂Te₆ Schottky contact; ITO interlayer; XPS; *I-V*

1. Introduction

MIT is a novel semiconductor material for near-infrared photoelectric detection^[1]. It's obviously important to get a stable schottky contact between the electrode and MIT wafer during the manufacture of the MIT infrared detectors. Some researchers have found that the ITO interlayer should reduce the leak current of the Schottky contact^[2-4]. In addition, the ITO interlayer could improve the quantum efficiency of the MIT photodiode^[5]. At present, the effect of ITO interlayer grown by pulsed laser deposition (shorted for PLD) on the property of MIT photodetector was not reported. In this paper, PLD was applied to prepare ITO interlayer on the surface of MIT crystal. The X-ray photoelectron spectroscopy (XPS) was applied to analyze interface characteristics of ITO/MIT structure. Meanwhile, the influence of ITO layer on the electrical properties of Au/ITO/MIT schottky contact was discussed in detail.

2. Experiments

MIT ingot with the diameter of 30 mm grown by vertical bridgman method was cut into $5 \times 5 \times 1$ mm³. After mechanical polishing, the wafers were then chemical polished in 2% (bulk concentration) Br₂-C₃H₇NO solution for 1 minute to remove the mechanical damage on the surface of MIT wafer. At the same time, the MIT wafers were cleaned in deionized water and dried. Then the ITO interlayer was deposited on cleaning MIT wafers by PLD. Finally, the Au electrode was deposited on the ITO layer and Cu electrode was evaporated on the other side of MIT wafer by means ofmethod to get the Au/interlayer/MIT Schottky contact.

In this paper, the elements distribution and core level at ITO/MIT interface was studied by the ESCALAB 250Xi X-ray photoelectron spectroscopy (XPS). The electrical properties of the Au/ITO/MIT Schottky barrier diode was analyzed by the Agilent 4155C semiconductor parameter analyzer.

3. Results and Discussion

Figure 1. show the core level spectra (a) and the distribution of elements (b) at ITO/MIT interface by XPS depth profiling. From Fig.1(a), it's obvious that the binding energy of O 1s, Sn 3d_{5/2} and In 3d_{5/2} were 530.11 eV, 486.61 eV and 444.81 eV respectively for the ITO layer on the MIT wafer before Ar⁺ etching. According to the XPS database, there are In₂O₃ and SnO₂ on the surface of ITO layer before Ar⁺ etching. After Ar⁺ etching seven times, the binding energy of O 1s increase about 0.5 eV. The binding energies of Sn 3d_{5/2} and In 3d_{5/2} were shifted to the high energy level about 0.3 eV and 0.2 eV respectively. It can be deduced that the element diffusion may happened at the interface between ITO layer and MIT wafer. After the etching eight times, it was found that the binding energy of O 1s and Sn 3d kept constant, as well as the In 3d_{5/2} binding energy were shifted 0.4 eV to the high energy level. It can be speculated that In-O bond instead of In-Te bond may happened during the deposition of ITO layer.

Figure.2 is the *I-V* characteristics of the Au/MIT contact and Au/ITO/MIT schottky contact at room temperature. It was found that the reverse leakage current decreased from 2.281×10^{-4} A to 8.11×10^{-5} A after the introducing of ITO interlayer. This may be due to the reduction of dangling bonds and decreasing the interface defect density on the surface of MIT when the ITO interlayer was applied

It is well known that the thermal Emission model (TE) was widely used for the calculation of the Schottky height. According to TE model, the relationship between current *I* and diode bias *V* under positive bias could be obtained as follows^[5]:

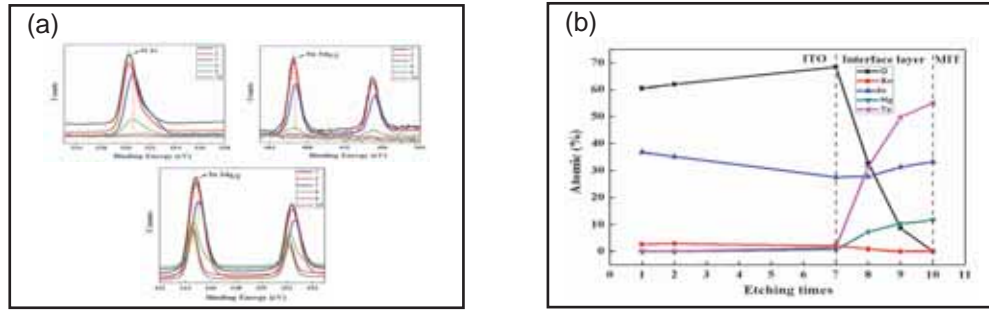


Fig.1. The core level spectra (a) and the distribution of elements (b) at the ITO/MIT interface by XPS depth profiling during the Ar⁺ etching process

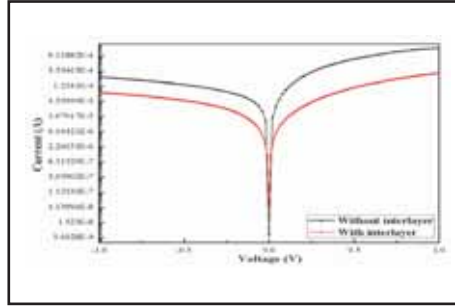


Fig.2 The *I-V* characteristics of Au/MIT and Au/ITO/Hg₃In₂Te₆ Schottky contact

$$I = I_s \left[\exp \left(\frac{qV}{nk_0T} \right) \right] \quad (1)$$

$$I_s = AA^*T^2 \exp \left(-\frac{q\phi_b}{k_0T} \right) \quad (2)$$

$$A^* = \frac{qm_n^*k_0^2}{2\pi^2h^3} \quad (3)$$

where I_s is the saturation current, n is the ideality factor, k_0 is Boltzmann's constant, T is thermodynamic temperature, A is the contact electrode area, A^* is the effective Richardson constant, q is the electronic charge, ϕ_b is the zero-bias barrier height, m_n^* is the electron effective mass. By TE model, the Schottky barrier heights of the Au/ITO/MIT and Au/MIT Schottky contacts were calculated to be 0.606 eV and 0.522 eV respectively. It was due to the mutual diffusion existed at the interface between the ITO layer and MIT wafer, which decreased lower energy level gaps in the depletion layer.

4. Conclusions

Through XPS depth profiling, it was found that the element diffusion at the interface between ITO layer and MIT wafer. Meanwhile, the binding energy of O 1s, Sn 3d and In 3d increased about 0.5 eV, 0.3 eV, 0.2 eV respectively at the interface. Compared with Au/MIT schottky contact, it can be obtained that the leakage current of Au/ITO/MIT schottky contact decreased from 2.28×10^{-4} A to 8.11×10^{-4} A and the Schottky barrier height increased from 0.522 eV to 0.606 eV.

References

- [1] P M Spencer, B Ray, "Phase Diagram of the Alloy System Hg₃Te₃-In₂Te₃", Journal of Physics D: Applied Physics, 3;299-301(1968).
- [2] L A Kosyachenko, Y S Paranchich, V N Makogonenko, V M Sklyarchuk, E F Sklyarchuk, I I German, "Electrical Performance of HgInTe Surface-barrier Photodiodes", Technical Physics, 48;647-650(2003).
- [3] L A Kosyachenko, I S Kabanova, V M Sklyarchuk, O F Sklyarchuk, I M Rarenko, "Hg₃In₂Te₆-Based Photodiodes for Fiber Optic Communication", Physica status solidi (a), 206;351-355(2009).
- [4] Z M Grushka, P N Gorley, O G Grushka, P H Paul, I R Yarema, Z Zhuang, "Mercury Indium Telluride- a New Promising Material for Photonic Structures and Devices", Materials and Nanostructures[C].International Society for Optics and Photonics,2006.
- [5] R T Tung. "Recent advances in Schottky barrier concepts", Materials Science and Engineering R, 35; 1-138(2001).

Low-temperature combustion joining of carbon/carbon composites

**A.A.Nepapushev¹, Ya-Cheng Lin², A.S. Rogachev^{1,3}, P.J. McGinn²,
A.S. Mukasyan^{1,2},**

¹ National University of Science and Technology, Moscow, Leninskiy pros. 4, 119049, Russia

² Depart. Chem. & Biomolec. Eng., University of Notre Dame, Notre Dame, IN, 46556, USA

³ Institute of Structural Macrokinetics and Materials Science Russian Academy of Sciences, Chernogolovka, Moscow Region, Acad. Osipyan street 8, 142432, Russia

Email: anepapushev@gmail.com



Keywords: joining of refractory materials, high energy ball milling, composites

1. Introduction

Combustion joining (CJ) is an attractive method for joining of a variety of materials. Due to short (seconds) processing time, energy efficiency, simple technological equipment and the ability of producing joint layers with functionally-graded properties this method has proved as an effective tool for joining of refractory and dissimilar substances.

Combinations of properties of carbon/carbon (C/C) composites, such as low density, high strength-to-weight ratio, as well as high thermo-elastic stability at elevated temperatures, make it attractive material for a variety of applications. These characteristics allow using C/C composites for producing rocket nozzles, noses and leading edges of reentry vehicles, as well as gas turbine engine components. As the demand for such materials increases, development of rapid and energy-efficient techniques for joining C/C composites are of great interest. White et al.[1], reported joining of refractory C/C composites via a class of refractory materials (carbides, borides, etc) by CJ. However, a short-term (~30 sec) but high-temperature (up to 2000 K) preheating of the joint stack was required in order to initiate the chemical reaction in the joint layer, which affected the composite properties.

Here is reported an improved combustion-based technique for bonding of C/C composites by using a CJ approach with a reactive mixture of titanium and mechanically activated Ni/Al powders. The present work focused primarily on validating the concept of low temperature joining of C/C composites with a reactive mixture of Ti powder and Ni/Al mechanically activated composites [2].

2. Experiments

Short-term (15min) high-energy ball milling (HEBM) of an equiatomic Ni + Al powder mixture (15g of Ni + Al mixture per batch) was carried out using a PM100 (Retsch, Germany) planetary ball mill with a 250 mL stainless steel jar and 2mm diameter stainless-steel balls as the milling medium in an inert atmosphere (argon). The ball-to-mixture ratio was 2:1. The rotational speed of the mill was 650 rpm. X-ray diffraction (XRD) analysis was performed to determine the phase composition of the initial Ni+Al mixture and after 15 min of MA. Results suggested that no new phases (NiAl, NiAl_x solid-solution, etc.) were formed after 15min ball milling of Ni+Al powder mixture under the investigated conditions. It was shown that such a mechanical activation treatment allows one to significantly decrease the self-ignition temperature of Ni/Al reactive mixture.

Cylindrical C/C samples (10 mm in diameter x 12.5 mm in length) were fabricated from a commercial C/C aircraft brake disk (Honeywell Aerospace, South Bend, IN) with a density of 1.67 g/cm³ and a total open porosity of 15%. A thin disk (0.3g, 10mm in dia. X 2 mm in height), cold-pressed from the powder medium, was placed in between the two C/C composite pieces to be joined. The disk was composed of 0.1 g of pure Ti powder (- 325 mesh, Alfa Aesar) and 0.2 g of mechanically activated Ni/Al composite with a molar ratio of 1:1 (initial Ni and Al powders, -325 mesh, AlfaAesar).

Figure 1 demonstrates a scheme of the C/C joining configuration. The reactive medium stack, i.e. Ti+(Ni/Al)MA+Ti is placed between two C/C composites. Once triggered, the heat release and high temperature of the Ni/Al reaction facilitates the interaction between the Ti and the C/C composites, forming a TiC phase and simultaneously bonding the C/C composites. After the joining process, it is expected that a functionally graded joint layer (i.e., C/C-TiC-NiAl-TiC-C/C) will be produced.

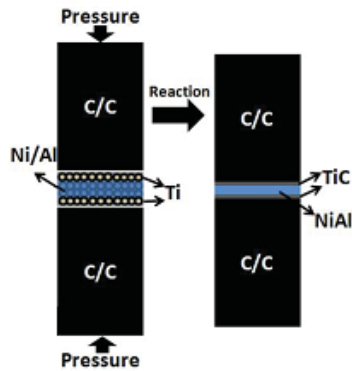


Fig. 1 Schematic illustration of the C/C joining

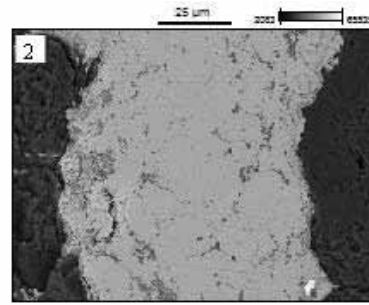


Fig. 2. Cross-sectional image of joined layer

3. Results and Discussion

Figure 2 shows typical back-scattered electron (BS) SEM images of a joined C/C sample cross-section in the vicinity of the joint layer. It can be seen at lower magnification that a crack-free joined layer $\sim 75\text{--}100\ \mu\text{m}$ in thickness was produced by the CJ method. Based on the joining scheme a three-step mechanism was suggested: (1) at an early stage the mechanically activated Ni/Al composite powders are rapidly initiated by direct heating of the C/C sample stack, forming NiAl solid solutions; (2) melting of the Ti powder (1900K) due to the chemical reaction of Ni/Al and the continued Joule heating of C/C sample; a minor part of the molten Ti diffuses into the NiAl solid solutions, while the majority of the mobile Ti stays active in the high temperature environment and is squeezed into the boundary of the intermediate layer and the C/C matrix; (3) the molten Ti reacts with the C/C composite and forms a TiC_y phase.

Joined samples were machined to a configuration suitable for tensile-strength testing. As expected in brittle C/C materials, the rupture occurred without a pronounced strain difference ($\varepsilon \sim 0.04$) in the course of elongation. In this typical case, the obtained ultimate tensile strength of a joined C/C sample was $\sim 5.8\ \text{MPa}$. More importantly, the rupture occurred through C/C composite, indicating that the joined layer was stronger than the C/C matrix.

4. Conclusions

The present work focused primarily on validating the concept of low temperature joining of C/C composites with a reactive mixture of Ti powder and Ni/Al mechanically activated composites. The novelty of the technique is that use of a mechanically activated reactive medium enables joining of C/C composites by a rapid and energy-efficient CJ method by preheating the C/C stack to only 630 K, and produces a robust joint layer. Such a method could be further applied to joining refractory C/C composites with a variety of configurations, and has the potential for scaling up to join larger specimens.

References

- [1] J.D.E. White, A.H. Simpson, A.S. Shteinberg, A.S. Mukasyan, "Combustion joining of refractory materials: Carbon - carbon composites", *J. Mater. Res.*, vol. 23, 160–169, (2008).
- [2] Y. C. Lin, A. A. Nepapushev, P. J. McGinn, A. S. Rogachev, A. S. Mukasyan "Combustion joining of carbon/carbon composites by reactive mixture of titanium and mechanically activated nickel/aluminum powders", *Ceram. Int.*, vol. 39(7), 7499-7505, (2013).

The mechanism of melting point depression in AlSi/AlN nanomultilayered systems

J. Lipecka¹, J. Janczak-Rusch^{1,2}, M. Andrzejczuk¹, M. Lewandowska¹, G. Richter³ and L.P.H. Jeurgens²

¹ *Warsaw University of Technology, Woloska 141, 02-507 Warsaw, Poland*

² *Empa, Swiss Federal Laboratories for Materials Science and Technology, Überlandstrasse 129, 8600 Dübendorf, Switzerland*

³ *Max Planck Institute for Intelligent Systems, Heisenbergstrasse 3, 70569 Stuttgart, Germany*

Email: joanna.lipecka@gmail.com



Keywords: Nanojoining, Melting Point Depression (MPD), Nanomultilayers (NML), Transmission Electron Microscopy (TEM)

1. Introduction

The aim of the study is to evaluate the structural changes in Al-Si/AlN nanomultilayers upon annealing for low temperature joining applications. It is known that due to relatively high thermal sensitivity of nanometals, standard methods of joining, e.g. furnace brazing or welding, are not suitable as they cause e.g. grain coarsening [1]. To overcome the limitations of conventional brazing technologies, our research strategy aims to employ the size-dependent melting behaviors of metals confined in a nanostructured multilayer geometry. As the literature shows, the use of such a nano-architected configuration can reduce the processing temperature, thus allowing benign joining of heat sensitive nanometals [2,3]. Evidently, the development and application of such new technologies requires fundamental understanding of the melting point depression phenomenon, as presented in this study.

2. Experiments

The system investigated consisted of Al-Si (12%) braze filler nanolayers (bulk $T_m=577^\circ\text{C}$) with a thickness of 4 nm alternated by aluminium nitride diffusion barrier layers with a constant thickness of 3 nm. The bilayer of AlN/Al-Si was repeated 10 times (with additional AlN layer on the top) on the Si substrate covered with additional two diffusion barrier materials of SiO_2 and Si_3N_4 , respectively. The nanomultilayer (NML) system was produced by magnetron sputtering and provided by Central Scientific Facility Thin Film Laboratory, Max Planck Institute for Metals Research, Stuttgart, Germany. In order to investigate the melting behavior, the system was heat treated at the following temperatures: 300°C , 400°C , 500°C and 550°C for 10 minutes in a small silica glass furnace with an argon shielding atmosphere. The evaluation of the temperature range of surface droplet formation and their chemical composition was carried out with the use of FEI NovaNanoSEM 230 Scanning Electron Microscope (SEM). Subsequently, cross section lamellae of the as-deposited and the heat treated multilayers were prepared directly under the surface droplets using a NB5000 FIB-SEM. The cross-sectional specimens were examined using a Hitachi-HD2700 Scanning Transmission Electron Microscope (STEM) and EM 912 Omega/Carl-Zeiss Transmission Electron Microscope (TEM).

3. Results and Discussion

The TEM observations of the as-deposited state showed that the Al-Si/AlN system consists of polycrystalline layers of AlN and Al-Si. The individual nanolayers possess a very fine structure with grain sizes similar to the corresponding film thicknesses. The chemical analysis using EDX revealed a homogenous distribution of both Al and Si throughout the Al-Si layers, which suggests that the layers consist of a single phase: i.e. a highly supersaturated solid solution of Si in an Al matrix. Annealing up to 300°C did not cause any significant changes in the multilayer structure. A distinct phase separation within the Al-Si layers was evidenced for annealing temperatures $T > 300^\circ\text{C}$, where the supersaturated solid solution phase-separates into Al-rich and Si-rich regions. As follows from the low mutual solubility of Si and Al at these intermediate temperatures, the phase separation is thermally activated at $T > 300^\circ\text{C}$ and governed by bulk thermodynamics.

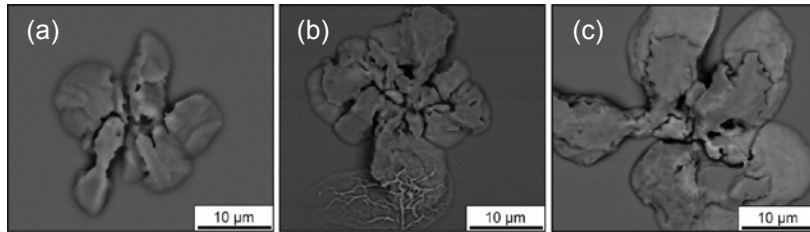


Fig. 1. Branched-shaped surface morphologies of Al and Si metal outflow during annealing of the Al-Si/AlN NML: (a) at 400°C, (b) at 500°C, (c) at 550°C.

Melting of the confined Al-Si alloy was evidenced by the emergence of branched-shaped protrusions of Al and Si on the outer surface of the NML. Fig. 1 shows the SEM micrographs of the branched-shaped structures developed on the Al-Si/AlN surface after annealing at different temperatures. First appearance of these structures was noticed at a temperature of 400°C, in parallel with the thermal activation of the phase-separation process. The droplets have an irregular shape and are randomly distributed on the surface. Their size as well as their surface density increase with the annealing temperature.

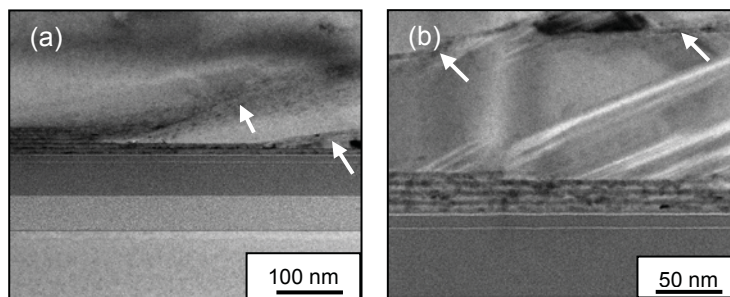


Fig. 2. STEM micrographs of the Al-Si/AlN NMLs annealed at 400°C in the central region underneath a branched-shaped structure

Local chemical analysis revealed that the branched-shaped protrusions constitute Si- and Al-rich phases. Cross-sectional STEM observations of central regions underneath these metal protrusions revealed that the NML structure was locally damaged and thinned. Some of the AlN layers were deformed and exhibited bumps due to the accumulation of the liquid Al-Si metal underneath (Fig. 2a), while others were fractured and their fragments were embedded in the branched-shaped protrusions (Fig. 2b). These results suggest that the melting in Al-Si NMLs at reduced temperatures is triggered by the phase separation of the confined metastable Al-Si solid-solution phase. The formation of cumulated liquid metal domains within the multilayer induces a deformation of the AlN barrier layers, which results in local fracture of the AlN barrier and subsequent outflow of confined liquid metal to the specimen surface.

4. Conclusions

A melting point depression of around 177°C was observed for nano-sized Al-Si(12%) brazing fillers (thickness: 4nm) confined between AlN diffusion barrier layers. The onset of melting at $300\text{ °C} < T < 400\text{ °C}$ proceeds after phase separation of Al and Si from the confined metastable Al-Si solid solution phase within the NML. As a result, branched-shaped dual-phase structures consisting of Al and Si emerge on the NML surface. Detailed analysis revealed that metal outflow is triggered by the phase separation process and the associated formation of large domains of accumulated liquid AlSi within the NML structure. The cumulation of liquid metal deforms the AlN nanolayer, which can lead to local rupture of the AlN barriers with subsequent outflow of liquid metal to the NML surface.

References

- [1] M. Lewandowska and K.J. Kurzydłowski, "Thermal stability of a nanostructured aluminium alloy", *Materials Characterization*, vol. 55, 395–401 (2005).
- [2] M. Türpe, J. Janczak-Rusch, B. Grünenwald and V. Bissig, "Approach for Al brazing with nano filler metals", *DVS-Berichte Band 289*, 125–129 (2012).
- [3] J. Janczak-Rusch, G. Pigozzi, B. Lehmert, M. Parlinska, V. Bissig, W. Tillmann, L. Wojarski and F. Hoffmann, "Deposition and utilization of nano-multilayered brazing filler systems designed for melting point depression", *Proceedings from the 5th International Brazing and Soldering Conference, Las Vegas, USA, 22–25 April, 162-168 (2012).*

Effects of warpage on HiP during BGA packaging

Zhenyu Zhao¹, Chuan Chen², Yuming Wang³, Chang Yong Park⁴, Lei Liu¹, Jian Cai², Qian Wang², Hailin Bai¹, Guisheng Zou¹

¹ Department of Mechanical Engineering, Tsinghua University, Beijing 100084, China

² Institute of Microelectronics, Tsinghua University, Beijing 100084, China

³ Training Center for Basic Industry, Tsinghua University, Beijing 100084, China

⁴ Samsung Electronics Co. Ltd, Asan-City, Chungnam, 336711, Korea

Email: eliayes@163.com (for poster)



Keywords: warpage, Head in pillow, BGA

1. Introduction

Head in pillow (HiP) is a BGA defect which occurs when solder ball and solder paste can't contact well during reflow soldering [1, 2]. For an HiP joint, there is neither metallurgical bonding between solder ball and paste nor an appropriate joint shape although mechanical contact has been established. Among the factors affecting HiP, warpage is the main reason which is induced by mismatch of thermal expansion between EMC (Epoxy Molding Compound), silicon chip and substrate. The warpage lifts solder balls out of paste and forms a poor contact during reflow[1]. Other factors such as oxidation worsen the situation[2]. This paper studies the warpage thresholds for HiP: above which HiP tends to occur and below which HiP normally does not form .

2. Experiments

Sn-3.0Ag-0.5Cu solder paste was a product of KOKI Inc. Three kinds of dummy packages were used in the experiment as shown in Fig.1. HIP000 had no chip inside the package, while HIP200 and HIP520 had 200 μ m and 520 μ m thick chip inside the package, respectively. The component warpage was calculated as Fig. 2 defined and measured with shadow moiré method. The symbols + or - represents the direction of warpage and the number represents the value of warpage. Acceleration experiment was performed by aging the surface mounted components (190 $^{\circ}$ C for 3~5min) before reflow process.



Fig.1 Package structures used in experiment

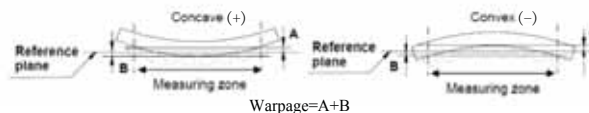


Fig.2 Definition of component warpage[3]

The smallest warpage that induces an HiP is defined as the warpage threshold for HiP. BGA package with warpage above the threshold tends to form HiP and below the threshold normally does not have HiP. To find this warpage threshold, the samples were put on the BGA rework station to go through a reflow process and the whole process was recorded with a high speed camera. The soldered BGA packages were analyzed to locate the soldering joint having HiP. Then the video was played back to measure the warpages of the same HiP joint and its adjacent joints did not have HiP (as shown in Fig. 3). Joints of HIP000, HIP200 and HIP520 in air or N₂ atmosphere were measured.

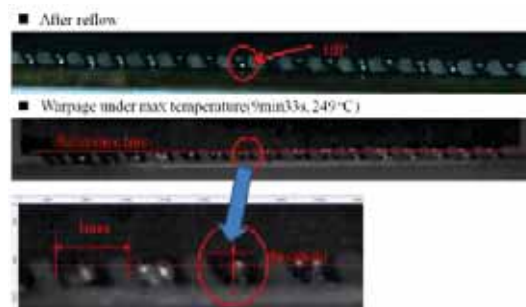


Fig.3 Analysis method for warpage threshold

3. Results and Discussion

Warpage of different packages were as measured in Fig. 4a. The initial package warpage was not zero, which was because the different shrinkage rates in EMC solidification process. As increasing the reflow temperature, the warpage direction of all three packages changed from concave (+) to convex (-) and reached the maximum at the reflow peak temperature. The package warpage peaked at the highest reflow temperature (250°C) and fell back to its initial value as the temperature cooling down. The warpage at the highest temperature is directly related to the HiP because the melting, wetting and joining occurs in this moment. Therefore, the following warpage value is the absolute warpage value at the peak temperature. Results demonstrate that the HIP520 had the smallest warpage (around 40µm), while HIP000 and HIP200 had a similar warpage (around 80µm). And the HiP occurrence rate of HIP000 and HIP200 were higher than that of HIP520, as shown in Fig. 4b. Besides HiP, opening defect was also observed. The defects occurrence rate of HIP200 and HIP000 was four times more than that of HIP520. Packages with a larger warpage (especially at high temperature) can induce more defects.

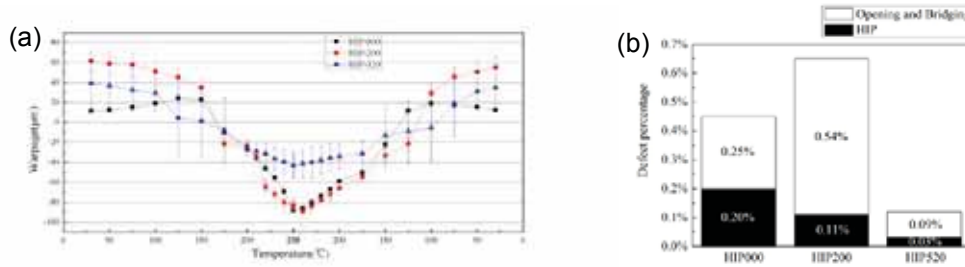


Fig.4 (a) Warpage versus temperature and (b) defect occurrence rate of HIP000, HIP200 and HIP520

The results for warpage threshold were counted in Table. 1. HIP200 had a smaller warpage threshold (101µm in N₂, 54µm in air) compared with HIP000 (150µm in N₂, 102µm in air) under same condition, which indicates that the large warpage change of HIP200 worsen the solder results and accelerate the forming of HiP or other defects. For HIP000 and HIP200, the threshold in N₂ atmosphere is 50µm less than that in air. The reason was that in N₂ atmosphere, a better contact condition was kept compared with joints in air. But for HIP520, the atmosphere seemed have no difference on results. It is because the largest warpage of HIP520 was about 50µm, so the threshold can't be larger than it (but it still happened at joints with the largest warpage).

Table.1 Thresholds for warpage

Package	Atmosphere oxygen content(ppm)	Position(number of solder joint counted from the left)	Threshold for HiP (µm)
HIP000	1100	6	150
	air	4	102
HIP200	180	8	101
	air	4	54
HIP520	1800	3	51
	air	4	49

4. Conclusions

- (1) Package with a thick chip (HIP520) inside had the smallest warpage (50µm) while the package with no chip (HIP000) or thin chip (HIP200) had a large warpage (above 90µm). The HiP occurrence rate increased by three times as warpage enlarged twice.
- (2) The smallest warpage inducing an HiP was defined as the warpage threshold for HiP. The threshold in N₂ atmosphere was measured 50µm larger than that in air for HIP000 and HIP200, indicating that the occurrence of HiP was a combined effects of warpage, solder oxidation, and flux.

References

- [1] Sidhu R S, Aspandiar R, and Vandervoort S, et al, "Impact of processing conditions and solder materials on surface mount assembly defects", JOM, 63(10), 47-51 (2011).
- [2] Liu Y, Pamela Fiacco M S, Lee N. "Testing and prevention of head-in-pillow", Electronic Process Technology, 33(5), 272-276 (2012).
- [3] JEITA ED-7306, "Measurement methods of package warpage at elevated temperature and the maximum permissible warpage", Japan Electronics and Information Technology Industries Association (2007).

Investigation of memory effect in the $\text{Ge}_2\text{Sb}_2\text{Te}_5$ thin films by DC and pulse measurements

**P. Lazarenko¹, A. Sherchenkov¹, S. Kozyukhin², S. Timoshenkov¹, D. Gromov¹,
M. Michaylova¹**

¹National Research University of Electronic Technology (MIET), Bld. 5, Pas. 4806, Zelenograd, Moscow, 124498, Russia,

²Kurnakov Institute of General and Inorganic Chemistry, RAS, Leninsky Pr., 31, Moscow, 119991, Russia

Email: aka.jum@gmail.com



Keywords: Chalcogenide materials, Phase change memory, Memory effect, Electrical properties, Thin films, $\text{Ge}_2\text{Sb}_2\text{Te}_5$

1. Introduction

Materials of the $\text{GeTe-Sb}_2\text{Te}_3$ pseudobinary line, in particular $\text{Ge}_2\text{Sb}_2\text{Te}_5$ (GST225), are considered to be most perspective materials for applications in memory devices - phase change memories (PCM) [1-3]. Principle of operation of the PCM is based on the rapid reversible phase transitions between amorphous and crystalline state, which take place in nanovolume of material under low-energy external influences. These phase transformations are accompanied by abrupt changes in electrical properties of the materials [4]. Phase change memory operated by electrical impulse is one of the main candidates for a new generation of memory devices [5, 6]. But many questions related to the electrical properties, in particular switching and memory effects in PCM materials, are still open. Therefore, the aim of this work is to investigate the effect of memory in the thin films of $\text{Ge}_2\text{Sb}_2\text{Te}_5$ by DC and pulse measurements.

2. Experiments

The initial $\text{Ge}_2\text{Sb}_2\text{Te}_5$ alloy was synthesized with using of quenching technique [7]. The materials (99.99% purity) were sealed in evacuated ($5 \cdot 10^{-3}$ Pa) quartz ampoules then step by step heated to 800 °C in a rocking furnace to ensure homogeneous melt. Thin films were prepared by thermal evaporation of the synthesized GST225 in vacuum. Residual pressure in the chamber was 10^{-4} Pa. The maximum temperature during evaporation was kept under 903 K.

The polycrystalline and amorphous structures of the synthesized alloys and as-deposited films, respectively, were checked by X-ray diffraction (Rigaku D/MAX, Cu K α $\lambda = 0.15481$ nm) [8]. Rutherford backscattering (RBS) method was used for study the composition of the thin films. The results of RBS studying showed that deposited thin films had a composition of the $\text{Ge}_2\text{Sb}_2\text{Te}_5$ with accuracy about $\pm 10\%$.

Special samples with a vertical structure were fabricated for the investigation of memory effect in GST225 thin films. Solid aluminum layer and gold probe were used as a bottom and top electrodes, respectively. The thicknesses of GST225 films were detected with using of AFM (NT-MDT SolverPro), which were in the range from 100 to 150 nm.

The research system on the basis of KEITHLEY 6486 and a voltage control unit NI6008 was used for the DC measurements. The set-up on the basis of rectangular pulse generator G5-61 and oscilloscope LeCroy WaveRunner 44xi with active probe LeCroy ZS-1000 was used for the pulse measurement.

3. Results and Discussion

Fig. 1 (a) shows current-voltage characteristic of thin film of GST225 by DC measurements. The experimental data suggest that there are four voltage-dependent regimes:

- ✓ A-B. OFF state. Initial thin film of GST225 in amorphous state has a high resistivity (~ 10 MOhm).
- ✓ B-C. A region of negative differential resistance can be seen, when threshold voltage ($U_{th} = 3,6$ V) is attained, which is transition from high resistance OFF state to low resistance ON state. This transition takes place during the time t_{sw} .
- ✓ C-D. ON state. Thin film of GST225 has a low resistance (~ 1 kOhm).
- ✓ E-D. Second measurement showed that thin film of GST225 kept low resistance state. Calculated resistivity for ON state is comparable to the resistivity of thin films in crystalline state.

Pulse voltage measurements were carried out for estimation of the recording time. The results of the pulse measurements are shown in Fig. 1 (b). Rectangular pulse with amplitude of 4 V and duration of 600 ns was applied to the investigated structure with load resistance in series (700 Ohm). Voltage of the structure was measured by oscilloscope.

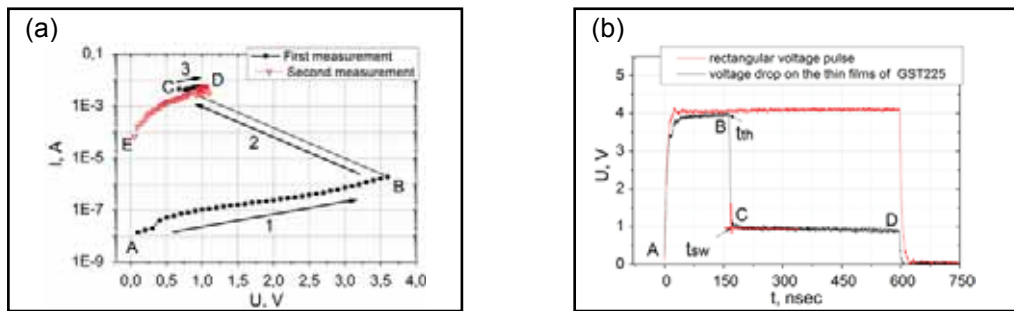


Fig. 1. Memory effect in the thin film of $\text{Ge}_2\text{Sb}_2\text{Te}_5$: (a) current-voltage characteristic by DC measurements; (b) transients from OFF state to ON state when applying a pulse.

The obtained data suggest that there are four regimes as for DC measurements. Voltage drop was observed after the time of $t_{th} = 160$ ns due to the transition from OFF to ON state. Transition time was as low, as $t_{sw} = 10$ ns. Thus the full recording time was 170 ns, which significantly less than recording time in the flash memory ($\sim 10\,000$ ns).

4. Conclusions

Memory effect in thin films of $\text{Ge}_2\text{Sb}_2\text{Te}_5$ was investigated by DC and pulse measurements. Memory programming was accomplished by applying a 160 ns voltage pulse to the vertical structure based on the $\text{Ge}_2\text{Sb}_2\text{Te}_5$ thin films, thus inducing the phase transition of the chalcogenide layer from amorphous (OFF) to crystalline (ON) state.

References

- [1] N. Yamada et al., "Rapid-phase transitions of $\text{GeTe-Sb}_2\text{Te}_3$, pseudobinary amorphous thin films for an optical disk memory", *J. Appl. Phys.*, vol. 69(5), 2849–2856 (1991).
- [2] G. Nicolescu, I. O'Connor, C. Piguet, *Design Technology for Heterogeneous Embedded Systems*, Springer, 339-364 (2012).
- [3] D. Lencer, M. Salinga, and M. Wuttig, "Design Rules for Phase-Change Materials in Data Storage Applications", *Adv. Mater.*, vol. 23, 2030–2058 (2011).
- [4] A. Lacaita, "Phase change memories: State-of-the-art, challenges and perspectives", *Solid-State Electronics*, vol. 50, 24–31 (2006).
- [5] H.-S. P. Wong et al., "Phase Change Memory", *Proceedings of the IEEE*, vol. 98(12), 2201–2227 (2010)
- [6] G. W. Burr et al., "Phase change memory technology", *Journal of Vacuum Science and Technology B*, vol. 28(2), 223- 262 (2010).
- [7] S. Kozyukhin, A. Vargunin., A. Sherchenkov et al., "Thermal effects in Ge-Sb-Te phase-change memory materials during multiple thermal cycling", *Physica Status Solidi (c)*, vol. 7(3-4), 848–851 (2010)
- [8] P. Lazarenko, A. Sherchenkov, H.P. Nguyen, S. Kozyukhin, "Influence of Bi doping on electrical and optical properties of phase change material $\text{Ge}_2\text{Sb}_2\text{Te}_5$ ", *Journal of Optoelectronics and Advanced Materials*, vol. 13(11-12), 1400–1404 (2011)

The reflow process under nitrogen and air atmosphere was compared. After soldering, the on-off test was carried for 28 soldered PCBs. The defect rate = (number of defect /total joints) × 100%. There were 2,586 solder points on each PCB, and a total of 72,408 points on 28 PCBs. The total number of defects in nitrogen atmosphere was 14, the defect rate was 0.019%. There were 19 defects under air atmosphere, and defect rate was 0.026%. It indicated that nitrogen atmosphere can lower the defect rate, comparing to air. It is believed that the wettability of lead free solder paste on PCB was improved in nitrogen atmosphere. Meanwhile, the oxidization was reduced, and the soldering reaction was speeded up. Therefore, the quality and the reliability of the soldering joint were improved comparing with the soldering in air.

As shown in Fig.2, the intermetallic compounds at the soldering interface varied with different surface conditions. According to the SEM results, $(Cu, Ni)_6Sn_5$ formed on ENIG pad. Whereas, Cu_6Sn_5 formed on OSP pad. The joints soldered under air had more cracks compared with joints soldered under nitrogen. Besides, the denser IMC on ENIG resulted in better reliability compared with that on OSP.

Table.2 On-off test results^[2]

PCB*	Component			
	201		402	
	Number of defect	Rate of defect	Number of defect	Rate of defect
N-O	11	0.015	2	0.003
N-Ni	1	0.001	0	0
A-O	11	0.015	0	0
A-Ni	7	0.009	0	0

*N-nitrogen atmosphere, A-air atmosphere, O-OSP, Ni-ENIG

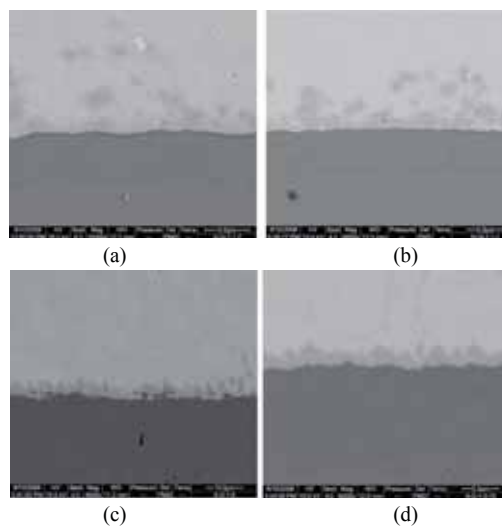


Fig.2 soldering results on (a) ENIG and (c) OSP under air atmosphere and (b) ENIG and (d) OSP under nitrogen atmosphere^[2]

3. Conclusions

1. An optimal PCB design was carried out for wave soldering, and the special soldering pad design is needed when QFP and DIP were soldered by wave soldering.
2. Quality and the reliability of the joint soldered in nitrogen were better than that soldered in air.

References

- [1] WANG Yu-ming, YANG Jian-xin, and WANG Tian-xi. DFM of Soldering Pad of QFP and DIP for Wave Soldering. Electronics Process Technology, 34(6):315-319(2013).
- [2] FENG Tao and WANG Yu-ming. Impact of Nitrogen on Lead-free Reflow Temperature. Electronics Process Technology, 31(4):191-195(2010).

Hermetic TLP bonding of MEMS for harsh environments

G. Spinola Durante¹, R. Jose James¹, S. Mohrdiek¹,
M. Despont², P. Niedermann²

¹CSEM Alpnach Untere Gründlistrasse 1, CH-6003 Alpnach Dorf (Switzerland)

²CSEM SA, Rue Jaquet-Droz 1, CH-2002 Neuchâtel (Switzerland)

Email: gsd@csem.ch



Keywords: TLP, bonding, MEMS, AuSn, hermetic, vacuum, harsh environment, reliable

1. Introduction

The main driving force for this development is to address the needs for low-cost and hermetic wafer-level packaging technologies targeting high yield, wafer scalability and improved reliability in harsh environments. Possible applications of this technology are in the field of TLP die-attach for MEMS operating in corrosive media or in high temperature conditions. Wafer-level high-vacuum hermetic MEMS TLP sealing, compatible to getter activation (350 °C – 450 °C), is also of interest for packaging microsystems requiring a stable vacuum atmosphere over life. Other possible applications are in the field of optoelectronic die-attach due to the shorter melting time and low chip-scale bonding pressure (<0.1 MPa) required for TLP bonding of the AuSn layers.

2. Experiments

This work addresses AuSn solder deposition overall process compatibility with wafer-level technologies. The main focus is in realizing high quality AuSn layers suitable for wafer-level TLP bonding (Fig.1), in continuity with former developments at CSEM. The first development task was concentrating in optimizing the Under-Bump Metallization (UBM) to increase solder joint shear strength [1]. A further development step was to solve AuSn galvanic deposition compatibility issues with Silicon wafer manufacturing standards [2-4].

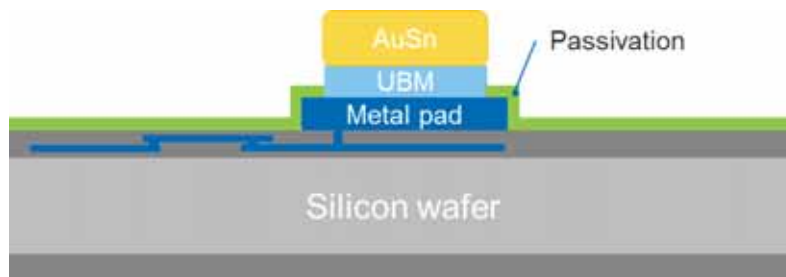


Fig. 1: Structured AuSn solder deposition on patterned UBM for standard wafer structures.

The key technical challenges are two-fold: at first the AuSn solder is deposited with very low roughness and thickness across the wafer and secondly the process is standardized to allow patterned AuSn deposition on top of a patterned UBM in a uniform fashion at wafer-level scale (Fig. 1).

3. Results and Discussion

Main achievements of this work are the following: high quality AuSn layer deposition with controlled in-wafer thickness uniformity below 10 % and low roughness <300 nm up to the edge of the wafer (Fig. 2a, b, c). Bonding line thickness is about ~15 μm and the bonding pressure can be as low as 0.01 MPa on each individual sealing ring of 100 μm width (chip-scale bonding).

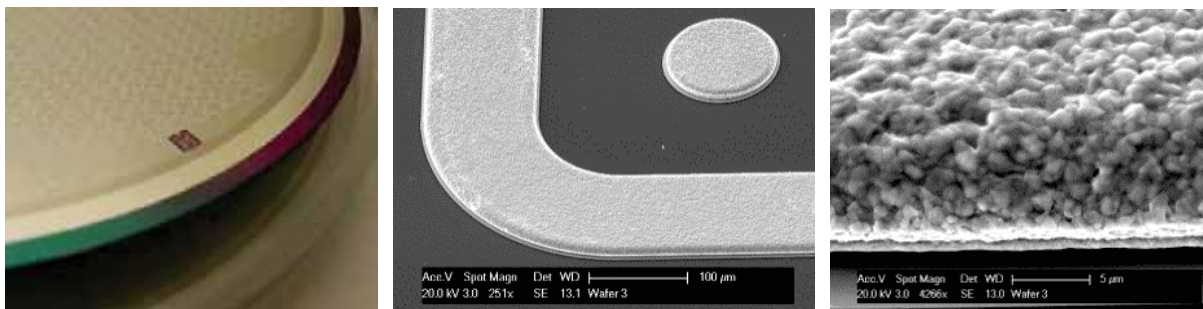


Fig. 2(a): AuSn deposition suited for TLP bonding on 4" Silicon wafer,
(b) Zoom on sealing ring detail, (c) Sn-grain structure on sealing ring surface

In Fig. 3(a) are shown the sealing rings at the edge of the un-diced wafer. The chip size after dicing is $1.5 \times 2 \text{ mm}^2$ and is shown in Fig. 3(b). These chips with AuSn sealing ring are bonded with TLP process on counterpart samples with the same ring layout but realized in pure gold. The bonded samples have a total bond line thickness of about $15 \text{ }\mu\text{m}$. Typical sheartest strength values of the samples bonded with TLP process are above 3 kg on 0.5 mm^2 sealing ring surface, and after annealing at $450 \text{ }^\circ\text{C}$ for 30 minutes the strength drops down with values still above 1.5 kg.



Fig. 3(a): Edge of the 4" wafer of the sealing ring structures (b) Zoom on one sealing ring structure with 4 contacts

The bonded sealing rings are proven to be hermetic using conventional helium spraying leak test method on a laser-milled bonded sample. This method allows normally a very high resolution down to $10^{-12} \text{ mBar}\cdot\text{l/s}$. Due to the small O-ring size required to connect the TLP bonded chip to the He-leaktester, a custom O-ring with very low Helium permeation has been used (Fig. 4a). With this configuration a resolution of about $10^{-11} \text{ mBar}\cdot\text{l/s}$ is still obtained (Fig. 4b).

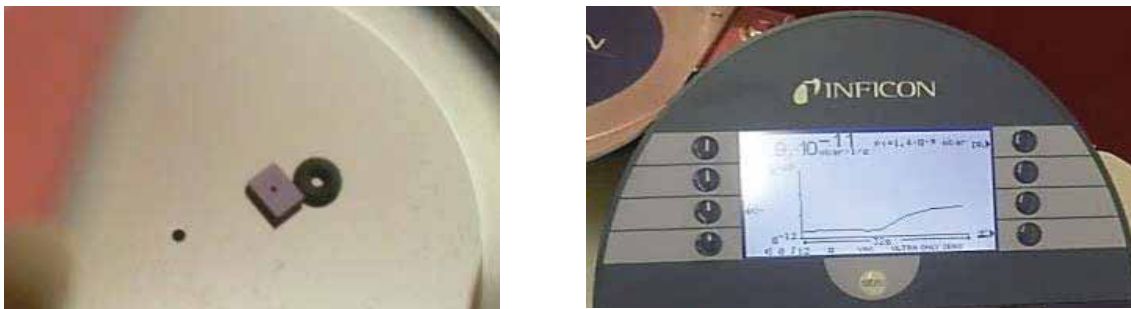


Fig. 4(a): Laser-milled hole in TLP bonded sample and O-ring, (b) O-ring permeation contribution for leak tight TLP bonded sample

4. Conclusions

CSEM offers structured AuSn galvanic depositions for wafer-level hermetic Transient Liquid Phase (TLP) bonding. Focus of this development is the high AuSn thickness uniformity (in-wafer $<10 \%$) and low roughness ($<300 \text{ nm}$ peak-to-peak), allowing for extended process window, high yield and wafer scalability. Applications are in the field of MEMS/IC packaging suited for harsh-environment and high-vacuum sealing. Know-how in bonding, reliability testing and failure analysis is also offered to adapt the solder deposition layers according to customer requirements.

References

- [1] G. Spinola Durante and R. Jose James et al., "Reliable Hermetic Chip-scale Packaging Targeting Wafer-level Bonding", CSEM Scientific and Technical Report 2010, pag. 100 (2010)
- [2] G. Spinola Durante and R. Jose James et al., "Gold-tin Galvanic Optimization for Hermetic Sealing", CSEM Scientific and Technical Report 2011, pag. 23 (2011)
- [3] G. Spinola Durante and R. Jose James et al., "Reliable hermetic MEMS chip-scale packaging", Proceedings, 18th IMAPS European Microelectronics & Packaging Conference (EMPC 2011), pp. 152-157, 2011
- [4] G. Spinola Durante and R. Jose James et al., "Gold-Tin Based Hermetic Wafer Level Packaging", CSEM Scientific and Technical Report 2013, pag. 43 (2013)

Laser Induced Microjoining

Hailin Bai¹, Lei Liu^{1,2}, Guisheng Zou¹, and Y. Norman Zhou³

¹Department of Mechanical Engineering, Tsinghua University, Beijing, , China

²The State Key Laboratory of Tribology, Tsinghua University, Beijing, China

³Department of Mechanical & Mechatronics Engineering, University of Waterloo, Waterloo, Canada,

Email: bhl@tsinghua.edu.cn (for poster)



Keywords: Laser, nanojoining, microjoining

1. Introduction

Laser microjoining/welding technology has been applied in many industries, such as defense, life science, medical, microelectronics etc. As the development of material science and product design, laser microjoining/welding technology needs to be developed accordingly. In this poster, laser induced microjoining is performed, including laser microbrazing of CNT yarn, laser micro braze welding of Pt to stainless steel, laser directly welding of glass.

2. Experimental procedure

(1) For laser microbrazing of CNT yarn

High strength and conductive super-aligned CNT yarns are made from the produced carbon nanotube wafer by a twisting and shrinking method. The brazing alloy used here is a ternary Ag-Cu-Ti alloy with a chemical composition of 3 wt. % Ti, 62.2 wt. % Ag and 34.8 wt. % Cu. A Nd:YAG pulse laser is used as the laser source with a pulse energy of 4.1J and repetition rate of 10Hz.

(2) For laser micro braze welding of Pt to stainless steel

Pt-10 pct Ir (wt pct) wire and cold-worked 316 LVM SS wire, both of 0.38-mm diameter, were used in this study, and a simple rectangular pulse profile was used for all welds[1].

(3) For laser directly welding of glass

Fused silica glass was directly welded by using a femtosecond laser (50fs, 1kHz, max. 4mJ/pulse, Gaussian beam profile).

2. Results and Discussion

Figure 1 shows micro brazing of CNT yarn by using a Nd:YAG pulsed laser. With increase of pulse number, the joint strength increased and peaked at 55 pulses. The cross section of the micro brazed joint showed that the CNT yarn was completely surrounded by the AgCuTi filler metal. The Ti element riched at the periphery region of the CNT yarn indicated that Ti-C compounds formed which contributed to the joint strength.

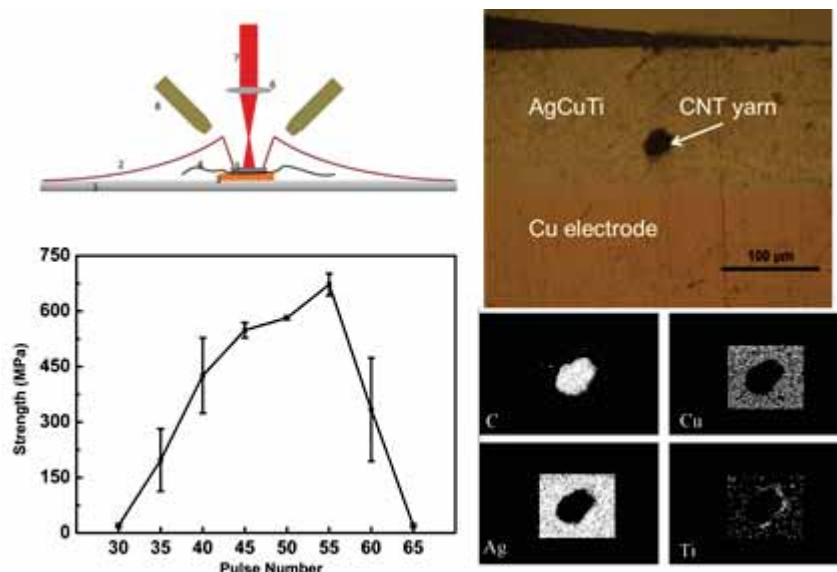


Figure 1 Laser micro brazing of CNT yarn

Figure 2 shows micro braze welding of Pt to stainless steel. The Pt and SS wire were cross clamped and the laser beam fired from the top. The cross section showed that top wire melted and wetted on the bottom wire. The joint strength increased with laser power and peaked at 40N between 0.3-0.4 peak power of laser. The joining mechanism showed in the schematic diagram.[1]

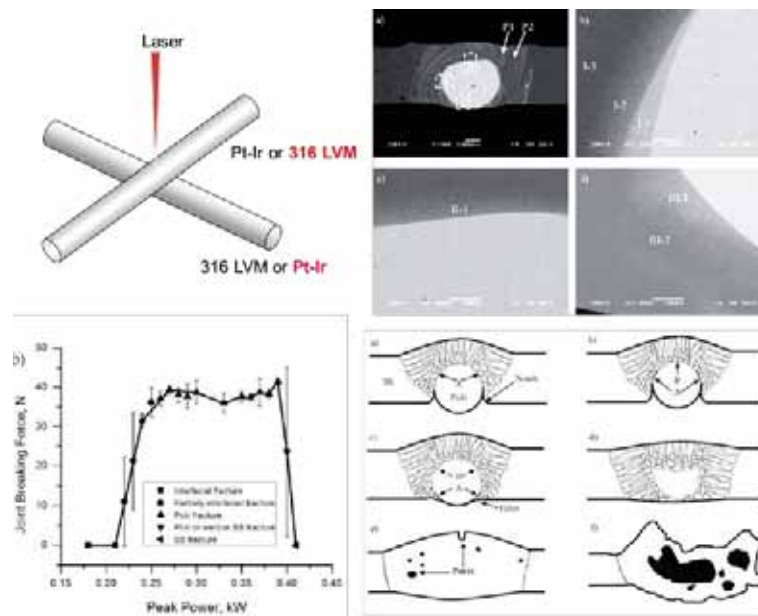


Figure 2 Laser braze welding of Pt to stainless steel[1]

Figure 3 shows the quartz glass joined by femtosecond laser. By utilizing the non-linear absorption of femtosecond laser, the transparent quartz glass was directly welded without any interlayers. The cross section clearly showed the weld seam width was around 30 μ m. The scanning electron microscopy image showed the fusion zone of the glass has few defects. The maximum shear strength of the joined glass was around 40 MPa.

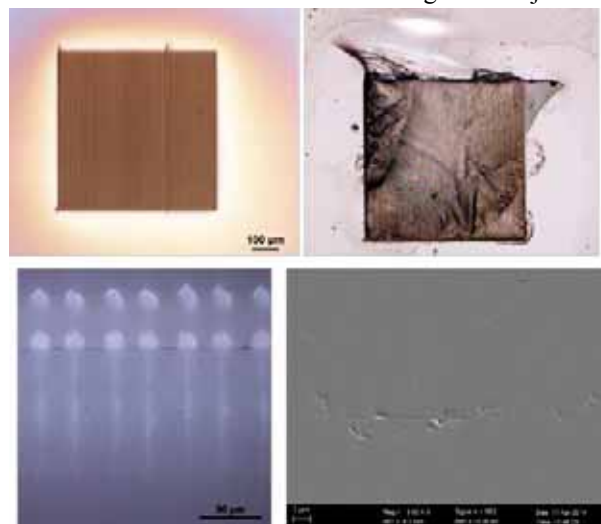


Figure 2 Femtosecond laser directly welding of quartz glass

4. Conclusions

CNT yarns, Pt micro wires, and quartz were successfully joined by laser micro joining. The configuration, microstructures, joining mechanisms and joint strength were investigated and discussed.

Acknowledgement

This work was supported by National Natural Science Foundation of China (Grant No. 51375261, 51075232), by The Natural Science Foundation of Beijing (Grant No. 3132020), by the Specialized Research Fund for Doctoral Program of Higher Education (Grant No.20130002110009) and by Tsinghua University Initiative Scientific Research Program (Grant No.2010THZ 02-1, 2013Z02-1).

References

[1] G. Zou, Y.D. Huang, A. Pequegnat, etc, Metall. Mater. Trans. A, 43 (4), 2012, 1223-33

Preparation and Sealing of Polymer Microchannels using EB Lithography to Pattern Absorber for Laser Welding

I. A. Jones¹, J. Griffiths²

1. TWI Ltd, Granta Park, Gt. Abington, Cambridge, CB1 6AL, UK

2. Cavendish Laboratory, University of Cambridge, JJ Thomson Avenue, Cambridge, CB3 0HE, UK

Email: ian.jones@twi.co.uk



Keywords: sub-micron welding, plastics, EB lithography, laser, microchannels, sealing

1. Introduction

With the drive towards ever smaller scale complex plastic products such as biological analysis chips, chemical micro-reactors and electronics products in plastics, there is a need for welding processes that meet these challenges. Laser welding developments in recent years have shown that the laser beam size can be used to limit the weld size. Welds of the order of 10 μ m in width have been demonstrated using a focused infrared laser beam of similar dimension [1-4]. Welds much smaller than this are not possible using this technique due to the resolution limits inherent in focusing a near infrared laser.

An alternative technique has been investigated using precise patterning of laser absorber dye on the plastics surface to define the weld position. This has enabled joints to be made an order of magnitude smaller than this. The new method used electron beam lithography to apply laser absorber in precise patterns, mimicking the methods used to build micro-electronic circuits. The lithographic methods were also used to generate the micro-channels with dimension of approximately 5 μ m width and depth. The absorber tracks have then been used to generate welds between two plastic parts using laser heating, sealing a lid over the channels.

2. Experiments

Electron beam (EB) lithography methods

EB lithography is typically used to generate patterns for electronic circuits in semi-conductor materials. The procedure is based upon deposition of coatings (resists) over a wide area, followed by local sensitisation of the resist material using electron beam patterning and then development of the pattern by flushing away the sensitised material with a solvent wash. The procedure can progress in two general forms:

- Positive resist, in which the EB degrades the resist in a pre-defined pattern such that the EB treated material can be dissolved away by the developer solvent.
- Negative resist, in which the EB locally cures the resist and the remaining uncured material is dissolved away.

In this work samples using both positive and negative resists were prepared with the addition of infrared absorbing dye, matching the wavelength of the laser to be used. The patterning therefore controlled the location of laser heating. Lithography was carried out using a Vistec VB6 UHR series equipment. The two resist/absorber mixes were applied to a glass substrate by spin coating at 4000rpm for 1min. This was expected to provide a 0.4 μ m thick coating of polymer, PMMA in the case of the positive resist, which was used in the bulk of the trials. Trials were carried out using 5, 1 and 0.5 μ m feature sizes. Grey-scale lithography was used to generate channels and weld tracks, prepared using two coats of PMMA, a 3.5 μ m thick coating without IR absorber overlaid with a 0.4 μ m coating with absorber.

Laser welding of tracks patterned using EB lithography

Once the tracks of resist containing IR absorber had been applied, the top was applied and clamped down. An IR laser was used to heat the absorber to melt and weld in precise locations. The laser beam was significantly larger than the absorber tracks, but passed through the plastics that were not coated with absorber to provide welds only in the required positions. Laser welding was carried out using a 150W diode laser (940nm wavelength) from Laserline defocused to a 3mm wide beam.

Welded samples were selected for sectioning and examination. Regions of the resist deposits that had not been patterned were also welded at the same conditions to assess whether strong welds could be made using the spin coated material. Tensile lap-shear tests were carried out with these samples.

3. Results and Discussion

Negative resist: When the initial laser welding trials were carried out on samples coated with negative resist, the joint strength was not good. Trials using IR absorber alone had shown good strength. Further work was not carried out with this resist due to these problems with poor dissolution of the absorber, unusual development and poor weld strength. The nature of the cured cross-linked negative resist material may have acted as a barrier to diffusion of the plastic during welding. This is likely to be a fundamental problem that would make the use of a negative tone resist difficult as a coating to promote heating and welding.

Positive resist: Initial weld trials showed that good weld strength could be achieved using PMMA positive resist with added IR absorber. In tensile lap-shear tests a 25mm wide sample failed at an average of 624N, with failure in the parent material at the edge of the weld. This is a similar result to that seen with a normal infrared coating. Patterned samples with 5 μ m and 0.5 μ m features were prepared as shown in Fig.1 and Fig.2. 5 μ m wide welds were formed between the two sheets of PMMA at the points where the lithographically formed tracks had been made.

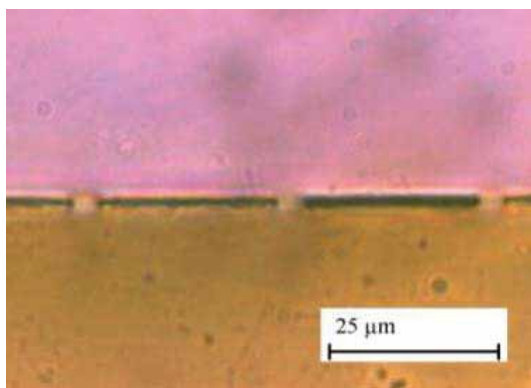


Fig. 1 Laser welded sample in cross section (48W, 100mm/min). The tops of the 5 μ m wide tracks have been welded to the top sheet of PMMA. Gaps with a height of a few hundred nanometres have been left on either side of the welded tracks.

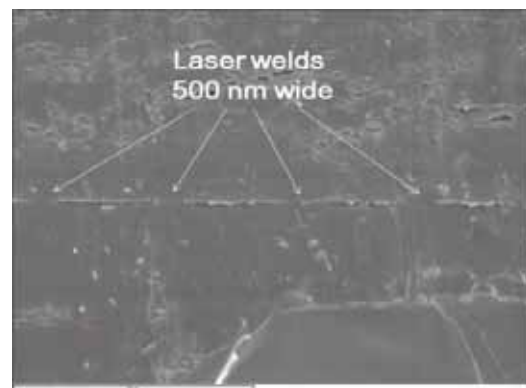


Fig.2 Laser welded sample showing 0.5 μ m wide welds (48W, 3000mm/min).

The samples using grey-scale lithography were also welded and showed 5 μ m wide channels with 1 μ m wide infrared absorber tracks on either side. These were processed using a laser power of 50W at a welding speed of 4000mm/min. The behaviour of a positive tone resist was better suited to use as a carrier for absorber dye and welding. There do not appear to be problems of reactions between the dye and the resist, or from the EB treatment that could have affected the dye absorber. In future, this allows new domains to be explored in welding of plastics applied to parts with micro- and nano-scale features such as in microfluidic devices.

4. Conclusions

Welds as small as 0.5 μ m width, believed to be the smallest ever made in plastics, have been demonstrated in polymethylmethacrylate (PMMA) using a combination of electron beam lithography of a positive tone resist material based on PMMA in anisole doped with an infrared laser absorber, and transmission laser welding using a near infrared diode laser. The size was accurately dictated by the dimensions of the resist pattern and the hence by the EB treatment.

References

- [1] Grewell D and Benatar A, 'Experiments in Micro-Welding of Polycarbonate with Laser Diodes', Proc. ANTEC conference of the Society of Plastics Engineers, pp1039-1044. (2003)
- [2] Chen J-W and Zykbo J M, 'Diode laser bonding of planar microfluidic devices, MOEMS, bioMEMS, diagnostic chips and microarrays', Proc. SPIE 5718, pp. 92-98. (2005)
- [3] Pflöging W, Baldus O, Bruns M, Baldini A, Bemporad E., 'Laser assisted welding of transparent polymers for micro-chemical engineering and life science', Proc SPIE 5713 pp. 479-488, (2005)
- [4] Ussing T, Petersen LV, Helbo B, Hoslet L.: 'Micro laser welding of polymer microstructures using low power laser diodes', Proc. Int. Conf. on multi-material micro manufacture, Karlsruhe, pp. 291-293. (2005)

Bondability of Mg₂Si Thermoelectric Element and Ni Electrode using Al

T. Tohei¹, S. Fujiwara¹, M. Tominaga², T. Jinushi² and Z. Ishijima³

¹ Hitachi, Ltd., Yokohama Research Laboratory, 292, Yoshida-cho, Totsuka, Yokohama, Kanagawa, 244-0817 Japan

² Hitachi Chemical Co., Ltd., Hitachi Powdered Metals, 5-2-1 Minoridai, Matsudo, Chiba, 270-2295 Japan

³ Hitachi Chemical Co., Ltd., Tsukuba Research Laboratory, 5-2-1 Minoridai, Matsudo, Chiba, 270-2295 Japan

Email: tomotake.tohei.yu@hitachi.com



Keywords: Thermoelectric, Powder generation, Bondability, Joint strength, Diffusion bonding

1. Introduction

Recently, the technology for power generating from recovered exhaust heat has been advancing. Thermoelectric generation is one such heat energy recovery technology. Thermoelectric modules can directly convert heat energy into electric energy^[1]. However, these modules have only been used in special applications, such as satellite power supply, because of the high cost and low conversion rate to electricity.

A thermoelectric generation system has many advantages that include ease of maintenance, because of its simple structure and lack of moving parts in the module. Therefore, many engineers have developed elements with higher conversion efficiencies using super lattice structures, nanocrystals, and new structure modules. We found that a Si-Ge thermoelectric element and electrode could be bonded reliably using low cost aluminum^[2].

Our research focused on the aluminum diffusion bonding technique for mid to high temperature (about 327–873 K) thermoelectric modules, specifically the use of aluminum for bonding between an Mg₂Si element and a nickel electrode.

2. Experiments

Aluminum foil 25 μm thick with a purity of 99 % was selected as the joint material. Fig. 1 shows a schematic view of the bonding process and specimen size. This process was performed in a chamber under a pure nitrogen atmosphere. The bonding pressure was set to 6.1×10^3 or 3.0×10^7 Pa, and the temperature of the hotplate was set to 953 K for 180 s.

Figure 2 shows a schematic view of the shear test for the Mg₂Si element/Al foil bonding/Ni electrode thermoelectric element. The Ni electrode was held on a shear tester stage, and the shear test was executed with a shear speed of 50 μm/s and a shear height of 200 μm. The available loading range was under 1000 N.

Characterization of Mg₂Si to Ni electrode joints with Al foil was conducted by field emission-scanning electron microscopy (FE-SEM).

Cross sections of the bonding interface were prepared after the joint sample was molded in epoxy resin. The surface of the cut sample was polished with polishing papers and diamond paste. FE-SEM observations and quantitative analysis by energy-dispersive X-ray spectroscopy (EDX) were then performed.

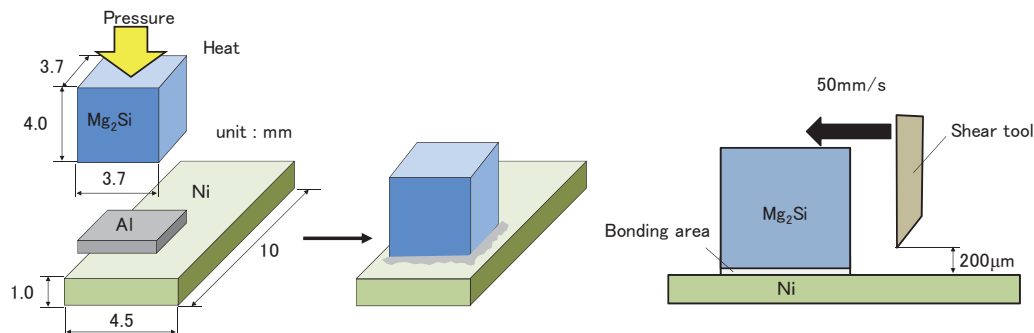


Fig. 1 Schematic views of bonding process to joint between Mg₂Si element and Ni electrode with Al foil.

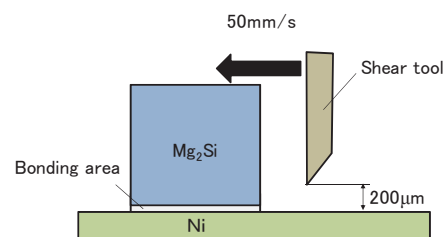


Fig. 2 Schematic view of shear test for Mg₂Si element to Ni electrode with Al bonding.

3. Results and Discussion

Figure 3 shows the results of shear testing one for each bonding condition. Elements No. 1 and 2 were bonded under low pressure (6.1×10^3 Pa) while No. 3 was bonded under high pressure (3.0×10^7 Pa). In addition, element No. 2 had its Mg_2Si surface polished before bonding. Element No. 1 showed the lowest strength because of low wettability between the Mg_2Si surface and molten aluminum. This low wettability can be explained by the surface oxide film on the Mg_2Si , which is consistent with the Ellingham diagram that magnesium is easily oxidized^[3]. Element No. 2, surface-treated Mg_2Si , exhibited a shear strength higher than element No. 1 because of the elimination of the oxide film. The shear strength of element No. 3 achieved 17 MPa and the joint formed an Al-Ni reaction layer that included magnesium and silicon. This demonstrated that bonding under high pressure has the largest effect on improving bondability under each tested condition.

A prototype Mg_2Si /Si-Ge twin couple module was bonded on the basis of the results of the shear test. This prototype Mg_2Si /Si-Ge twin couple module, bonded at 3.0×10^7 Pa, generated 1 W without damage at $\Delta T = 620$ K. This output level is 20 % higher than that of a conventional Si-Ge/Si-Ge twin couple module.

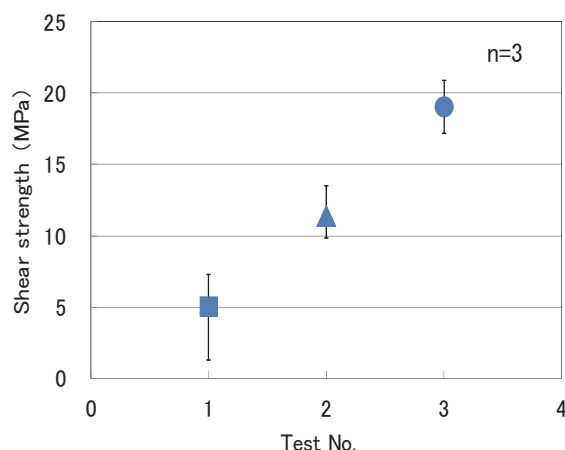


Fig. 3 Results of shear strength tests between the Mg_2Si element and Ni electrode ('n' is the number of samples for each test condition).

4. Conclusions

Aluminum foil was tested as an alternative material to conventional silver alloy braze because of its cost advantage and bondability.

- (1) The shear strength of the aluminum joint between the Mg_2Si element and the nickel electrode was 17 MPa when bonded at 3.0×10^7 Pa.
- (2) The generation capacity of the prototype Si-Ge/ Mg_2Si twin couple module was 20 % higher than that of a conventional silver alloy braze Si-Ge/Si-Ge twin couple module.

References

- [1] D. Rowe, ed.: 'Thermoelectrics and its energy harvesting', 1st edition, CRC, (2012), pp. 1-2.
- [2] T. Tohei, et al.: J. Jpn. Soc. Powder Metall., Vol. 60 (2013), pp. 360-366.
- [3] The Japan Institute of Metals, ed.: 'Material data book', 3rd edition, Maruzen, (1993), pp. 96.

Wetting properties of borosilicate glass on microstructured Kovar surfaces by high-energy density beam texturing

Hong Li¹, Ming Tie¹, Zhuoxin Li¹ and Wolfgang Tillmann²

¹ College of materials science and engineering, Beijing University of Technology, Beijing 100124

² Dortmund University of Technology, Dortmund 44227

Email: hongli@bjut.edu.cn



Keywords: Glass-to-metal seals, Borosilicate glass, Kovar alloy, wetting, micro- and nanostructured, high-energy density beam texturing, oxide film

1. Introduction

Glass-to-metal seals (GTMS) have wide applications in the electrical and solar industries, e.g. complex miniature electrical and electronic components, solid oxide fuel cells (SOFC) and solar receiver tubes etc. [1]. Kovar alloy (Fe-Ni-Co), which has similar coefficient of thermal expansion (CTE) to hard borosilicate glass, has been extensively used for matched GTMS [2]. However, due to the different chemical bonds, it is hard to achieve a perfect contact between molten glass and solid metal surface. In general, the metal surface are pre-oxidized at elevated temperatures before sealing to generate thick oxide layer. Then the oxide layer is dissolved into glass in fusion bonding process, which promotes chemical bonding of glass to metal.

However, despite of the effect of thickness and type of oxide layer on the interface reaction, the quality of matched seal depends on the wetting behavior of molten glass on the metal surface. Recent work has shown that solid surface in micro and nanometer structure can promote liquid-solid interface wettability. Electron beam surf-sculpt technology developed by TWI can create various micrometer surface textures, which has been used in composite to metal joining [3]. In the present research, we address an interesting possibility of using electron beam and femtosecond laser to produce a variety of microstructures respectively. And the wetting behavior of borosilicate glass on micro- and nanostructured Kovar alloy surface were investigated.

2. Experiments

Kovar alloy (ASTM F-15) samples were cut into squares of 20mm×20mm×2.2mm. Two scanning waveforms of electron beam surf-sculpt were designed, i.e. spiral line and hexagon shape. And the parameters of electron beam texturing with an accelerating voltage 150kV, beam current 3mA and scanning frequency 1000Hz were set up. Furthermore, femtosecond laser pulses were applied to induce formation of micrometer-width projection. Then, the textured Kovar specimens are pre-oxidized in an electric furnace under normal atmosphere at 700, 750 and 800°C with isothermally time of 0, 5, 10, 15 and 30min respectively, followed by cooling to room temperature. The oxidation rate was calculated and the phase composition of oxide layer was analyzed using XRD. Afterwards, the borosilicate glass was cut into 3mm×3mm×2mm and placed horizontally at the center of the textured Kovar alloy for wetting experiment. Then the samples are heated from room temperature to 950, 975, 1000, 1025 and 1050°C respectively, and held for 20 min, followed by cooling to room temperature. The contact angle between borosilicate glass and Kovar alloy is measured by OCA Video based Contact Angle Measuring Device. The cross-section microstructure of glass/metal interface was observed by S-3400N SEM. The element diffusion in the interfacial region was characterized by EDS attached to SEM.

3. Results and Discussion

Figure 1 shows the metal bump on the surface of Kovar substrate with a depth of 1mm, which exits an ordered arrangement of spiral line and hexagon morphology by electron beam texturing respectively. Figure 2 shows the metal bump on the surface of Kovar substrate, which exits an ordered arrangement of circular morphology by femtosecond laser texturing. Fig. 3 are photos showing the spreading of glass on the underlying Kovar alloy as observed from the side. Fig.3 (a) shows a good wettability with a contact angle of 35° for samples which are textured and pre-oxidized in the atmosphere. Surf-sculpt treatment increase the roughness and surface area, decrease the interfacial tension between solid and liquid (F_{sl}), thus reduce the contact angle, which is beneficial to the wetting of glass on the Kovar substrate. In addition, interfacial roughening helps to produce mechanical interlocking and contributed to the strength of the seal. Fig. 4 shows the relationship between the contact angle and temperature for wetting of glass on pre-oxidized Kovar alloy. Below 1000°C, the contact angle on the non-

¹ Funded by NSFC (51275008) and Beijing Municipal Natural Science Foundation (3122008)

textured substrate decrease slowly, but decrease more quickly on the textured substrate. Above 1000°C, the difference of contact angle is diminishing until the temperature rise to 1050°C. In a certain range, the textured surface contributes to the wetting of glass on Kovar alloy. In addition, spiral line type textured morphology exhibits a good wettability compared with hexagon type, as well as femosecond laser textured morphology. Fig. 6 displays the interface microstructure of bonded glass/Kovar alloy, which formed when heated to 1050°C and held isothermally for 20min. The distribution of Fe can be clearly delineated into four zones: Kovar alloy zone, Fe-depleted zone, Fe-rich zone, and glass zone. The EDS analysis of grey substance in the glass zone proves the atom ratio of Fe, Si and O is about 2:1:4. It is not difficult to deduce that grey substance is actually Fe_2SiO_4 , which results from the solution of Fe_3O_4 into molten glass, and react with SiO_2 in glass substrate.

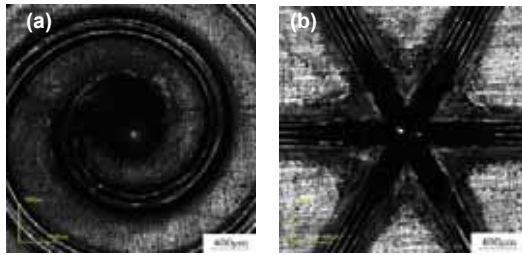


Fig. 1. The morphology of Kovar alloy by electron beam texturing (a) Spiral line type (b) Hexagon type

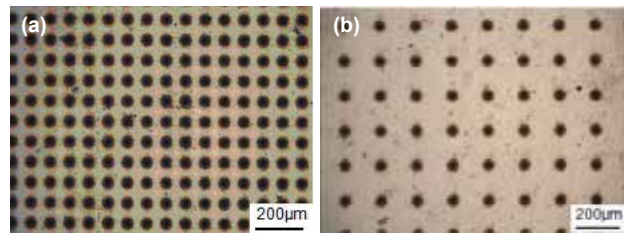
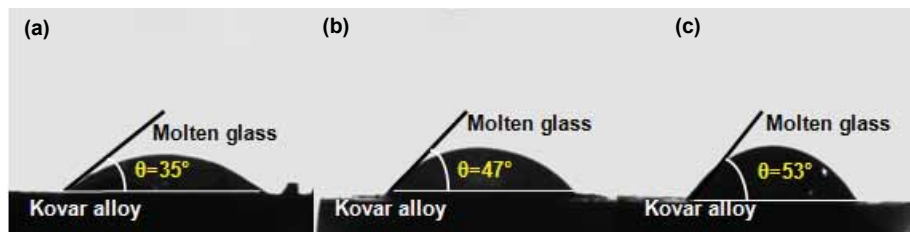


Fig. 2. The morphology of Kovar alloy by femosecond texturing (a) Clearance=0.1mm (b) Clearance=0.2mm



(a) texturing+pre-oxidation (b) no texturing+pre-oxidation (c) no texturing+no pre-oxidation
Fig. 4 Spreading of glass on the underlying alloy observed from the side

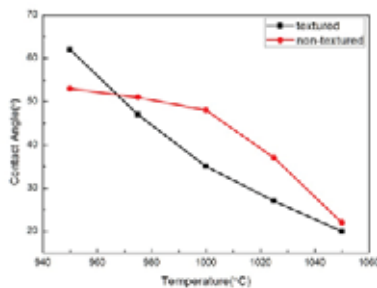


Fig.5 Curve of wetting angle and heating temperature

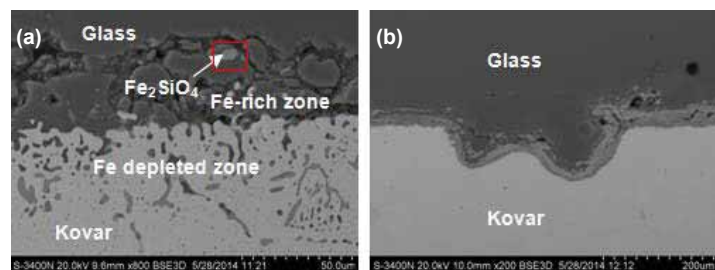


Fig.6 SEM images of glass/Kovar interface microstructure (a) non-textured Kovar alloy (b) textured Kovar alloy

4. Conclusions

The ultimate goal of glass-to-metal seal (GTMS) is to produce a consistently reliable end product. The textured surface of Kovar alloy prepared by using high-energy electron beam surf-sculpt method contribute to the wetting of glass on the substrate compared with femosecond laser pulse texturing method. Reaction between borosilicate glass and oxide layer of Kovar alloy leads to the dissolution of Kovar alloy in the glass, and the main reaction product is Fe_2SiO_4 . Besides chemical reactions, the textured Kovar alloy with higher surface roughness promotes better mechanical interlocking of glass to substrate, ensuring a better wetting behavior than the non-textured Kovar alloy.

References

- [1] I.W. Donald, P.M. Mallinson, B.L. Metcalfe, et al., "Recent developments in the preparation, characterization and applications of glass- and glass-ceramic-to-metal seals and coatings". *Journal of Materials Science*, 46(7): 1975-2000(2011).
- [2] T.S. Chern, and H.L. Tsai., "Wetting and sealing of interface between 7056 Glass and Kovar alloy". *Materials Chemistry and Physics*, 104(2-3): 472-478(2007).
- [3] Wang Xichang, Guo Enming, Gong Shuili, et al., "Study of Electron Beam Surf-sculpt during Composite Materials Joining". *Rare Metal Materials and Engineering*, 40(S4): 292-296(2011).

Recent advances in micro- and nanojoining technologies at Empa and University of Waterloo

L.P.H. Jeurgens¹, Y. N. Zhou², J.Janczak-Rusch¹

¹ Empa, Swiss Federal Laboratories for Materials Science & Technology, Dübendorf, Switzerland

² University of Waterloo, Centre for Advanced Material Joining, Waterloo, Canada

Email: lars.jeurgens@empa.ch



Keywords: nanojoining, thin films, nanoparticles, melting point depression

1. Introduction

Micro- and nanojoining processes driven by present needs as miniaturisation, material and energy efficiency, environmental friendliness are the key factor for the utilisation of nanomaterials and for enabling quantum leaps in technological advancement. The development of new joining concepts and a comprehensive treatment of joining in research as well as in education have become inalienable. Empa, Swiss Federal Laboratories for Materials Science and Technology and University of Waterloo (UW) are working together to elaborate strategies and the road-map to meet the complex scientific and technological challenges in this field [1-13]. In particular new joining concepts are developed to integrate nanomaterials in assemblies and to produce micro and nanoscale joints. With this aim nanoeffects are exploited and integrated in advanced joining schemes.

2. Experiments

Recent experimental and theoretical results of both research groups towards the development of micro- and nanojoining concepts will be presented. They involve:

- ➔ Joining **WITH** nanomaterials (utilizing nano effects)
 - ✓ Adhesives filled with nano-belts (UW)
 - ✓ Low-temperature bonding by nanowires (UW)
 - ✓ Brazing at reduced temperatures using nanostructured filler materials (Empa)
 - ✓ Nano-thermite welding (Empa, UW)
- ➔ Joining **OF** nanomaterials (e.g. nano-scale building blocks)
 - ✓ Cold welding by nanoindenter (UW)
 - ✓ Room temperature bonding by self-oriented joining (UW)
 - ✓ Room temperature joining of nanostructured metals with Nanofoils (Empa)
 - ✓ Femtosecond laser joining (UW)

3. Results and Discussion

Novel type of **nano-structured brazing fillers** with an exceptionally **high interface-to-volume ratio**, constituted of alternating nano-layers of a pure brazing metal (Cu, Ag) or an eutectic alloy (Ag-40at.% Cu) and a chemically inert diffusion barrier (e.g. AlN, Al₂O₃, C, W) have been developed at Empa, Fig.1.

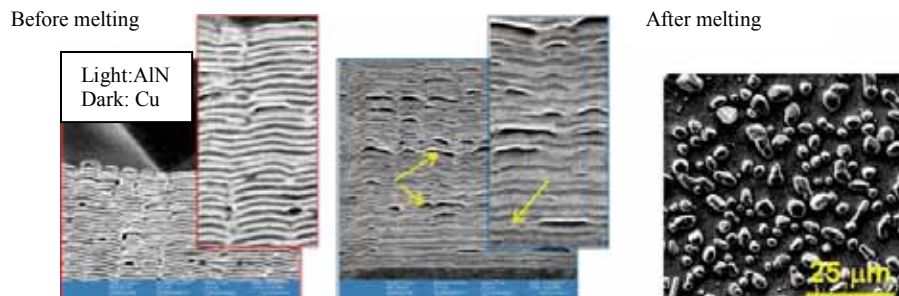


Fig.1: [Empa] Nanostructured brazing filler (10nm-Cu/10nm-AlN on Al₂O₃) in nanomultilayer (NML) configuration showing significant melting point depression of around 500°C, thus allowing a reduced brazing temperature: a) He-FIB cross-sectional micrographs of NML before (left) and after heating up to 750°C in Ar (right). Molten Cu flows out, causing local sintering of adjacent AlN layers. b) molten Cu droplets formed on NML surface after heating up to 700°C in N₂/H₂.

Femtosecond laser irradiation elaborated at UW allows joining of nanoparticles and nanowires at very low temperature, as shown on the example of Ag nanoparticles in Fig. 2 (see also Refs. [2,3]). The fs laser induces non-thermal surface melting of nanoparticles [7]. Enhanced atomic diffusion between nanoparticles owing to their high surface energy is utilized.

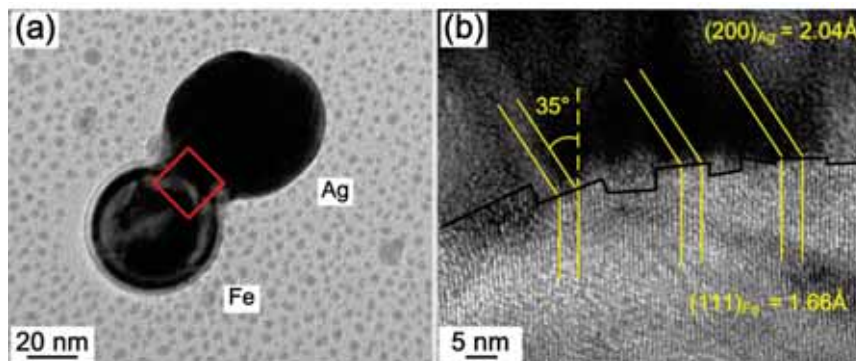


Fig.2: [University of Waterloo]Femtosecond Laser Joining of Ag NPs (a)-(b)shows joined Ag-Fe (immiscible) NPs. Note lattice matching and structural ledges at the interface to reduce interfacial energy.

4. Conclusions

A drastic melting point depression (e.g. more than 500°C for Cu nano-layers) can be achieved by nanostructuring brazing fillers and controlling interface thermodynamics. This allows brazing at temperatures much below the bulk melting point of the braze filler.

Low-temperature joining of nanoparticles is possible with femtosecond laser processes and can be preferentially used in the packaging technology for flexible electronics.

References

- [1] A. Hu, J.Y. Guo, H. Alarifi, G. Patane, Y. Zhou, G. Compagnini, C.X. Xu, *Appl. Phys. Lett.* 97 (2010) 153117.
- [2] E. Marzbanrad, A. Hu, B. Zhao, Y. Zhou, *J. Phys. Chem. C*, 117 (2013), 16665-16676.
- [3] Z. Jiao, M. Sivayoganathan, W. Duley, P. He, Y. Zhou, *J. Phys. Chem. C*, 118 (2014) 24746-24751.
- [4] J. Yan, G. Zou, A. Hu, Y. Zhou, *J. Mater. Chem.* 21 (2011) 15981.
- [5] J. Guo, C. X. Xu, A. Hu, K. Oakes, F. Sheng, Z. Shi, J. Dai, Z. Lin, *J. Phys. Chem. Solid* 73 (2012) 1350.
- [6] P. Peng, L. Liu, A. P. Gerlich, A. Hu, Y. Zhou, *Part. Syst. Charact.* 30 (2013) 420-426.
- [7] H. Huang, L. Liu, P. Peng, A. Hu, W.W. Duley, Y. Zhou, *J. Appl. Phys.* 112 (2012) 123519.
- [8] Patent No. DE 10 2008 050 433 A1 2010.04.15
- [9] G. Pigozzi, A. Antušek, J. Janczak-Rusch et al. *Appl. Phys. Lett.* 101 (2012).
- [10] J. Janczak-Rusch, G. Pigozzi, B. Lehmert et al. *BSC 2012: Proceedings from the 5th International Brazing and Soldering Conference* (2012).
- [11] G. Kaptay, J. Janczak-Rusch, G. Pigozzi, L.P.H. Jeurgens, *JMEP* 23(2014)1600-1607.
- [12] J. Janczak-Rusch, G. Kaptay, L.P.H. Jeurgens, *JMEP* 23(2014)1608-1613.
- [13] S. Brodacka, M. Kozłowski, R. Kozubski, J. Janczak-Rusch, *Comput. Mater. Sci.* (2014) 30-35.

Acknowledgment

The authors acknowledge the financial support of EU FP7-PEOPLE-2013-IRSES Project *EXMONAN - Experimental investigation and modelling of nanoscale solid state reactions with high technological impact*.

INDEX OF PARTICIPANTS

NAME	1 ST NAME	TITLE	AFFILIATION	COUNTRY	PART NO.
Alarifi	Hani	Dr.	Materials Science Research Institute, King Abdulaziz City for Science and Technology (KACST)	Saudi Arabia	R27
Bai	Hailin	Mr.	Department of Mechanical Engineering, Tsinghua University	China	R24, P3, P9
Baras	Florence	Dr.	Laboratoire ICB, Université de Bourgogne	France	R18
Breyen	Mark D.	Mr.	Medtronic Ltd.	USA	-
Buhl	Sebastian	Dr. sc. ETH	ABB Semiconductors Lenzburg	Switzerland	-
Chichkov	Boris N.	Prof. Dr	Institut für Quantenoptik, Leibniz Universität Hannover and Laser Zentrum Hannover e.V.	Germany	K4
Chiodi	Mirco	PostDoc	Empa	Switzerland	R14
Favre	Sebastian	Dr.	Medtronic Ltd.	Switzerland	-
Frey	Claudia	Mrs.	Empa	Switzerland	-
Fu	Li	Prof.	Northwestern Polytechnical University	China	R31
Fukumoto	Shinji	Associate Prof.	Graduate School of Engineering, Osaka University	Japan	R12
Gromov	Dmitry	Prof.	National Research University of Electronic Technology	Russia	R20, P4
Gröning	Pierangelo	Dr.	Empa	Switzerland	-
Grossmann	Günther	Mr.	Empa	Switzerland	R7
Habegger	Thomas	Mr.	Johnson Matthey & Brandenberger AG	Switzerland	-
Hausner	Susann	Dipl. Ing	Chemnitz University of Technology, Institute of Materials Science and Engineering	Germany	R4
He	Peng	Prof.	Welding Department, Harbin Institute of Technology,	China	I8
Hirose	Akio	Prof.	Course of Manufacturing Science, Division of Materials and Manufacturing Science, Graduate School of Engineering, Osaka University	Japan	R3, R26, P6
Hodulova	Erika	Assoc. Prof. Ing. PhD	Slovak University of Technology in Bratislava Faculty of Materials Science and Technology in Trnava, Institute of Production Technologies, Dept. of Welding and Foundry	Slovakia	I6
Hong	Won Sik	Dr.	Components & Materials Physics, Research Center, Korea Electronics, Technology Institute	South Korea	R21
Hu	Anming	Prof.	University of Tennessee Knoxville, Dept. Mech. Aerospace & Biomed. Engr.	USA	I13, R27
Huang	Yongde	Dr.	School of Aeronautical Manufacturing Engineering, Nanchang Hangkong University	China	R30
Ionescu	Adrian M.	Prof.	Ecole Polytechnique Fédérale (EPFL)	Switzerland	I9
Jung	Seung-Boo	Prof.	Sungkyunkwan University	South Korea	R0
Janczak-Rusch	Jolanta	Prof. Dr.	Empa	Switzerland	I3, R2, R10, R14, P2, P13
Jeurgens	L.P.H.	Dr.	Empa	Switzerland	I3, R10, R14, P2, P13
Jose James	Rony	Mr.	CSEM	Switzerland	R28, P8
Jung	Jaepil	Prof.	University of Seoul	South Korea	R9

INDEX OF PARTICIPANTS

NAME	1 ST NAME	TITLE	AFFILIATION	COUNTRY	PART NO.
Kaplan	Wayne David	Prof	Departement of Materials Science & Eng., Technion – Israel Institute of Technology	Israel	K3
Kashiba	Yoshiro	Dr.	Mitsubishi Electric Corp.	Japan	K1
Kenel	Christoph	PhD student	Empa	Switzerland	-
Kirkpatrick	Damian	Mr.	TWI Ltd	UK	P10
Kirihara	Soshu	Ass. Prof.	Joining and Welding Research Institute Osaka University	Japan	R23
Korvink	Jan G.	Prof.	Dept. of Microsystems Eng. IMTEK, Simulation, University of Freiburg	Germany	I7
Kovarikova	Ingrid	Ing., PhD student	Slovak University of Technology in Bratislava, Faculty of Materials Science and Technology in Trnava, Institute of Production Techn.	Slovakia	I6
Lebedev	Egor	PhD Student	National Research University of Electronic Technology	Russia	R20
Lehmert	Benjamin	Dipl.-Ing.	Lehrstuhl für Werkstofftechnologie	Germany	R22
Levina	Iryna		Medtronic Ltd.	USA	-
Lewandowska	Malgorzata	Prof.	Warsaw University of Technology, Faculty of Materials Science and Engineering	Poland	I3, P2
Li	Hong	Associate Prof/Dr	Beijing University of Technology	China	P12
Li	Mingyu	Prof.	Harbin Institute of Technology, Shenzhen University	China	R17
Li	Yujie	Dr.	School of Material Science and Engineering, Harbin Institute of Techn. at Weihai	China	R16
Lipecka	Joanna	MSc.	Warsaw University of Technology, Faculty of Materials Science and Engineering	Poland	P2
Lis	Adrian	PhD student	Empa	Switzerland	-
Liu	Lei	Assistant Prof.	Dept-of Mechanical Eng., The State Key Laboratory of Tribology Tsinghua University,	China	R24, P3, P9
Lu	Sheng	Prof.	School of Materials Science & Engineering, Jiangsu University of Science and Technology	China	R6
Mayer	Michael	Dr.	Dept. Mechanical & Mechatronics Eng., University of Waterloo	USA	-
Mei	Yunhui	Dr.	Tianjin University	China	R26
Mikhailova	Mariya	Dr.	National Research University of Electronic Technology (MIET)	Russia	-
Mohrdiek	Stefan	Dr.-Ing	CSEM	Switzerland	P8
Mori	Hiroaki	Dr.	Graduate School of Eng., Osaka University	Japan	R29
Moszner	Frank	Dr.	Empa	Switzerland	R14
Neels	Antonia	Dr.	Empa	Switzerland	R10
Nishikawa	Hiroshi	Prof.	Joining and Welding Inst., Osaka University	Japan	R8, R13

INDEX OF PARTICIPANTS

NAME	1 ST NAME	TITLE	AFFILIATION	COUNTRY	PART NO.
Ogino	Toshio	Prof.	Yokohama National University	Japan	I10
Ogura	Tomo	Dr.	Graduate School of Eng., Osaka University	Japan	R3, P6
Quintino	Luisa	Exec. Dir.	Instituto Superior Tecnico, Portugal	Portugal	R25
Richter	Gunther	Dr.	Max Planck Institute for Intelligent Systems	Germany	I12, P2
Ricolleau	Christian	Dr.	Laboratoire MPQ, Univ. Paris Diderot	France	I2
Rogachev	Alexander	Prof.	Institute of Structural Macrokinetics and Materials Science RAS	Russia	I11, P1
Sano	Tomokazu	Dr.	Graduate School of Engineering	Japan	I14, P6
Sivasubramaniam	Venkatesh	Dr.	ABB Switzerland Ltd.	Switzerland	-
Spinola Durante	Guido	Mr.	CSEM SA	Switzerland	P8
Suganuma	Katsuaki	Prof.	Institute of Scientific and Industrial Research, Osaka University	Japan	I5
Suter	Thomas	Dr.	Empa	Switzerland	R2
Szymczak	Hubert	Msc.	Admedes Schüssler GmbH	Germany	-
Tian	Yanhong	Prof.	Advanced Welding and Joining, Harbin Institute of Technology, Nangang	China	R5
Tillmann	Wolfgang	Prof. Dr-Ing.	TU Dortmund, Institute of Materials Engineering	Germany	R22, P12
Timoshenkov	Sergey	Prof.	National Research University of Electronic Technology	Russia	R20, P4
Tohei	Tomotake	Mr.	Processing Innovation Research Dept. Hitachi Ltd., Yokohama Research Laboratory	Japan	P11
Türpe	Matthias	Prof. Dr.	MAHLE Behr GmbH & Co. KG	Germany	R1
Wang	Chunqing	Prof.	State Key Lab. of Advanced Welding and Joining, Harbin Institute of Technology	China	K2, R5, R17
Wang	Fengjiang	Dr.	School of Materials Science and Engineering, Jiangsu University of Science and Technology	China	R19
Wang	Jianxin	Dr.	Jiangsu Provincial Key Laboratory of Advanced Welding Technology, Jiangsu University of Science and Technology	China	R6, R8
Wang	Yuming	Senior Engineer	The Fundamental Industrial Training Center, Tsinghua University,	China	P3, P5
Wen	John	Prof.	Department of Mechanical & Mechatronics Engineering, University of Waterloo	Canada	I4
Weyrich	Nico	PhD student	Empa	Switzerland	-
Wielage	Bernhard	Univ.-Prof. Dr. Ing.	Chemnitz University of Technology, Institute of Materials Science and Engineering	Germany	R4
Yavuz	Mustafa	Prof.	Waterloo Institute for Nanotechnology (WIN), University of Waterloo,	Canada	R15, R27
Zhao	Zhenyu	PhD student	Department of Mechanical Engineering, Tsinghua University	China	P3
Zhou	Norman	Prof.	University of Waterloo, Centre for Advanced Materials Joining	Canada	I8, R24, R27, R30, P9, P13
Zou	Guisheng	Prof.	Department of Mechanical Engineering, Tsinghua University	China	R24, P3, P9



SPONSORS



PARTNERS

